A Multi-Methodology Approach to Secondary Flow Investigations in a Low-Pressure Turbine Cascade Under Periodic Inflow Conditions

Tobias Schubert, M.Sc.

Vollständiger Abdruck der von der Fakultät für Luft- und Raumfahrttechnik der Universität der Bundeswehr München zur Erlangung des akademischen Grades eines

Doktor-Ingenieurs (Dr.-Ing.)

angenommenen Dissertation.

Gutachter:

1. Prof. Dr.-Ing. Dragan Kožulović
2. Prof. Dr.-Ing. Ronald Mailach

Die Dissertation wurde am **30.04.2025** bei der Universität der Bundeswehr München eingereicht und durch die Fakultät für Luft- und Raumfahrttechnik am **27.11.2025** angenommen. Die mündliche Prüfung fand am **16.01.2026** statt.

Danksagung

Die vorliegende Arbeit entstand während meiner Tätigkeit als wissenschaftlicher Mitarbeiter am Institut für Strahlantriebe der Universität der Bundeswehr München in den Jahren 2015 bis 2021.

Mein besonderer Dank gilt dem damaligen Institutsleiter, Herrn Prof. Dr. Reinhard Niehuis, für sein Vertrauen sowie die langjährige fachliche und persönliche Unterstützung. Herrn Prof. Dr. Dragan Kožulović danke ich herzlich für die Übernahme des Erstgutachtens. Bereits während meines Studiums in Braunschweig weckte er mein Interesse an Flugantriebwerken und prägte damit maßgeblich meinen beruflichen Werdegang. Weiterhin möchte ich Herrn Prof. Dr. Ronald Mailach für das Zweitgutachten und Herrn Prof. Dr. Christian J. Kähler für den Vorsitz des Promotionsverfahrens danken.

Ein besonderer Dank gilt auch meinen ehemaligen Kolleginnen und Kollegen am Institut für die stets angenehme und produktive Zusammenarbeit. Den technischen Mitarbeitenden des Instituts danke ich für ihren Einsatz bei der Fertigung der Versuchsträger sowie beim Aufbau und der Durchführung der experimentellen Arbeiten.Unter den wissenschaftlichen Mitarbeitenden möchte ich folgende Personen besonders hervorheben: Herrn Dr. Roberto Ciorciari danke ich für die Einführung in CFD-bezogene Forschungsarbeiten. Herrn Dr. Silvio Chemnitz danke ich für seine Unterstützung im Bereich Windkanal-Messbetrieb, Kaskaden-Design und Sonden-Messtechnik. Mein ausdrücklicher Dank gilt Herrn Dr. Martin Bitter, dessen fachliche Expertise und Unterstützung entscheidend für die Implementierung und Durchführung der optischen Messungen waren. In der späteren Phase der Forschungsarbeiten und bei der Ausarbeitung der Dissertation stand er mir stets mit wertvollen Ratschlägen zur Seite. Zusätzlich möchte ich Herrn Dr. Sebastian Brehm und Herrn Sebastian Riebl für ihre Unterstützung bei der Vorbereitung des Promotionsvortrags danken.

Zu guter Letzt gilt mein größter Dank meinen Eltern, Jochen und Ramona Schubert. Sie haben mich in jungen Jahren geprägt, inspiriert und mir stets ihre uneingeschränkte Unterstützung geschenkt.

Ingolstadt, Januar 2025 Tobias Schubert

Kurzfassung

Es wird eine umfangreiche Untersuchung der Sekundärströmungen in einer Niederdruckturbinenkaskade bei periodisch-instationärer Zuströmung vorgestellt. Die initialen Analysen zeigen einige Unsicherheiten hinsichtlich der Eintrittsgrenzschicht an der Seitenwand. Der Grund hierfür ist eine Leckageströmung durch den Spalt des Stabnachlaufgenerators. Deshalb wird ein verbessertes Kaskadendesign auf Grundlage von CFD-Studien vorgestellt. Das Hauptmerkmal dieses Designs ist eine zweiteilige ebene Platte, die in die Schaufelpassage eingezogen wird und als neue Seitenwand dient. Durch eine Verstellung in Schaufelhöhenrichtung, kann die Seitenwandgrenzschicht unabhängig der sonstigen Zuströmbedingungen eingestellt und variiert werden. Eine experimentelle Validierung bestätigt das Erreichen aller Entwurfsziele insbesondere stärker ausgeprägte Sekundärströmungen und eine eindeutigere Wirkung der periodisch-instationären Zuströmung. Anschließend wird der klassische Untersuchungsansatz auf Basis von Sondenmessungen stromauf und -ab der Schaufelpassage durch einen fortschrittlichen multimethodischen Ansatz erweitert und verbessert. Dafür werden optische Messverfahren wie Particle Image Velocimetry (PIV) and instationäre drucksensitive Farbe (i-PSP) innerhalb der Schaufelpassage implementiert. Darüber hinaus wird das hohe Potential einer ultra-schnellen temperatursensitiven Farbe (TSP) auf Ru(phen)-Basis in einem vereinfachten Testfall mit ebener Platte unter relevanten Strömungsbedingungen demonstriert. Die experimentellen Daten der Kaskadenströmung werden kontinuierlich kombiniert und mit numerischen Strömungssimulationen ergänzt und verglichen. Die Synergien aus diesem multimethodischen Ansatz ermöglichen die Quantifizierung der dämpfenden Wirkung der Nachläufe auf die Sekundärströmungen und die Analyse der zugrundeliegenden Mechanismen. Im zeitlich gemittelten Strömungsfeld stromab der Passage zeigt sich die Sekundärströmungsdämpfung durch eine Verringerung der Über-/Unterumlenkung, der Sekundärverluste und des Seitenwandabstands des Kanalwirbels. Um die Relevanz der Nachlaufeffekte einzuordnen, werden die damit verbundenen Verluste stromauf, -ab und innerhalb der Schaufelpassage mit dem Einfluss geringerer Schaufelbelastung und verringerter Seitenwandgrenzschichtdicke verglichen. Während stromab alle drei Faktoren zu geringeren Sekundärverlusten führen, sind die Mechanismen innerhalb der Passage unterschiedlich. Außerdem ist der Effekt der Schaufelbelastung etwa eine Größenordnung höher als der vergleichsweise kleine Nachlaufeffekt. Durch eine Kombination der phasenstarren und synchronisierten PIV- und PSP-Messungen kann die Bewegung der Stabnachläufe durch die Schaufelpassage nachverfolgt werden. An der Schaufelsaugseite führt der 'negative-jet-effect' der Nachläufe zu einem negativen räumlichen Druckgradienten beziehungsweise positiven zeitlichen Gradienten. In Seitenwandnähe ist dieser Effekt um ca. 33% stärker und verändert somit die Wechselwirkung zwischen Profilströmung und Sekundärströmung. In der Abströmung weist der Kanalwirbel eine periodische Verringerung der turbulenten kinetischen Energie und einen verringerten Abstand von der Seitenwand ('penetration depth') auf. Seine Ausdehnung in Schaufelteilungsrichtung wird jedoch aufgrund einer verstärkten Wirbeldissipation durch die Stabnachläufe vergrößert. Dies führt zu einer weniger

ausgeprägten beziehungsweise diffuseren Sekundärströmung stromab. Basierend auf einer Phasenverschiebung dieser Effekte zur Bewegung der Stabnachläufe kann deren Ursprung identifiziert werden. Es handelt sich um ein großes Ablösegebiet auf der Seitenwand innerhalb der Passage. Diese Ablösung scheint durch die Translation des druckseitigen Astes des Hufeisenwirbels ausgelöst zu werden. Durch die Wechselwirkung mit turbulenten Stabnachläufen wird die Robustheit der Seitenwandgrenzschicht erhöht und somit die Ablösung deutlich verringert. Insgesamt verdeutlichen die vorgestellten Mechanismen der Sekundärströmungsentwicklung und -beeinflussung, dass periodisch-instationäre Zuströmungen bei der Bewertung von Sekundärströmungseffekten im Turbinenentwurf berücksichtigt werden sollten.

Abstract

A comprehensive investigation of the secondary flow in a low-pressure turbine cascade under periodic inflow conditions is conducted. Initial analysis reveals some uncertainties regarding the inlet endwall boundary layer due to leakage flow through the gap of a bar wake generator. Therefore, an improved cascade design is presented based on CFD studies. The main design feature is an adjustable two-part flat plate, integrated at part-span and acting as a cascade endwall. This enables an independent variation of the inlet boundary layer. An experimental validation confirms the achieved design goals of more distinctive secondary flow and a more consistent effect of the periodically incoming wakes. The classic investigation approach centered around probe-based measurements up- and downstream of the blade passage is extended and enhanced by an advanced multi-methodology approach. Optical measurement setups are implemented inside of the blade passage utilizing Particle Image Velocimetry (PIV) and unsteady Pressure-Sensitive Paint (PSP). Furthermore, the potential of ultra-fast Ru(phen)-based Temperature-Sensitive Paint (TSP) is demonstrated in a flat plate test case under relevant operating conditions. A continuous combination of the experimental results and supplementation by CFD clearly showcases the added value in their synergy. This multi-methodology approach enables the quantification of the attenuating effects of periodically incoming wakes on the secondary flow and the analysis of the underlying mechanisms. In the time-averaged flow field downstream of the passage, the secondary flow attenuation is apparent by a reduction of over-/underturning, secondary losses, and the passage vortex liftoff. In order to put the relevance of wake effects into perspective, the associated losses up-, inside, and downstream of the blade passage are compared to the effects of reduced blade loading and reduced endwall boundary layer height. While all three factors lead to lower downstream secondary losses, the mechanisms inside the passage are quite different. Also, the loss reduction due to lower blade loading is about one order of magnitude higher than the relatively small periodic wake effect in this regard. By combining phase-locked and synchronized PIV and PSP measurements, the movement of the bar wakes can be traced throughout the blade passage. On the blade suction surface, the 'negative-jet-effect' of the wakes induces a negative pressure gradient in space i.e. positive gradient in time. This effect is intensified by around 33% near the endwall and alters the interaction of the blade flow with the secondary flow. The passage vortex exhibits a periodic reduction in turbulent kinetic energy and reduced spanwise distance from the endwall ('penetration depth'). However, its pitchwise extension is increased due to augmented vortex dissipation by the wakes which leads to less pronounced i.e. more diffuse downstream secondary flow. Based on a phase lag to the downstream wake passing and the measured blade-to-blade velocity field, the origin of these effects can be retraced to a large endwall separation area inside the passage. This separation appears to be triggered by the migration of the horseshoe vortex pressure side leg. The interaction with turbulent wakes significantly increases the robustness of the endwall boundary layer against this separation. The presented findings on the mechanisms of

secondary flow development demonstrate that periodically unsteady inflow conditions should be taken into account during secondary flow evaluations in turbine design.

Contents

List of Figures

1 Introduction

According to the International Civil Aviation Organization [55], the global passenger air traffic has seen a compound annual growth rate of about 5 % between 1970 and its peak before the COVID-19 pandemic. A continued growth of 3.8 % per year until 2043 is expected by the International Air Transport Association (IATA) [53]. In the same pre-pandemic time period, the average fuel burn of new commercial jet aircraft has decreased by 1.0 % per year as stated by Zheng and Rutherford [109]. A major driver for this reduction has been a continuous effort to lower the operator's cost of ownership. Additionally, emission regulations in the aviation sector have become progressively more demanding in recent years and will continue to do so. Several aviation organizations representing the industry, operators and authorities such as the ICAO, IATA, and the Advisory Council for Aviation Research and Innovation in Europe (ACARE) have committed to the long-term goal of achieving net-zero carbon emissions by 2050 [54], [52] & [1]. Additional severe reductions are expected in areas such as NOx emissions, contrails, and noise levels. The final goals will necessitate the development of novel concepts such as fuel cell powered propulsion. However, the commercial aviation sector will have to rely on continued innovation in turbomachinery based propulsion for the intermediate progress for years to come. The evolving requirements have prompted research and development efforts on the overall propulsion level as well as each jet engine module. According to Hodson and Howell [47], up to 80 % of thrust in a modern turbofan engine is provided by the high-bypass ratio fan. Since the low-pressure turbine (LPT) drives the fan plus additional booster stages, it is of high significance in terms of power generation. Also, according to Curtis et al. [26] it accounts for around 30 % of the overall engine weight. As a result of decades of aerodynamic optimization, low-pressure turbines in modern jet engines have reached high efficiencies above 90 % as stated by Hodson and Howell [47]. Since further improvement is becoming progressively more difficult, there has been an ongoing design trend towards a reduction in the stage count and number of blades per stage with the goal of weight savings and lower operating costs. The consequent need for airfoils with higher aerodynamic loading leads to strong transverse pressure gradients in the blade passage and thus to intensified secondary flow also referred to as endwall flow. Especially in the first LPT stage with a lower aspect ratio, the secondary flow extends over a larger range of the blade span and accounts for a significant part of the overall losses. Secondary flow effects in turbines are therefore a highly relevant topic in the turbomachinery industry as well as the research community.

An overview of the vast amount of research which has been conducted on secondary flow and its influencing factors is given in Chapter 2. The majority of this research has been conducted in turbine cascades under steady inflow conditions. Periodically unsteady inflow conditions have also been investigated extensively in the past. However, the analysis of the wake convection and blade boundary layer interaction has mostly been limited to the undisturbed blade passage flow near midspan. Available research which simultaneously

considers periodical wakes and secondary flow effects is quite limited. Moreover, as is described in Section 2.4 the research is not universally consistent in terms of findings and conclusions. Therefore, the effect of periodically incoming wakes on the secondary flow is not fully understood. In terms of applied methods, the vast majority of modern research dealing with secondary flow has been centered around pressure probe and/or CTA-probe measurements to analyze the upstream inflow conditions and downstream secondary flow. Here, the secondary flow properties are usually evaluated by means of total pressure loss and local over-/under turning. Measurements inside the blade passage are rarer and usually limited to selective points instead of entire fields. While this classic approach is completely valid and has contributed many valuable findings, it generally does not provide a complete picture. In recent years, some published works have diverged from this classic approach by selectively incorporating more modern experimental methods. For example, Sinkwitz et al. [96] and Lopez et al. [73] utilized hot-film sensor arrays on the near-endwall suction surface. Volino et al. [101] & [100] and Chemnitz and Niehuis [14] analyzed the potential of Particle Image Velocimetry (PIV) in comparison to five-hole-probe and CTA-probe measurements in a turbine cascade exit flow.

Therefore, the present work aims to complement the current state of research by combining secondary flow investigations in a low-pressure turbine cascade with periodically incoming wakes as well as other influencing factors. The main objectives are summarized below. Achieving these objectives will provide a step forward in gaining a better understanding of the secondary flow development and the associated loss generation mechanisms. If continued, the research knowledge will ultimately benefit the design of ultra-high-lift blades for low-pressure turbines with reduced weight and high overall efficiency.

1. The first objective is to demonstrate how the classic investigation approach can be extended and enhanced by a multi-methodology approach to form a more complete data set and therefore a more comprehensive view on the secondary flow phenomena in a turbine cascade. This includes improved test case design, implementation and appropriate combination of advanced measurement techniques, and continuous utilization of supplemental CFD. This objective will lay the foundation for the subsequent work towards the achievement of the following objectives.

2. The second objective is to quantify the effects of periodically unsteady inflow generated by incoming wakes on the time-averaged secondary flow phenomena and the associated losses up-, inside and downstream of the blade passage. In order to put the wake effects into perspective and get a sense of scale and relevancy, a crucial point is to compare the results to other influencing factors. For this purpose, the effects of blade loading and inlet endwall boundary layer conditions will also be evaluated.

3. The third objective is to quantifiable resolve the wake convection throughout the blade passage near the endwall instead of at midspan. Here, the negative-jet-effect will be analyzed to determine the mechanisms of wake disturbance of the time-resolved secondary flow development and the secondary flow interaction with the suction surface.

2 Secondary Flows in Turbines

2.1 Secondary Flow Models

Secondary flow phenomena caused by endwall effects alter the undisturbed quasi-2D flow in blade passages and have been studied extensively in the past. The groundwork of secondary flow theory was laid in the 1950s and 60s as most notably Hawthrone [43] & [44] described the secondary circulation in flows with non-uniform velocity passing through a blade cascade and Lakshminarayana and Horlock [67] presented a generalized analytical expression in terms of secondary vorticity. Initial research focused on the basic understanding of the balance of flow inertia forces and blade induced pressure forces, its influence on streamline curvature, and how it is altered by the presence of an endwall. Subsequently, secondary flow visualization using foremost smoke and oil patterns became popular and the topic has since become a classic field of aerodynamic turbomachinery research. Up to the 1980s, individual phenomena in the complex system of secondary flows in turbomachinery blading were identified, analyzed, and repeatedly summarized in secondary flow models. A review of these models, whose purpose is a universal secondary flow depiction for compressors or in the present case turbines, was given by Sieverding [94], Langston [70], and more recently by Lampart [68]. Two of the most influential and comprehensive models of secondary flows in low-pressure turbine cascades are illustrated in Figure 2.1. They also provide an indication of the varying level of detail and some of the most common differences in the classic secondary flow models. In this context it must be kept in mind that while these models are supposed to be universal, in reality every flow is unique with slight differences in terms of occurrence, shape, size, and location of individual flow components. While tip gap leakage flows are included in the general definition of secondary flows and play a significant role in unshrouded rotor blading, they will not be considered in the following turbine cascade investigation.

Horseshoe Vortex
Due to the total pressure gradient inside the incoming endwall boundary layer, the rising static pressure upstream of the blade's leading edge has a stronger effect on the near-wall flow. Consequently, the boundary layer detaches from the endwall, rolls up, and thereby induces lateral vorticity. Due to the pressure gradients of the blade passage, the lateral component is quickly converted to streamwise vorticity and deflected to both sides of the blade forming the characteristic horseshoe shape. The suction side and pressure side leg of the horseshoe vortex (HSVs and HSVp) have an opposite sense of rotation and act as separate vortices inside the blade passage. While earlier secondary flow models generally depicted a single vortex pair as in Figure 2.1a, Wang et al. [102] described a roll-up of the fresh boundary layer closely upstream of the leading edge and thus the formation of a second horseshoe vortex as illustrated in Figure 2.1b. However, as a result of strong interaction

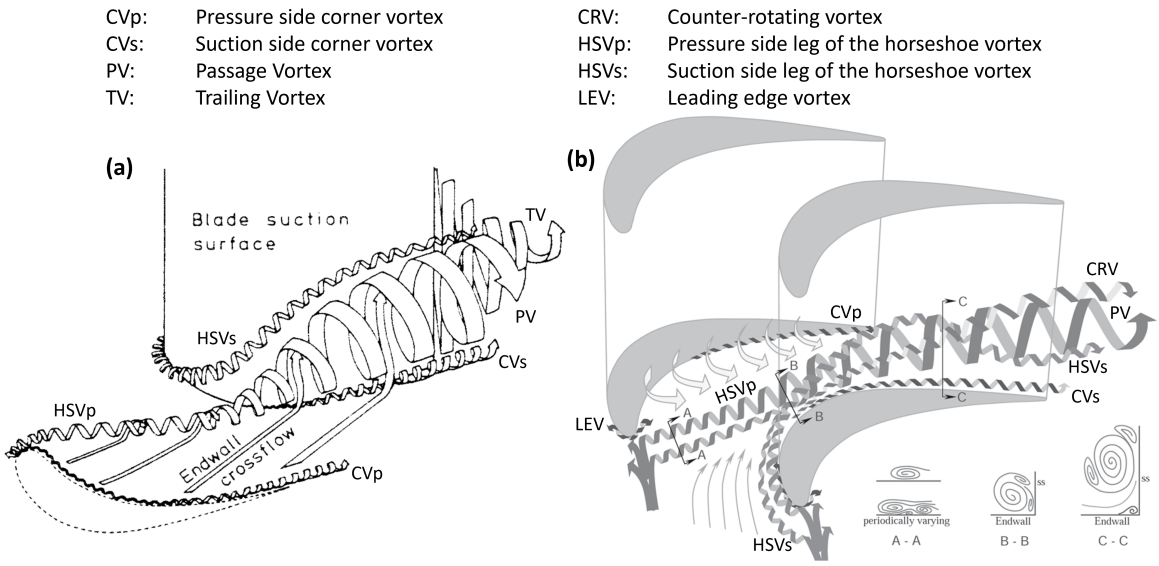

Fig. 2.1: Classic secondary flow models adapted from (a) Kawai et al. [60] and (b) Wang et al. [102].

the adjacent co-rotational vortices tend to merge quickly inside the passage, especially the suction side legs. Strong transverse pressure gradients inside the passage induce near-wall crossflow which drives the HSVp towards the suction surface of the adjacent blade. Based on the sense of rotation, the HSVp is augmented by entrainment of the moving boundary layer fluid while the HSVs is weakened. According to Wang et al. [102], the meeting point of the two vortex legs at the blade suction surface is located near the peak profile Mach number. Here, the HSVs might partially merge with the stronger HSVp, but is mainly deflected upwards on the suction surface i.e. away from endwall. Further downstream, the secondary flow models differ in regard to the HSVs. In contrast to the continued slightly upward trajectory along the suctions surface according to Kawai et al. [60], Goldstein and Spores [37] and Wang et al. [102] described an entrainment by the stronger HSVp which ultimately leads to a rotation around the passage vortex further downstream.

Passage Vortex

The key driver for the development of the passage vortex (PV) is the aforementioned crossflow from the pressure side to the suction side of the blade passage. Similarly to the initial trigger of the horseshoe vortex development, this crossflow is caused by static pressure gradients acting on the total pressure gradient inside the endwall boundary layer. Consequently, the balance between the lower inertia forces near the endwall and the transverse pressure forces leads to increased local streamline curvature. With respect to the undisturbed flow around midspan this appears as flow overturning. An opposing flow (underturning) is induced outside of the boundary layer which satisfies mass continuity and forms the closed vortex. According to Wang et al. [102], the passage vortex appears near the collision point of the suction side leg and adjacent pressure side leg of the horseshoe vortex. Due to the same sense of rotation, the HSVp becomes the main component of the PV which is continuously

augmented throughout the passage by entrainment of boundary layer fluid from the crossflow. A strong interaction of the PV with the suction surface completely alters the near-endwall blade profile flow by inducing a vertical component and changing the local boundary layer conditions. The continuous increase in vortex size and a liftoff from the endwall towards the rear of the passage increase the spanwise extend of the affected secondary flow region.

Counter-Rotating Vortex
This vortex results from the interaction of the passage vortex with the blade suction surface flow and is located just above the PV. Contrary to most other vortices, a universal denotation has not been adopted in the secondary flow literature. In the present work, the name 'counter-rotating vortex' (CRV) is used as it clearly describes one of its most distinguishable characteristics besides its location. Some secondary flow models as for example in Figure 2.1a depict the CRV as a continuation of the co-rotating HSVs. On the other hand, models with a rotation of the HSVs around the PV, as in Figure 2.1b, depict the CRV as a stand-alone vorticity reactively induced by the PV.

Corner Vortex
The corner vortex (CV) is a reaction to the merged horseshoe vortex pressure side leg and the passage vortex and is therefore counter-rotating. Its name is rooted in its location in the corner between the endwall and the blade suction surface. The CV is usually significantly smaller than the surrounding vortices and due to the walls in its close proximity, it can be difficult to resolve experimentally. Despite being often disregarded in secondary flow models and investigations, a small corner vortex also develops on the pressure side with an opposite sense of rotation to its suction-sided counterpart as illustrated for example by Sieverding [94].

Trailing Vortex
A description of the trailing vortex based on potential flow theory was first presented by Hawthrone et al. [44]. It is caused by a reactive motion due to the shear layers between two co-rotating passage vortices of two adjacent passages. The low-inertia flow inside the trailing edge wake is especially susceptible to these shear forces which leads to the vortex formation with opposite sense of rotation to the PV downstream of the trailing edge. The trailing vortex usually features a narrow shape and extends vertically i.e. in spanwise direction next to the PV and can merge with the CRV at the top. Many secondary flow models disregarded the trailing vortex as in Figure 2.1b, but Kawai et al. updated their previous model [59] to include the trailing vortex [60] as illustrated in Figure 2.1a. In an attempt to create a comprehensive secondary flow illustration, Goldstein et al. [36] extended the model of Wang et al. [102] with the trailing vortex depiction of Kawai et al. [60], basically combining the two illustrations in Figure 2.1.

Endwall Boundary Layer Topology
The development and propagation of the secondary flow is closely linked to boundary layer separation on the endwall and the blade surface. Based on oil pattern visualization, Sieverding [94] presented a model of limiting streamline patterns which coincide with skin friction lines. It can be utilized to describe the key structures of the endwall flow including separation lines (S), reattachment i.e. stagnation lines (R), and the saddle points (A) at their intersections. As illustrated in Figure 2.2, upstream of the blade leading edge the separation lines associated with the HSV development S_1 and S_2 are located along the stagnation line R_1.

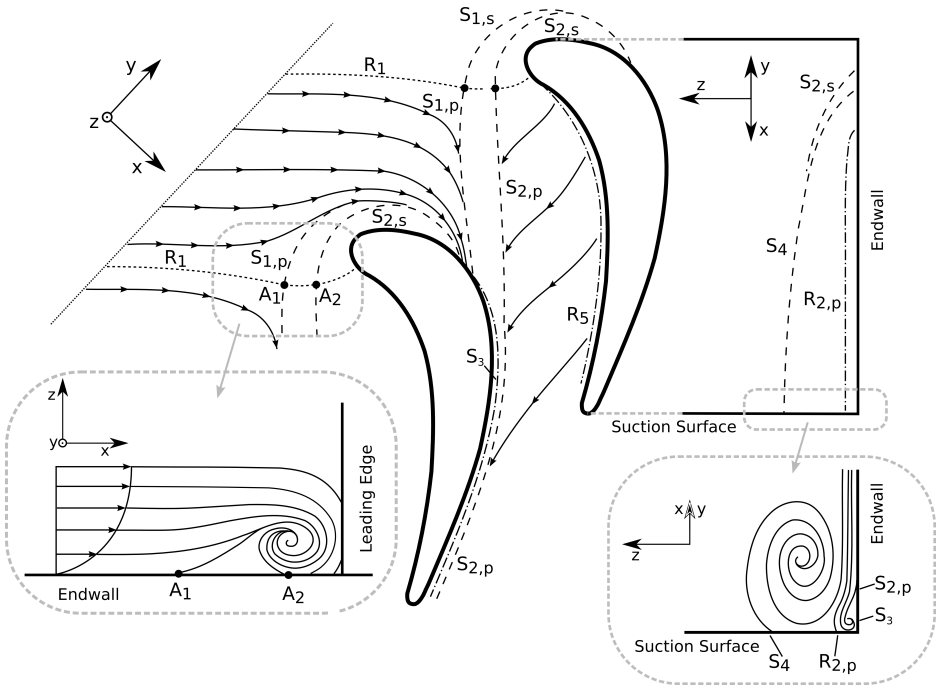

Fig. 2.2: Endwall boundary layer topology in a turbine cascade illustrated by limiting streamlines adapted from Sieverding [94] and Bode [10].

The latter leads to the stagnation point on the blade profile with continuously rising static pressure. As the HSVp is driven towards the adjacent suction surface and collides with the HSVs, the merged separation lines $S_{1/2,s}$ and $S_{1,p}$ form a funnel shaped pattern. According to concentration measurements based on naphthalene sublimation by Goldstein et al. [38], relatively large amounts of boundary layer material are transported in this region. As the HSVs is deflected upwards on the suction surface ($S_{1/2,s}$), Sharma and Butler [93] describe that a part of the transported boundary layer material is fed into the counter-rotating vortex. The developed vortices further downstream in the passage can also be linked to limiting streamlines. In general terms, a vortex interacting with a wall boundary layer generates a separation line where the vortex streamlines point away from the wall and in return a reattachment line where they point towards it. This is for example the case at the separation line S_4 which continuously extends over the span of the suction surface and corresponds to the upper side of the passage vortex. On the endwall, $S_{2,p}$ continues downstream adjacent to the suction surface. Due to the merging of the HSVp with the passage vortex it can be viewed as a second PV separation line. Similarly, S_3 on the endwall and $R_{2,p}$ on the suction surface represent the suction side corner vortex. Finally, due to the opposite sense of rotation, the pressure side corner vortex corresponds to the reattachment line R_5 on the endwall.
Additional information on the endwall boundary layer conditions based on measured intermittency distributions in a turbine cascade was presented by Moore and Gregory-Smith [78]. Förster et al. [34] mostly validated and refined these results by using a combination of CTA and fast-response pressure probe measurements and Bode [10] provided a detailed review of the topic in his dissertation. Considering a transitional incoming endwall boundary layer,

they found that the high flow acceleration near the forward suction surface leads to a laminar boundary layer between $S_{1/2,s}$ and the blade. Inside the funnel shaped pattern between $S_{1/2,s}$ and $S_{1,p}$, the boundary layer transitions to fully turbulent due to interaction with the horseshoe vortex. However, this turbulent area is limited, because downstream of the HSVp translation to the suction surface indicated by $S_{2,p}$ a relaminarization of the boundary layer occurs.

Following the visualization and definition of secondary flow models in the 1980s, research has mostly been focused on the associated losses (Section 2.2), methods of secondary flow control (Section 2.3), and the influence of various geometrical and flow parameters on the secondary flow (Section 2.4).

2.2 Associated Losses

In the vast amount of research on secondary flow, no universal approach in loss accounting has been established yet. Therefore, when comparing quantitative loss values one must carefully consider if the endwall boundary layer loss is listed individually in the loss component breakdown. In other cases it might be combined with losses due to secondary vortical structures as 'secondary loss' or 'endwall loss'. Also, inlet losses from upstream flow components might be excluded in some studies. Nevertheless, based on the published overviews of the loss mechanisms in turbomachinery by for example Denton [28], Curtis et al. [26] or Cui and Tucker [25], it becomes evident that secondary flows accounts for a significant part of the overall losses up to around one third in axial turbines. Especially relevant in this regard are highly-loaded low-aspect-ratio LPT blades in which the secondary flows affect a larger range of the blade span. Denton and Pullan [29] investigated secondary losses based on (U)RANS simulations and concluded that there is no single dominant source of loss, but rather several components which need to be considered. These include secondary flow interaction with the suction surface and the downstream mixing losses. Utilizing high-fidelity eddy-resolving simulations, Cui and Tucker [25] identified two regions of high loss generation rate near the blade suction surface. The first is the corner vortex region at the blade-endwall juncture and the second is the interaction region of the passage vortex and the blade boundary layer, resulting in the counter-rotating vortex. This finding was seconded by Bear et al. [2], who investigated the loss development in a LPT cascade by using a combination of pressure measurements, Particle Image Velocimetry (PIV) in axial planes, and Large Eddy Simulations (LES). The interaction of the secondary vortices with the blade suction surface was once more found to be a major contributor to the overall losses. Consequently, the majority of the losses associated to the passage vortex are generated within the blade passage, while other secondary vortex structures like the counter-rotating vortex and trailing vortex generate significant losses downstream of the blade. Based on a numerical parametric design study on secondary losses in LPT cascades, Coull [23] proposed a decomposition of secondary losses into two major components; dissipation in the endwall boundary layer and induced losses by secondary flows which scale with streamwise vorticity. He also concluded that further investigations on the effects of inlet conditions are necessary to relate secondary losses in linear cascades to real turbines. Moreover, Denton and Pullan [29] stated that the prediction and reduction of secondary losses will remain a challenge for many years to come.

2.3 Control Methods

Motivated by earlier research findings regarding secondary flows and their associated losses many ensuing studies have been focused on a variety of methods of secondary flow control i.e. management to limit secondary losses.

Boundary Layer Fences
In the late 1980s Kawai et al. [59] & [60] first presented the use of boundary layer fences (or endwall fences) in steam turbines. The fences, whose height is in the range of the inlet endwall boundary layer, are positioned inside the passage around mid-pitch. Their purpose is to limit the endwall crossflow from the pressure to the suction side. As illustrated in Figure 2.3a, the migration of the pressure side leg of the horseshoe vortex is prevented and thus keeps the passage vortex away from the suction surface. Chung et al. [17] evaluated the effectiveness of an endwall fence in a low-speed turbine passage. Based on five-hole-probe measurements in the exit plane and caloric liquid crystals on the suction surface, they found a reduction of the vortical motion, the vortex interaction with the suction surface, and the associated aerodynamic losses. In the following years, a series of studies for example by Moon and Koh [77] and Chen et al. [15] were presented on the optimal geometric fence parameters such as height, length, and pitchwise position. As fence height is increased, the HSVp cross-passage migration is increasingly blocked and consequently there is a pitchwise shift of the passage vortex away from the suction surface. At intermediate height, two passage vortices are present whose size is inversely proportional; one on the fence suction surface and one near the blade suction surface. Furthermore, a detailed analysis of the resulting secondary flow revealed the formation of a new counter-rotating fence vortex on the pressure side of the fence. Further downstream, this fence vortex interacts with the passage vortex on the suction side. Recently, Yuan et al. [107] built an automatic optimization platform to design a non-uniform height endwall fence (NHEF) as well as a version with around 50% reduced length for a high-lift low-pressure turbine cascade. A subsequent CFD evaluation predicted a reduction in outlet total pressure loss of around 15%. While the published investigation results in linear cascades are promising, inherent drawbacks as for example additional weight need to be included in an overall evaluation of the stage performance.

Splitter Vanes
According to Clark et al. [20] the rationale behind the use of splitter vanes is based on two methods leading to a reduction in secondary flow intensity; first, an increase in the number of blade passages and second, an even pitchwise distribution of the inlet endwall boundary layer material between the passages. Although this could also be achieved by simply increasing blade row solidity, the final goal is to find the optimal balance between all loss components as well as weight considerations. Since splitter vanes are not primarily supposed to contribute to the aerodynamic stage work, their thin and high-aspect-ratio design as illustrated in Figure 2.3b is less detrimental in this regard. In order for a splitter configuration to be effective, the pressure side leg of the main blade horseshoe vortex must enter the adjacent passage and not 'jump' in front of the splitter leading edge. Here, the axial leading edge location and thus chord length is dependent on the load distribution of the main blade which determines the cross-passage horseshoe vortex migration. Clark et al. [20] analyzed the effectiveness of splitter vanes in a low-aspect-ratio low-pressure turbine

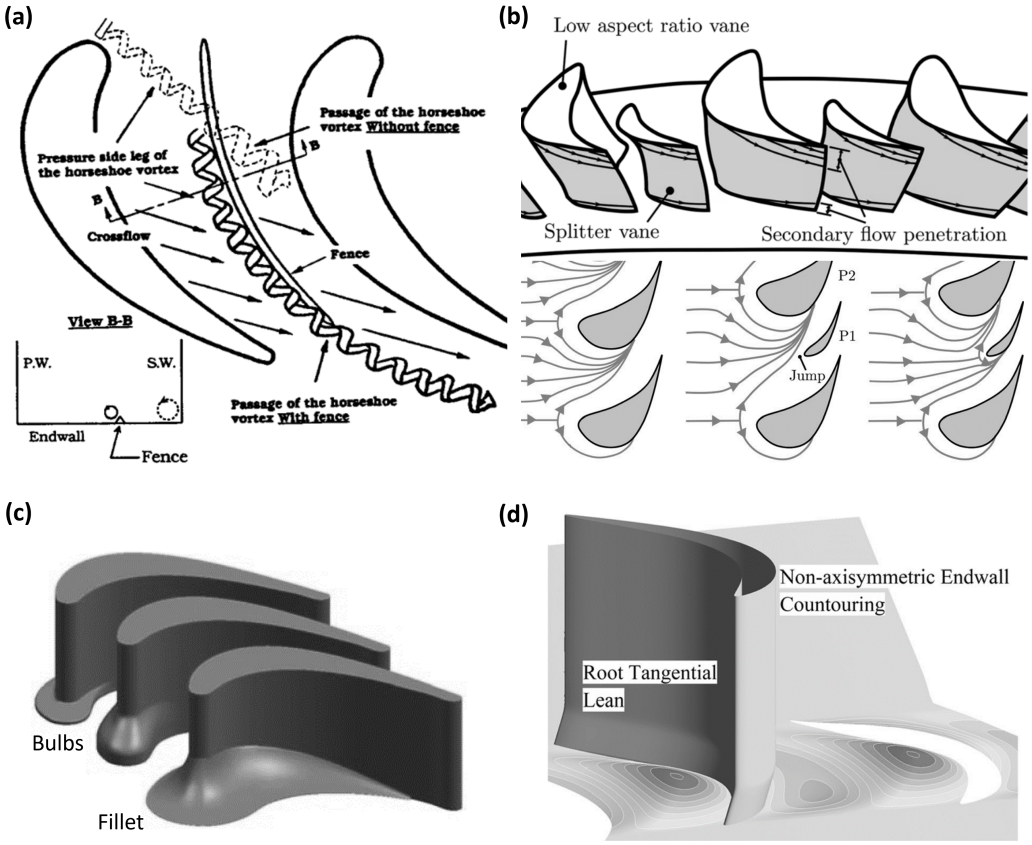

Fig. 2.3: Schematics of secondary flow control methods; (a) Boundary layer fences adapted from Chung et al. [17]; (b) High-aspect ratio splitter vanes adapted from Clark et al. [20]; (c) Leading edge modification adapted from Becz et al. [4]; (d) Endwall contouring adapted from Xue et al. [105].

vane illustrated in Figure 2.3b. The resulting exit flow field was more uniform in both the circumferential and radial directions and exhibited a secondary kinetic energy reduction by up to 85 % and mixed-out loss reduction by 15.3 %.

Leading Edge Modifications

Two types of leading edge modifications designed for secondary flow control are illustrated in Figure 2.3c. Bulbs are created by increasing the blade leading edge thickness near the endwall and their effectiveness to reduce secondary losses has been demonstrated by Sauer et al. [88]. A fillet placed at the leading edge-endwall juncture has a similar effect as presented among others by Zess and Thole [108]. Both methods, which were compared by Becz et al. [4], effectively accelerate the incoming boundary layer and thereby significantly weaken the horseshoe vortex development. According to Schobeiri and Lu [91], one advantage of leading edge modifications lies in their relatively straight forward design especially in comparison to endwall contouring which requires extensive design efforts.

Endwall Contouring
In the past, extensive research has been conducted on the effectiveness of endwall contouring i.e. profiling to reduce secondary flows. Numerical and experimental studies performed in turbine cascades with steady inlet flow such as by Ingram et al. [57] have shown a reduction of total pressure losses by as much as 50 %. Design processes can vary significantly in complexity. A simpler method by Hartland and Gregory-Smith [42] is based on contours mirroring the blade curvature. More complex approaches include the continuous diffusion method by Schobeiri and Lu [91] & [86] and the genetic algorithm optimization presented by Xue et al. [105]. Nevertheless, all methods basically aim at a deceleration of the passage crossflow by manipulating the transverse pressure gradients from the pressure to the suction side. As illustrated in Figure 2.3d, this is usually achieved by positive contouring near the blade pressure surface elevating the endwall and thus creating a convex surface. Near the blade suction surface, a concave surface is created by negative contouring. Xue et al. [105] demonstrated an increase in effectiveness by superimposing the effects of non-axisymmetric endwall contouring and tangential lean (dihedral) at the blade root.

Active Flow Control
In contrast to the passive geometric flow control methods described above, active flow control is based on the input of small amounts of external energy to improve the secondary flow field structure. Benton et al. [7] & [6] implemented small jets along the blade suction surface to force further distance to the passage vortex and thus reduce its interaction with the blade profile flow. Steady state jets were effective but required a relatively high mass flow and momentum ratio. In comparison, pulsed jets exhibited slightly less effectiveness but significantly less energy demand. Wall normal jets located on the endwall slightly downstream the leading edge were analyzed by means of LES by Romero and Gross [87] and experimentally by Donovan et al. [30]. Both found that by manipulating the pitchwise position of the passage vortex and reducing the endwall boundary layer separation it is possible to weaken the downstream vortex strength. The effectiveness of pulsed jets was maximized when its frequency amplified the natural instabilities of the passage vortex which decreased the coherence of the vortex structure. Instead of using jets, Bloxham and Bons [9] and Bons et al. [12] investigated the effect of endwall boundary layer suction on the secondary flow. This method is based on a reduction of available fluid material in the endwall boundary layer for separation, entrainment, and thus vortex development. Although active control technology has been proven to be effective for secondary flow attenuation, Yuan et al. [107] summarize that it generally comes along with higher complexity, increased failure probability, and increased weight.

2.4 Key Influencing Factors

Over the last decades, a lot of research has been conducted on various geometrical and flow parameters affecting secondary flows. These influencing factors can have strong design implications in turbine development. Furthermore, their underlying mechanisms are mostly identical to those being utilized in secondary flow control methods. Therefore, it is important to have a solid understanding of these influencing factors and their individual and superimposed effects.

Blade Aspect Ratio

The blade aspect ratio is a key geometrical parameter with regard to secondary flow. In low-aspect-ratio blade rows, the relevance of secondary flow is significantly higher due to the increased relative spanwise extension. This so called 'penetration depth' of the secondary flow is usually evaluated at the blade trailing edge as indicated in Figure 2.4. According to Schobeiri [90], the associated secondary loss is almost inversely proportional to the blade aspect ratio. In the past, various empirical correlations have been published to estimate the penetration depth of the secondary flow based on various geometrical and flow parameters. A more recent correlation formulated by Benner et al. [5] is given by

$$\frac{Z_{TE}}{H} = 0.1(F_t)^{0.79}\, CR^{-0.5} \left(\frac{H}{C}\right)^{-0.55} + 32.7 \left(\frac{\delta_1}{H}\right)^2 . \tag{2.1}$$

Here, δ_1 denotes the endwall boundary layer displacement thickness, C the blade chord length, and H the blade height. The tangential loading coefficient F_t is a modification of the more commonly used Zweifel coefficient and is defined as

$$F_t = 2\left(\frac{P}{C_x}\right) cos^2\left(\alpha_m\right) \Big(tan\left(\alpha_1\right) + tan\left(\alpha_2\right)\Big) = Z_W \frac{cos^2\left(\alpha_m\right)}{cos^2\left(\alpha_2\right)}. \tag{2.2}$$

P denotes the blade pitch and α_1 and α_2 are the pitchwise in- and outflow angles measured from the axial direction[1]. Lastly, the mean flow angle through the blade row α_m and the convergence ratio CR are given by

$$tan\left(\alpha_m\right) = 1/2\left|tan\left(\alpha_1\right) - tan\left(\alpha_2\right)\right| \tag{2.3}$$

$$CR = \frac{cos\left(\alpha_1\right)}{cos\left(\alpha_2\right)}. \tag{2.4}$$

The first term of the penetration depth correlation (2.1) represents the impact of the geo-

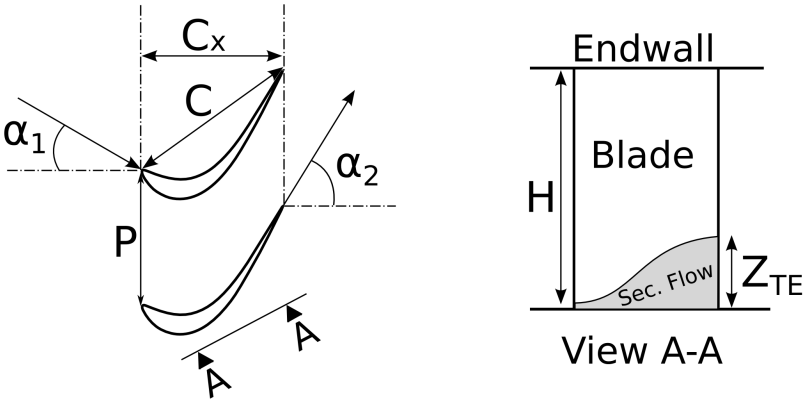

Fig. 2.4: Schematic of the secondary flow penetration depth and relevant geometrical and flow parameters.

[1] Contrary to the definition by Benner et al. [5], the flow angles in the cumulative publications in Chapter 4 are measured relative to the pitchwise direction: $\beta_1 = \alpha_1 + \pi/2$ and $\beta_2 = \pi/2 - \alpha_2$.

metrical parameters. Here, an increase in penetration depth can be caused by an increased pitch-to-chord ratio i.e. decreased solidity, increased flow turning ($\Delta\alpha = \alpha_1 + \alpha_2$), increased blade loading, or decreased blade aspect ratio. The convergence ratio is a measure of channel acceleration which affects the relative stretching of the passage vortex inside the blade passage. Hence, an increased CR leads to a decrease in penetration depth. In the second term, increased boundary layer displacement thickness relative to the blade height results in a significant increase in penetration depth.

Blade Loading
As the blade surface pressure distribution is the driving force for the cross-passage endwall flow, it has an immense impact on the secondary flow development, especially the frontal blade loading. Weiß and Fottner [103] analyzed two turbine cascades with the same overall blade loading but different load distributions. They found that a lower magnitude of secondary loss was generated in case of delayed pressure gradients in the aft-loaded cascade. Chibli et al. [16] demonstrated this effect in an extreme case by designing a turbine blade profile with almost zero pressure difference over the first 50 % of the axial chord which virtually eliminated the secondary flow. However, the overall blade loading in this academic design study was limited. The application of a highly aft-loaded pressure distribution in a turbine nozzle guide vane by Pullan et al. [83] resulted in a reduction of 0.5 % in stage efficiency. As the blade solidity has a direct effect on the blade loading, its increase consequently leads to weaker secondary flow as presented by Hodson and Dominy [46] who conducted pneumatic probe measurements in a high-speed linear LPT cascade.

Endwall Boundary Layer Conditions
As described in Section 2.1, two key mechanisms of the secondary flow development are the roll-up of the inlet endwall boundary layer into the horseshoe vortex and the entrainment of boundary layer material by the passage vortex. Therefore, the resulting vortices contain a large fraction of the endwall boundary layer within their cores. Thus, the secondary flow is significantly affected by the inlet boundary layer thickness and its separation robustness depending on its state in terms of laminar-turbulent transition. These two factors are usually superimposed in research studies. De la Blanco et al. [27] conducted five-hole-probe measurements in the exit flow fields of two different LPT cascades. In case of a laminar inlet boundary layer the secondary flow exhibited two main loss cores. A thicker turbulent boundary layer resulted in the presence of one dominant loss core at a further distance from the endwall which led to overall higher integral losses. In a similar turbine cascade study by Sauer et al. [89], a variation of the inlet boundary layer displacement thickness did not result in a consistent trend of the downstream secondary loss. However, they did manage to find a correlation between increased local friction coefficients of the boundary layer and higher secondary loss. In a study by Volino [100] an increase in endwall boundary layer thickness by 200 % in a high-pressure turbine cascade resulted in an increase in total pressure loss by around 20 %.

Flow Incidence
Yamamoto and Nouse [106] presented a relation of positive flow incidence to increased frontal blade loading which in return leads to stronger secondary flow. Furthermore, according to Murty and Venkatrayulu [79] a flow incidence variation alters the adverse pressure gradients acting on the boundary layer upstream of the blade leading edge and thus the trajectory

of the horseshoe vortex roll-up. Endwall flows usually exhibit a positive incidence due to a lower axial velocity inside the boundary layer with respect to the free stream. This can be counteracted by applying an 'end-bend' near the endwall which either means increasing the blade inlet metal angle (increased camber) or stagger angle (constant camber). Pullan et al. [84] applied a similar method to a turbine nozzle guide vane to eliminate endwall overturning by reducing the exit metal angle near the endwall and increasing it in the secondary loss core i.e. underturning region. While the spanwise exit flow angle distribution was in fact more homogenous, a detrimental effect occurred in which the trailing vortex sheet rolled up into an intensified vortex.

Reynolds and Mach Number
In an off-design analysis of a LPT rotor cascade, Hodson and Dominy [46] observed an increase in secondary losses at lower Reynolds numbers. This trend was confirmed experimentally by Coton [22] who identified the main factor to be the low Reynolds number effect on the blade profile flow and specifically the increased suction surface separation bubble size. Consequently, an intensified trailing vortex and counter-rotating vortex leads to increased downstream total pressure losses. Furthermore, Benton et al. [7] attributed an additional minor impact on the passage vortex to an indirect effect of the Reynolds number on the inlet endwall boundary layer. The effects of the flow Mach number were investigated by Perdichizzi [81] utilizing five-hole-probe measurements in a turbine cascade. High Mach numbers led to decreased over-/underturning and reduced passage vortex liftoff. Based on numerical analysis, Mahendran and Sitaram [74] attributed the observed secondary flow attenuation to compressibility effects on the pressure gradients inside the blade passage.

Freestream Turbulence
When Chung and Simon [17] analyzed the exit flow field of a turbine cascade at two levels of free stream turbulence intensity (TI), the high-TI case exhibited a lower spanwise position of the passage vortex core i.e. a reduced liftoff. This first effect can be attributed to a delayed vortex formation due to increased separation robustness of the endwall boundary layer induced by the free stream turbulence. The second observed effect was a coherent decrease in vortex core intensity and more homogeneous distribution of vorticity. Five-hole-probe measurements at different axial positions of a turbine outlet guide vane cascade by Hjärne et al. [45] revealed that this effect is caused by increased mixing within and between the vortical structures. They also found that the altered boundary layer transition and separation bubble properties on the suction surface influence the trailing vortex and counter-rotating vortex, similarly as the aforementioned Reynolds number effect.

Periodic Inflow Conditions
Unsteady flow phenomena due to rotor-stator-interaction have been, to this day, a major research field in turbomachinery. As opposed to the random nature of turbulence, this inherent unsteadiness in multi-blade-row flows is caused by periodic inflow distortion. In blade cascades for research activities this is commonly simulated by moving bar wakes. Here, the vast majority of research has been focused on the wake effects on the 2D blade flow around midspan. Hodson et al. [48] described the 'negative-jet-effect' of a wake as its velocity deficit forming a jet with negative flow direction relative to the free stream velocity. The wake's relative streamline direction points from the blade pressure surface towards the suction surface. Here, the boundary layer is periodically affected by high levels of turbulence

and pressure fluctuations. The number of wakes inside the blade passage at any instant in time and the wake orientation are a function of the relative periodic wake passing frequency i.e. Strouhal number and the flow coefficient respectively. The understanding of how induced transitional/turbulent patches can limit the size of laminar suction surface separation bubbles at low Reynolds numbers has prompted particular research efforts for example by Halstead et al. [41], Curtis et al. [26], Howell et al. [50], Vera et al. [99], Coull and Hodson [24], Clinckemaillie et al. [21], and Lengani et al. [71]. An overview of the research activities in Germany with respect to periodically unsteady flow can be found in the summary by Mailach and Vogeler [75]. The past research findings on this topic have provided a major contribution to the design of high-lift low-pressure turbine blades and reduced turbine stage and blade count.

In comparison to the large amount of research on wake disturbance of the 2D blade flow around midspan, the effects of periodically unsteady inflow conditions on the secondary flow are far less explored. Ciorciari et al. [19] utilized validated (U)RANS simulations of the T106A turbine cascade to illustrate an attenuation of the secondary flow including a shift towards the endwall caused by periodically incoming wakes. While the intensity of these effects was dependent on the periodic inflow Strouhal number and flow coefficient, the observed trends remained unchanged. However, the observed influence of the incoming wakes on the time-averaged secondary loss in the turbine exit flow was very small. Koschichow et al. [66] were able to confirm these findings using incompressible DNS in a lower Reynolds number case. Similar results regarding the affected secondary flow structures were found in high-pressure turbine cascade measurements by Volino et al. [101]. Here, the same wake effects were observed in cases with thick and thin boundary layers [100]. A measured 20 % increase in exit flow loss was mostly attributed to the additional inlet loss of the incoming wakes. This highlights the importance of being aware of different approaches in loss accounting. Some studies exclude the inlet loss of the incoming wakes from the integral downstream loss and some do not. Infantino et al. [56] applied a CTA-ensemble-averaging technique in an atmospheric low-speed cascade wind tunnel to analyze the time-dependent velocity and turbulence intensity distributions in a downstream tangential plane during a wake period. In the periodically unsteady case, a shift of the passage vortex toward the endwall was observed as well as a reduction in peak vorticity. They concluded that this is caused by the combination of the turbulence carried by wakes and their velocity defect. The previous findings were partially opposed in a recent investigation by Lopes et al. [73]. They utilized hot-film sensors on the blade surface and multi-hole pressure probes in the exit flow field to analyze the wake effects on the secondary flow in a high-speed low-pressure turbine cascade. They also observed a time-averaged shift of the passage vortex towards the endwall. However, the underturning and the secondary losses were increased, the latter by 25 %. It was suggested that these differences are linked to an unintended variation of the endwall boundary layer conditions. This stems from a newly formed boundary layer after the wake generator gap which was not present in the steady inflow case. The experimental setup by Kirik and Niehuis [63], [62] & [64] exhibited similar uncertainties regarding the inlet boundary layer, but different results of slight secondary flow attenuation due to incoming wakes. This highlights a common challenge regarding wake generator usage, especially in non-atmospheric cascade wind tunnels. This topic is addressed in the present work by presenting a cascade design feature providing a solution to the boundary layer uncertainty (Section 4.3). Sinkwitz

et al. [95] & [96] placed hot-film sensor arrays at different stator blade span positions of a low-speed 1.5-stage turbine to provide time-resolved data. Near the endwall, they found that the periodic wake passing is accompanied by an energy transfer at low-frequencies from the highly turbulent wake to the suction surface boundary layer. This altered the interaction with the secondary flow structures. The intensity of the periodic boundary layer perturbations was dependent on the intermittent return to a relaxed state in-between the wake passing i.e. the wake passing frequency. Also, they were able to illustrate the non-stationary nature of the secondary flow system which was mainly driven by a periodic motion of the horseshoe vortex pressure side leg. As opposed to cascade studies which focus on upstream wakes without secondary vortices, Pullan [82] investigated the 3D stator-rotor interaction in a turbine stage. Here, he illustrated the presence of the remains of the upstream stator passage vortex in the downstream flow field of the rotor. He also found additional vortical structures away from the endwalls which would not be present if the rotor were tested in isolation. An unsteady computation of the rotor row with periodic inflow boundary conditions revealed that these rotor-exit vortices are mainly attributed to stator wake fluid with steep spanwise total pressure gradients. In comparison to a steady simulation which included the upstream mixing losses at the inlet, 10 % higher loss was produced in the unsteady simulation.

3 Multi-Methodology Approach

As stated in Chapter 1, the first objective of the present work is to utilize an advanced multi-methodology approach to generate a comprehensive data set. The benefit of this approach shall be evident compared to the classic secondary flow investigations with probe-based measurements up- and downstream of the blade passage. It is important to clarify that it is not the intention of the author to criticize the use of classic experimental methods or diminish any previous work. To the contrary, in the beginning of this research project up- and downstream probe measurements were in fact utilized to characterize the flow in a modified test case. Subsequently the results were combined with advanced optical measurements and CFD to showcase the immense benefit for secondary flow investigations. A key aspect in this approach was the appropriate combination of different experimental methods as well as CFD to tap their full potential by synergy. This chapter presents the different methods applied in all stages of the research project and the utilized test case. The latter is based on an improved turbine cascade design which was critical to the success of the research.

3.1 Methods

This section provides an overview of the utilized data acquisition methods including their theoretical working principles and basic implementation. A detailed description of each particular implemented setup can be found in the respective cumulative publication in Chapter 4. The particulars of the pressure and temperature measurements to set the wind tunnel operating conditions as well as the static pressure taps along the blade surface are presented in Publication 2 (Section 4.3). Also included are details on the utilized five-hole-probe and CTA i.e hot-wire-probe measurements including probe geometry and placement, data processing, and the resulting measurement uncertainty. An overview of the CFD setup for supplemental (U)RANS-based simulation data can be found in Publication 3 (Section 4.4). The second half of the overall research project was mainly based on the results of the following advanced optical measurements; Particle Image Velocimetry (PIV) in Publication 4 (Section 4.5), unsteady Pressure-Sensitive Paint (i-PSP) in Publication 5 (Section 4.6), and ultra-fast Temperature-Sensitive Paint (TSP) in Publication 6 (Section 4.7).

Computational Fluid Dynamics (CFD)
CFD was a key element in most stages of the research project. In the turbine cascade design process, extensive pre-test CFD studies were conducted to determine critical geometrical and flow parameters. Also, validated post-test CFD was utilized to supplement the experimental data by providing advanced flow parameters and time-resolved data especially in areas of limited accessibility. All CFD data was generated using the (U)RANS-solver of the TRACE simulation suite by DLR. TRACE has been developed, tested, and validated for more than three decades in close co-operation with universities and industrial partners specifically for

turbomachinery applications as presented by Becker et al. [3] and Franke et al. [33]. TRACE solves the compressible three-dimensional Navier-Stokes equations in stationary and rotating frame of reference. As it is a density-based solver, Favre-averaging is applied to all terms except for pressure and density itself. This results in a split of the instantaneous values into a density-weighted averaged mean and a fluctuating component. The spatial discretization of the governing equations is based on a finite-volume method with an upwind scheme for the flux approximation over the cell boundaries. A pseudo-transient Predictor-Corrector method is used for steady state solutions. For unsteady solutions, implicit time-integration schemes are available to discretize the physical time such as the Euler backward method, second-order accurate Crank-Nicolson method, or Runge Kutta method. Furthermore, TRACE provides high quality, non-reflecting boundary conditions and a wide range of higher-order turbulence, transition, and heat-transfer models. A detailed overview of the TRACE code theory and all available setup options can be found in the DLR TRACE-portal [35].

Constant Temperature Anemometry (CTA)
In order to characterize the inlet boundary layer conditions on the endwall, constant temperature anemometry (CTA) measurements were conducted by traversing a 1D-hot-wire-probe normal to the wall. This was done in two locations along the upstream extension of the central blade's leading edge. The basic principle of this measuring technique is based on the convective cooling effect of a flow on a heated body. In case of a hot-wire-probe, the heated body is a tungsten wire sensor mounted between two needle-shaped prongs. Here, the convective heat transfer rate is a function of the temperature difference between the fluid and the wire, the wire geometry, and the fluid properties including flow velocity. The basic relation between heat transfer and flow velocity for a wire placed normal to the flow is also called King's Law [61]. In order to keep the wire resistance and hence its temperature constant regardless of the rate of heat transfer, the probe is connected to a Wheatstone bridge and a servo amplifier. The latter keeps the bridge in balance by controlling the electrical current. Ultimately, the bridge voltage can be continuously evaluated as a measure of the heat transfer and consequently the flow velocity. A velocity calibration is usually conducted prior to the measurements in order to account for the geometric influence of the particular hot-wire probe. In order to derive time-domain statistics such as the turbulence intensity and power spectra, the response time of the bridge to flow fluctuations needs to be very short. This is achieved by a low thermal inertia of the probe wire as well as a high electric gain of the servo amplifier. During the boundary layer traverses for the present work, high spatial resolution very close to the endwall was ensured by a wall-contact indication based on electric conduction. Here, the stability and vibration-resistance of the probe mount are essential for robust measurements. This was ensured by an adjustable custom probe mount guided by integrated sleeve bearings in the turbine cascade endwall. Also, the near-wall velocity samples in the laminar sub-layer of the boundary layer were corrected for the effects of conductive heat transfer between the probe wire and the wall using an approach based on Lange et al. [69].

Five-Hole-Probe (FHP)
Five-hole-probe measurements are by far the most common method of secondary flow evaluation in turbine cascade exit flow fields. They provide 3D flow data in the form of the time-averaged flow velocity as well as the flow angles in pitch and yaw direction. This is achieved by relating the measured pressure distribution on the surface of the probe head to a

calibrated flow velocity in terms of amplitude and direction. The necessity of Reynolds number variations in the calibration is dependent on the expected range of the mean probe-head Reynolds number in the measurements which was analyzed in detail by Bohn [11]. As with all probe-based measurement techniques, a detrimental alteration of the flow is unpreventable due to upstream blockage effects of the probe itself. Thus an appropriate FHP size needs to be selected and the probe alignment and mounting needs to be optimized. When conducting the measurements, the pressure in the measurement system consisting of the probe, tubing, and transducers needs to settle to a steady value in every distinct measuring location. This aspect is especially relevant in a low-static-pressure environment due to a higher inertia of the measurement system which significantly increases the overall measurement time. In the present work, a rapid five-hole-probe traversing technique based on Gomes et al. [39] and Chemnitz [13] was applied. Thereby, the full-range exit flow field could be resolved with a high number of data points in the secondary flow region within a reasonable time frame. Instead of measuring the settled pressure in hundreds of distinct locations, the probe was continuously traversed in pitchwise-direction. This process was repeated in opposite traversing direction. Finally, an algorithm determined a system-specific transfer function based on the two transient pressure signals (back and forth traversing) so that they can be converted into settled pressure values.

Particle Image Velocimetry (PIV)
In addition to the up- and downstream probe measurements, Particle Image Velocimetry (PIV) measurements were conducted to resolve the dynamics of the periodic bar wake effects on the secondary flow inside and downstream of the blade passage. PIV is a non-intrusive measurement technique capturing instantaneous velocity vector fields. The working principle illustrated in Figure 3.1 is based on tracking the movement of seeding particles within the flow, instead of the flow itself. The particle tracking is achieved by illuminating the measurement area and thus the seeding particles with a light sheet from a high-powered LASER. More precisely, two light pulses are emitted and captured by the sensor array of a high-speed sCMOS camera in a sequence of two image frames. Subsequently, the images are divided into subsections called interrogation areas and cross-correlated with each other on a pixel-by-pixel basis. The spatial relation between the images and the actual measurement area is determined by a separate image calibration. Based on the correlation signal peaks, the image calibration, and sub-pixel interpolation, each particle's displacement is identified. Due to the know time between two light pulses the instantaneous velocity vectors can ultimately be determined. Important factors for obtaining a good signal peak in the cross-correlation and thus high quality velocity vectors include the particle image size and dynamics in relation to the size and overlap of the interrogation areas. Therefore, the particle size, image magnification factor, and time between pulses need to be adjusted to the respective flow structures which shall be resolved. Otherwise, a particle displacement beyond the constraints of the interrogation area in-between two light pulses ('out-of-plane motion') will result in non-correlation and a loss of information. Other potential uncertainty factors which are recognizable in the image data include LASER intensity fluctuation, insufficient particle image density, camera image noise, and insufficient or inappropriate post-processing methods. Wienecke [104] analyzed the contribution of each factor to the uncertainty of the displacement vectors and presented a correlation statistics method for an a-posteriori quantification of the instantaneous velocity uncertainty. Based on this, Sciacchitano and Wieneke

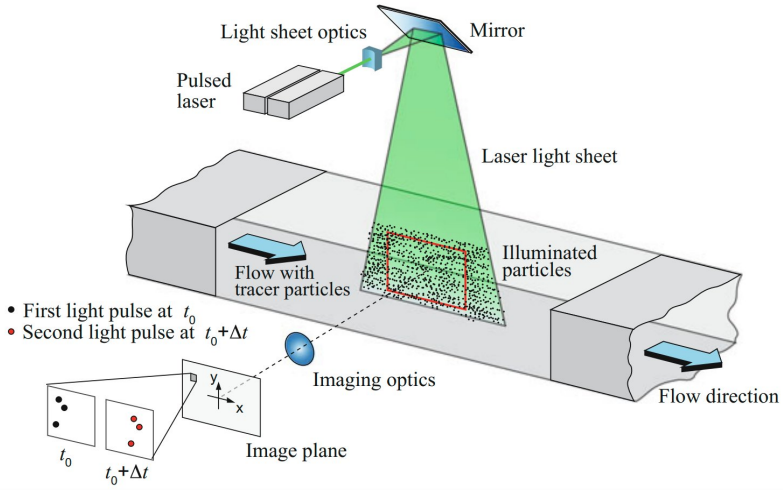

Fig. 3.1: Schematic of the working principle of Particle Image Velocimetry (PIV) adapted from Raffel et al. [85].

[92] investigated the uncertainty propagation to commonly derived flow quantities such as mean velocity, vorticity, or Reynolds stresses. By applying best practice guidelines in the conducted PIV measurements in accordance to Raffel et al. [85], a relative mean velocity uncertainty below 1 % can be expected. Another category of potential uncertainty factors cannot be directly reconstructed based on the image data. These 'hidden' factors such as inaccurate calibration, timing errors, or fluctuation of the light sheet due to vibrations have to be minimized by diligent measurement setup and execution. In the present work, a 2D2C-PIV setup with one camera was applied in a blade-to-blade measurement plane inside the blade passage. Additionally, by using two cameras in a stereoscopic setup (2D3C-PIV) all three velocity components were recorded in an axial plane downstream of the blade passage resulting in instantaneous 3D velocity vector fields. To minimize the impact of vibrations, the measuring equipment was mounted on structures adjacent to the wind tunnel to keep direct contact especially to the moving bar wake generator to a minimum. Measuring a highly resolved passage flow field under high-speed conditions and particularly in close vicinity to a parallel endwall and under vibrations of the wake generator was extremely challenging. Also, it required optical access via a camera endoscope. To deal with the aforementioned uncertainty factor of particle image density, the seeding was adjusted to ensure a sufficient number of particle images in each interrogation area of around 10–25. In addition to the number of seeding particles, the type of particle must be carefully chosen to ensure sufficient dynamic response to the flow. This 'hidden' uncertainty factor is especially relevant in low-static-pressure flows which negatively affect the balance between the flow-induced pressure forces and the inertia forces on the particles as presented by Humble et al. [51] and Bitter et al. [8]. In air flows, the seeding particles are typically oil droplets with a size in the range of 1 µm to 5 µm. The lower end of this droplet size range was chosen for the present low-static-pressure application.

Pressure-Sensitive Paint (PSP)

Conventional pressure measurement techniques are only capable of resolving a pressure distribution at discrete locations on a surface by implementing pressure sensors such as taps or transducers. These sensor locations of interest need to be known prior to testing and will introduce inherent flow disturbance. In contrast, Pressure-Sensitive Paint (PSP) provides two-dimensional undisturbed pressure data on an entire surface. The high spatial and potentially temporal resolution enables the analysis of local flow characteristics, disturbances, and time-dependent statistics. Those were the key aspects driving the choice of PSP in the present work. Capturing the pressure distributions on the suction surface enabled an analysis of the unsteady interaction between the blade profile flow, the periodically incoming wakes, and the secondary flow. As illustrated in Figure 3.2, the basic principle of intensity-based Pressure-Sensitive Paint (PSP) is based on the illumination of a multi-layer photo-chemically reactive coating on the measurement surface. Subsequently, the intensity of the emitted light by the PSP is recorded by a high-speed camera and evaluated as a measure of the local surface pressure. More precisely, the luminophore, in the present case platinum(II)-tetrakis-fluorphenyl-porphyrin (PtTFPP), must be photo-chemically exited by near ultra-violet illumination. The oxygen dependency of the fluorescent intensity comes from a process known as oxygen quenching. Here, the excited molecules collide with ambient oxygen molecules and release their radiation energy until a relaxed state is reached. Therefore, the degression of fluorescence and hence the intensity at a certain instance can be linked to oxygen concentration, i.e. oxygen partial pressure. According to Henry's law, the static pressure of a gas mixture, in this case ambient air, is directly proportional to its oxygen partial pressure. Finally, a calibration is needed to determine the temperature-dependent coefficients of the Stern–Volmer polynomial which relates the relative change in intensity to the relative change in pressure. The relation is also greatly affected by the composition of the active PSP layer. In the present work, the luminophore was embedded in a

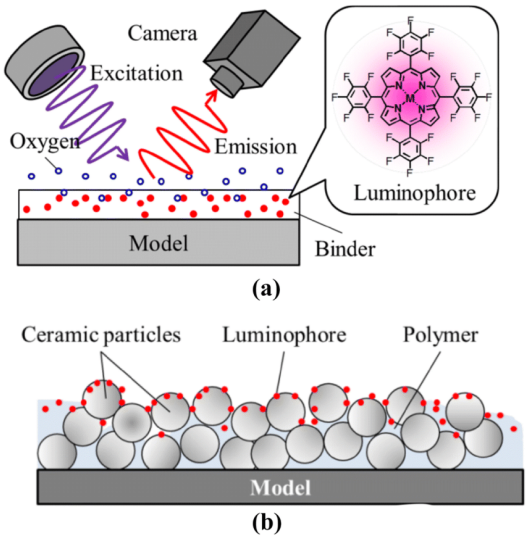

Fig. 3.2: Schematic of the working principle of Pressure-Sensitive Paint (PSP) in a polymer-ceramic binder adapted from Sugioka et al. [98].

porous oxygen-permeable polymer-ceramic binder according to the formulation presented by Gregory et al. [40]. While a fast PSP for transient measurements usually features a cut-off frequency of around 5 kHz, the implemented setup was optimized for shorter response times which ultimately led to a sampling rate of 30 kHz.
The potential of PSP has been demonstrated in most branches of experimental aerodynamics, however, turbomachinery applications are far less progressed and still rare. In fact, the author is unaware of any previous application of PSP specifically for a secondary flow investigation in a turbine cascade. The same holds true for Temperature-Sensitive Paint.

Temperature-Sensitive Paint (TSP)
Multiple potential measurement techniques were evaluated in the present work to supplement the PSP measurements by providing wall shear stress and surface temperature data. Liquid crystals have become an established measurement technique for reliable surface temperature and heat transfer analysis in gas turbine research. Moreover, Ireland and Jones [58] described how the measurement of wall shear stress using liquid crystals has found increasing application. However, a typical response time of 5–150 ms is severely limiting potential time-resolved measurements of high-frequency flow phenomena. Sinkwitz et al. [96] and Lopez et al. [73] have demonstrated the successful use of hot-film sensor arrays on a near-endwall blade suction surface. However, the measurement technique only provides data at distinct locations, only quasi shear stress instead of absolute values, and no temperature data. After diligent consideration, Temperature-Sensitive Paint was selected due to its non-intrusive nature, fast responsiveness, high spatial resolution, potential to provide absolute values of temperature and wall shear stress, and finally its methodological similarities to PSP. The working principle of TSP is very similar to the illustrated principle of PSP in Figure 3.2. A luminophore within a polymer binder is coated on the measurement surface, illuminated with an LED of the appropriate wavelength, and recorded using a camera with a long-pass filter to separate the luminescent signal from the excitation light. Instead of oxygen-quenching in the case PSP, TSP is based on thermal quenching. Here, the probability of a molecule returning to its ground state without emitting fluorescence is increased at high local temperature. Thus, each pixel on the camera image essentially acts as a temperature sensor. In order to minimize the effect of pressure, a binder that is impermeable to oxygen is preferred. The correlation of the fluorescence intensity to the surface temperature can either be determined by placing a TSP test sample in a calibration chamber or performing an in situ calibration during the measurements. Furthermore, the intensity-temperature relation is usually not evaluated using absolute values but instead using ratios to a reference condition called 'wind-off' images. With this so called radiometric TSP approach, the influence on the fluorescence intensity by factors other than the temperature can be minimized, assuming these influences remain constant over time. The main difference to PSP is the need for a heating layer underneath the active TSP coating to ensure sufficient flow induced variation in the local heat transfer and thus a high signal-to-noise ratio. The implemented setup in the present work utilized ultra-fast Ru(phen)-based Temperature-Sensitive Paint. In terms of layering, composition, and surface heating power and homogeneity, the TSP setup was optimized for high sensitivity and fast response. In a flat-plate test case, the implemented setup with a high sampling rate of 40,000 Hz enabled the resolution of temperature fluctuation down to 10^{-5} K as well as pattern reconstruction of dominant coherent flow structures and their higher harmonics through SPOD analysis.

3.2 Test Case

The T106A low-pressure turbine cascade served as the main test case in the present work. The T106 is a high-lift airfoil with an elliptical leading edge and represents the midspan section of the LPT rotor of the PW2037 turbofan engine. It was designed in the 1970s by MTU Aero Engines [72] and was later published as an open test case by Hoheisel [49]. Since then the airfoil has been used extensively in several blade cascade variants for turbine research. Compared to the baseline T106A, the T106C [76] and T106D [97] feature a decreased blade solidity i.e. increased pitch-to-chord ratio of 0.799, 0.95, and 1.05 respectively. The T106Div[2] [31], which was also used in the present work, is a T106A derivative with divergent endwalls. This leads to an increased loading in the front part of the normally aft-loaded blade profile. The tests in the present work were conducted in the High-Speed Cascade Wind Tunnel at the University of the Bundeswehr Munich [80]. The low-static-pressure environment of the wind tunnel inside a pressure chamber provided realistic Mach and Reynolds numbers and thus increased the relevancy of the investigation. Furthermore, periodically unsteady inflow conditions were generated by a moving bar wake generator located upstream of the blade leading edges. As part of the first research objective (Chapter 1) of utilizing a multi-methodology approach to enhance the investigation results, a modification of the T106A cascade was conducted without changing the blade profile. The main motivation was to minimize previous uncertainties regarding the inlet endwall boundary layer conditions and to prepare for the subsequent implementation of advanced optical measurement techniques. The main design feature was an adjustable two-part flat plate, integrated at part-span and acting as a cascade endwall. Thereby the influence of the leakage flow through the gap of the bar wake generator was minimized. This enabled an independent variation of the inlet endwall boundary layer conditions. A detailed description of the improved design and an experimental validation of the design goals of more distinctive secondary flow and a more consistent effect of the periodically incoming wakes can be found in Publication 2.

In the following, the key assumptions and simplification with respect to the test case and the investigation approach are addressed. While all of these facts are important to acknowledge, they are commonly used in research to enable the investigation of individual effects. Especially the implementation of advanced measurement techniques would otherwise not be possible in most cases.

- The use of a linear turbine cascade instead of an annular turbine with 3D blades is a simplification in itself. The same applies to the common use of cylindrical bar wakes to simulate the periodic inflow generated by upstream blades. Therefore, some effects such as the remains of upstream secondary flows, cavities, cooling flows, leakages, and Coriolis effects were not considered in the present work.
- The bar pitch is inversely proportional to the number of wakes present in the blade passage at any given instant. In the present work, this is represented by the Strouhal number. The second periodic inflow parameter which is related to the bar speed is

[2]Note that the denotation 'T106D' is also used for the T106Div, but it should not be mistaken for the variant with decreased solidity.

the flow coefficient. A lower flow coefficient means the wake orientation tends more towards perpendicular to the mean streamwise direction. Multi-stage turbomachinery usually exhibits higher Strouhal numbers and lower flow coefficients which could not be simulated in the conducted experiments due to mechanical limitations of the bar wake generator. This is an experimental limitation which was accepted in the high-speed wind tunnel tests. Atmospheric wind tunnels might achieve more realistic relative bar speeds, but they may have other limitations such as unrealistic Mach and/or Reynolds numbers. The goal of the present work is not to accurately predict the quantitative effect of periodically unsteady inflow conditions in turbomachinery components, but rather to capture the mechanisms in which the incoming wakes interact with the secondary flow. Nevertheless, the results of Ciorciari et al. [19] as well as Publication 1 of the present work (Section 4.2) have shown that increased bar velocity and/or lower bar pitch mostly impact the intensity of the secondary flow effects. The observed trends however, remained unchanged within a reasonable range of unsteady inflow parameters. As the cascade flow conditions were defined based on the theoretical exit Mach and Reynolds number, the divergent endwalls of the T106Div cascade used in Publication 1 led to an increase in axial inlet flow velocity. Thus, at constant wake generator settings the Strouhal number was lower and the flow coefficient higher with respect to the baseline T106A cascade.

- A simple and common definition of secondary flow is the deviation to the undisturbed 2D flow around the midspan region of the blade. This approach was used for the determination of over-/underturning in the secondary flow region. Also, in the analysis of loss development, the overall losses were separated into constant midspan losses, i.e. profile losses and secondary losses. At first glance, one might question the definition of secondary losses as the difference of overall losses and midspan losses because the profile losses are obviously not constant outside of the 2D flow region around midspan. However, since the changes in profile losses are a direct result of endwall effects, it is reasonable to account for them in the secondary loss component.
- Due to the high complexity of ultra-fast TSP, a simplified flat-plate test case was utilized for a capability demonstration. However, the tests were conducted under the same inflow conditions as in the T106A turbine cascade. The test signal for the measurements was generated by the vortex shedding of a vertical cylinder. A detailed description of the test case can be found in Publication 6.

4 Cumulative Publications

4.1 Overview

The present dissertation is based on a total of six cumulative peer-reviewed publications. In this chapter, each publication is presented by a brief summary of the main findings and aspects linking it to previous results or motivating subsequent work. This is followed by a postprint of the respective publication and in case of Publication 2 & 5 also relevant supplemental figures and results are discussed. Each publication contains an individual nomenclature and bibliography which are not included in the framework text of this dissertation to avoid redundancy.

To further highlight the publication's inter-dependencies and overarching themes, a graphic depiction of the entire research project is provided in Figure 4.1. Publication 1 comprised a CFD based analysis of the secondary flow and axial loss development in the baseline T106A turbine cascade and the T106Div with increased blade loading. However, the available reference experimental data revealed some uncertainties regarding the inlet boundary layer conditions. This fact motivated the first research objective of utilizing a multi-methodology investigation approach in a modified test case as stated in Chapter 1. The multi-methodology approach was a recurring theme throughout the research project, starting with the presentation of an improved cascade design with an inserted part-span flat-plate-endwall in Publication 2. Following an experimental flow characterization and validation of the design goals, the modified test case provided an appropriate foundation for the implementation of advanced optical measurement techniques (PIV and PSP) in Publication 4 & 5. Additionally, the potential of ultra-fast TSP was demonstrated in a flat-plate test in Publication 6. The multi-methodology approach was complemented by supplemental pre- and post-test CFD presented in Publication 1–3 & 5. One important use case was the identification of particular areas of interest which was crucial in the selection of the measurement setups.
The second objective of quantifying the wake effects on the time-averaged secondary flow and its associated losses was addressed in Publication 1–3. Based on CFD analysis of the original cascade design without the inserted flat-plate-endwall, Publication 1 was focused on the additional influencing factor of increased blade loading. Subsequent probe-based measurements up- and downstream of the modified cascade's blade passage were presented in Publication 2. This data was subsequently utilized to validate further post-test CFD investigations presented in Publication 3. Furthermore, similarities of the measured wake effects in the exit flow field to the effects of decreasing the inlet endwall boundary layer height motivated an in-depth analysis in Publication 3. Here, the effects were compared inside the blade passage with a focus on the associated loss development.
The final objective was addressed by combining phase-locked and synchronized PIV and PSP measurements presented in Publication 4 & 5 with supplemental CFD data. Thereby, the

periodic wake disturbance of the secondary flow and its interaction with the blade suction surface could be analyzed. A detailed summary of the achievement of each research objective can be found in the conclusions in Chapter 5.

The conducted research was part of a collaborative German research activity funded by the Deutsche Forschungsgemeinschaft (DFG). An overview by Engelmann et al. [32] highlighted the combined findings on secondary flow phenomena in linear and annular compressor and turbine blade rows utilizing experiments and multi-fidelity CFD.

List of Cumulative Publications

1. Ciorciari, R., Schubert, T., and Niehuis, R.: *Numerical Investigation of Secondary Flow and Loss Development in a Low Pressure Turbine Cascade with Divergent Endwalls.* J. Turbomach. Propuls. Power 3(1), 5, 2018. https://doi.org/10.3390/ijtpp3010005.

2. Schubert, T., Chemnitz, S., and Niehuis, R.: *The Effects of Inlet Boundary Layer Condition and Periodically Incoming Wakes on Secondary Flow in a Low Pressure Turbine Cascade.* J. Turbomach. 143(4), 2021. https://doi.org/10.1115/1.4050116.

3. Schubert, T. and Niehuis, R.: *Numerical Investigation of Loss Development in a Low-Pressure Turbine Cascade with Unsteady Inflow and Varying Inlet Endwall Boundary Layer.* Proceedings of the ASME Turbo Expo 2021: Turbomachinery Technical Conference and Exposition, GT2021-59696, Virtual, Online, June 7–11, 2021. https://doi.org/10.1115/GT2021-59606.

4. Schubert, T., Kožulović, D., and Bitter, M.: *Characterization of the Endwall Flow in a Low-Pressure Turbine Cascade Perturbed by Periodically Incoming Wakes. Part 1: Flow Field Investigations with Phase-Locked Particle Image Velocimetry.* Aerospace 11(403), 2024. https://doi.org/10.3390/aerospace11050403.

5. Schubert, T., Kožulović, D., and Bitter, M.: *Characterization of the Endwall Flow in a Low-Pressure Turbine Cascade Perturbed by Periodically Incoming Wakes. Part 2: Unsteady Blade Surface Measurements Using Pressure-Sensitive Paint.* Aerospace 11(404), 2024. https://doi.org/10.3390/aerospace11050404.

6. Bitter, M., Hilfer, M., Schubert, T., Klein, C., and Niehuis, R.: *An Ultra-Fast TSP on a CNT Heating Layer for Unsteady Temperature and Heat Flux Measurements in Subsonic Flows.* Sensors 22(657), 2022. https://doi.org/10.3390/s22020657.

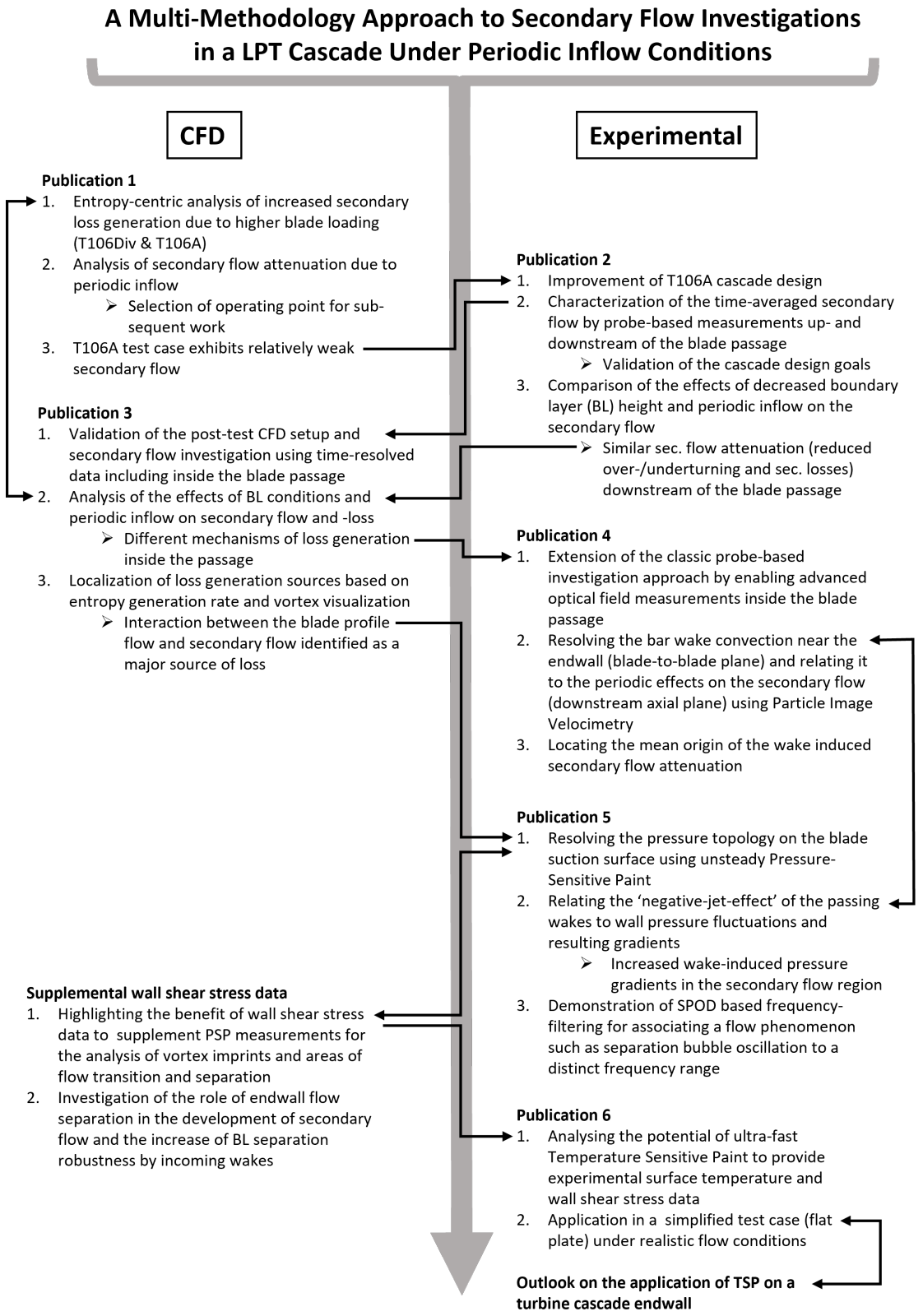

Fig. 4.1: Overview of the research timeline and the inter-dependencies of all cumulative publications.

4.2 Publication 1

4.2.1 Summary

The first cumulative publication which motivated the subsequent research activities comprised secondary flow investigations based on CFD. The work was particularly focused on the effect of increased frontal blade loading on the secondary flow and axial loss development throughout the T106Div cascade under periodically unsteady inflow conditions. By means of comparison to the aft-loaded T106A with parallel endwalls, it was found that the front-loaded T106Div produces more intense secondary flow. Furthermore, the secondary loss development throughout the blade passage was significantly increased to around half of the also increased overall losses of the T106Div. This is the case, because the blade loading causes a transverse pressure gradient in the passage which in turn is the driving force for the development of the secondary vortices, especially in the front part of the passage. Further analysis of the effect of periodic inflow conditions revealed a redistribution of the loss generation components inside the passage. In the front-loaded T106Div, the incoming wakes caused a premature loss generation in the front part of the passage but a lower loss increase near the trailing edge due to lower intensity of the secondary flow. In sum, the periodically incoming bar wakes led to an increase in overall loss generation.
As described in Section 2.1, some secondary flow models do not specifically distinguish between the counter-rotating vortex (CRV) and the trailing vortex (TV) due to their proximity and identical sense of rotation. This approach was also applied in Publication 1 with the notation 'trailing edge wake vortex' (TEWV) to ensure consistency to the previous work of Ciorciari et al. [19]. Subsequently, a new stage of the research project was initiated based on a modified T106A test case. Thus, in the subsequent series of publications the CRV and TV were distinguished in accordance to Section 2.1.
The following three findings of Publication 1 had a significant impact in steering the research topics and approach in the subsequent publications.

1. For the comparison of the loss development in case of steady and periodically unsteady inflow conditions, the change in entropy was evaluated. Since temperature effects are more relevant in unsteady cases, entropy offers a better representation of the entirety of losses than a sole total pressure loss consideration. While this approach is advantageous for axial loss development visualization, it is inherently problematic for identifying the sources of loss, since entropy can only increase in streamwise direction. This motivated an extension of the entropy-centric analysis approach by adding the flow parameter of entropy generation rate per unit volume. This method was utilized in Publication 3 in order to identify the mechanisms of secondary flow development, interaction, and associated loss generation.

2. The effect of periodically unsteady inflow conditions was investigated in two cases of different bar pitches i.e. Strouhal numbers. While the intensity of the effect increased with the Strouhal number, the characteristic of the redistribution in loss generation within the blade passage could be observed in both cases. Therefore, one set of unsteady inflow conditions at the mechanical limit of the available test facility was chosen for all subsequent investigations. Also, the CFD was intentionally conducted under the

same operating conditions, so that the numerical results could be validated and used to supplement the experimental results.

3. The numerical predictions in Publication 1 were validated using experimental reference data by Kirik and Niehuis [62]. The blade pressure distribution as well as the downstream flow field were well reproduced and allowed further analysis of the flow phenomena. However, some uncertainties remained with respect to the inlet flow conditions of the experimental test case. The issue was caused by a gap between the wind tunnel and the cascade endwalls upstream of the blade row. This gap was required for the moving bar wake generator. Due to a negative pressure gradient between the test section and its surroundings, a leakage flow was formed in the bar gap. While the freestream flow was not affected, it acted as an endwall boundary layer suction and ultimately led to weak secondary flow in the T106A. Also, the cascade design did not allow direct access to upstream or inside of the passage. Therefore, CTA measurements had to be conducted with an extended probe inserted from downstream. These issues motivated the main focus of Publication 2; a modification of the test case to provide a solid foundation for a new comprehensive experimental data set. The T106A turbine cascade was chosen as a basis instead of the T106Div, because the improved cascade design ensured sufficiently strong secondary flow by an alternative method. Unlike divergent enwalls, a variation of the endwall boundary layer is thereby independent of the blade loading. Additionally, the numerical setup was enhanced to include the bar gap effects (Publication 2 & 3).

4.2.2 Postprint

International Journal of
Turbomachinery
Propulsion and Power

MDPI

Article

Numerical Investigation of Secondary Flow and Loss Development in a Low-Pressure Turbine Cascade with Divergent Endwalls †

Roberto Ciorciari *, Tobias Schubert * and Reinhard Niehuis

Institute of Jet Propulsion, Bundeswehr University Munich, Werner-Heiseberg-Weg 39, 85577 Neubiberg, Germany; reinhard.niehuis@unibw.de

* Correspondence: roberto.ciorciari@unibw.de (R.C); tobias.schubert@unibw.de (T.S)

† This paper is an extended version of our paper published in Proceedings of the European Turbomachinery Conference ETC12 2017, Paper No. 335.

Received: 7 December 2017; Accepted: 1 February 2018; Published: 9 February 2018

Abstract: Secondary flow and loss development in the T106Div-EIZ low-pressure turbine cascade are investigated utilizing (U)RANS simulations in cases with and without periodically incoming wakes at $Ma_{2th} = 0.59$ and $Re_{2th} = 2 \times 10^5$. The predictions are compared to experimental data presented by Kirik and Niehuis (2015). The axial mid-span and overall loss development in the T106Div-EIZ and the T106A-EIZ in the steady case are analyzed regarding the effects caused by the different loading distributions and by the divergent endwall geometry. Furthermore, the entropy generation is analyzed in the T106Div-EIZ with periodically incoming wakes in several axial positions of interest and compared to the undisturbed steady case. It is found that in the front-loaded T106Div-EIZ, the incoming wakes cause a premature endwall loss production in the front part of the passage, resulting in a lower intensity of the secondary flow downstream of the passage and a redistribution of the loss generation components.

Keywords: low-pressure turbine; unsteady flow; secondary flow; loss development; (U)RANS

1. Introduction

The trend of high-lift airfoils in modern low-pressure turbines of high-bypass jet engines has led to higher pressure gradients in the blade passages. In this context, secondary flow can be intensified and the corresponding losses increase. As alluded to in Denton's [1] overview of the loss mechanisms in turbomachinery, it is evident that the secondary flows make a significant contribution to the overall losses, especially for low aspect ratio blades in which the secondary flows extend over a large portion of the blade span. In current axial turbines, secondary losses account for approximately 30 % of the overall losses (Cui and Tucker [2]). Whereas early studies on secondary flows and endwall losses focused on steady flow states, the loss development and unsteady interaction mechanisms in the endwall region are currently not understood in full detail. Thus, the influence of periodically incoming wakes on the endwall flow has been increasingly investigated in recent years.

Previous investigations of the endwall flow in the T106A-EIZ turbine cascade with parallel endwalls by Ciorciari et al. [3] have shown that periodically incoming wakes can influence the over- and under-turning in the secondary flow region depending on Strouhal number and flow coefficient. However, the influence of incoming wakes on the time-averaged endwall losses in the presented case was relatively small, which was confirmed by Koschichow et al. [4] utilizing incompressible direct numerical simulations (DNS) in a lower Reynolds number flow case. Similar conclusions were drawn by Volino et al. [5], who conducted measurements of unsteady secondary flows in a high-pressure turbine cascade, induced by upstream moving bars. The time-averaged total pressure losses exhibited

very small differences between the cases with and without incoming wakes. In contrast to the relatively small effect of the incoming wakes, Volino et al. [6] described how the development of the endwall flow is greatly influenced by the inflow boundary layer.

Furthermore, an additional impacting factor on the loss development in modern turbines is the loading distribution of the airfoil. Wakelam et al. [7] investigated the profile losses in three different low-pressure turbine cascades with incoming wakes. The cascades had identical pitch, axial chord, inlet angle, and exit Mach number, but featured different airfoil designs. They highlighted the importance of blade loading distribution in regard to loss generation, particularly the maximum velocity location and diffusion on the suction surface. The ideal location of maximum velocity is dependent on wake passing frequency, diffusion factor, and Reynolds number. Muth and Niehuis [8] presented a method to deconstruct the integral loss of a low-pressure turbine cascade, enabling an analysis of profile loss components at low Reynolds numbers. Experimental data and predicted results from (U)RANS simulations were used to evaluate the axial loss development and to investigate the effect of incoming wakes among other influencing parameters. However, since the presented investigation was focused solely on mid-span profile and mixing losses, it did not cover the contribution of endwall losses. The relevance of loading distribution on full-span losses was investigated by Praisner et al. [9] on four aft- and front-loaded high-lift turbine airfoils. In terms of mid-span efficiency, the front-loaded designs showed great performance at low Reynolds numbers, essentially matching the low losses of the baseline design. However, an analysis of the full-span losses revealed a higher increase in endwall losses in the case of front-loaded airfoils with respect to designs that employ an aft-loaded approach. Weiss and Fottner [10] came to the same conclusion after investigating secondary flow and endwall losses in the aft-loaded T106 and the front-loaded T104 turbine cascades. Endwall loss generation and the effect of wake-disturbed inflow in the T106A turbine cascade have recently been investigated by Cui and Tucker [2]. Utilizing high fidelity eddy-resolving simulations, they identified two major regions of high loss generation rate: the corner vortex region and the interaction between the passage vortex and the blade suction surface.

The work presented in this paper combines multiple aspects of the aforementioned works in its investigation of the effects of periodically incoming wakes and blade loading distribution on loss generation in a turbine cascade. More precisely, the secondary flows and endwall losses in the T106Div-EIZ low-pressure turbine cascade are investigated in cases with and without periodically incoming wakes using computational fluid dynamics (CFD) predictions. In the T106Div-EIZ cascade, the divergent endwalls and the higher front-loading of the blades cause different inflow endwall boundary layer development and stronger secondary flows compared to the parallel endwall case under the same exit flow conditions, which has shown relatively weak secondary flows in previous investigations. The T106Div-EIZ cascade therefore provides a better basis for an analysis of the axial overall and endwall loss development throughout and downstream of the blade passage.

2. Experimental Reference Data

All experimental data presented in this paper was obtained in the High Speed Cascade Wind Tunnel of the Institute of Jet Propulsion of the University of the German Federal Armed Forces Munich (Universität der Bundeswehr München) and was published in detail by Kirik and Niehuis [11].

3. Investigated Test Cascade and Configurations

The investigated T106Div-EIZ turbine cascade consists of seven blades with a pitch to chord ratio of 0.8 featuring the aft-loaded T106 profile geometry investigated by Duden [12], Acton [13], and Stadtmüller [14]. The same airfoil has also been used in previous investigations of the T106A-EIZ cascade with parallel endwalls by Ciorciari et al. [3], where a new developing endwall boundary layer after the wake generator and upstream of the cascade was identified as the cause for the relatively weak secondary flows and the observed minor influence of the periodically incoming wakes in the endwall region. The T106D-EIZ cascade is equipped with straight divergent endwalls with an inclination of

15° with respect to the axial direction and an inflow aspect ratio of 1.55 ($c = 100$ mm, $H_1 = 155$ mm). Under constant exit flow conditions, the flow in the T106Div-EIZ cascade induces a higher blade loading due to the divergent endwalls with respect to the T106A-EIZ cascade with an aspect ratio of 1.7 ($c = 100$ mm, $H = 170$ mm) and parallel endwalls. In particular, the axial pressure distribution on the suction surface of the airfoil is altered, with the T106Div-EIZ exhibiting a higher loading in the front area. The higher front-loading in conjunction with the divergent endwall geometry cause different inlet endwall boundary layer development with the intention to produce more relevant secondary flows in the cascade and allow a better analysis of the effect of the incoming wakes on the endwall flow than in the parallel endwall case. Due to a constant exit Mach and Reynolds number in all configurations, the ratio of the mass flow rate in the T106Div-EIZ to the T106A-EIZ cascade is approximately 1.3.

In Figure 1, the geometry of the inlet region of the cascade is shown together with the modeled numerical multi-block domain. The investigated exit flow conditions $Ma_{2th} = 0.59$ and $Re_{2th} = 2 \times 10^5$ are defined by setting the total pressure and total temperature at the inlet as well as the static pressure downstream of the cascade, using the same fluid properties and constants as described in Ciorciari et al. [15].

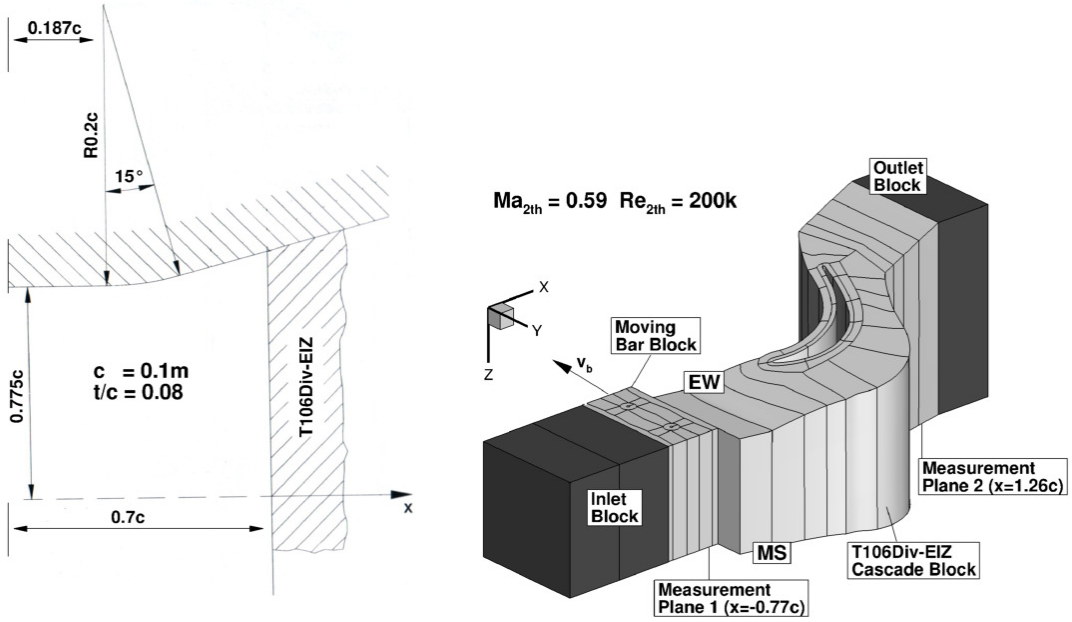

Figure 1. Geometry of the T106Div-EIZ inlet region and the modeled numerical domain.

Table 1 summarizes the investigated cases with and without periodically unsteady inflow. The denotation of the investigated cases is composed of the bar pitch t_b in millimeters and bar speed v_b in meters per second. The relatively high flow coefficients ϕ in the investigated cases are due to the realistic high speed inflow conditions featured in the experiment. In the experimental setup, the speed of the moving bars, which have a diameter of two millimeters, is limited due to mechanical safety concerns. However, CFD can be used in this context to extend the range of the investigated cases as published by Ciorciari et al. [15]. The unsteady T40 20 case is used for a comparison of the predicted results with the experimental data. Since the T80 20 case features a single bar wake in the computational domain, it is utilized for an analysis regarding the interaction of the incoming wakes with the secondary flow inside the passage and the axial loss development in the cascade. The inlet turbulence intensity value measured in the experiment in the wind tunnel at measurement plane 1, without a mounted wake generator, was of approximately 5 %.

Table 1. Investigated configurations for the T106Div-EIZ.

Conf.	t_b (mm)	v_b (m/s)	ϕ(–)	Sr(–)	*EXP*	*CFD*
Steady	-	-	-	-	Kirik and Niehuis [11]	x
T80 20	80	20	5.5	0.23	-	x
T40 20	40	20	5.5	0.45	Kirik and Niehuis [11]	x

t_b, bar pitch; v_b, bar speed; $Sr = (v_b/t_b \cdot (c/v_{ax,0})$, Strouhal number; $\phi = v_{ax}/v_b$, flow coefficient.

4. CFD Setup

4.1. Flow Solver and Domain Discretization

The flow solver TRACE, developed by DLR Cologne (Institute of Propulsion Technology), has been used for all simulations presented in the present work. The code provides a numerical solution of the RANS equations using a finite volume approach. A detailed description of the implemented numerical methods and models can be found on the TRACE online portal by DLR [16] and in Eulitz [17], Yang et al. [18], Nürnberger [19], Kügeler [20], Yang et al. [21] and Becker [22]. In the present work, the RANS turbulent closure is modeled using the Wilcox $k-\omega$ two-equation turbulence model, including the additional Kato and Launder pressure stagnation anomaly fix (Kato and Launder [23], Kozulovic et al. [24]). The transition model used in this work is the $\gamma - Re_{\theta t}$ transport equation model (Marciniak et al. [25], Menter and Langtry [26]).

4.2. Domain Definition and Boundary Conditions

Figure 1 shows the spanwise symmetrical 3D numerical domain which is used for all simulations of the T106Div-EIZ. A high boundary layer resolution is assured by a fine OC-Grid with $y^+ \leq 1$ on the viscous blade walls. The entire domain includes a total number of around 4.7 million grid cells. For the temporal resolution in the unsteady simulations, the number of time steps per moving domain period is set to 1200, which enables a resolution of the moving bar vortex shedding frequency. In order to ensure sufficient periodic convergence, the unsteady simulations are run for 15 moving domain passing periods. Additional blocks are added at the domain inlet and outlet. The non-divergent outlet block, which features an inviscid endwall, is implemented to assure an adequate setting of the static outlet pressure as a non-reflecting boundary condition in a radial equilibrium state. In the steady cascade investigations, the sensitivity of the variation of the inlet flow angle $\beta_{1steady}$ has been evaluated starting from the design angle ($\beta_{1design} = 127.7°$). A pressure-sided incidence angle of 1° resulted in an improved prediction of the experimental isentropic Mach number distribution at mid-span as seen in Figure 2 and is therefore used for all unsteady calculations in the plane upstream of the wake generator ($\beta_0 = \beta_{1steady} = 128.7°$). The predicted results of the T106A-EIZ are obtained using an inlet flow angle of $\beta_0 = 129.7°$ (Ciorciari et al. [3]).

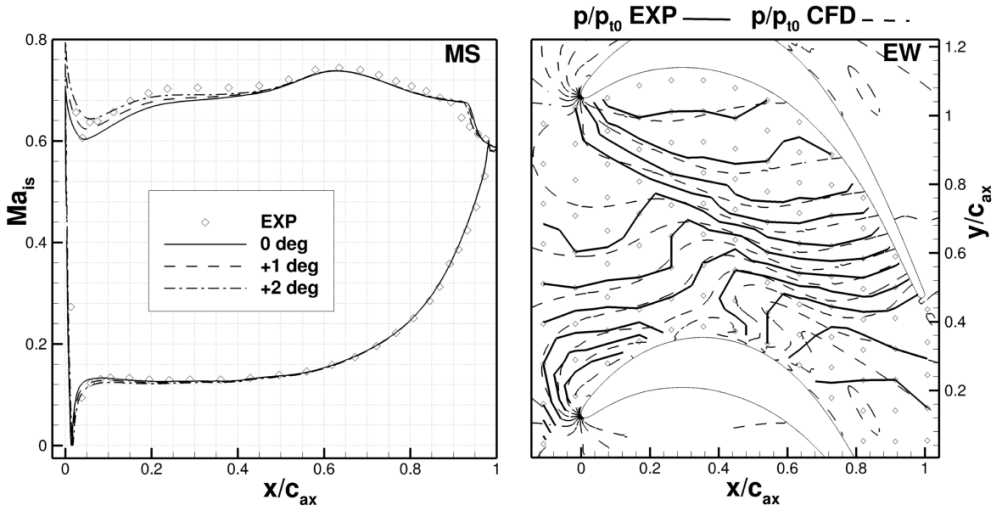

Figure 2. Predicted Ma_{is} distribution at mid-span (left) and isobars near the endwall (right) for three inflow angles at $Ma_{2th} = 0.59$ and $Re_{2th} = 200k$ compared to measured data by Kirik and Niehuis [11].

5. Results

5.1. Comparison with Measured Data

On the left-hand side of Figure 2, the comparison between the predicted isentropic Mach number distributions at mid-span in the T106Div-EIZ at $Ma_{2th} = 0.59$ and $Re_{2th} = 200k$ with the measured data shows a good agreement. The larger extension of the separation bubble in the prediction is attributed to a quicker turbulence decay in the numerical domain, resulting in a lower free-stream turbulence intensity with respect to the experiment. The turbulence decay and the propagation of flow properties throughout the computational domain are influenced by the choice of turbulence model as well as the grid resolution in (U)RANS simulations. However, the laminar boundary layer on the suction surface upstream of the separation bubble appears well modeled using the turbulent length scale of the order of 1 %, and the resulting profile losses match well with the downstream measured values. On the right-hand side of Figure 2, the measured isobar distribution on the endwall shows a stronger distortion of the isobars at the inlet of the passage with respect to the simulations. This appears to be caused by an earlier roll-up of the inlet endwall boundary layer in the experiment. The difference with respect to the predicted values is related to uncertainties regarding the modeling of the inlet endwall boundary conditions due to the mounted wake generator in the experimental setup and the upstream effect of the endwall divergence. The earlier roll-up of the inlet boundary layer results in a more intense passage vortex (PV) and causes higher total pressure loss values ζ_{2exp} with respect to ζ_{2CFD} in the vortex interaction region near $z/h = 0.4$ shown on the bottom of Figure 3. The experimental $\Delta\beta_{2sec}$ values at the top of Figure 3 confirm this observation, indicating a higher underturning with respect to the predictions. Furthermore, the higher lift-off of the passage vortex in the experiment is partially attributed to the earlier roll-up of the inlet endwall boundary layer. It also appears that the more intense trailing edge wake vortex (TEWV) in the CFD ($0.4 < z/h < 0.5$) is constraining the lift-off of the passage vortex. The higher intensity of the predicted TEWV is attributed to the aforementioned longer separation bubble simulated on the suction side and the lower free-stream turbulence intensity. Additionally, the linear eddy viscosity model used in all simulations, in which the Boussinesq approximation is adopted, works under the assumption of isotropic turbulence. As observed by Michelassi et al. [27] and Pichler et al. [28] in DNS studies of mid-span flow in the T106A cascade, the linear stress–strain coupling is error-inducing in regions where significant anisotropic stress is present. Considering that anisotropic stress is highly relevant in the investigated secondary

flow region with complex vortex interaction, the underlying limitations of the chosen turbulence model present an uncertainty in the flow predictions and may contribute to the observed differences in the experimental data.

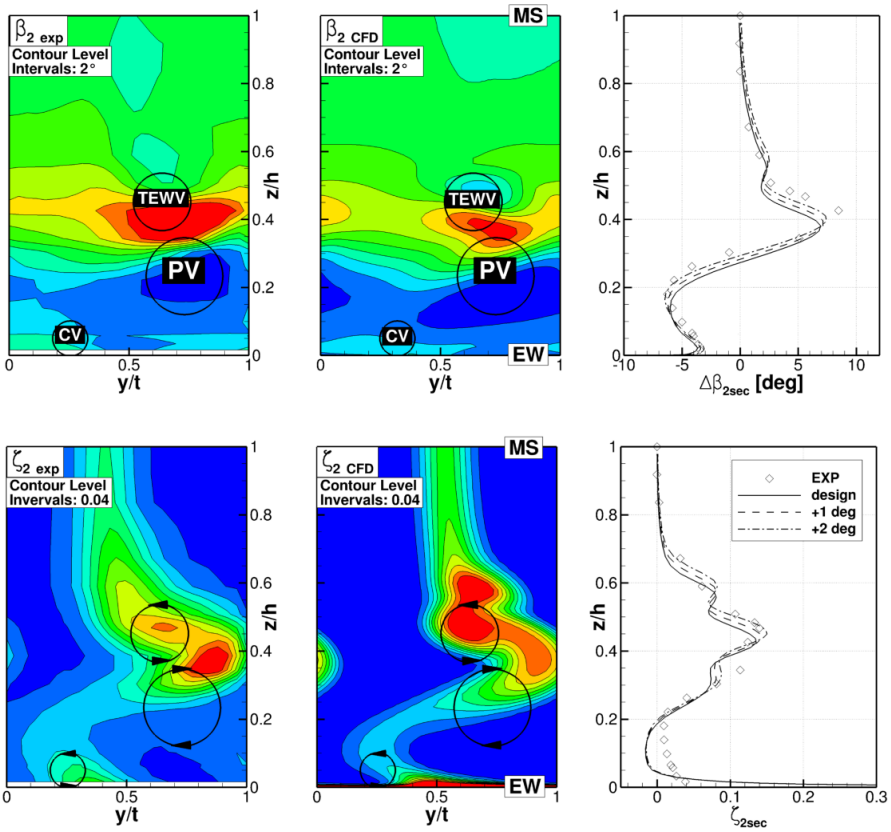

Figure 3. Predicted spanwise distribution of the pitchwise averaged secondary outflow yaw angle $\Delta\beta_{2sec}$ and total pressure losses ζ_{2sec} compared to the measured data by Kirik and Niehuis [11] in the measurement plane 2 downstream of the cascade.

5.2. Steady Numerical Analysis

The previous results highlight the influence of the inlet endwall boundary layer development on the secondary flows in and downstream of the passage. The development of the inlet boundary layer, in turn, is directly related to the pressure field upstream of the cascade. In the T106Div-EIZ, the presence of the endwall divergence induces a spanwise pressure gradient and different diffusion properties with respect to the parallel endwall case. A comparison of the velocity v/v_1 and total pressure p_t/p_{t0} profiles perpendicular to the endwall upstream of the T106Div-EIZ for two pitchwise positions, in Figure 4, is useful to gain a better understanding of the inlet endwall boundary layer development considering its three-dimensional characteristics. The strings of perpendicular lines are defined starting at the two pitchwise positions at $x_w = -0.06$ and respectively following a theoretical streamline with the given design inflow angle. The first streamline shown at the top of Figure 4 passes through the center of the passage and the second streamline is designed to impinge near the leading edge of the blade. After the EIZ gap, a new boundary layer is developing and overlapping with the spanwise non-uniformly accelerated flow near the beginning of the endwall divergence, which is evident at $x_w = -0.06$ and $x_w = -0.036$. The local acceleration is a result of the flow following the endwall curvature, which induces a spanwise pressure gradient in a radial equilibrium state. At these axial positions, the v/v_1 and p_t/p_{t0} profiles at both pitchwise positions are very similar, indicating that the potential effect of the downstream airfoils is negligible at that distance. At the axial positions

$x_w = -0.027$ and $x_w = -0.017$, the potential effect of the airfoil on the incoming endwall flow is visible considering the differences shown in the v/v_1 profiles in the two pitchwise positions. However, the p_t/p_{t0} profiles are similar at both pitchwise positions.

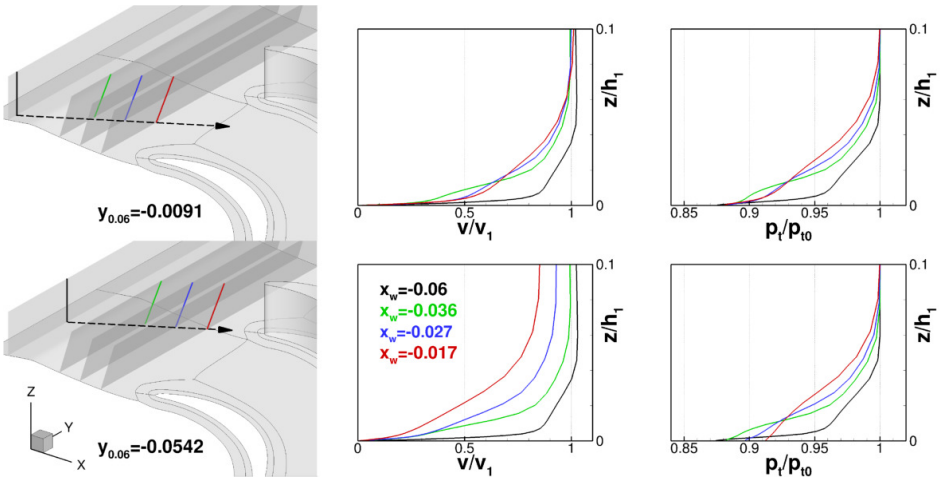

Figure 4. Boundary layer development on the divergent endwall at two pitchwise positions.

The mass flow-averaged overall axial total pressure loss $\Delta p_{(t1-tx)}/q_{2th}$ developments throughout the T106Div-EIZ and the T106A-EIZ in Figure 5 confirm an alteration of the endwall boundary layer loss development at around $x/c_{ax} = -0.6$, not related to the increased frontal loading, but rather to the start of endwall divergence. In front of the leading edge ($x/c_{ax} = 0$), the endwall boundary layer losses in the T106Div-EIZ are higher than those in the T106A-EIZ; however, at mid-span, no significant free stream losses are produced in both cases. Approaching the leading edge, the mid-span profile losses are higher in the T106Div-EIZ with respect to the T106A-EIZ considering the higher front-loading, inflow velocity, and shear stress. Due to the higher frontal loading, the position of the separation/transition region on the suction side in the T106Div-EIZ is located further upstream than in the T106A-EIZ. An apparent convergence of the values occurs near the trailing edge before the T106Div-EIZ finally produces higher profile losses downstream of the trailing edge ($x/c_{ax} > 1$). The differences in mid-span total loss production in the two cascades are relatively small compared to the differences observed in the secondary flow region in Figure 5. The different development of the inlet endwall boundary layer effectively causes a stronger endwall boundary layer vorticity at the inlet of the cascade in the case of the T106Div-EIZ. The higher endwall losses observed in the T106Div-EIZ are mainly attributed to the higher momentum deficiency in the incoming endwall boundary layer, but also partially to the longer wetted shear surface due to the divergence and the stronger front-loading of the cascade with respect to the T106A-EIZ. In a front-loaded cascade, high transverse pressure gradients act on the relatively thick boundary layer in the front section of the passage, resulting in a stronger passage vortex. The dissipation of the kinetic energy of the vortex motion causes higher endwall losses in the aft section and downstream of the passage. On the contrary, the maximum pressure gradient in the aft-loaded T106A-EIZ does not occur until further downstream, where the endwall boundary layer is much thinner and weaker secondary flow ensues. Aside from the different overall loss levels, the loss developments far downstream of the trailing edge in Figure 5 show a similar behavior in both cascades. Following the mixing loss region, which extends to approximately $x/c_{ax} = 1.3$, there is a quasi-linear loss increase as a result of the endwall flow in this region. This observation is consistent with the findings published by Muth and Niehuis [8], which showed a rapid increase in mixing losses near the trailing edge, especially at low Reynolds numbers, followed by a decreased loss gradient once the flow is mixed out.

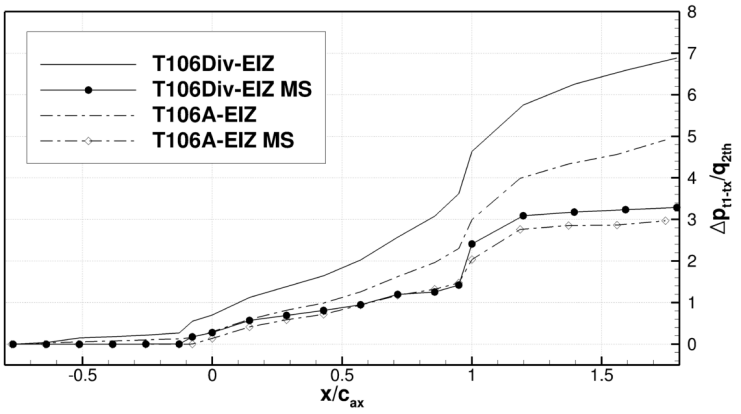

Figure 5. Comparison of mid-span (MS) and overall losses for the T106A-EIZ and T106Div-EIZ.

5.3. Steady and Unsteady Comparison

In order to obtain a better understanding of the loss production mechanisms due to periodically incoming wakes and their interaction with the secondary flows, the overall entropy generation in the T106Div-EIZ is presented in Figure 6. Considering the relatively weak secondary flows in the T106A-EIZ as well as the relatively minor effects due to the incoming wakes, only the T106Div-EIZ is analyzed. As mentioned before, the unsteady simulations were conducted using a high temporal and spatial resolution. Therefore, the change over time in the computational domain shows two main signals, the periodical inflow disturbance as well as the superimposed fluctuations of the vortex shedding in the bar wakes featuring distinctly different frequencies and amplitudes. The periodical inflow disturbance appears to be well reproduced in the numerical simulations of the investigated cases, whereas the amplitude of the vortex shedding is afflicted with numerical uncertainties considering the limitations of the (U)RANS approach and the linear eddy viscosity model. Resolving the vortex shedding in the numerical simulation leads to an energy separation phenomenon as observed by Adami et al. [29], which implies that in this region both total pressure and total temperature variations have to be considered collectively in order to evaluate overall losses in the domain. The predicted non-dimensional entropy generation $\Delta s \,/\, (v_{2th}^2/T_{t0})$ for the undisturbed, the T80 20 and the T40 20 cases was calculated by

$$\frac{\Delta s(x)}{v_{2th}^2/T_{t0}} = \frac{c_v \, ln \, \frac{p_t(x)}{p_{t,0}} + c_p \, ln \, \frac{\rho_t(x)}{\rho_{t,0}}}{v_{2th}^2/T_{t0}} \,. \tag{1}$$

The reference total temperature and total pressure values as well as the fluid properties are defined by the inlet conditions of the calculation. For the evaluation of the axial entropy development, the local values are interpolated from the numerical grid onto a defined structured grid utilizing inverse distance weighting at each respective axial position. Subsequently, the mass flow weighted average is calculated. The structured uniform grid for the interpolation was defined in three regions, $x/c_{ax} < 0$, $0 < x/c_{ax} < 1$, and $x/c_{ax} > 1$ featuring different resolutions, 90×100, 100×100 and 200×200 node elements respectively. These grid resolutions are obtained through a grid sensitivity analysis and are also used for the evaluation of $\Delta p_{(t1-tx)}/q_{2th}$ in the T106Div-EIZ in Figure 5. The ratio of grid nodes of the interpolation grid to the non-uniform numerical grid is approximately 1.1 in the domain section of the blade passage $(0 < x/c_{ax} < 1)$. For the T106A-EIZ configuration, a smaller resolution (100×100) is sufficient in the region $x/c_{ax} > 1$ downstream of the trailing edge considering the constant span height in this case.

The overall corrected entropy value $\Delta s_{corr} \,/\, (v_{2th}^2/T_{t0}) = [\Delta s(x) - \Delta s(x_{ref})] \,/\, (v_{2th}^2/T_{t0})$ is defined in order to filter the incoming wake losses at the cascade inlet in Figure 6 and thus allow a separate analysis of the effect of the incoming wakes on the entropy development throughout the cascade ($x/c_{ax} > x_{ref}/c_{ax} = -0.6$), with $x/c_{ax} = 0$ at the airfoil leading edge. In front of the leading

edge, the differences in $\Delta s_{corr} / (v_{2th}^2/T_{t0})$ between the undisturbed and the two unsteady cases appear to be negligible with respect to the values inside and downstream of the passage. Entering the blade passage $0 < x/c_{ax} < 1$, a relevant divergence of the entropy generation lines is apparent, where a stronger entropy increase is observed in the cases of disturbed inflow with respect to the steady case. At the trailing edge and downstream, the entropy generation lines are converging again, which will be explained with the help of Figure 7. The overall higher losses produced in the passage in the two cases with incoming wakes are attributed to the bar wake interaction with the endwall flow and with the airfoil boundary layer. The bar wake mixing losses, however, are considered to be negligible in the passage region with respect to the aforementioned factors. In Figure 7, the comparison of time-averaged entropy values in different axial slices illustrates the effect of the incoming wakes in the T80 20 case with respect to the steady case. The time-averaged values result from an arithmetic averaging of 120 flow solutions out of the overall 1200 time-steps calculated in one bar passing period of the unsteady simulation. The roll-up of the passage vortex and the pressure-driven transport towards the suction surface is delayed by the interaction with the incoming wakes, causing a less distinct system of secondary vortices with respect to the undisturbed case in this front-loaded configuration. This mechanism is correlated to a premature loss production as seen at about $x/c_{ax} = 0.1$ in Figure 6. Furthermore, a smaller lift-off of the passage vortex and a homogenizing effect in terms of under- and over-turning is apparent in the predicted results, which is consistent with the experimental data presented by Kirik and Niehuis [11]. The weaker passage vortex is transported downstream with lower streamwise vorticity, which results in smaller secondary loss production near the trailing edge and mixing losses in the downstream flow field, causing the aforementioned convergence of the entropy generation lines in Figure 6. In the investigated case at $Re_{2th} = 2 \times 10^5$, the profile losses in the unsteady cases are augmented with respect to the steady case due to the interaction of the incoming wakes with the profile boundary layer. More precisely, the periodically incoming wakes cause the transition/separation region to move further upstream on the suction surface, resulting in a longer reattached turbulent boundary layer and therefore higher profile losses. The contribution of the profile losses appears to be a relevant cause of the higher $\Delta s_{corr} / (v_{2th}^2/T_{t0})$ values observed downstream of the cascade in the unsteady cases. The first divergence of the entropy generation lines near the leading edge in conjunction with the convergence near the trailing edge in Figure 6 confirm the redistribution of the loss components in the passage due to the incoming wakes. The incoming wakes reduce the intensity of the secondary flows in and downstream of the passage, but the reduction appears to be insufficient to compensate for the augmented profile losses.

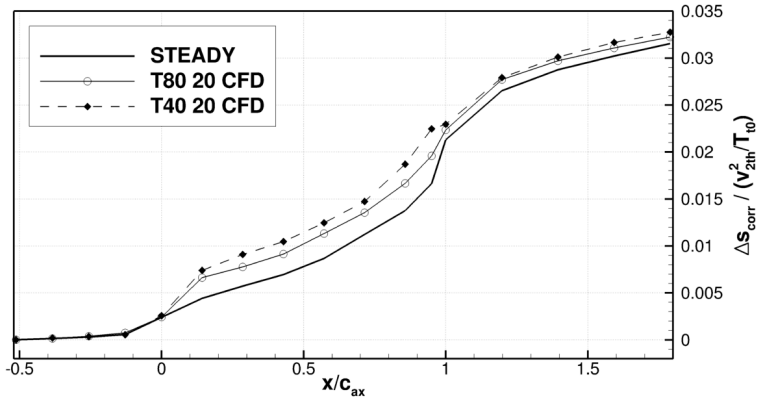

Figure 6. Comparison of the axial entropy development in the steady and the two investigated unsteady cases (T80 20 and T40 20).

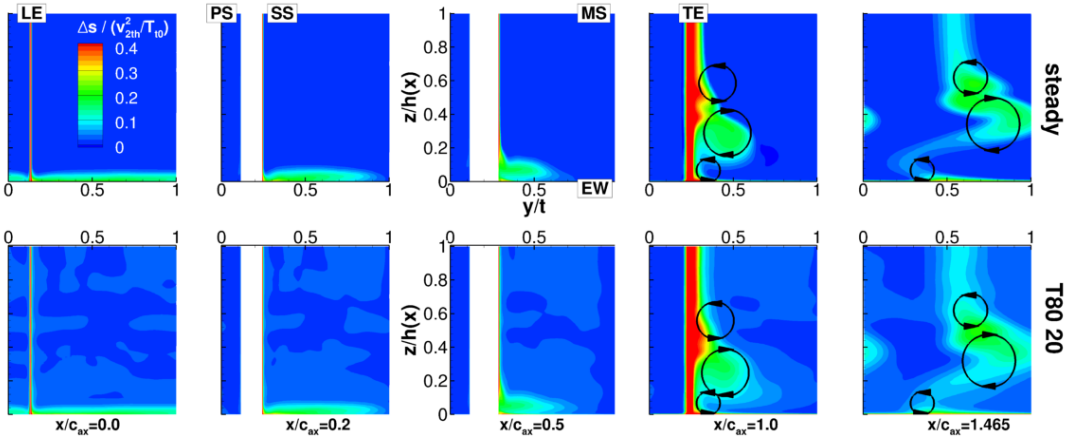

Figure 7. Comparison of the entropy distribution at different axial positions in the T106Div-EIZ in the steady and the unsteady T80 20 cases.

6. Conclusions

Steady and unsteady numerical analyses were conducted in order to investigate the effect of periodically incoming wakes on the axial loss development throughout the T106Div-EIZ turbine cascade. The comparison with experimental data at mid-span, near the endwall, and downstream of the cascade provides a verification of the predicted results. Some differences with respect to the measured data are attributed to uncertainties related to the inlet flow conditions of the investigated cascade and to the turbulence/transition modeling of the (U)RANS approach. Nevertheless, the main flow phenomena are well reproduced and allow an analysis of the effect of the incoming wakes on the flow into and downstream of the passage. A comparison between the T106Div-EIZ and the T106A-EIZ with parallel endwalls under the same exit flow conditions indicates that the T106Div-EIZ produces more intense secondary flows in the passage. This is caused not only by the higher front-loading, but also by the endwall geometry, which influence the roll-up of the incoming endwall boundary layer and the axial loss development in front of the cascade. The overall loss development indicates that the increased values in the case of divergent endwalls are mainly related to the endwall flow. A comparison of the steady and unsteady cases at $Ma_{2th} = 0.59$ and $Re_{2th} = 2 \times 10^5$ shows a redistribution of the loss generation components due to the incoming bar wakes. In the front-loaded T106Div-EIZ, the incoming wakes cause a premature endwall loss production in the front part of the passage resulting in a lower intensity of the secondary flow downstream of the trailing edge and smaller secondary mixing losses. Nevertheless, in the investigated cases, the profile losses are augmented by an earlier transition/separation and a longer reattached turbulent boundary layer due to the incoming wakes, causing an increased overall entropy generation with respect to the undisturbed case.

Acknowledgments: The investigations were conducted as part of the Deutsche Forschungsgemeinschaft joint research project PAK-530. The authors acknowledge Ilker Kirik, who carried out the experimental measurement campaign and Alexander Jörger for his contribution to the post processing. Furthermore, the authors wish to acknowledge DLR Cologne, Institute of Propulsion Technology, for provision of the flow solver TRACE and for the very productive collaboration.

Author Contributions: The presented work stems from a joint research effort of Roberto Ciorciari and Tobias Schubert, including data acquisition, post-processing, analysis and paper writing, resulting in equal contributions to the paper. As the head of the Institute of Jet Propulsion Reinhard Niehuis was responsible for the supervision of all research activities associated with the presented work.

Conflicts of Interest: The authors declare no conflict of interest. The founding sponsors had no role in the design of the study; in the collection, analyses, or interpretation of data; in the writing of the manuscript, and in the decision to publish the results.

Nomenclature

Latin Symbols

c	chord length
H, h	height in spanwise direction, $h = 1/2 \cdot H$
Ma	Mach number
p	pressure
q	dynamic pressure
Re	Reynolds number
s	entropy
Sr	Strouhal number, $(v_b/t_b) \cdot (c/v_{ax,0})$
T	temperature
t	pitch
v	velocity
x	axial coordinate
y	pitch-wise coordinate
z	span-wise coordinate

Greek Symbols

β	yaw (pitch-wise) angle
$\Delta p_t/q_{2th}$	total pressure losses
Δs	entropy generation
ϕ	flow coefficient, v_{ax}/v_b

Abbreviations

CFD	Computational Fluid Dynamics
CV	Corner Vortex
DNS	Direct Numerical Simulation
EIZ	Erzeuger Instationärer Zuströmung (wake generator)
EW	EndWall
EXP	Experimental
LPT	Low-Pressure Turbine
MS	Mid-Span
PV	Passage Vortex
TEWV	Trailing Edge Wake Vortex
(U)RANS	(Unsteady) Reynolds-Averaged Navier-Stokes equations

Subscripts

0	domain inlet
1,2	measurement planes
ax	axial
b	bar
corr	corrected
t	total
th	theoretical
sec	secondary

References

1. Denton, J.D. The 1993 IGTI Scholar Lecture: Loss Mechanisms in Turbomachines. *J. Turbomach.* **1993**, *115*, 621–656, doi:10.1115/1.2929299.
2. Cui, J.; Tucker, P.G. Numerical Study of Purge and Secondary Flows in a Low Pressure Turbine. *J. Turbomach.* **2017**, *139*, 021007.
3. Ciorciari, R.; Kirik, I.; Niehuis, R. Effects of Unsteady Wakes on the Secondary Flows in the Linear T106 Turbine Cascade. *J. Turbomach.* **2014**, *136*, 091010.
4. Koschichow, D.; Fröhlich, J.; Kirik, I.; Niehuis, R. DNS of the Flow Near the Endwall in a Linear Low Pressure Turbine Cascade with Periodically Passing Wakes. In Proceedings of the ASME Turbo Expo 2014: Turbine Technical Conference and Exposition, Düsseldorf, Germany, 16–20 June 2014; Paper No. GT2014-25071.
5. Volino, R.; Galvin, C.D.; Ibrahim, M. Effects of Periodic Unsteadiness on Secondary Flows in High Pressure Turbines. In Proceedings of the ASME Turbo Expo 2013: Turbine Technical Conference and Exposition, San Antonio, TX, USA, 3–7 June 2013; Paper No. GT2013-95881.
6. Volino, R. Effects on Endwall Boundary Layer Thickness and Blade Tip Geometry on Flow Through High Pressure Turbine Passages. In Proceedings of the ASME Turbo Expo 2014: Turbine Technical Conference and Exposition, Düsseldorf, Germany, 16–20 June 2014; Paper No. GT2014-27013.
7. Wakelam, C.T.; Höger, M.; Niehuis, R. A Comparison of Three Low Pressure Turbine Designs. *J. Turbomach.* **2013**, *135*, 051026.
8. Muth, B.; Niehuis, R. Axial Loss Development in Low Pressure Turbine Cascades. *J. Turbomach.* **2013**, *135*, 041024.
9. Praisner, T.J.; Grover, E.A.; Knezevici, D.C.; Popovis, I.; Sjolander, S.A.; Clark, J.P.; Sondergaard, R. Toward the Expansion of Low-Pressure-Turbine Airfoil Design Space. *J. Turbomach.* **2013**, *135*, 061007.
10. Weiss, A.P.; Fottner, L. The Influence of Load Distribution on Secondary Flow in Straight Turbine Cascades. *J. Turbomach.* **1995**, *117*, 133–141, doi:10.1115/93-GT-086.
11. Kirik, I.; Niehuis, R. Comparing the Effect of Unsteady Wakes on Parallel and Divergent Endwalls in a LP Turbine Cascade (T106A-EIZ and T106D-EIZ). In Proceedings of the 11th International Gas Turbine Congress, Tokyo, Japan, 15–20 November 2015.
12. Duden, A. Strömungsbeeinflussung zur Reduzierung der Sekundärströmungen in Turbinengittern. Ph.D. Thesis, Universität der Bundeswehr München, München, Germany, 1999.
13. Acton, P. Untersuchungen des Grenzschichtumschlages an Einem Hochbelasteten Turbinengitter unter Inhomogenen und Instationären Zuströmbedingungen. Ph.D. Thesis, Universität der Bundeswehr München, München, Germany, 1998.
14. Stadtmüller, P. Grenzschichtentwicklung und Verlustverhalten von Hochbelasteten Turbinengittern unter Einfluß Periodisch Instationärer Zuströmung. Ph.D. Thesis, Universität der Bundeswehr München, München, Germany, 2002.
15. Ciorciari, R.; Kirik, I.; Niehuis, R. Investigating Unsteady Secondary Flows in a Linear Low Pressure Turbine: A Combined Experimental and Numerical Study. In Proceedings of the 11th European Conference on Turbomachinery Fluid Dynamics and Thermodynamics, Madrid, Spain, 23–27 March 2015; Paper No. ETC2015-134.
16. DLR TRACE User Guide. Available online: http://www.trace-portal.de/userguide/trace/index.html (accessed on 9 January 2016).
17. Eulitz, F. Numerische Simulation und Modellierung der Instationären Strömung in Turbomaschinen. Ph.D. Thesis, Ruhr-Universität Bochum, Bochum, Germany, 2000.
18. Yang, H.; Kügeler, E.; Weber, A. A Conservative Zonal Approach with Applications to Unsteady Turbomachinery Flows; Presented at the DGLR Jahrestagung, Stuttgart, Germany, 23–26 September 2002; Paper No. DGLR-JT2002-073.
19. Nürnberger, D. Impliziete Zeitintegration für die Simulation von Turbomaschinenströmungen. Ph.D. Thesis, Ruhr-Universität Bochum, Bochum, Germany, 2004.
20. Kügeler, E. Numerisches Verfahren zur genauen Analyse der Kühleffektivität filmgekühlter Turbinenschaufeln. Ph.D. Thesis, Ruhr-Universität Bochum, Bochum, Germany, 2014.

21. Yang, H.; Nürnberger, D.; Kersken, H.-P. Toward Excellence in Turbomachinery Computational Fluid Dynamics: A Hybrid Structured-Unstructured Reynolds-Averaged Navier-Stokes Solver. *J. Turbomach.* **2006**, *128*, 390–402.
22. Becker, K.; Heitkamp, K.; Kügeler, E. Recent Progress in a Hybrid-Grid CFD Solver for Turbomachinery Flows. In Proceedings of the Fifth European Conference on Computational Fluid Dynamics (ECCOMAS CFD 2010), Lisbon, Portugal, 14–17 June 2010.
23. Kato, M.; Launder, B. The Modelling of Turbulent Flow Around Stationary and Vibrating Square Cylinders. *Turbul. Shear Flow* **1993**, *1*, 10-4.
24. Kozulovic, D.; Röber, T.; Kügeler, E.; Nürnberger, D. Modifications of a Two-Equation Turbulence Model for Turbomachinery Fluid Flows. Presented at the DGLR Jahrestagung, Dresden, Germany, 20 September 2002.
25. Marciniak, V.; Kügeler, E.; Franke, M. Predicting Transition on Low-Pressure Turbine Profiles. In Proceedings of the Fifth European Conference on Computational Fluid Dynamics (ECCOMAS CFD 2010), Lisbon, Portugal, 14–17 June 2010.
26. Menter, F.R.; Langtry, R.B.; Likki, S.R.; Suzen, Y.B.; Huang, P.G.; Völker, S. A Correlation-Based Transition Model Using Local Variables: Part I—Model Formulation. *J. Turbomach.* **2006**, *128*, 413–422.
27. Michelassi, V.; Chen, L.-W.; Pichler, R.; Sandberg, R.D. Compressible Direct Numerical Simulation of Low-Pressure Turbines: Part II—Effect of Inflow Disturbances. *J. Turbomach.* **2015**, *137*, 071005.
28. Pichler, R.; Sandberg, R.D.; Michelassi, V.; Bhaskaran, R. Investigation of the Accuracy of RANS Models to Predict the Flow Through a Low-Pressure Turbine. *J. Turbomach.* **2016**, *138*, 121009
29. Adami, P.; Montomoli, F.; Belardini, E.; Martelli, F. Interaction Between Wake and Film Cooling Jets: Numerical Analysis. In Proceedings of the ASME Turbo Expo 2004: Power for Land, Sea, and Air, Vienna, Austria, 14–17 June 2004; Paper No. GT2004-53178.

4.3 Publication 2

4.3.1 Summary

The initial investigations presented in Publication 1 provided valuable findings about the loss generation inside the passage and the effect of blade loading. However, it also revealed some uncertainties regarding the experimental reference data, more precisely the inlet endwall boundary layer conditions. Having consistent and well-defined endwall boundary layer conditions is essential for secondary flow investigations. Therefore, before expanding the investigation scope or implementing any advanced measurement techniques, the first point of action was to design and validate an improved T106A test case for a new comprehensive experimental data set. The following three main aspects and findings of Publication 2 had a large impact on the overall research project.

1. First, without changing the T106 blade profile, the turbine cascade was re-designed particularly for high quality secondary flow investigations in the High-Speed Cascade Wind Tunnel at the University of the Bundeswehr Munich under engine relevant flow conditions ($M_{2th} = 0.59$, $Re_{2th} = 2 \cdot 10^5$) with and without periodically incoming wakes. Subsequently, probe-based measurements were conducted in order to characterize the cascade flow and evaluate the effect of the implemented features. The main differentiating feature of the improved design was a two-part flat plate, integrated at part-span and acting as a cascade endwall. Thereby the previously detrimental effects of the bar gap leakage flow were minimized resulting in well-defined inflow conditions. Consequently, the design goals of more distinctive secondary flow and a more consistent effect of the periodically incoming wakes were achieved. Extensive pre-test CFD studies were conducted in the design process. The (U)RANS-based computational approach was enhanced and adapted from the previous T106A and T106Div cascade simulations presented in Publication 1 and proved to be critical in determining e.g. the front and aft flat plate shape and position including the shedding vortex suppression by a trailing edge splitter plate. Also, one of the key features of the two-part flat plate was the ability to vary the inlet endwall boundary layer conditions while keeping constant mean flow conditions. Furthermore, significant improvements regarding the implementation of measurement techniques were achieved with respect to previous experimental setups. A rapid five-hole-probe traversing technique based on Gomes et al. [39] and Chemnitz [13], allowed to capture highly resolved full-range exit flow fields within reasonable time frames. For upstream CTA probe measurements, a guided traversing mechanism through the flat-plate-endwall was implemented instead of inserting an extended probe from downstream. The improved accuracy and robustness, even at vibration-intense wake generator operation, provided high quality inlet endwall boundary layer data. A concept for optical accessibility through multiple cascade side- and endwalls is discussed in the context of Publication 4.

2. Subsequently, a thorough flow characterization was conducted using the classic probe-based approach up- and downstream of the passage. Thereby, the desired functionality of varying the inlet endwall boundary layer conditions could be successfully validated. Here, all three measured boundary layers appeared to be in the laminar-turbulent

transition process and exhibited a correlation of decreasing boundary layer thickness with increasing shape factor. Under periodic inflow, the boundary layer exhibited a slightly lower shape factor and an increase of the turbulence intensity by around 2 % near the endwall (Section 4.3.3). Towards the boundary layer edge, the latter remained on a constant high level and doubled the turbulence in the steady inflow case. Downstream of the blade passage, two spanwise regions of high secondary losses were identified by highly-resolved five-hole-probe measurements. Close to the endwall the losses are driven by the endwall boundary layer and coincide with flow overturning. In the region of underturning further from the endwall, the losses are driven by the secondary vortices. The characteristics of the transition between the two regions are dependent on the passage vortex liftoff from the endwall and can exhibit very low losses close to midspan levels.

3. The exit flow field was analyzed in three cases of varying endwall boundary layer conditions with and without periodically incoming wakes. Both factors had consistent and reproducible effects on the downstream secondary flow. Furthermore, a strong similarity was found between the time-averaged wake effects and a decrease in boundary layer height. Both resulted in an attenuation of secondary flow with a reduction in maximum secondary losses and over-/underturning. Also, the passage vortex exhibited a spanwise shift towards the endwall. It is important to point out, that this statement holds true for an isolated analysis of the wake effects by excluding the changes in the inlet losses due to incoming wakes or lower endwall boundary layer height. Consequently, the question arose if the observed similarities in the exit flow field persisted in other flow regions. This motivated a subsequent CFD investigation of the upstream secondary flow development and corresponding loss generation throughout the blade passage in Publication 2.

Overall, the experimental results presented in Publication 2 have shown that all intended design goals for the improved T106A cascade test case were successfully achieved. Thus, it provided significant improvements upon the previous test case including independent variation of the boundary layer conditions, robust implementation of measurement techniques, and consistency in the observed flow phenomena.

4.3.2 Postprint

The Effects of Inlet Boundary Layer Condition and Periodically Incoming Wakes on Secondary Flow in a Low Pressure Turbine Cascade

Tobias Schubert[1]
Institute of Jet Propulsion,
Bundeswehr University Munich,
Neubiberg 85577, Germany
e-mail: tobias.schubert@unibw.de

Silvio Chemnitz
Institute of Jet Propulsion,
Bundeswehr University Munich,
Neubiberg 85577, Germany
e-mail: silvio.chemnitz@unibw.de

Reinhard Niehuis
Institute of Jet Propulsion,
Bundeswehr University Munich,
Neubiberg 85577, Germany
e-mail: reinhard.niehuis@unibw.de

A particular turbine cascade design is presented with the goal of providing a basis for high quality investigations of endwall flow under high-speed conditions with unsteady inflow. The key feature of the design is an integrated two-part flat plate serving as a cascade endwall at part-span, which enables a variation of the inlet endwall boundary layer conditions. The new design is applied to the T106A low pressure turbine cascade for endwall flow investigations in the High-Speed Cascade Wind Tunnel of the Institute of Jet Propulsion at the Bundeswehr University Munich. Measurements are conducted under realistic flow conditions ($M_{2th} = 0.59$, $Re_{2th} = 2 \cdot 10^5$) in three cases of varying endwall boundary layer conditions with and without periodically incoming wakes. The endwall boundary layer is characterized by 1D-CTA measurements upstream of the blade passage. Secondary flow is evaluated by five-hole-probe measurements in the turbine exit flow. A strong similarity is found between the time-averaged effects of unsteady inflow conditions and the effects of changing inlet endwall boundary layer conditions regarding the attenuation of secondary flow. Furthermore, the experimental investigations show that all design goals for the improved T106A cascade are met. [DOI: 10.1115/1.4050116]

Keywords: turbine cascades, boundary layer development, unsteady inflow, measurement advancements

Introduction

In modern jet engines, the trend to higher loaded airfoils in low pressure turbines remains ongoing. The resulting high pressure gradients in the blade passage lead to intensified secondary flow. As Denton [1] provides an overview of the loss mechanisms in turbomachinery, it becomes evident that the secondary flow represents a significant part of overall losses. Especially relevant are low-aspect ratio LPT blades in which secondary flow extends over a larger range of the blade span. According to Cui and Tucker [2], secondary losses account for approximately 30% of the overall losses in current axial turbines. Utilizing high-fidelity eddy-resolving simulations, they identified two major regions of high loss generation rate, the corner vortex region near the endwall and the interaction region of the passage vortex and the blade suction surface, resulting in the counter vortex. The development of endwall flow and the corresponding loss production is dependent on a multitude of factors such as blade loading, unsteadiness of inlet flow, and inlet boundary layer conditions. In terms of blade loading, not only the overall level of loading is relevant but also the blade loading distribution. The impact of the loading distribution on full-span losses was investigated by Weiss and Fottner [3] and later Praisner et al. [4] on several high-lift turbine airfoils. While front-loaded designs showed great performance in terms of midspan efficiency at low Reynolds numbers, increased endwall losses were apparent in case of front-loaded airfoils compared to aft-loaded designs. Alternatively, there are ways to investigate increased endwall flow in a turbine cascade without altering the blade profile. One is to increase the blade loading by means of a higher pitch-to-chord ratio. Examples of this are the T106C and T106D turbine cascades, which were used for midspan investigations by Stotz and Niehuis [5] as well as Zhang and Hodson [6]. Another approach is to force the blades to be more front-loaded by using divergent endwalls. The resulting augmentation of secondary flow was successfully demonstrated with the T106Div cascade in numerical investigations by Ciorciari et al. [7] and experimentally by Kirik and Niehuis [8].

The effect of unsteady inflow conditions on the endwall flow in the T106A turbine cascade was compared in experimental and numerical investigations by Ciorciari et al. [9]. Both approaches have shown an attenuation of secondary flow caused by periodically incoming wakes depending on Strouhal number and flow coefficient. However, the observed influence of the incoming wakes on the time-averaged secondary losses was very small. Koschichow et al. [10] were able to confirm these findings using incompressible DNS in a lower Reynolds number case. Similar results were also found in high pressure turbine cascade measurements by Volino et al. [11]. In contrast to the relatively small effect of incoming wakes, Volino [12] described how the development of endwall flows is greatly influenced by the inlet boundary layer. Kirik and Niehuis [13] were also able to demonstrate more pronounced secondary flow in the T106A cascade by using what they called a *boundary layer simulator* (BLS), essentially a turbulator, perturbing the incoming endwall boundary layer far upstream the cascade. However, the experimental setups used by Kirik and Niehuis [8,13] exhibited some unfavorable circumstances affecting the inflow conditions and consequently the cascade endwall flow. Therefore, a new turbine cascade is designed specifically for the present work, improving on several aerodynamic aspects and measurement techniques, providing an ideal test case for endwall flow investigations. Finally, the focus of the investigation is put on a comparison of the effects of unsteady inflow conditions to the effects of changing inlet endwall boundary layer conditions on the secondary flow.

[1]Corresponding author.
Contributed by the International Gas Turbine Institute (IGTI) of ASME for publication in the Journal of Turbomachinery. Manuscript received September 21, 2020; final manuscript received January 7, 2021; published online March 2, 2021. Assoc. Editor: David G. Bogard.

Experimental Setup

High-Speed Cascade Wind Tunnel. The experimental investigations presented in this paper were conducted in the High-Speed Cascade Wind Tunnel (HGK) of the Institute of Jet Propulsion at the Bundeswehr University Munich. The HGK test facility shown in Fig. 1 is a continuously operating, open loop wind tunnel with a linear cascade test section. The wind tunnel itself is located inside a cylindrical pressure chamber while the driving unit is located on the outside. Within the pressure chamber, a three-stage axial compressor drives the wind tunnel flow toward the test section passing through a cooler and a series of components providing a homogeneous flow profile. The inlet total temperature is measured within the settling chamber with a precision of ±0.3 K. The special design of the HGK allows a variation of the absolute pressure level in the range of 4 kPa $\leq p_c \leq$ 120 kPa inside the pressure chamber. This feature enables an independent Mach and Reynolds number variation. The operating range covers Mach numbers of $0.1 \leq M \leq 1.06$ and Reynolds numbers of $8 \cdot 10^5\ \mathrm{m}^{-1} \leq \mathrm{Re}/C \leq 2.5 \cdot 10^7\ \mathrm{m}^{-1}$, demonstrating a wide range of realistic turbomachinery conditions. The freestream turbulence level can be varied in a range of approximately $0.5\% \leq \mathrm{Tu}_1 \leq 9\%$ [14]. A more detailed description of the HGK is given in Ref. [15]. For investigations of turbine cascades, isentropic flow through the cascade is assumed leading to the following definition of the theoretical exit Mach and Reynolds number, which define the operating point:

$$M_{2th} = \sqrt{\frac{2}{\gamma - 1} \cdot \left[\left(\frac{p_{t1}}{p_c} \right)^{\frac{\gamma - 1}{\gamma}} - 1 \right]} \tag{1}$$

$$Re_{2th} = \sqrt{\frac{\gamma}{R}} \frac{c}{C_{S1}} \frac{M_{2th} \cdot p_c \cdot \left(\dfrac{T_{t1}}{1 + \left(\dfrac{\gamma - 1}{2} \right) \cdot M_{2th}^2} + C_{S2} \right)}{\left(\dfrac{T_{t1}}{1 + \left(\dfrac{\gamma - 1}{2} \right) \cdot M_{2th}^2} \right)^2} \tag{2}$$

Moving Bar Wake Generator. Unsteady inflow conditions that simulate an upstream airfoil row are generated by periodically incoming wakes of moving bars with a diameter of 2 mm which is equal to 111% of the T106 trailing edge diameter. The moving bar plane runs parallel to the blade passage inlet plane and is located 86% C upstream of the blade leading edge. The opposite plane of the circulating bars has enough distance from the cascade outlet, such that an upstream influence on the turbine cascade flow can be ruled out. A detailed description of the wake generator is found in Ref. [16]. Purge air is used at the top and bottom bar gap between the wind tunnel and the mounted cascade, ensuring uniformity of the inlet flow as well as periodicity of the outlet flow. All investigated cases with periodically incoming wakes in the present work refer to constant unsteady inflow conditions of $\mathrm{Sr} = 0.66$ and $\phi = 3.8$. The bar pitch is 40% C which is ≈50% P. In order to investigate the effects of incoming wakes on the blade passage loss production, a p_{t1} correction must be performed. The bar losses are calculated based on an analytical control volume method.

Measurement Techniques. The operating conditions for all present experimental investigations are summarized in Table 1. The high turbomachinery relevance of the present work is underlined by a realistic Mach number of $M_{2th} = 0.59 \pm 0.003$ and Reynolds number of $\mathrm{Re}_{2th} = 2 \cdot 10^5$. The freestream turbulence intensity of $\mathrm{Tu}_1 \approx 6.8\% \pm 0.5$ is deduced by interpolation using a range of previous 3D-CTA measurements in the HGK test section [17] that cover the present aerodynamic conditions defined by inlet Reynolds number Re_1/c and inlet Mach number Ma_1. The corresponding longitudinal integral length scale is $L_x \approx 43$ mm. The present experimental investigations comprise the following three measurement techniques. 1D-hot-wire-probe measurements upstream of the blade passage provide an inlet endwall boundary layer characterization. The blade Mach number distribution is evaluated using surface pressure taps. Five-hole-probe measurements are conducted to characterize the losses and secondary flow field downstream of the blade passage. All results are presented using an axial coordinate system [x, y, z] with a right-hand-side angle definition (see Fig. 5). The HGK test section is equipped with a five-axes traverse system with a relative precision of 0.01 mm and 0.01 deg. The manually mounted probes are aligned with an absolute positioning accuracy of ±0.5 mm for all linear distances and ±0.15 deg for all probe angles.

Pressure Measurements: For operation point monitoring, pressure transducers with a full-scale range of ±750 hPa and an uncertainty of less than 0.01% full scale provide the static pressure inside the HGK chamber and the inlet total pressure p_{t1}. Measurement plane 1 is located at an axial distance of 150% C upstream of the blade passage. The blade surface pressure is tapped at 51 midspan positions by differential pressure transducers covering ±345 hPa with a maximum uncertainty of less than 0.05% of full-scale range. All pressure systems are sampled with a frequency of 50 Hz and averaged over a period of at least 10 s.

Five-Hole-Probe (FHP) Measurements: The FHP measurements are conducted in measurement plane 2, located 34% C (i.e., 40% C_x)

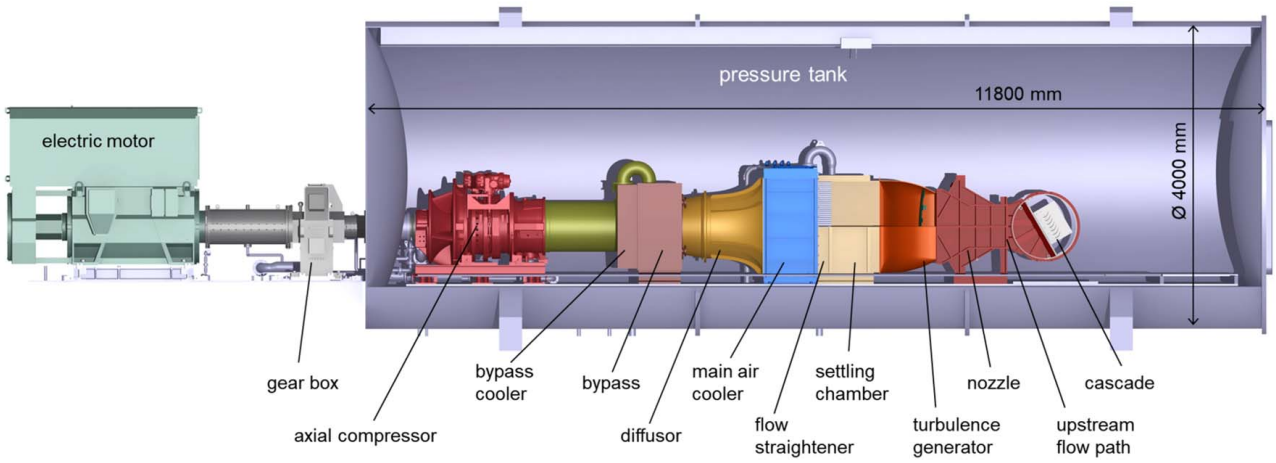

Fig. 1 High-Speed Cascade Wind Tunnel (HGK) test facility

Table 1 T106A linear turbine cascade

Geometric parameters:	
No. of blades	7
Chord length C	100 mm
Pitch-to-chord ratio P/C	0.799
Aspect ratio H/C	1.31
Flow conditions:	
Exit Mach number M_{2th}	0.59
Exit Reynolds number Re_{2th}	$2 \cdot 10^5$
Design inflow pitch angle β_1	127.7 °
Design outflow pitch angle β_2	26.8 °
Turbulence intensity Tu_1	≈6.8%
Unsteady inflow conditions:	
Strouhal number, Sr	0.66
Flow coefficient ϕ	3.8

downstream of the blade passage. The field traverse covers a single blade pitch centered around the trailing edge over the full blade span. The closest wall distance is $z = 3.5$ mm or equally $z/H = 2.7\%$. A spherical FHP is used with a head diameter of 2.6 mm. The FHP stem is aligned in design exit flow direction ($\beta_2 = 26.8$ deg) minimizing upstream blockage effects. The FHP calibration is performed under atmospheric ambient pressure covering a complete subsonic Mach number range of $0.1 \leq M \leq 0.998$. Although the FHP measurements are conducted at low static pressure inside the HGK chamber, Reynolds number effects on the calibration are negligible at the present mean probe head Reynolds number of $\mathrm{Re}_p = 5.2 \cdot 10^3$ [18]. The angular calibration range covers ±2 deg for the pitch angle β and ±21 deg for the yaw angle α, in 3 deg increments. Bias errors based on finite probe head dimensions are minimized using the probe head correction algorithm by Vinnemeier et al. [19]. A high spatial resolution of the FHP measurements is achieved in reasonable measurement time using the transient data acquisition procedure published by Gomes et al. [20]. By knowledge of a system-specific transfer function, any pressure signal of a continuously moving probe can be converted into its settled pressure value. An algorithm estimates the transfer function by evaluating the transient pressure signals of two independent measurements of the same flow region using opposite traversing directions. In this procedure, no prior calibration of the pneumatic system is needed. The total pressure loss coefficient is defined by

$$\zeta_2 = \frac{p_{t1} - p_{t2}}{p_{t1} - p_c} \tag{3}$$

Based on linear error progression, the maximum FHP measurement errors in the present work are $M_{2,err} = 0.0043$, $\zeta_{2,err} = 0.321\%$, $\beta_{2,err} = 0.093$ deg, and $\alpha_{2,err} = 0.14$ deg. All integral values of the FHP measurement data refer to a massflow-weighted average.

Temperature Anemometry (CTA): The inlet boundary layer measurements are conducted using a *Dantec Dynamics* 55P15 CTA-probe with a tungsten wire of 1.25 mm length and 5 μm diameter. High cutoff frequencies are achieved applying an overheat ratio of 0.8. The stable dynamic response of the hot-wire system was tested by a 1 kHz square wave test and a hardware low-pass filter of 30 kHz is used to prevent aliasing effects. The sampling time is set to 5 s at a rate of 60 kHz. The velocity calibration is performed in a range of $0.0 \leq M \leq 0.5$ at constant angles of pitch, yaw, and pressure levels with respect to the ensuing measurements. The overall uncertainty for a velocity sample is estimated to $\Delta U \leq 2.5$ m/s [21]. When conducting near wall hot-wire measurements, a series of factors potentially impairing boundary layer characterization must be considered [21,22]:

(1) Improper boundary layer edge criteria
(2) Misalignment of the probe and/or probe wire
(3) Heat flux between the probe wire and the wall

Due to the absence of strong shear or cross flows at the investigated wall positions and minor velocity change at a sufficient traversing distance from the wall, maximum freestream velocity is used for the boundary layer edge criterion. A possible misalignment of the probe is corrected using a linear regression approach considering velocity samples within the laminar sub-layer not affected by wire to wall heat transfer. Distortions of near-wall velocities caused by conductive heat transfer are corrected using an approach by Lange et al. [23].

Turbine Cascade Design. The T106A turbine cascade has previously been used for endwall flow investigations in the High-Speed Cascade Wind Tunnel. However, the experimental setups used by Kirik and Niehuis [8,13] exhibited some unfavorable circumstances affecting the inlet endwall boundary layer and consequently the cascade endwall flow. The issues stem from a gap between the wind tunnel and the cascade endwalls, upstream of the blade passages, which is needed for the moving bar wake generator. A schematic illustration of the bar gap and its effect on the inlet endwall boundary layer is shown in Fig. 2. Due to a negative pressure gradient between inside the wind tunnel and the surrounding pressure chamber ($p_1 > p_c$), a leakage flow is formed in the bar gap. Even though sealing measures in the cavity adjacent to the bar gap are taken, reducing the pressure gradient ($p_1 > p_{gap} > p_c$), the bar gap cannot be sealed off completely. While the resulting leakage flow is not affecting the freestream flow, it is acting as an endwall boundary layer suction. This triggers the development of a fresh boundary layer downstream of the bar gap, which is superimposed with the remains of the perturbed inlet endwall flow. Three issues arise from this situation; uncertainty about the inlet boundary layer conditions, weak secondary flow downstream of the blade passage, and a small effect of periodically incoming wakes on secondary flow. Before starting new investigations into expanded aspects of endwall flow, it was therefore decided to design a particular new T106 turbine cascade which improves on these challenging issues. The overarching design goals for the new T106 turbine cascade are as follows:

(1) Minimizing the detrimental effect of the bar gap leakage flow and thereby generate more distinctive secondary flow, which is on par with realistic levels of secondary flow observed in modern low pressure turbine cascades without the use of a moving bar wake generator.
(2) Displaying a more pronounced effect of periodically incoming wakes on the endwall flow without changing the bar position, diameter, or the unsteady inflow conditions.

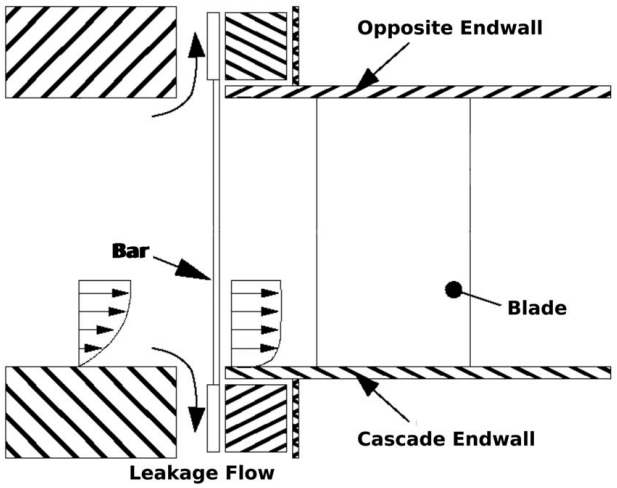

Fig. 2 Leakage flow in the bar gap of the previous experimental setups by Kirik and Niehuis [8,13] and its effect on the inlet endwall boundary layer

(3) Enabling a robust method of improved CTA measurements providing high quality data on the inlet endwall boundary layer.
(4) Providing the ability to conduct a variation of the inlet endwall boundary layer conditions while keeping constant mean flow conditions.

A variety of possible approaches for achieving an augmentation of endwall flow in a turbine cascade were mentioned in the "Introduction" section. However, none of these choices would address the issue regarding the suction of inlet endwall boundary layer. Therefore, the method of choice for the new design is to stick to the T106A with parallel endwalls and force more distinct endwall flow by augmenting the inlet endwall boundary layer instead. A rather simple way of doing so can be to place a turbulator or trip wire somewhere between the bar gap and the blade passage inlet. However, internal tests of trip wires on a similar turbine cascade endwall in the HGK have not shown the desired impact. While immediately near the wall, the boundary layer profile was affected, the overall boundary layer height merely showed a percentage increase in the single digits. Trip wires can be used to induce transition and thus decrease the boundary layer form factor. However, in the present case, they are not suitable to achieve the design goal of performing a variation of the boundary layer conditions strong enough to significantly impact the secondary flow. Also, the ultimate purpose of the experimental setup must be considered, which is to investigate the effects of incoming wakes on the endwall flow. Therefore, it should be avoided to place any boundary layer perturbations downstream of the moving bar plane. An endwall flow perturbation upstream of the bar plane on the other hand will create a local boundary layer augmentation; however, this effect will be negated by the boundary layer suction in the bar gap. Also, placing any kind of obstacle far upstream of the test section as Kirik and Niehuis [13] did with their *boundary layer simulator* (BLS) will result in a total pressure deficit that is highly mixed by the time the cascade inlet is reached instead of a desired distinctive boundary layer profile.

For these reasons, the new design uses an integrated flat plate at part-span, which serves as a turbine endwall. Using a modular composition of the flat plate, various measurement techniques for future investigations can be implemented with relatively low effort. Inserting the flat plate divides the overall flow channel into two spanwise sections as shown in Fig. 3. The larger main channel is used for all flow investigations in which the endwall flow of interest is near the flat plate. The second smaller section is the bypass channel, which is not considered in the investigations. Furthermore, the flat plate is divided into two parts, one upstream *front plate* and one downstream *aft plate* of the moving bar plane of the wake generator. Obviously, there is still a bar gap between the two plates in this design, resulting in a break in the inlet boundary layer development. However, the desired boundary layer augmentation is achieved by the developing boundary layer on the aft plate feeding on the total pressure deficit of the front plate wake. Thus, there are three improved aspects that differentiate the new design from the previous experimental setups. All lead to a significant reduction of the pressure forces acting on the flow between the flat plates, reducing the boundary layer suction. First, there is a distance between the outer endwall gap, where the leakage occurs, and the midspan-facing-surface of the flat plate where the boundary layer of interest develops. Second, there is flow on both sides of the integrated flat plate, dampening the leakage effects. Finally, the sealing of the cavity adjacent to the bar gap is further improved, reducing the pressure gradient ($p_1 > p_{gap} > p_c$). The aerodynamic design of the new turbine cascade was supported by 3D-(U)RANS simulations using the flow solver TRACE by DLR with the Wilcox $k-\omega$ turbulence model [24], $\gamma Re_{\theta t}$ transition model by Langtry and Menter [25], and low-Reynolds wall treatment ($y^+ \leq 1$). Leakage panels are incorporated at the bar gap boundaries to simulate the leakage flow. The imposed static pressure condition is approximated based on data from Kirik and Niehuis [8], [13]. One critical issue aided by pre-test simulations is the optimal spanwise position of the flat plate. Here, it must be avoided that the secondary flow merges within the blade passage ensuring a 2D-flow region at midspan. Thus, the requirement is maximizing the main channel height while preventing an induced inflow yaw angle deviation due to blockage in the bypass channel below. Finding a compromise for all aerodynamic requirements in addition to structural constrains and manufacturing aspects is quite challenging in the present case. This is mainly because the overall channel height is restricted to 170% C due to the moving bar wake generator. Different spanwise flat plate locations are evaluated by comparing the predicted blade Mach number distributions to a baseline case simulation of the T106A without an integrated flat plate and full 170% C channel height. Based on the pre-test simulations, the integrated flat plate location chosen for the experimental investigations results in $H = 131\%\, C$ for the main channel and $H_{bypass} = 31\%\, C$. Furthermore, it is apparent that the 2D-flow region, undisturbed by endwall flow, is quite narrow in the present case. Therefore, it is necessary to relocate the blade surface pressure taps to the new geometrical midspan of the main channel.

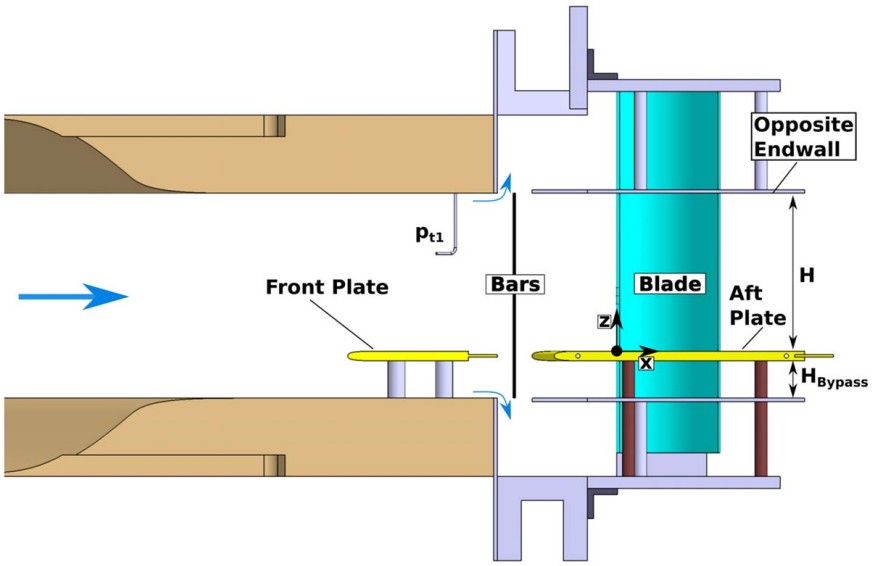

Fig. 3 Illustration of the new turbine cascade design

Both flat plates have a thickness of $d = 2b = 8\%\,C$ and are equipped with super-elliptical leading edge profiles defined by

$$\left(\frac{a-x}{a}\right)^n + \left(\frac{y}{b}\right)^n = 1 \quad \text{with} \quad n = 3, \text{ and } \frac{a}{2b} = 3 \tag{4}$$

Based on a flat plate nose shape study by Narasimha und Prasad [26], who conducted boundary layer calculations using the Thwaites method, the chosen profile parameters provide an optimum regarding prevention of flow separation, practical leading edge length, and sufficient robustness against incidence variation. The latter is especially important in a flow with incoming wakes. The trailing edge of both plates feature a splitter plate which significantly reduces vortex shedding. This ensures that the dominant source of unsteadiness in the inlet flow comes from the periodically incoming bar wakes. The aft plate splitter is important to prevent any influence on the pressure field in measurement plane 2. Lower fluctuations at the outlet plane in case of numerical simulations are an additional benefit. The splitter plates have a length of $l_{sp}/d = 3$ and a thickness of $d_{sp}/d = 0.25$. A key benefit of the chosen design, using integrated flat plates, is the ability to conduct variations of the inlet endwall boundary layer conditions. This is achieved by manually displacing the front plate in spanwise direction while the position of the aft plate remains unchanged. The resulting misalignment of the two flat plates creates an increase or decrease in boundary layer augmentation on the aft plate, as predicted by pre-test simulations shown in Fig. 4. The present experimental investigations include three different flat plate alignments, denoted by $\Delta z = 0$, $\Delta z = -1\%\,C$, and $\Delta z = -2\%\,C$, where negative values denote a spanwise displacement away from midspan.

As described above, uncertainties remain about the state of the inlet endwall boundary layer in the previous experimental setups. Therefore, it is deemed crucial to obtain reliable experimental boundary layer data for the present investigations. In addition to the described aerodynamic precautions taken to improve the incoming endwall flow, the new cascade design offers better accessibility and minimized probe-flow interactions. Similar to the setup of Chemnitz and Niehuis [21], the hot-wire probe was fixed in an adaptable probe holder, guided by integrated sleeve bearings in the flat plate and outside casing. This setup allows robust boundary layer measurements in a wide upstream area from a single mounting position (see Fig. 5). Two traverse locations 1*a* and 1*b* are chosen for the present investigations at an axial distance of 45% *C* and 20% *C* upstream of the blade passage. Both spots are located along the upstream extension of the central blade leading edge with respect to the design inflow angle of $\beta_1 = 127.7$ deg. They should therefore share a common streamline, which is confirmed by pre-test simulations. Furthermore, predicted shear-stress and pressure distributions on the flat plate surface are analyzed to avoid areas of boundary layer separation and significant pressure gradients. Traverse location 1*a* is positioned closely behind the super-elliptical leading edge of the aft plate, such that the surface curvature is zero at this point.

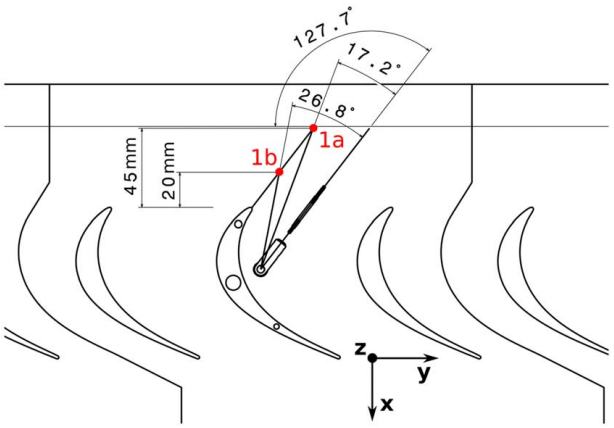

Fig. 5 CTA traverse locations for inlet endwall boundary layer measurements

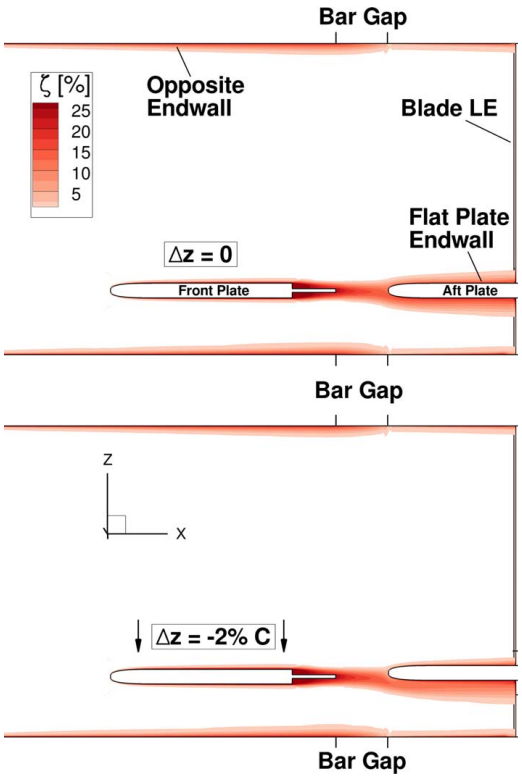

Fig. 4 Predicted effect of the flat plate misalignment on the inlet boundary layer

Experimental Results

Blade Mach Number Distribution. The present turbine cascade flow was designed and setup to match the Mach number distribution at midspan of the previous T106A turbine cascade ($H/C = 1.7$) measured by Kirik and Niehuis [8]. In Fig. 6, it is

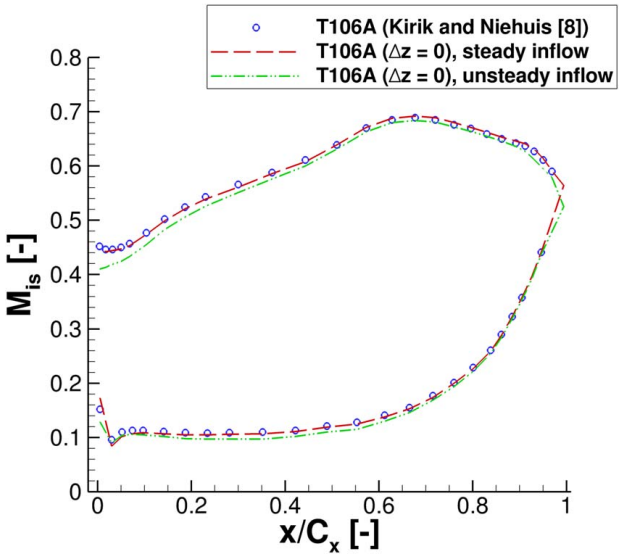

Fig. 6 Measured M_{is} distributions at midspan of the T106A turbine cascade at $M_{2th} = 0.59$, $Re_{2th} = 2 \cdot 10^5$

shown that the measured Mach number distributions indeed match very well. This is also true for the aft section of the blade suction surface, which is especially critical in the present case with a decreased aspect ratio of $H/C = 1.31$. Under the present operating conditions, shown in Table 1, both cases of the T106A feature a very small separation bubble at steady inflow conditions caused by an adverse pressure gradient in the aft section of the blade suction surface. Therefore, it can be deduced that even in the most critical case of $\Delta z = 0$, secondary flow does not affect the 2D-flow at midspan inside the blade passage, as it was predicted by pre-test simulations. In the case of unsteady inflow conditions, a pitchwise incidence of $i \approx -1.7$ deg (based on analytical method) is induced, resulting in decreased blade loading in the front part of the blade suction surface. The unsteady inflow conditions also influence the aft section of the suction surface, where the separation bubble is suppressed due to wake induced transition.

Inlet Endwall Boundary Layer Conditions. The inlet boundary layer profiles on the integrated flat plate, measured in traverse location 1*b* are shown in Fig. 7. For a better interpretation of the measured values, two theoretical boundary layer profiles are added to the $u^+ y^+$-chart, Blasius and Van Driest, which represent the fully laminar and turbulent boundary layers. First, it is apparent that displacing the front plate away from midspan as in the cases of $\Delta z = -1\%\, C$ and $\Delta z = -2\%\, C$ leads to a decrease in boundary layer thickness δ_{99} and increased shape factor H_{12}, which are listed for both traverse locations in Table 2. Judging by the shape factor as well as the $u^+ y^+$-profiles, none of the present cases resemble a laminar boundary layer. All measured boundary layers appear to be in the laminar-turbulent transition process, with the case of $\Delta z = 0$ being most advanced while $\Delta z = -2\%\, C$ indicates the earliest stage of transition. As boundary layer theory suggests, with increasing run length from traverse location 1*a* to 1*b* comes an increase in measured boundary layer thickness and decrease in shape factor. The amount of change is not constant in the present cases, but dependent on the starting conditions of the respective boundary layer. In case of a relatively thick boundary layer ($\Delta z = 0$), both the relative change and absolute change, due to increased run length, are smaller than in the thinner-boundary layer cases of $\Delta z = -1\%\, C$ and $\Delta z = -2\%\, C$. In addition to the mean velocity change, the velocity fluctuations inside the boundary layer are also affected by misaligning the flat plates, judging by the Tu profiles in Fig. 7. The measured freestream turbulence intensity at traversing location 1*b* is $Tu_{1D-CTA} = 5.7\%$ in all three cases. Since not all spatial components of the velocity fluctuation are captured in a 1D-CTA measurement and turbulence is not isotropic in the cascade inlet flow, the measured value must be smaller than the 3D inlet turbulence intensity of $Tu_1 \approx 6.8\%$ listed in Table 1. Considering the boundary layer is partially composed of the front plate wake, the measured velocity profiles as well as Tu profiles exhibit a quite homogenous and consistent behavior. Therefore, the variation of inlet endwall boundary layer conditions generated by the flat plate design is considered by the authors to be highly satisfactory for the following investigations of secondary flow. It is a significant improvement upon the previous setup, i.e., the intended design is achieved successfully.

Table 2 Integral endwall boundary layer parameters

Traverse location	Flat plate alignment	δ_{99} (mm)	H_{12} (−)
1*a* ($x = -45\%\, C$)	$\Delta z = 0$	6.52	1.59
	$\Delta z = -1\%\, C$	4.62	1.86
	$\Delta z = -2\%\, C$	3.18	2.17
1*b* ($x = -20\%\, C$)	$\Delta z = 0$	6.91	1.57
	$\Delta z = -1\%\, C$	6.30	1.70
	$\Delta z = -2\%\, C$	4.87	2.00

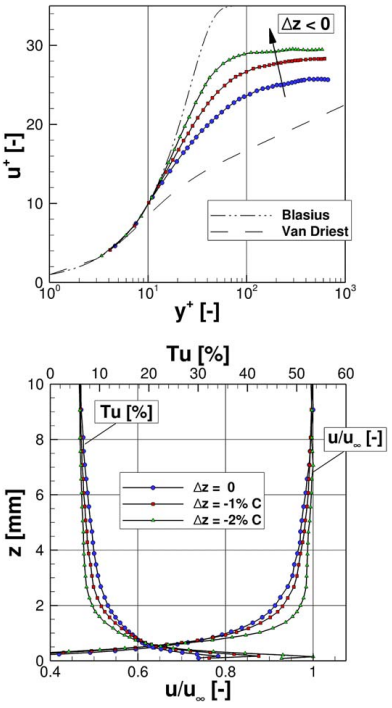

Fig. 7 Measured Tu- and velocity profiles of the inlet endwall boundary layer at 1D-CTA traverse location 1*b* (20% *C* upstream of the blade passage)

Downstream Flow Field. The time-averaged downstream flow fields measured in plane 2 are shown in Fig. 8. The pitchwise-averaged secondary outflow angle $\Delta\beta_{2,sec}$ and secondary total pressure losses $\zeta_{2,sec}$ are defined by

$$\zeta_{2,sec} = \zeta_2 - \bar{\zeta}_{2\,MS} \tag{5}$$

$$\Delta\beta_{2,sec} = \beta_2 - \bar{\beta}_{2\,MS} \tag{6}$$

While the investigations focus on the flat plate endwall flow in the lower channel half, here, full-span distributions are shown to demonstrate the new turbine cascade flow. It is apparent that the varying inlet endwall boundary layer conditions result in varying degrees of secondary flow in the lower channel half near the integrated flat plate. The case of $\Delta z = 0$, representing the thickest boundary layer, exhibits the strongest secondary flow with a maximum underturning of $(\Delta\beta_{2,sec})_{Max} = 4.14$ deg at $z/H = 0.220$ and a secondary loss peak of $(\zeta_{2,sec})_{Max} = 5.62\%$ at $z/H = 0.246$, see Table 3. Lowering the inlet boundary layer thickness in the cases of $\Delta z = -1\%\, C$ and $\Delta z = -2\%\, C$ results in a reduction of peak values of over-/underturning as well as secondary losses. Additionally, the regions of secondary losses and over-/underturning are shifted toward the endwall. This is caused by a less pronounced liftoff of the passage vortex. Overall, it is noticeable that the level of change in $\Delta\beta_{2,sec}$, $\zeta_{2,sec}$ as well as the spanwise shift between the investigated cases is highly uniform. Additionally, it is important to note that in the upper channel half, opposite the flat plate, both the secondary outflow angle as well as total losses remain almost unchanged at different flat plate alignments. This means the variation of endwall flow on the flat plate does not influence the opposite secondary flow region in any significant way as intended. It also speaks to a high level of repeatability of the experimental setup. The pitchwise averaged loss distribution in Fig. 8 shows two spanwise regions of elevated secondary losses in each channel half. In the lower half, the first region ranges from the endwall to $z/H \approx 0.05$, where the endwall boundary layer and corner vortex are the main drivers of loss generation. This region,

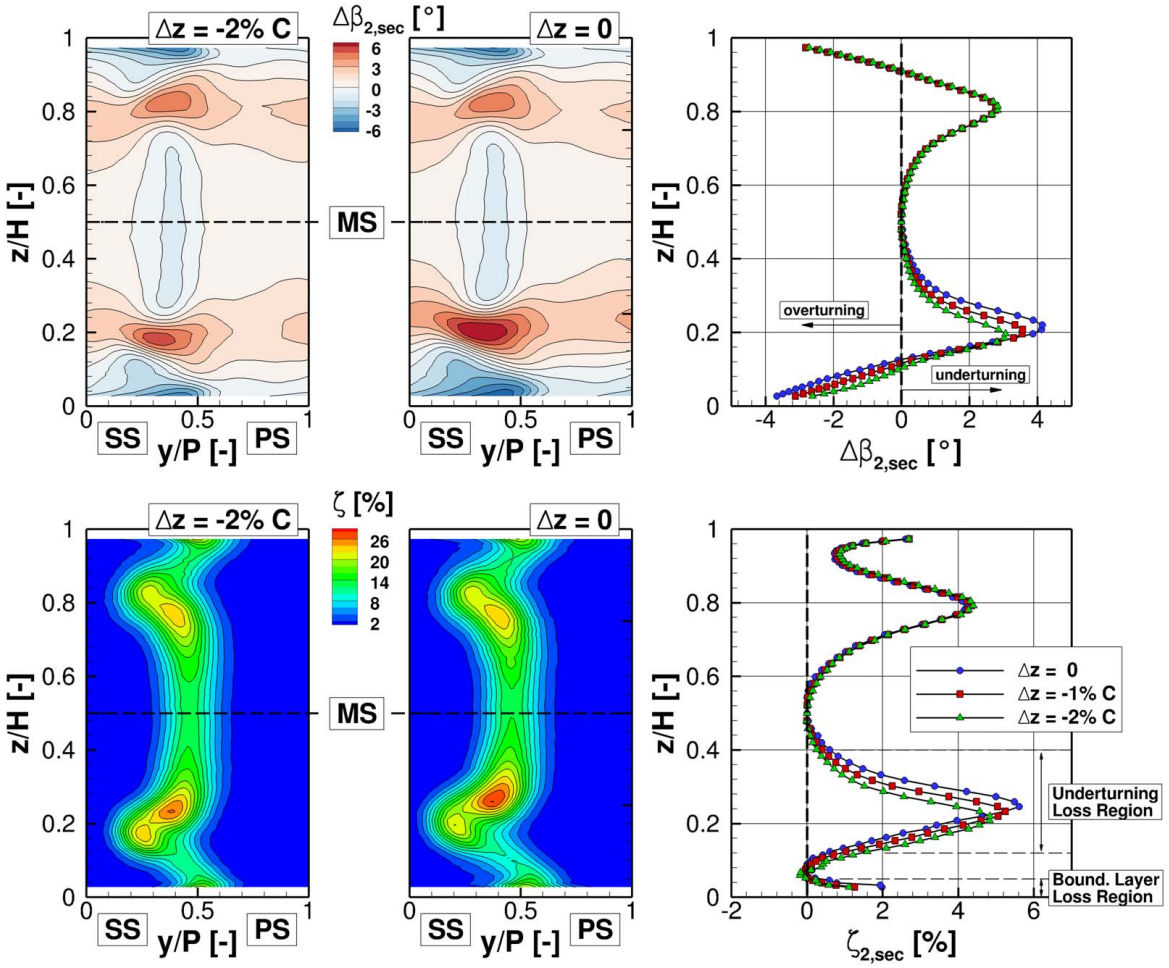

Fig. 8 Downstream time-averaged flow field measured under steady inflow conditions with different flat plate alignments (Δz). Spanwise distribution of the pitchwise-averaged secondary pitch angle $\Delta\beta_{2,sec}$ and secondary total pressure losses $\zeta_{2,sec}$ in the measurement plane 2.

labeled the *boundary layer loss region* would exhibit even higher loss values, if the finite dimensions of the FHP head would allow closer distances to the endwall. The second is the interaction region of the passage vortex and trailing edge wake vortex, where high levels of secondary losses go along with high underturning. It is therefore labeled as the *underturning loss region*. When the passage vortex exhibits a highly pronounced liftoff as in the lower channel half, it consequently shifts the underturning loss region further towards midspan creating more distance to the boundary layer loss region. In the transition of those two high-loss regions, a narrow spanwise range at about $0.05 < z/H < 0.12$ can be identified, where overturning is present. Here, the measured total pressure losses are relatively low and can even be as low as midspan values. The contour plot of total pressure losses in Fig. 8 provides additional information on the pitchwise loss distribution. The mentioned low-loss overturning region does not exhibit any significant loss peaks and the area of elevated losses is relatively narrow in pitchwise direction even compared to midspan. Given the definition of secondary losses in Eq. (5), it must be considered that profile losses are not constant over the entire blade span. Therefore, a change in downstream secondary losses near the endwall may not solely originate from the secondary vortices themselves but also from local changes in profile losses due to altered pressure distributions on the blade. These local changes can be caused by boundary layer separation, altered transition behavior, or separation bubble suppression.

The blade Mach number distribution in Fig. 6 has shown that the secondary flow does not affect the 2D-flow at midspan. Furthermore, the outflow angle distributions in Fig. 8 indicate that the secondary flow neither extends into midspan in measurement plane 2. However, the flow field is continuously subject to a mixing process, among others in spanwise direction as the flow travels further downstream. As a result, the variation of the inlet endwall boundary layer in the three investigated cases leads to a slight change in total pressure losses at midspan of measurement plane 2.

Unsteady Inflow Conditions. A comparison of the effects of steady and unsteady inflow conditions is shown in Fig. 1 by means of the spanwise distribution of $\Delta\beta_{2,sec}$ and $\zeta_{2,sec}$. For better visualization, only the two cases of $\Delta z = 0$ and $\Delta z = -2\%\ C$ are illustrated in the line plots. However, the lower channel half maxima and integral values of all investigated cases are listed in Table 3. The investigation focus lies on the lower channel half, since the well-defined variable inlet boundary layer conditions are generated on the flat plate endwall. It is apparent that periodically incoming wakes cause an attenuation of secondary flow, leading to a reduction in maximum values of over-/underturning and secondary losses as well as a shift towards the endwall. Comparing all three boundary layer cases, a consistently diminishing effect of unsteady inflow conditions is apparent, where $\Delta z = 0$ shows the highest level of secondary flow attenuation and $\Delta z = -2\%\ C$ the least. Furthermore, looking at the case of $\Delta z = 0$, it is noticeable that the reduction in peak values and the spanwise shift by means of unsteady inflow conditions is very similar to the effect of changing the inlet boundary layer

Table 3 Maxima and integral values of underturning and secondary losses in the lower channel half of measurement plane 2

Inflow	Flat plate alignment	$(\beta_{2,sec})_{Max}$	at z/H	$(\zeta_{2,sec})_{Max}$	at z/H	$(\zeta_{2,sec})_{Int}$
Steady	$\Delta z = 0$	4.14 deg	0.220	5.62%	0.246	1.90%
	$\Delta z = -1\%\ C$	3.56 deg	0.208	5.28%	0.233	1.74%
	$\Delta z = -2\%\ C$	3.06 deg	0.196	4.90%	0.220	1.60%
	[13] T106A (BLS)	2.62 deg	–	–	–	2.67%
	[13] T106A	2.41 deg	–	–	–	1.69%
Unsteady	$\Delta z = 0$	2.77 deg	0.196	5.02%	0.220	1.84%
	$\Delta z = -1\%\ C$	2.55 deg	0.185	4.91%	0.208	1.67%
	$\Delta z = -2\%\ C$	2.32 deg	0.174	4.8%	0.196	1.58%
	[13] T106A (BLS)	1.94 deg	–	–	–	2.28%
	[13] T106A	1.85 deg	–	–	–	1.61%

conditions from $\Delta z = 0$ to $\Delta z = -2\%\ C$. While the maximum values are all located in the underturning loss region, the spanwise distributions in Fig. 9 show that the effects on the boundary layer loss region are not as similar. Here, an inlet boundary layer variation has a greater effect, which is reasonable considering the incoming losses are changing in this case. Comparing the results to the measurements by Kirik and Niehuis [13], it is apparent that the incoming wakes have a significantly higher effect on the underturning loss region than in the previous experimental setups. However, the change in integral secondary losses is very small. This is consistent with the findings of Ciorciari et al. [9] and a recent investigation on axial loss development within the blade passage [7]. The later showed that instead of a clear reduction of integral losses, incoming wakes cause a spatial redistribution of loss generation within the blade passage. The exceedingly high integral losses in combination with moderate underturning, in case of the T106A (BLS) is attributed to the unique flow conditions caused by the *boundary layer simulator* used by Kirik and Niehuis [13] far upstream the blade passage.

Conclusion and Outlook

A new design of the T106A turbine cascade was developed particularly for high quality endwall flow investigations in the

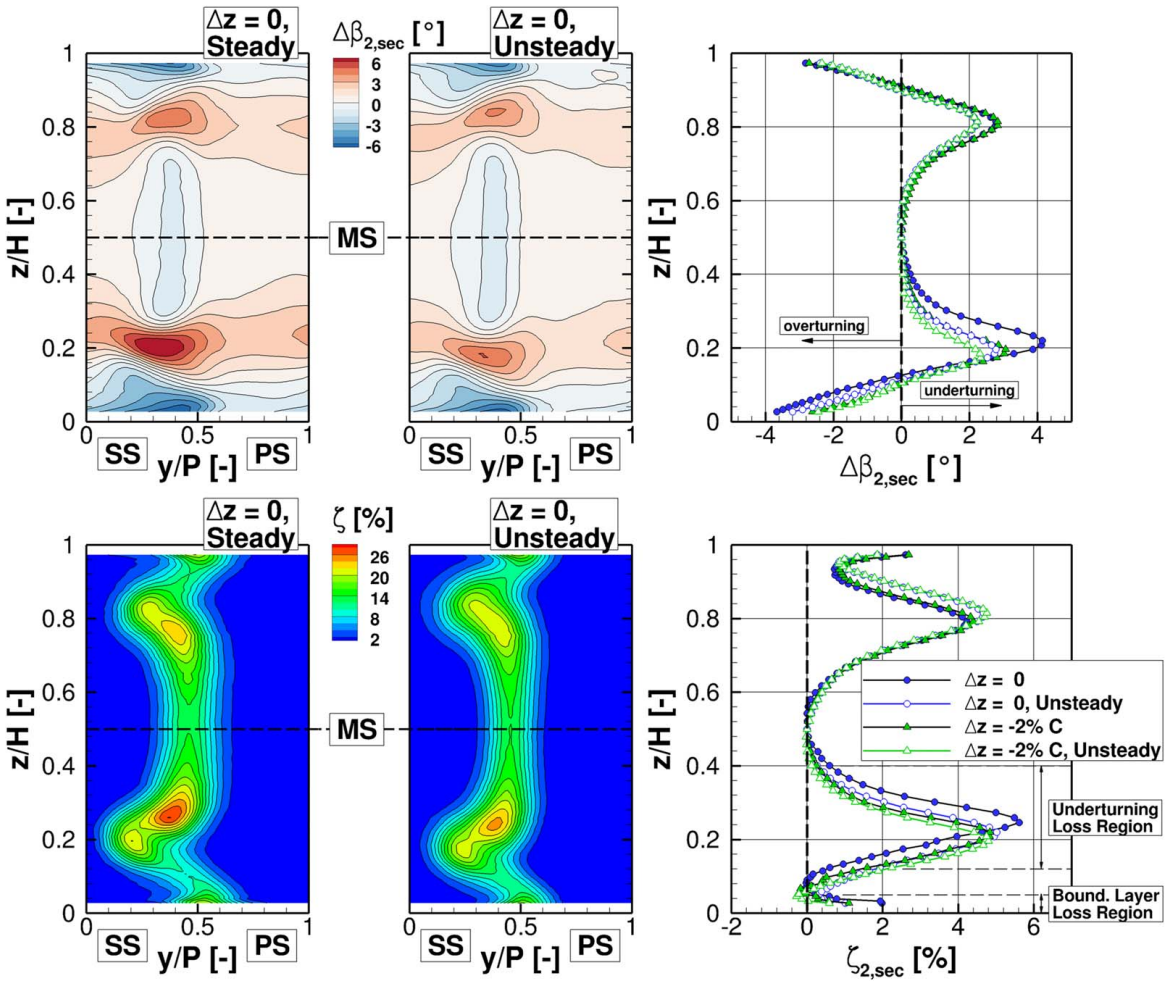

Fig. 9 Downstream time-averaged flow field measured under steady and unsteady inflow conditions. Spanwise distribution of the pitchwise-averaged secondary pitch angle $\Delta\beta_{2,sec}$ and secondary total pressure losses $\zeta_{2,sec}$ in the measurement plane 2.

High-Speed Cascade Wind Tunnel under engine relevant flow conditions ($M_{2th} = 0.59$, $\mathrm{Re}_{2th} = 2 \cdot 10^5$) with and without periodically incoming wakes. Significant improvements of the aerodynamic conditions and implementation of measurement techniques were achieved with respect to previous experimental setups. The main differentiating feature of the new design is a two-part flat plate, integrated at part-span acting as a cascade endwall and providing well-defined inflow conditions even when using the bar wake generator. Three cases of varying inlet endwall boundary layer conditions were established and investigated with and without periodically incoming wakes. Overall, the experimental investigations have shown, that all intended design goals for the new T106A cascade were met.

(1) The previously detrimental effects of the bar gap leakage flow were minimized resulting in more distinctive secondary flow with a 70% increase in maximum underturning.
(2) A more pronounced effect of periodically incoming wakes on the endwall flow was achieved without changing the bar position, diameter or unsteady inflow conditions.
(3) The integration of an improved robust CTA traversing method provided high quality inlet endwall boundary layer data.
(4) Changing the flat plate alignment provided the desired ability to create a variation of well-defined inlet endwall boundary conditions while keeping constant mean flow conditions.

Looking at the measurement results in the downstream flow field, high secondary losses are present in two spanwise regions, labeled as the boundary layer loss region and the underturning loss region. Between the two regions, an additional, low-loss overturning region can be distinguished. The characteristics of this region are dependent on the passage vortex liftoff from the endwall and can exhibit losses, as low as midspan levels. A strong similarity is found between the time-averaged effects of unsteady inflow conditions and changing the inlet endwall boundary layer conditions regarding the attenuation of secondary flow, especially in the region of underturning. Both measures show a consistent reduction in maximum secondary losses and over-/underturning as well as a spanwise shift towards the endwall. Overall, the presented results have shown a significant improvement of the experimental setup upon the previous designs ensuring well-defined boundary conditions, robust measurement techniques, and consistency in the observed flow phenomena. The successful design of the new setup provides an ideal basis for upcoming highly relevant investigations on expanded aspects of endwall flow. This is planned to be achieved by obtaining flow data inside the blade passage and time-resolved flow fields from a combination of experiments, including optical- and endwall surface measurements as well as (U)RANS simulations. The goal is to take a step forward in ultimately gaining a better understanding of the effects of periodically incoming wakes on the development of endwall flow in low pressure turbine cascades and the associated loss generation mechanisms.

Acknowledgment

The present work was conducted as a part of the Deutsche Forschungsgemeinschaft (DFG) joint research project PAK-948.

Conflict of Interest

There are no conflicts of interest.

Data Availability Statement

The authors attest that all data for this study are included in the paper. Data provided by a third party are listed in Acknowledgment.

Nomenclature

d	=	diameter, flat plate thickness
p	=	pressure
u	=	velocity
C	=	chord length
H	=	channel height
M	=	Mach number
P	=	pitch
R	=	ideal gas constant
T	=	temperature
H_{12}	=	boundary layer shape factor
L_x	=	integral length scale
EW	=	endwall
MS	=	midspan
Re	=	Reynolds number
Sr	=	Strouhal number, $(u_b/(P_b) \cdot (C/u_{x1})$
x, y, z	=	axial, pitchwise, and spanwise coordinate
C_{S1}, C_{S2}	=	Sutherland constants

Greek Symbols

α	=	yaw angle
β	=	pitch angle
δ_{99}	=	boundary layer thickness
γ	=	heat capacity ratio
ϕ	=	flow coefficient, u_{x1}/u_b
ζ	=	total pressure loss coefficient

Subscripts

1,2	=	measurement planes
b	=	bar
c	=	chamber
is	=	isentropic
t	=	total
th	=	theoretical
sec	=	secondary
sp	=	splitter plate

References

[1] Denton, J. D., 1993, "Loss Mechanisms in Turbomachines," ASME J. Turbomach., **115**(4), pp. 621–656.
[2] Cui, J., and Tucker, P. G., 2016, "Numerical Study of Purge and Secondary Flows in a Low Pressure Turbine," Proceedings of the ASME Turbo Expo 2016, Seoul, South Korea, June 13–17, Paper No. GT2016-56789.
[3] Weiss, A. P., and Fottner, L., 1995, "The Influence of Load Distribution on Secondary Flow in Straight Turbine Cascades," ASME J. Turbomach., **117**(1), pp. 133–141.
[4] Praisner, T. J., Grover, E. A., Knezevici, D. C., Popovis, I., Sjolander, S. A., Clarka, J. P., and Sondergaard, R., 2013, "Toward the Expansion of Low-Pressure-Turbine Airfoil Design," ASME J. Turbomach., **135**(6), p. 061007.
[5] Stotz, S., Niehuis, R., and Guendogdu, Y., 2016, "Experimental Investigation of Pressure Side Flow Separation on the T106C Airfoil at High Suction Side Incidence Flow," Proceedings of the ASME Turbo Expo 2016, Seoul, South Korea, June 13–17, Paper No. GT2016-56287.
[6] Zhang, X. F., and Hodson, H., 2010, "Effects of Reynolds Number and Freestream Turbulence Intensity on the Unsteady Bounday Layer Development on An Ultra-High-Lift Low Pressure Turbine Airfoil," ASME J. Turbomach., **132**(1), p. 011016.
[7] Ciorciari, R., Schubert, T., and Niehuis, R., 2018, "Numerical Investigation of Secondary Flow and Loss Development in a Low Pressure Turbine Cascade with Divergent Endwalls," J. Turbomach. Propuls. Power 2018, **3**(1), p. 5.
[8] Kirik, I., and Niehuis, R., 2015, "Comparing the Effect of Unsteady Wakes on Parallel and Divergent Endwalls in a LP Turbine Cascade (T106A-EIZ and T106D-EIZ)," Proceedings of the 11th International Gas Turbine Congress 2015, Tokyo, Japan, Nov. 15–20, Paper No. IGTC2015-137.
[9] Ciorciari, R., Kirik, I., and Niehuis, R., 2014, "Effects of Unsteady Wakes on Secondary Flows in the Linear T106 Turbine Cascade," ASME J. Turbomach., **136**(9), p. 091010.
[10] Koschichow, D., Fröhlich, J., Kirik, I., and Niehuis, R., 2014, "DNS of the Flow Near the Endwall in a Linear Low Pressure Turbine Cascade with Periodically Passing Wakes," Proceedings of the ASME Turbo Expo 2014, Düsseldorf, Germany, June 16–20, Paper No. GT2014-25071.

[11] Volino, R., Galvin, C. D., and Ibrahim, M., 2013, "Effects of Periodic Unsteadiness on Secondary Flows in High Pressure Turbines," Proceedings of the ASME Turbo Expo 2013, San Antonio, TX, June 3–7, GT2013-95881.
[12] Volino, R., 2014, "Effects on Endwall Boundary Layer Thickness and Blade Tip Geometry on Flow through High Pressure Turbine Passages," Proceedings of the ASME Turbo Expo 2014, Düsseldorf, Germany, June 16–20, GT2014-27013.
[13] Kirik, I., and Niehuis, R., 2016, "Influence of Unsteady Wakes on the Secondary Flows in the Linear T106 Turbine Cascade," Proceedings of the ASME Turbo Expo 2016, Seoul, South Korea, June 13–17, GT2016-56350.
[14] Kiock, R., Laskowski, G., and Hoheisel, H., 1982, "Die Erzeugung höherer Turbulenzgrade in der Messstrecke des Hochgeschwindigkeits-Gitterwindkanals: Braunschweig, zur Simulation turbomaschinenähnlicher Bedingungen," DFVLR-FB, **82**(25).
[15] Niehuis, R., and Bitter, M., 2021, "The High-Speed Cascade Wind Tunnel at the Bundeswehr University Munich after a Major Revision and Upgrade," Proceedings of the 14th European Conference on Turbomachinery Fluid Dynamics and Thermodynamics, Gdansk, Poland, April 12–16, Paper No. ETC2021-647 (to be published).
[16] Acton, P., and Fottner, L., 1996, "The Generation of Instationary Flow Conditions in the High-Speed Cascade Wind Tunnel of the German Armed Forces University Munich," Proceedings of the 13th Symposium on Measuring Techniques for Transonic and Supersonic Flow in Cascades and Turbomachines, Zürich, Switzerland, Sept. 5–6, Session 1(1).
[17] Chemnitz, S., and Niehuis, R., 2020, "A Comparison of Turbulence Levels From PIV and CTA Downstream of a Low-Pressure Turbine Cascade At High-Speed Flow Conditions," ASME J. Turbomach., **142**(7), p. 071008.
[18] Bohn, D., 1977, *Untersuchung zweier verschiedener axialer Überschallverdichterstufen unter besonderer Berücksichtigung der Wechselwirkungen zwischen Lauf- und Leitrad*, PhD Thesis, RWTH Aachen, Aachen, Germany.
[19] Vinnemeier, F., Simon, L., and Koschel, W., 1990, "Correction Method for the Head Geometry Influence of a Five-Hole Pressure Probe on the Measurement Results," tm - Technisches Messen, **57**(7/8), pp. 704315.
[20] Gomes, R., Kurz, J., and Niehuis, R., 2018, "Development and Implementation of a Technique for Fast Five-Hole Probe Measurements Downstream of a Linear Cascade," J. Turbomach. Propuls. Power., **3**(1), p. 6.
[21] Chemnitz, S., and Niehuis, R., 2020, "Accurate Boundary Layer Measurements using Hot-Wire Anemometry – Improvements and Error Analysis," Proceedings of the 18th International Symposium on Transport Phenomena and Dynamics of Rotating Machinery, Online, Nov. 23–26, Paper No. ISROMAC2019-00030.
[22] Hutchins, N., and Choi, K.-S., 2002, "Accurate Measurements of Local Skin Friction Coefficient Using Hot-Wire Anemometry," Progress Aeros. Sci., **38**(4–5), pp. 421–446.
[23] Lange, C. F., Durst, F., and Breuer, M., 1999, "Correction of Hot-Wire Measurements in the Near-Wall Region," Experiments in Fluids, **26**(5), pp. 475–477.
[24] Wilcox, D. C., 2004, *Turbulence Modeling for CFD (forth Printing)*, DCW Industries, USA.
[25] Langtry, R. B., and Menter, F. R., 2005, "Transition Modeling for General CFD Applications in Aeronautics," Proceedings of the 43rd AIAA Aerospace Sciences Meeting and Exhibit 2005, Reno, NV, Jan. 10–13, Paper No. 2005-522.
[26] Narasimha, R., and Prasad, S. N., 1994, "Leading Edge Shape for Flat Plate Boundary Layer Studies," Exp. Fluids, **17**(5), pp. 358–360.

4.3.3 Supplemental Data

Unsteady Inlet Endwall Boundary Layer (CTA)

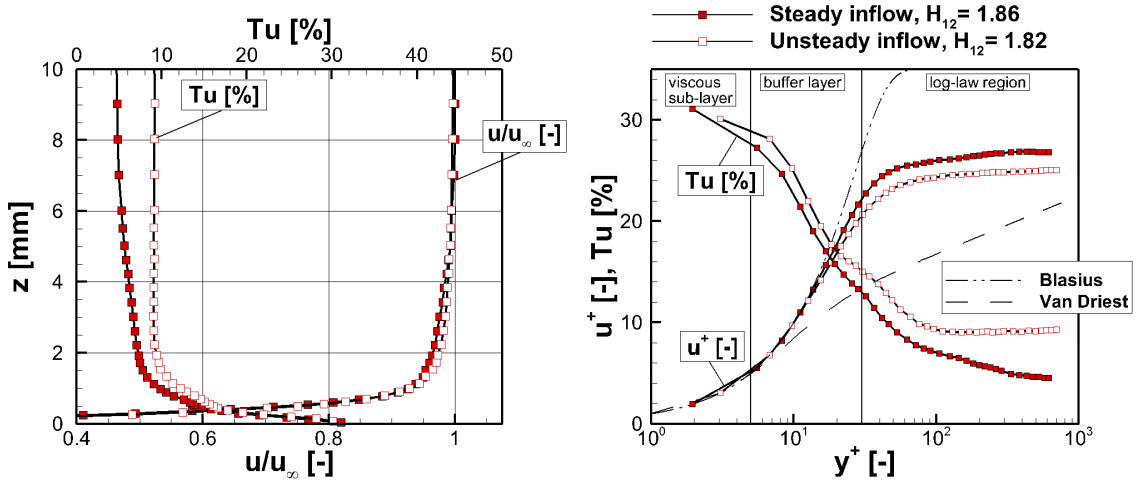

Fig. 4.2: Effect of periodically incoming wakes on the measured time-averaged turbulence intensity and velocity profiles of the inlet endwall boundary layer (45 % blade chord upstream of the leading edge).

To supplement the boundary layer data presented in Publication 2, the effect of the periodically incoming wakes on the inlet endwall boundary layer is illustrated in Figure 4.2. In close proximity to the wall, the time-averaged turbulence intensity is increased by around 2 %. Outside of the buffer layer, the turbulence intensity remains on an almost constant high level while it decreases with further distance from the wall in case of steady inflow. Ultimately this leads to a doubled freestream turbulence at the edge of the boundary layer. The measured relative velocity exhibits a slightly more turbulent profile with periodically incoming wakes which leads to a slightly lower shape factor. The boundary layer thickness on the other hand is nearly constant. According to DNS analysis of the T106A performed by Koschichow et al. [65], the saddle point and separation lines corresponding to the formation of the horseshoe vortex (Figure 2.2) consequently experience a streamwise shift closer to the blade leading edge.

4.4 Publication 3

4.4.1 Summary

Based on the experimental results presented in Publication 2, the next step in the overall research project was focused on the following three main investigation aspects utilizing CFD.

1. The first task was to generate a post-test CFD setup building upon the pre-test CFD which provided valuable initial predictions in the cascade redesign process. Further tweaking and validation by the experimental data was required for an accurate modeling of new cascade features, such as the inclusion of the part-span flat-plate-endwall in the computational domain, the vortex-suppressing splitter plate, and the modeling of the bar gap leakage flow. The latter enables a consideration of the massflow mismatch between in- and outflow and thus a better prediction of the measured axial inflow velocity. The validation of the final (U)RANS-based computational approach confirmed an overall good match with the measured flow phenomena. Noticeable deviations were limited to an exaggerated suction surface separation bubble in the steady inflow cases and a slightly lower spanwise reach of the secondary flow in the turbine exit flow field. The numerical simulations were consequently used to complement the experimental results providing additional information in areas of limited accessibility as well as phase-averaged flow fields. The latter were used to analyze the periodic change of integral total pressure losses and levels of over-/underturning. In terms of amplitude, the secondary losses were less effected by the periodically incoming wakes than the midspan losses which significantly increased due to overlapping with the bar wakes in the downstream measurement plane. Also, a slight phase lag was found which indicated an earlier secondary flow perturbation in the wake passing period with respect to the midspan flow. A streamwise vorticity plot was used to identify a temporary attenuation of the passage vortex which corresponds to a reduced liftoff of the secondary vortex system caused by a less pronounced horseshoe vortex pressure side leg.

2. The next investigation aspect in Publication 3 was motivated by one of the main findings of the turbine exit flow analysis in Publication 2 which was a strong similarity between the time-averaged effects of periodic inflow conditions and reduced inlet endwall boundary layer thickness regarding the attenuation of the secondary flow. Both factors led to a reduction in maximum secondary losses and over-/underturning as well as a spanwise shift towards the endwall which was consistent with the CFD results. Consequently, the upstream secondary flow development and corresponding loss generation throughout the blade passage was investigated to answer the question if the observed similarities in the exit flow persist in other flow regions. Indeed the mechanisms of wake perturbation and effects on the secondary loss generation were quite different inside the blade passage. Decreasing the inlet endwall boundary layer height resulted in a nearly constant reduction of the secondary- and overall loss generation. This effect started around the midpoint of the blade passage. On the contrary, the effect of periodic inflow can be summarized as a spatial redistribution between the loss

components. Wake interaction with the blade boundary layer and migration of the dissipating wakes caused a premature loss increase. This was followed by an attenuation of the profile- and secondary loss generation in the aft section of the blade passage. As a reminder, the investigation of the effect of blade loading presented in Publication 1 showed that an increased frontal blade loading leads to increased profile losses and increased transverse pressure gradients in the front part of the passage. Consequently, an augmentation of the secondary flow development results in higher secondary losses further downstream.

3. As described in Section 4.2, the entropy-centric analysis approach utilized in Publication 1 was enhanced in order to identify the sources of loss generation. In case of steady inflow, three major contributors to the secondary losses were identified. First, in the front part of the passage the loss generation is dominated by the pressure-induced crossflow, boundary layer separation and vortex entrainment. Secondly, the loss-intense interaction of the secondary vortices with the suction surface ultimately results in the formation of the counter-rotating vortex. This finding motivated the subsequent unsteady optical measurements of the suction surface pressure distribution presented in Publication 5. Finally, the vortex dissipation was found to be the main source of loss generation downstream of the blade passage. All identified loss generation mechanisms were affected by the periodically incoming wakes.

4.4.2 Postprint

Proceedings of ASME Turbo Expo 2021
Turbomachinery Technical Conference and Exposition
GT2021
June 7-11, 2021, Virtual, Online

GT2021-59606

NUMERICAL INVESTIGATION OF LOSS DEVELOPMENT IN A LOW-PRESSURE TURBINE CASCADE WITH UNSTEADY INFLOW AND VARYING INLET ENDWALL BOUNDARY LAYER

Tobias Schubert[*], **Reinhard Niehuis**
Institute of Jet Propulsion
Bundeswehr University Munich
85577 Neubiberg, Germany
Email: tobias.schubert@unibw.de

ABSTRACT

An investigation of endwall loss development is conducted using the T106A low-pressure turbine cascade. (U)RANS simulations are complemented by measurements under engine relevant flow conditions ($M_{2th} = 0.59$, $Re_{2th} = 2 \cdot 10^5$). The effects of unsteady inflow conditions and varying inlet endwall boundary layer are compared in terms of secondary flow attenuation downstream of the blade passage, analyzing steady, time-averaged, and time-resolved flow fields. While both measures show similar effects in the turbine exit plane, the upstream loss development throughout the blade passage is quite different. A variation of the endwall boundary layer alters the slope of the axial loss generation beginning around the midpoint of the blade passage. Periodically incoming wakes, however, cause a spatial redistribution of the loss generation with a premature loss increase due to wake interaction in the front part of the passage followed by an attenuation of the profile- and secondary loss generation in the aft section of the blade passage. Ultimately, this leads to a convergence of the downstream loss values in the steady and unsteady inflow cases.

INTRODUCTION

In recent years a lot of research activity has been focused on analyzing the performance of high-lift blade designs. The reason is an ongoing trend in modern jet engines to reduce weight by lowering solidity in low-pressure turbine vanes. The resulting high pressure gradients in the blade passage lead to intensified secondary flow. As Denton [1] provides an overview of the loss mechanisms in turbomachinery, it becomes evident that the secondary flow contributes a significant part to overall losses. Especially relevant in this regard are low aspect ratio LPT blades in which secondary flows affect a larger range of the blade span. Overall, it is approximated that endwall losses account for one third of overall losses in axial turbines [2]. In a more recent study on endwall losses by Denton and Pullan [3], they conclude based (U)RANS simulations, that there is no single dominant source of loss, but rather several components which need to be considered, such as secondary flow interaction with the suction surface and the downstream mixing loss. They also state that the prediction and reduction of endwall loss will remain a challenge for many years to come.

Utilizing high-fidelity eddy-resolving simulations, Cui and Tucker [2] identified two major regions of high loss generation rate, the corner vortex region near the endwall and the interaction region of the passage vortex and the blade suction surface, resulting in the counter rotating vortex. This finding was seconded by Bear et al. [4], who recently investigated the loss development through a highly loaded low-pressure turbine cascade by using a combination of total pressure measurements, non-intrusive measurements and LES simulations. The interaction of the secondary vortices with the blade suction surface was once more found to be a major contributor to overall losses. Furthermore, the loss generated by the passage vortex is mainly restricted to the blade passage, while other secondary vortex structures, like the trailing edge shed vortex, generate significant loss downstream in the blade wake. Based on a numerical parametric design study on endwall losses in low-pressure turbine cascades, Coull [5] found that endwall losses can be decomposed into two major components: dissipation in the endwall boundary layer and induced

[*]Address all correspondence to this author.

losses by secondary flows, which scale with streamwise vorticity. However, he concludes that further investigations on the effects of inlet conditions are necessary to relate cascade endwall losses to real turbines.

Two significant factors in terms of inlet conditions are the endwall boundary layer and the unsteadiness of the inlet flow. The effect of periodically incoming wakes on midspan flow has been studied extensively for a long time. Lengani et al. [6] recently applied proper orthogonal decomposition (POD) to measurements in order to identify different dynamics affecting the midspan losses in a low-pressure turbine cascade with unsteady inflow conditions. The midspan losses under steady inflow are almost entirely generated by the blade boundary layers. In case of unsteady inflow, however, two sources are identified, which increase the midspan loss: first, the interaction of the incoming wakes with the blade boundary layers and second, the wake migration inside the blade passage, which generates loss in the potential flow outside the blade boundary layers. The effect of unsteady inflow conditions on the endwall flow were investigated in the T106A and T106Div turbine cascades using measurements and (U)RANS simulation by Ciorciari et al. [7], [8]. Both approaches have shown an attenuation of the secondary flow caused by periodically incoming wakes depending on the Strouhal number and flow coefficient. However, the observed influence of the incoming wakes on the time-averaged secondary losses in the turbine exit flow was very small. Koschichow et al. [9] were able to confirm these findings using incompressible DNS in a lower Reynolds number case. Similar results were also found in high pressure turbine cascade measurements by Volino et al. [10]. In contrast to the relatively small effect of incoming wakes, Volino et al. [11] describe how the development of endwall flow is greatly influenced by the inlet boundary layer.

The present work builds on the experimental investigations by Schubert et al. [12], who used a particular cascade design of the T106A low-pressure turbine profile to investigate the effects of varying inlet endwall boundary layer and periodically incoming wakes on the secondary flow in a turbine exit plane. It aims to provide a further step in the continued research of endwall loss and its determining factors. After all it is critical to consider endwall effects as well as unsteady effects in the aerodynamic design process of modern jet engine components. After evaluating the computational approach with the help of reference measurements, the downstream flow field is investigated in three different cases of inlet endwall boundary layer. Furthermore, steady state results are compared to time-averaged and time-resolved solutions of the unsteady inflow cases. The investigation focus then shifts towards the axial loss development throughout the blade passage, where local regions of high entropy generation rate are identified. The overall losses are split into midspan, i.e. profile loss and secondary loss and compared in cases with varying endwall boundary layer and unsteady inflow.

Test Case

METHODS

The present numerical investigations as well as the reference experiments were conducted using a linear cascade design of the T106A low-pressure turbine profile, which was specifically developed for experimental endwall flow investigations under high-speed conditions and unsteady inflow. The latter is generated by periodically incoming wakes of moving bars with a diameter of 2 mm, i.e. 111% of the T106 trailing edge diameter. The moving bar plane, which runs parallel to the blade passage inlet plane, is located $86\%C$ upstream of the blade leading edge. The bar speed is $V_b = 20 m/s$ and the ratio of bars to blade count is two-to-one, i.e. $P_b/P = 0.5$. The resulting flow conditions are summarized in Tab. 1. Whereas the Strouhal number Sr describes the number of wakes present in the blade passage at any given instant, the flow coefficient Φ dictates the orientation of the wake in the blade-to-blade plane. Previous experimental and numerical studies of the

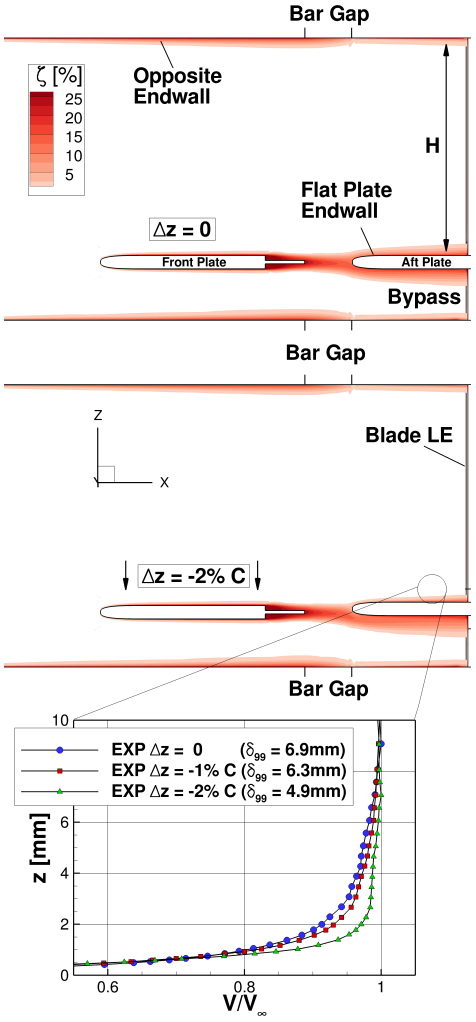

FIGURE 1: Effect of the flat plate misalignment on the inlet endwall boundary layer of the T106A cascade

TABLE 1: T106A linear turbine cascade

Geometric Parameters:	
Pitch-to-chord ratio P/C	0.799
Aspect ratio H/C	1.31
Flow Conditions:	
Exit Mach number M_{2th}	0.59
Exit Reynolds number Re_{2th}	$2 \cdot 10^5$
Design inflow pitch angle β_1	127.7°
Design outflow pitch angle β_2	26.8°
Turbulence intensity Tu_1	6.8%
Unsteady inflow conditions:	
Strouhal number Sr	0.66
Flow coefficient ϕ	3.8

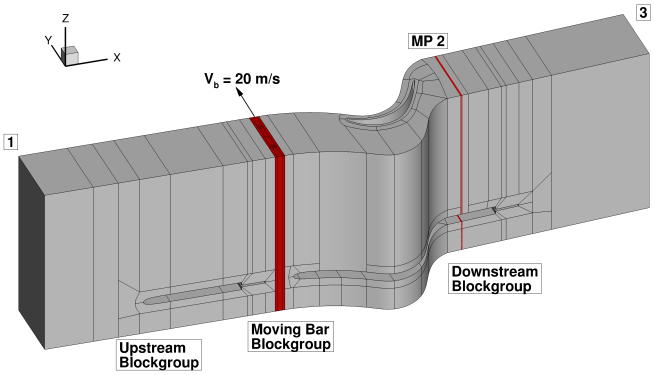

FIGURE 2: Block topology in the computational domain of the T106A cascade with an integrated two-part flat plate and a moving bar wake generator

T106A turbine cascade have shown that increased bar velocity (higher Sr and lower Φ) results in intensified effects on the secondary flow [7]. However, the observed trends remain constant within a reasonable range of unsteady inflow parameters. Furthermore, when keeping a constant value of Strouhal number by varying the bar speed proportional to the bar pitch, the influence of the flow coefficient is relatively minor. In fact, in case of the T106A, lowering Φ at constant Sr slightly decreases the effects on the downstream integral loss. Therefore, the present investigation on loss generation is highly relevant for a wide range of unsteady inflow cases, including more realistic high-Sr-low-Φ-cases.

The main motivation for the particular cascade re-design for the present investigations is improving upon unfavorable aerodynamic circumstances in previous experimental setups. The issue stems from a gap between the wind tunnel and the cascade endwalls, upstream of the blade passages, which is needed for the moving bar wake generator. Due to a negative pressure gradient, a leakage flow is formed in the bar gap. While the freestream flow is not affected, it is acting as an endwall boundary layer suction ultimately leading to weak secondary flow. Compared to a conventional turbine cascade, the present design, which is discussed in detail by Schubert et al. [12], delivers several improvements regarding aerodynamics and integration of measurement techniques. The central feature is an integrated flat plate at part-span which serves as a turbine cascade endwall and provides well defined, and adjustable, inlet endwall boundary layer conditions. The flat plate is divided into two parts, one upstream and one downstream of the moving bar plane. Inserting the flat plate divides the overall flow channel into two spanwise sections as shown in Fig. 1. The larger main channel is used for all flow investigations, where the lower channel half near the flat plate is of particular interest. The second smaller section is the bypass channel, which is not considered in the investigations. While the position of the downstream plate remains unchanged, the upstream plate can be displaced in spanwise direction, changing the boundary layer augmentation on the aft plate. The value of Δz denotes the misalignment of the two flat plates, with $\Delta z < 0$ resulting in decreased inlet endwall boundary layer height, as shown by the measured velocity profiles at the bottom of Fig. 1. The trailing edges of both flat plates are equipped with thin splitter plates. The front plate splitter ensures that the dominant source of unsteadiness in the inlet flow originates from the periodically incoming bar wakes. The aft plate splitter has two benefits, first, it prevents any influence on the downstream pressure field. Second, lower fluctuations decrease the required distance to the outlet of the computational domain (plane 3 in Fig. 1) to ensure numerical convergence and stability.

Experimental Reference Data

All experimental data referenced in this paper was measured at realistic flow conditions ($M_{2th} = 0.59$, $Re_{2th} = 2 \cdot 10^5$) in the High-Speed Cascade Wind Tunnel of the Institute of Jet Propulsion at the Bundeswehr University Munich, which recently underwent a major revision and upgrade [13]. The unsteady inflow conditions were generated by moving bars, matching the position, size, and dynamics of the CFD model. Measurements of the turbine exit flow field were performed using a five-hole-probe traverse in measurement plane 2 (MP 2), located 34%C, i.e. 40%C_x downstream of the blade passage. Based on linear error propagation, the maximum FHP measurement errors in the experimental reference data are $M_{2,err} = 0.0043$, $\zeta_{2,err} = 0.321\%$, and $\beta_{2,err} = 0.093°$. Mass-flow-weighted-averaging is applied for all integral values of the measured and CFD data. Further details on the experimental setup, measurement techniques, the particular turbine cascade design, and a discussion of the experimental results can be found in [12].

CFD Setup

The numerical simulations are performed using the (U)RANS approach of the flow solver TRACE by DLR with the $k-\omega$ turbulence model by Wilcox [14] and $\gamma Re_{\theta t}$ transi-

tion model by Langtry and Menter [15]. The computational domain shown in Fig. 2 covers a single blade pitch with periodic boundary conditions. It is divided into an upstream block group encompassing the front plate, the moving domain containing two bar pitches, and a downstream block group which encompasses the blade passage and aft plate. Due to the asymmetric geometry caused by the integrated flat plate, the full blade span including the lower bypass channel is resolved in the computation. The flux discretization is performed using a 3rd order upwind scheme with 2nd order accuracy in space. In the unsteady calculations the physical time is resolved with the 2nd order Crank-Nicolson method. The blade passage is meshed using an OCGH-topology and low-Reynolds wall treatment ($y^+ \leq 1$), resulting in high boundary layer resolution. A sensitivity study was conducted to ensure a sufficient spatial and temporal discretization. The number of nodes in the blade o-grid of the main channel are 354, 31 and 110 in i,j,k-direction and the overall number of nodes in the entire computational domain is approximately $8 \cdot 10^6$. In the unsteady simulations, each moving domain period is resolved in 800 time steps. The convergence criterion is set to a relative mass flow rate residual of less than 10^{-6} and an average density residual of less than 10^{-7} in the steady computations. In the unsteady computations, the limits were adjusted to 10^{-5} and 10^{-7}. Leakage panels are incorporated at the bar gap boundaries to simulate the leakage flow. The imposed static pressure condition is determined based on experimental data. The flow conditions prescribed at the in- and outlet plane match the wind tunnel conditions in the experiment (M_{2th}, $Re_{2th} = f(T_{t1}, p_{t1}, p_3)$ and Tu_1). A pressure sided incidence of $i = 2°$, i.e. $\beta_{1,CFD} = 129.7°$ is used in the simulations to increase loading in the front part of the blade and therefore match the measured Mach number distribution with higher accuracy (see Fig. 3). A comprehensive report on the sensitivity of a related T106 turbine cascade flow simulation in terms of temporal and spatial resolution, turbulence boundary conditions and convergence can be found in [16].

RESULTS

Blade Mach Number Distribution

The most important gauge for evaluating the numerical predictions of the 2D turbine cascade flow is the isentropic blade Mach number distribution at midspan, shown in Fig. 3. The T106A is a predominantly aft-loaded profile which features a small separation bubble under the investigated steady inflow conditions (see Tab. 1), caused by the adverse pressure gradient in the aft section of the blade suction surface. The numerical predictions and the measurements match well except for two locations: the front of the pressure surface, where the applied incidence angle is not sufficient and a more pronounced suction surface separation bubble in the CFD. The later discrepancy is attributed to a quicker turbulence decay in the computational domain resulting in a lower local turbulence intensity even though $Tu_{1,CFD}$ matches the experimental level. The turbulent dissipation rate could be adjusted by tweaking the inlet level of the turbulent length scale, however, a low level of this quantity is imperative for an accurate prediction of the loss generation. In the case of unsteady inflow conditions, the blade loading in the front part of the suction surface is reduced by an induced pitchwise incidence of $i = -1.5°$. Furthermore, wake-induced transition causes a suppression of the suction surface separation bubble. Both these effects are predicted well in the numerical simulations.

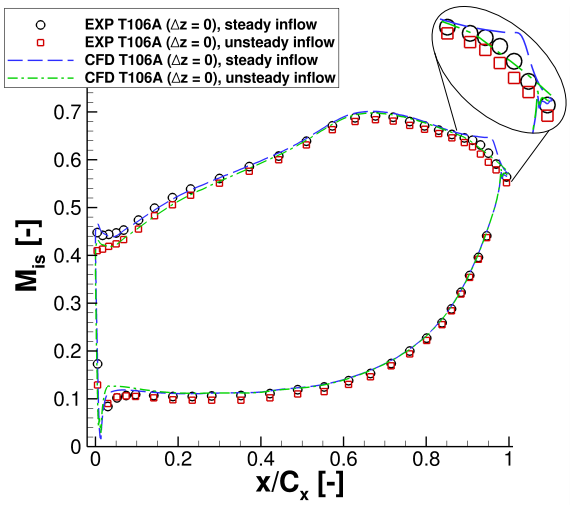

FIGURE 3: Comparison of the predicted and measured isentropic Mach number distributions at midspan of the T106A turbine cascade at $M_{2th} = 0.59$, $Re_{2th} = 2 \cdot 10^5$

For a viable investigation of endwall losses it is important to note that the secondary flow does not affect the 2D flow at midspan inside the blade passage of the present T106A cascade with a reduced aspect ratio of $H/C = 1.31$. This fact was verified by comparing measurements of the thickest endwall boundary layer case ($\Delta z = 0$) to a high-aspect-ratio ($H/C = 1.7$) reference case of the T106A [12].

Downstream Flow Field

Achieving a satisfactory match with the experimental results in the endwall region generally poses a bigger challenge than at midspan due to complex vortex interaction with high levels of anisotropic turbulence. Best suited for a quantitative evaluation of the distinction of the secondary flow are spanwise distributions of over-/underturning and losses in the turbine exit flow (measurement plane 2). The pitchwise-averaged secondary outflow angle $\Delta\beta_{2,sec}$ and secondary total pressure losses $\zeta_{2,sec}$, shown in Fig. 4, are defined by

$$\zeta_2 = \frac{p_{t1} - p_{t2}}{p_{t1} - p_3}, \tag{1}$$

$$\zeta_{2,sec} = \zeta_2 - \zeta_{2,MS}, \tag{2}$$

$$\Delta\beta_{2,sec} = \beta_2 - \beta_{2,MS}. \tag{3}$$

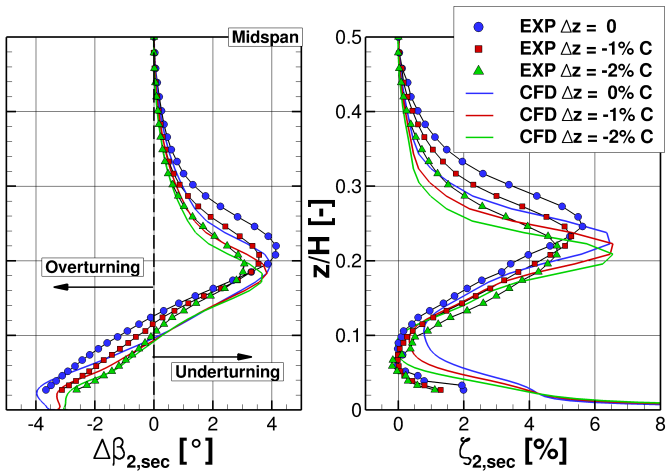

FIGURE 4: Spanwise distribution of the pitchwise-averaged secondary pitch angle $\Delta\beta_{2,sec}$ and secondary total pressure losses $\zeta_{2,sec}$ with steady inflow and different endwall boundary conditions in measurement plane 2

By this definition a common assumption of constant profile losses in spanwise direction is implied, which in reality is not the case. However, since the change in profile loss near the endwall is inherently linked to secondary flow effects, it is reasonable to count it towards the secondary losses. Comparing the numerical simulations to the experimental results shows a good agreement of the general shape of the spanwise distributions. Although it appears that the predicted distributions are slightly shifted towards the endwall. In measurements, this is usually a sign of weaker secondary flow with a less pronounced liftoff of the passage vortex. However, in this case it does not go along with reduced peak values of underturning and total pressure loss. The narrower region of elevated losses in combination with an overshoot of the loss peak is commonly observed in numerical simulations solving the (U)RANS equations with an eddy-viscosity model (e.g. similarly in blade trailing edge wakes). Despite the slight differences in the spanwise distribution, the important quantity of overall losses, defined here as integral half-span losses, are predicted with very good accuracy by the simulations, e.g. in the $\Delta z = -1\%C$ case $(\zeta_{2,HS})_{EXP} = 4.7\% \approx (\zeta_{2,HS})_{CFD} = 4.6\%$. For this specific comparison, the CFD value was integrated only within the experimentally accessible area of $0.027 \leq z/H \leq 0.5$.

Steady inflow conditions Looking at the three cases of front plate misalignments Δz in Fig. 4, it is apparent that the different inlet endwall boundary layer conditions result in varying degrees of secondary flow. The effect is not limited to the *boundary layer loss region* ($0 < z/h < 0.05$), where the endwall boundary layer and the corner vortex are the main drivers of loss generation. In fact, the entire secondary flow is affected, ranging from the endwall far into the flow channel. The case of $\Delta z = 0$, representing the thickest boundary layer, exhibits the strongest secondary flow with high levels of over-/underturning and secondary losses covering a large spanwise range of the flow channel. Lowering the inlet boundary layer thickness in the cases of $\Delta z = -1\%C$ and $\Delta z = -2\%C$, results in an attenuation of the secondary flow. This is manifested by a reduction of the peak values of over-/underturning combined with a shift towards the endwall. The observed reduction in the measured secondary loss peaks in the underturning region is not present in the simulations, the trend of a shift towards the endwall, however, is predicated well. In conclusion, with the one exception, the effects of the inlet endwall boundary layer changes on the secondary flow in *MP* 2 are quite uniform in the investigated CFD and experimental cases. However, the level of change in $\Delta\beta_{2,sec}$, $\zeta_{2,sec}$ in the CFD is slightly less severe in the underturning region, but higher in the overturning region. Considering the (U)RANS approach and comparable CFD studies in recent literature [3], [7], [8], [17], the present numerical results show a good qualitative prediction of the experiment with reasonable deviations in absolute terms. Therefore, the numerical setup is deemed to be well suited for further investigations into the turbine cascade endwall flow.

Unsteady inflow conditions After evaluating the effects of an inlet boundary layer variation on the secondary flow, the effects of unsteady inflow conditions are investigated. The change over time in integral losses in *MP* 2 is given in Fig. 5, where the overall losses are split into individual loss components, the midspan losses, i.e. profile losses and secondary losses. The additional incoming wake loss is accounted for by subtracting the time-averaged values upstream of the blade passage at $x = x_{ref}$.

$$\Delta\zeta = \zeta_x - \bar{\zeta}_{x_{ref}}, \quad \text{with} \quad x_{ref} = -45\%C = -52.4\%C_x \tag{4}$$

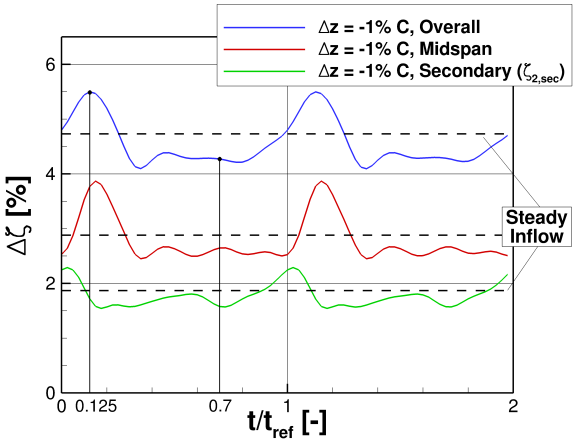

FIGURE 5: Predicted change in integral total pressure losses over time in measurement plane 2

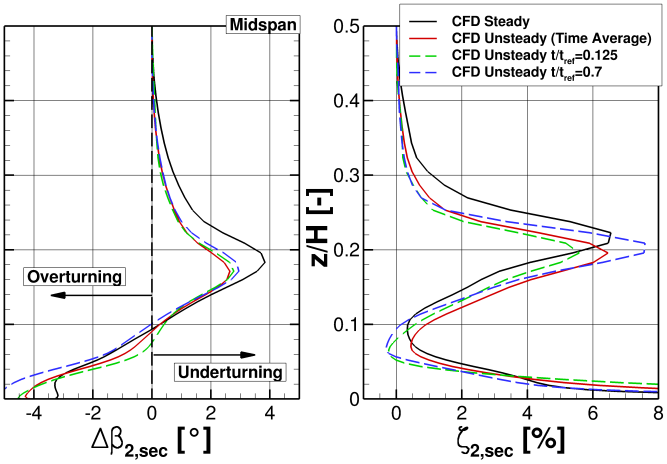

FIGURE 6: Spanwise distribution of the pitchwise-averaged secondary pitch angle $\Delta\beta_{2,sec}$ and secondary total pressure losses $\zeta_{2,sec}$ with steady and unsteady inflow conditions in measurement plane 2

As expected, the fluctuations caused by the periodically incoming bar wakes are dominant in all loss components. The midspan losses exhibit an additional minor fluctuation with a higher frequency of about $4 \cdot f_b$ but much lower amplitude. It seems to stem from the aft section of the blade suction surface flow. However, in the overall loss sequence, this minor midspan loss fluctuation is damped almost completely since in the present low-aspect-ratio blade channel ($H/C = 1.31$), the secondary flow covers a wide range of the span. In this region of the blade suction surface the boundary layer is highly disturbed by secondary flow interaction. For a more detailed description of the effects of the unsteady inflow on the downstream flow field, a steady state simulation without incoming bar wakes is compared to the time-averaged unsteady inflow solution in *MP* 2 in Fig. 6. In all cases the inlet endwall boundary layer remains unchanged in terms of flat plate misalignment ($\Delta z = -1\%C$), but is periodically disturbed by the incoming bar wakes in the unsteady cases. Judging from the spanwise $\Delta\beta_{2,sec}$ and $\zeta_{2,sec}$ distributions, the periodically incoming wakes cause an attenuation of the time-averaged secondary flow. This is apparent by a reduction in over-/underturning as well as a shift towards the endwall. Similarly to the previous variation of inlet boundary layer in Fig. 4, the reduction of the secondary loss peak in the underturning region is rather small in the CFD. Even though only one inlet boundary layer case is shown here, the level of secondary flow attenuation due to unsteady inflow is higher in cases with more pronounced secondary flow [12]. It is noticeable that the reduction in time-averaged peak values and the spanwise shift by means of unsteady inflow conditions is similar to the effect of varying the inlet endwall boundary layer conditions, especially in the underturning region.

The time-resolved flow field in *MP* 2 is shown at two distinct times in the moving bar period t_{ref} in Fig. 6 & 7. The first instant at $t/t_{ref} = 0.125$ corresponds to the maximum overall losses in a bar period (see Fig. 5). Around this time, the remains of an incoming bar wake, which has been stretched and bowed in the blade passage, first interact with the passage vortex in *MP* 2. The bar wake then travels in pitchwise direction, where it affects the suction surface and ultimately overlaps with the blade wake at $y/P = 0.5$, which corresponds with the extension of the trailing edge. The consequence is a very wide blade wake with high maximum pitchwise-averaged midspan losses. Considering the definition of the secondary losses in Eq. (2), the peaks of midspan and overall losses occur around the same time as the secondary loss minimum (see Fig. 5). This is confirmed by the streamwise vorticity (SVO*) plot, non-dimensionalized by dividing by $V_{2,th}^2/C$, on the right side of Fig. 7, where a temporary attenuation of the passage vortex can be seen. The reduced liftoff of the secondary vortex system correlates with a less distinct horseshoe vortex pressure side leg, which has already begun to merge with the passage vortex in *MP* 2. The same observation was made by Sinkwitz et al. [18] and Winhart et al. [17] in measurements and simulations of a low-speed adaptation of the T106A in an annular cascade. The second instant at $t/t_{ref} = 0.7$ exhibits further pitchwise distance between the bar wake and the blade wake in *MP* 2, so there is no overlapping. In combination with the temporary suppression of the suction surface separation bubble, this results in a very narrow blade wake, even narrower than the steady inflow case.

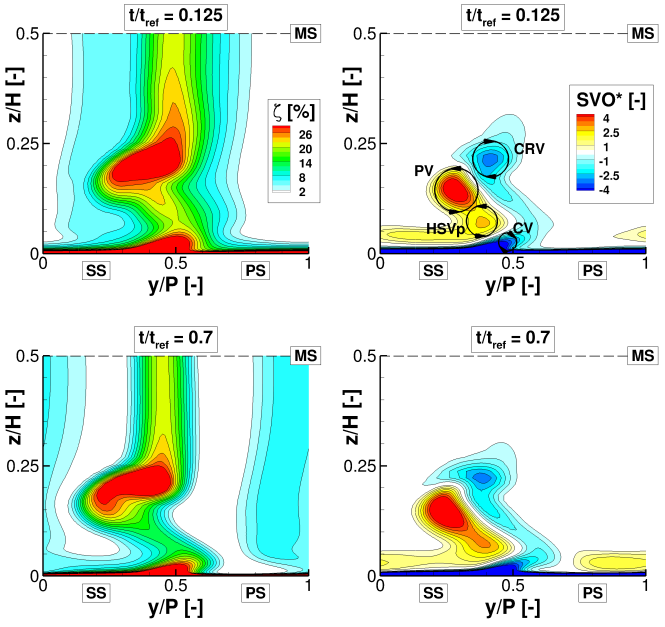

FIGURE 7: Predicted total pressure loss and streamwise vorticity in the time-resolved downstream flow field in measurement plane 2 with unsteady inflow conditions

The pitchwise secondary loss distribution at $t/t_{ref} = 0.7$ in Fig. 6 exhibits a high peak in the underturning region, but lower values near the endwall $z/H < 0.12$. Overall, this adds up to relatively low levels of integral midspan, secondary, and overall losses falling below the steady inflow case (see Fig. 5). Both instantaneous flows in Fig. 6 exhibit levels of underturning close to the time-averaged value. While larger deviations of the outflow angle do appear within the moving bar period, the level of underturning present under steady inflow conditions is never reached, nor is the spanwise extension of the secondary flow. In this regard, it is important to understand that the flow properties in *MP* 2, or any axial plane for that matter, are not only influenced by the bar wake in that specific location, but especially by upstream interactions with the blade passage flow. This means at no point during a moving bar period the turbine exit flow is truly undisturbed.

Axial Loss Development

The analysis of the turbine exit flow in measurement plane 2 has shown a similarity between the time-averaged effects of unsteady inflow conditions and varying the inlet endwall boundary layer conditions regarding the attenuation of the secondary flow, especially in the region of underturning. Thus, the question arises as to the upstream secondary flow development and corresponding loss generation throughout the blade passage leading up to the similar effects seen in *MP* 2. Therefore, the following investigation is focused on the axial loss development, comparing the different inlet endwall boundary layer cases in Fig. 8 and steady to unsteady inflow conditions in Fig. 9. In order to thoroughly consider the entirety of losses, the change in entropy is evaluated which is directly proportional to the lost efficiency. The change in specific entropy with respect to x_{ref} (see Eq. (4)) is calculated by

$$\Delta s = c_v \, ln\left(\frac{p_{t,x}}{p_{t,x_{ref}}}\right) - c_p \, ln\left(\frac{\rho_{t,x_{ref}}}{\rho_{t,x}}\right) \tag{5}$$

and non-dimensionalized (Δs^*) by dividing by $V_{2,th}^2/T_{2,th}$. Since entropy can only increase along a streamline, its value offers no information on the location of the sources of loss. Therefore, additionally the entropy generation rate per unit volume, as defined by [19], [20] as

$$\dot{S}_v = \underbrace{\frac{1}{T}\,\tau_{ij}\frac{\partial V_i}{\partial x_j}}_{viscous} + \underbrace{\frac{k_{eff}}{T^2}\left(\frac{\partial T}{\partial x_j}\right)^2}_{thermal}, \tag{6}$$

is calculated by flux summation over the cell faces of each computational cell. In the present turbine cascade case, the viscous dissipation term of the entropy generation rate is dominant. $\dot{S}_v$, which has the unit $W/(m^3 K)$, is non-dimensionalized ($\dot{S}_v^*$) by dividing by $\rho_{2,th} V_{2,th}^3/(C T_{2,th})$.

The overall losses, shown in three cases of different inlet endwall boundary layer in Fig. 8, are again split into individual loss components. Upstream of the blade leading edge ($x/C_x < 0$) the overall losses slowly increase almost linearly, which is fully attributed to the growing endwall boundary layer while the midspan losses remain virtually unchanged. Entering the blade passage ($x/C_x \geq 0$), the loss generation increases due to the blade surface boundary layers and the pressure gradients acting on the endwall flow. Towards the aft section of the blade passage ($0.5 \leq x/C_x \leq 1$), the increase of all loss components accelerates, especially since the T106A is a predominately aft-loaded turbine profile. Here, strong transverse pressure gradients act on the endwall flow, which leads to boundary layer fluid being driven towards the suction surface, rolling up, being fed into the passage vortex, and lifting off the endwall. As the passage vortex and the horseshoe vortex pressure side leg impinge on the blade suction surface, relatively high levels of secondary losses are generated, matching, and in case of ($\Delta z = 0$) even slightly surpassing, the profile losses. This process is well illustrated by the secondary vortices in Fig. 10 visualized by an isosurface of the Q-criterion and colored by streamwise vorticity indicating the sense of rotation. It also becomes apparent that while the loss generation rate is low at the vortex cores, high levels of loss are generated in the shear layers surrounding the vortices and especially in the interaction with the suction surface flow. Near the trailing edge ($x/C_x = 1$) there is a steep increase in profile losses attributed to the strong adverse pressure gradients acting on the blade suction surface which lead to the formation of a separation bubble. Since the separation bubble is suppressed in the secondary flow region, this marks the only spot, where the profile losses increase faster than the overall losses, resulting in a local plateau of the secondary losses. Due to high gradients in the shear layers of the blade trailing edge wake, the midspan loss generation is still high immediately downstream of the blade passage ($1 \leq x/C_x \leq 1.2$), but starts to level off with increasing distance from the trailing edge. Finally, at $x/C_x \geq 1.2$ the midspan loss increase settles on a very moderate slope, as the only remaining sources of loss are continuous mixing and turbulence decay. The formation of the secondary vortices inside the blade passage left behind a relatively thin endwall boundary layer near the trailing edge, which starts growing again with increasing run-length downstream of the blade passage. Thus, the secondary losses continue to increase in a quasi-linear fashion and gain on the midspan loss level due to a combination of vortex and boundary layer dissipation. In *MP* 2 at $x/C_x = 1.4$ the secondary losses make up about 40% of overall losses.

The variation of the inlet endwall boundary layer shows no effect on the loss generation upstream of the blade leading edge. However, once the transverse pressure gradients start acting on the endwall flow inside the blade passage, the loss generation lines start to slowly diverge as the thicker boundary layers lead to an augmentation of the secondary flow. Since the endwall flow does not affect the 2D flow at midspan, the increase in overall losses due to inlet boundary layer variation is

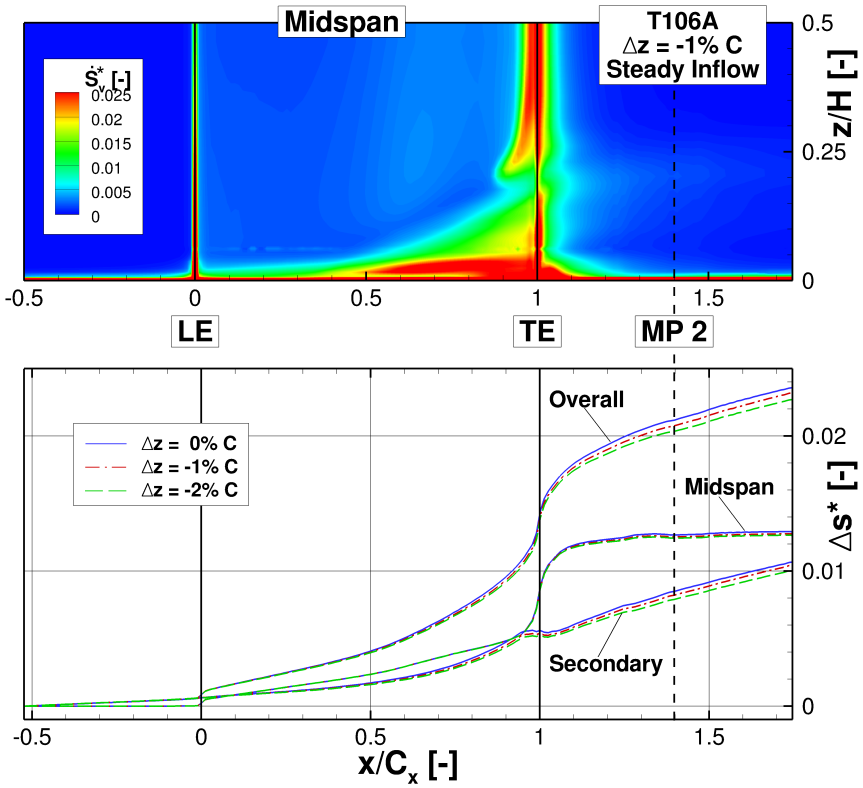

FIGURE 8: Axial entropy development and pitchwise-averaged entropy generation rate per unit volume throughout the T106A blade passage with different inlet endwall boundary layer conditions

solely based on the secondary losses inside the blade passage. Downstream of the blade passage ($x/C_x > 1$) the trend of slightly higher secondary loss generation in cases of thicker inlet boundary layer is continued as the secondary flow is propagated towards the midspan due to flow mixing where it covers a wider spanwise range in the $\Delta z = 0$ case. Here, there is a minimal influence on the midspan losses, because the thicker boundary layer cases start mixing with the midspan flow.

In Fig. 9, the time-averaged axial loss development in case of unsteady inflow conditions is compared to the steady state. An accelerated overall loss increase in the front part of the blade passage is visible in the unsteady inflow case. Despite the decreased frontal blade loading as seen in the Mach number distribution in Fig. 3, this is caused by higher blade profile losses, apparent in Fig. 10 by the increased entropy generation rate at midspan of the blade leading edge and the front part of the suction surface. Here, the blade surface boundary layers are perturbed by the incoming bar wakes with high levels of turbulence and the deformation of migrating bar wakes affect the potential flow field. In contrast to the profile losses, the secondary loss generation is not increased by the incoming wakes inside the blade passage ($0 \leq x/C_x \leq 1$). In fact, entering the passage, the interaction of the wakes with the endwall boundary layer periodically delays the development of passage vortex. This leads to the attenuation of the secondary vortex system further downstream including the corner vortex and counter rotating vortex. Therefore, a reduction of the secondary loss increase occurs in the aft section of the blade passage. Outside the near-endwall region, the wake-induced transition periodically forces the suppression of the suction surface separation bubble. This unsteady effect is visible in the time-averaged flow in Fig. 10 by a lack of alternating vorticity on the rear suction surface. Thereby wake-induced transition is identified as the cause of the attenuation of the rapid increase of the profile losses near the trailing edge ($x/C_x = 1$) in Fig. 9. In sum, the steady case overall losses are catching up to the unsteady inflow case and the loss component lines converge with further downstream distance from the blades. Thus, despite the flow field changes seen in measurement plane 2 (Fig. 6 & Fig. 7), the time-averaged integral losses in the turbine exit flow are barely affected by the periodically incoming wakes. This finding is consistent with the corresponding total pressure field measurements [12]. Overall, the effect of unsteady inflow conditions can be summarized as a spatial redistribution of the loss generation with a premature loss increase due to wake interaction with the blade surface boundary layer and wake migration in the potential flow field followed by an attenuation of the profile- and secondary loss generation in the aft section of the blade passage.

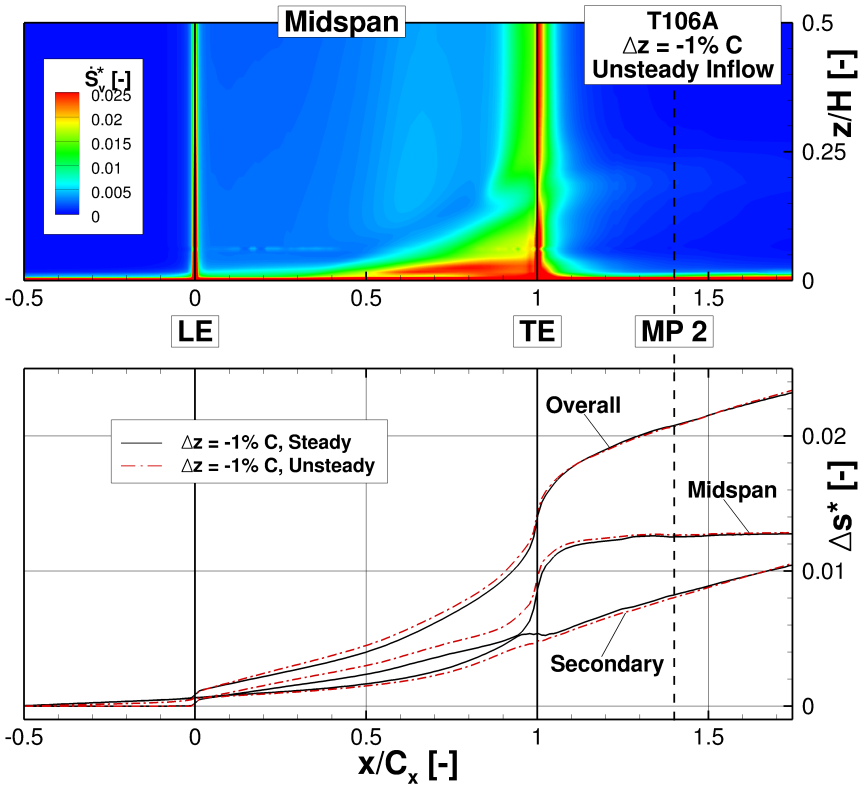

FIGURE 9: Axial entropy development and pitchwise-averaged entropy generation rate per unit volume throughout the T106A blade passage with steady and unsteady inflow conditions

CONCLUSIONS

A particular design of the T106A low-pressure turbine cascade is utilized to allow an investigation under engine relevant flow conditions ($M_{2th} = 0.59$, $Re_{2th} = 2 \cdot 10^5$) with and without periodically incoming wakes as well as a variation of the inlet endwall boundary layer. (U)RANS simulations have been deployed to complement the experimental results providing additional information in areas of limited accessibility as well as time-resolved flow fields. In return, measurements of the blade Mach number distribution and the turbine exit flow field were utilized to evaluate the computational approach. Under the present flow conditions the suction surface separation bubble is exaggerated in the steady inflow cases due to turbulence transition modeling and the spanwise reach of the secondary flow is slightly lower. Nonetheless, the numerical results show a good agreement with the flow phenomena observed in the experiment. Subsequently, a detailed investigation of the downstream flow field is conducted with the following results:

1. Reducing the inlet endwall boundary layer height leads to an attenuation of the secondary flow. This is apparent by lower levels of over-/underturning along with a spanwise shift towards the endwall, which limits the reach of the secondary flow.
2. Cases with unsteady inflow conditions also show lower levels of over-/underturning as well as the spanwise shift of the secondary vortices towards the endwall.
3. When excluding the change in inlet losses due to incoming wakes or lower endwall boundary layer height, both approaches show slightly lower time-averaged integral losses in the turbine exit plane. The level of loss reduction in case of unsteady inflow is very small though, which is consistent with the experimental results.
4. Overall, applying unsteady inflow conditions or thinning the inlet endwall boundary layer appear to have similar time-averaged effects regarding the attenuation of the secondary flow, especially in the region of underturning.

In order to analyze the flow phenomena leading to the observed effects in the turbine exit plane, the axial development of the overall losses throughout the blade passage is separated into midspan losses, i.e. profile loss and secondary losses. It is found that the effects of unsteady inflow conditions and varying inlet endwall boundary layer on the loss development inside blade passage are quite different:

1. Decreasing the inlet endwall boundary layer height results in a nearly constant reduction of the axial endwall loss generation, beginning around the midpoint of the blade passage where the secondary flow is formed.
2. On the contrary, the effect of unsteady inflow conditions on

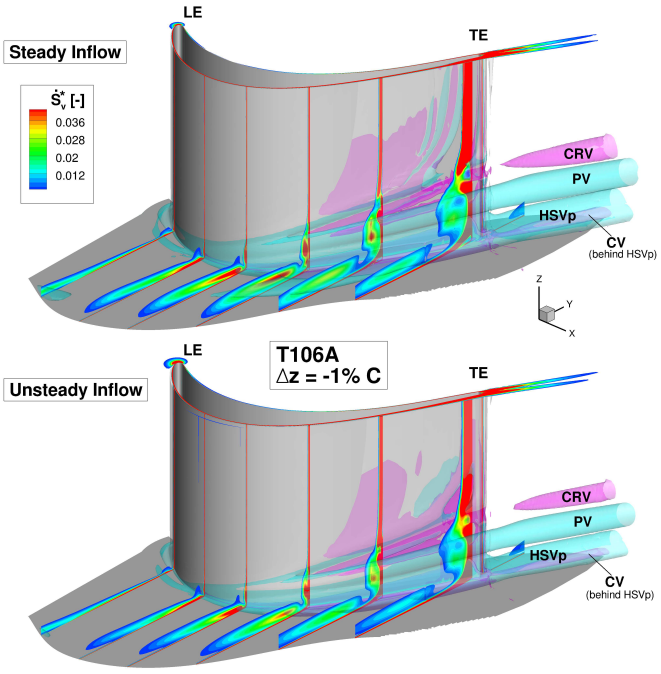

FIGURE 10: Entropy generation rate per unit volume at several axial slices inside the T106A blade passage ($0 \leq x/C_x \leq 1$) with steady and unsteady inflow conditions

the integral loss components is not constant in axial direction. It is rather as a spatial redistribution of the loss generation with a premature loss increase due to wake interaction with the blade surface boundary layer followed by an attenuation of the profile- and secondary loss generation in the aft section of the blade passage.

Considering unsteady effects in the aerodynamic turbine design process can lead to valuable increases in efficiency and reaching previously unattainable operating points with high blade loading within reasonable loss levels. Therefore, it is critical to take further steps in gaining a better understanding of the effects of unsteadiness on all components of the passage flow and the associated loss generation mechanisms.

ACKNOWLEDGMENT

The present work was conducted as a part of the German Research Foundation (DFG) joint research project PAK-948. The authors wish to acknowledge the German Aerospace Center (DLR) Institute of Propulsion Technology Numerical Methods for provision of the flow solver TRACE and their support.

NOMENCLATURE

Latin Symbols

C	chord length
c_p, c_v	specific heat capacities
k_{eff}	effective thermal conductivity, $k_{eff} = k + k_T$
H	channel height
i	incidence angle
M	Mach number
p	pressure
P	pitch
Re	Reynolds number
s	specific entropy, Eq. (5)
$\dot{S}_v$	entropy generation rate per unit volume, Eq. (6)
Sr	Strouhal number, $(V_b/(P_b) \cdot (C/V_{x1})$
SVO	streamwise vorticity, $\omega_x \cdot V_x + \omega_y \cdot V_y + \omega_z \cdot V_z$
T	temperature
Tu	turbulence intensity
t	time
V	velocity
x, y, z	axial, pitchwise, and spanwise coordinate

Greek Symbols

β	flow pitch angle (0° in positive pitchwise direction)
ϕ	flow coefficient, V_{x1}/V_b
τ_{ij}	viscous stress tensor
ζ	total pressure loss coefficient, Eq. (2)

Abbreviations

CV	corner vortex
CRV	counter rotating vortex
HSVp	horse show vortex pressure side leg
MP2	measurement plane 2, 40% C_x downstream TE
MS	midspan
PV	passage vortex

Subscripts

1,3	in- / outlet plane
2	downstream measurement plane
b	bar
t	stagnation quantity
th	theoretical value after isentropic change of state
sec	secondary

REFERENCES

[1] Denton, J. D., 1993. "Loss Mechanisms in Turbomachines". *J. Turbomach. 115.*

[2] Cui, J., and Tucker, P. G., 2016. "Numerical Study of Purge and Secondary Flows in a Low Pressure Turbine". *ASME Paper No. GT2016-56789.*

[3] Denton, J., and Pullan, G., 2012. "A Numerical Investigation into the Sources of Endwall Loss in Axial Flow Turbines". *ASME Paper No. GT2016-56350.*

[4] Bear, P., Wolff, M., Gross, A., Marks, C. R., and Sondergaard, R., 2018. "Experimental Investigation of Total Pressure Loss Development in a Highly Loaded Low-Pressure Turbine Cascade". *J. Turbomach. 140.*

[5] Coull, J. D., 2017. "Enwall Loss in Turbine Cascades". *J. Turbomach. 139.*

[6] Lengani, D., Simoni, D., Ubaldi, M., Zunino, P., Bertini, F., and Michelassi, V., 2017. "Accurate Estimation of Profile Losses and Analysis of Loss Generation Mechanisms in a Turbine Cascade". *J. Turbomach. 139.*

[7] Ciorciari, R., Kirik, I., and Niehuis, R., 2014. "Effects of Unsteady Wakes on Secondary Flows in the Linear T106 Turbine Cascade". *J. Turbomach. 136*.

[8] Ciorciari, R., Schubert, T., and Niehuis, R., 2018. "Numerical Investigation of Secondary Flow and Loss Development in a Low Pressure Turbine Cascade with Divergent Endwalls". *J. Turbomach. Propuls. Power 2018, 3(1), 5*.

[9] Koschichow, D., Fröhlich, J., Kirik, I., and Niehuis, R., 2014. "DNS of the Flow Near the Endwall in a Linear Low Pressure Turbine Cascade with Periodically Passing Wakes". *ASME Paper No. GT2014-25071*.

[10] Volino, R., Galvin, C. D., and Ibrahim, M., 2013. "Effects of Periodic Unsteadiness on Secondary Flows in High Pressure Turbines". *ASME Paper No. GT2013-95881*.

[11] Volino, R., 2014. "Effects on Endwall Boundary Layer Thickness and Blade Tip Geometry on Flow through High Pressure Turbine Passages". *ASME Paper No. GT2014-27013*.

[12] Schubert, T., Chemnitz, S., and Niehuis, R., 2021. "The Effects of Inlet Boundary Layer Condition and Periodically Incoming Wakes on Secondary Flow in a Low Pressure Turbine Cascade". *J. Turbomach. 143(4)*.

[13] Niehuis, R., and Bitter, M., 2021. "The High-Speed Cascade Wind Tunnel at the Bundeswehr University Munich after a Major Revision and Upgrade". *ETC14 Paper No. ETC2021-647 (to be published)*.

[14] Wilcox, D. C., 2004. "Turbulence Modeling for CFD (forth printing)". *DCW Industries, USA*.

[15] Langtry, R. B., and Menter, F. R., 2005. "Transition Modeling for General CFD Applications in Aeronautics". *AIAA Paper 2005-522*.

[16] Ciorciari, R., 2017. "Analysis of Unsteady Secodary Flows in Linear Low-Pressure Turbine Cascades". PhD Thesis, Bundeswehr University Munich.

[17] Winhart, B., Sinkwitz, M., Schramm, A., Engelmann, D., di Mare, F., and Mailach, R., 2019. "Experimental and Numerical Investigation of Secondary Flow Structures in an Annular Low Pressure Turbine Cascade Under Periodic Wake Impact - Part 2: Numerical Results". *J. Turbomach. 141*.

[18] Sinkwitz, M., Winhart, B., Engelmann, D., di Mare, F., and Mailach, R., 2019. "Experimental and Numerical Investigation of Secondary Flow Structures in an Annular Low Pressure Turbine Cascade Under Periodic Wake Impact - Part 1: Experimental Results". *J. Turbomach. 141*.

[19] Moore, J., and Moore, J. G., 1983. "Entropy Production Rates from Viscous Flow Calculations. Part 1 - A Turbulent Boundary Layer Flow". *ASME Paper No. 83-GT-70*.

[20] Moore, J., and Moore, J. G., 1983. "Entropy Production Rates from Viscous Flow Calculations. Part 2 - A Flow in a Rectangular Elbow". *ASME Paper No. 83-GT-71*.

4.5 Publication 4

4.5.1 Summary

The inclusion of the blade passage in the investigation scope of Publication 3 using CFD provided valuable findings. This motivated the next step in the overall research project of extending the experimental data set beyond the classic probe-based approach up- and downstream of the passage. The primary goal was to validate, complement, and specify the previous findings and thereby demonstrate the benefit of an advanced multi-methodology approach to secondary flow investigations. Thus, considerable efforts were made to implement experimental setups which enable optical phase-locked measurements inside the passage. More precisely, Particle Image Velocimetry (PIV) and unsteady Pressure-Sensitive Paint (i-PSP) were chosen in particular for two main reasons. They enable simultaneous high-speed measurements of entire flow fields or surfaces and secondly, a flow alteration in the narrow passage by upstream probe effects can be prohibited. A phase-locking method was universally applied to synchronize the experimental data as well as supplemental CFD. This step is crucial in a multi-methodology approach for a comprehensive investigation of time-dependent flow phenomena. The results were split into a two-part publication with part 1 covering the following three main aspects.

1. The implementation of two individual phase-locked PIV measurement setups was achieved in a very challenging environment. The first one utilized optical access via a camera mirror for measurements in the previously used axial downstream plane. The second setup featured a camera endoscope guided through the cascade side- and endwalls to resolve the unsteady passage flow field in a blade-to-blade plane close to the endwall. In order to calculate the secondary flow parameters defined as the difference to the undisturbed 2D flow, an additional plane was resolved at midspan. Thus, the time-averaged change in underturning caused by the incoming wakes could be evaluated inside the passage. The results were consistent with the downstream pressure probe data presented in Publication 2.

2. An analysis of the phase-locked flow fields enabled the tracing of the bar wake dynamics including the negative-jet-effect throughout the blade passage and beyond the trailing edge. Subsequently, the wake transport was related to the periodic effects on the secondary flow in the axial plane downstream of the passage. Here, the width of the blade wake was periodically increased by up to 165 % due to overlapping bar wakes. In comparison, the downstream fully developed secondary flow exhibited an around three times higher resistance to pitchwise extension due to periodic wake perturbation. The wakes also forced a periodic decrease in passage vortex turbulent kinetic energy. Both effects, which led to less pronounced secondary flow, were in phase, but exhibited a phase lag of -108° to the bar wake overlap. It was concluded that the secondary flow attenuation is caused further upstream by wake interaction with the endwall boundary layer and hence the vortex formation.

3. In order to locate the mean origin of the periodic wake effect on the passage vortex core, the two phase-locked PIV measurements were combined. By retracing the blade-to-blade velocity field based on the identified phase lag in the downstream axial plane,

the mean origin was located inside the blade passage at around 72 % of the axial passage length. Its projection on the endwall was located just upstream of a large separation area in the supplemental CFD data as indicated by $P2_{EW}$ in Figure 4.4c. The migration of the horseshoe vortex pressure side leg across the passage appeared to play a significant role in triggering the flow separation. Under periodic inflow conditions, the CFD data exhibited a significant size reduction of the flow separation area. This was attributed to increased boundary layer separation robustness due to the perturbation by the highly turbulent wakes. This was supported by the boundary layer measurements presented in Publication 2. Consequently, less entrainment of the boundary layer material affected the vortex development and thus in part led to the observed attenuation of the downstream secondary flow.

4.5.2 Postprint

aerospace

MDPI

Article

Characterization of the Endwall Flow in a Low-Pressure Turbine Cascade Perturbed by Periodically Incoming Wakes, Part 1: Flow Field Investigations with Phase-Locked Particle Image Velocimetry

Tobias Schubert, Dragan Kožulović and Martin Bitter *

Institute of Jet Propulsion, University of the Bundeswehr Munich, Werner-Heisenberg-Weg 39, 85577 Neubiberg, Germany
* Correspondence: martin.bitter@unibw.de

Abstract: Particle image velocimetry (PIV) measurements were performed inside a low-pressure turbine cascade operating at engine-relevant high-speed and low-Re conditions to investigate the near-endwall flow. Of particular research interest was the dominant periodic disturbance of the flow field by incoming wakes, which were generated by moving cylindrical bars at a frequency of 500 Hz. Two PIV setups were utilized to resolve both (1) a large blade-to-blade plane close to the endwall as well as midspan and (2) the wake effects in an axial flow field downstream of the blade passage. The measurements were performed using a phase-locked approach in order to align and compare the results with comprehensive CFD data that are also available for this test case. The experimental results not only support a better understanding and even a quantification of the wake-induced over/under-turning inside and downstream of the passage, they also enable the tracing of the 'negative-jet-effect', which is widely known in the CFD branch of the turbomachinery community but is seldom visualized in experiments. The results also reveal that the bar wake periodically widens the blade wake by up to 165%, while the secondary flow is less affected and exhibits a phase lag with respect to the 2D-flow effects. The results presented here are an essential basis for the subsequent investigation of the near-endwall blade suction surface effects using unsteady pressure-sensitive paint in the second part of this two-part publication.

Keywords: rotor–stator interaction; negative jet; passage flow field; phase-locked particle image velocimetry (PIV)

Citation: Schubert, T.; Kožulović, D.; Bitter, M. Characterization of the Endwall Flow in a Low-Pressure Turbine Cascade Perturbed by Periodically Incoming Wakes, Part 1: Flow Field Investigations with Phase-Locked Particle Image Velocimetry. *Aerospace* **2024**, *11*, 403. https://doi.org/10.3390/aerospace11050403

Academic Editor: Lin Chen

Received: 14 March 2024
Revised: 25 April 2024
Accepted: 3 May 2024
Published: 16 May 2024

1. Introduction

The establishment of high-lift blade designs in modern jet engines and the ongoing trend to reduce weight by lowering the solidity in low-pressure turbine (LPT) vanes has triggered a lot of research on endwall flow in recent years. The main motivation is the significant contribution to overall losses due to high pressure gradients in the blade passage and thus intensified endwall flow. In the case of low-aspect-ratio LPT blades, for which a larger range of the blade span is affected, the endwall losses are approximated to account for one third of the overall losses, see [1]. Based on a numerical parametric design study in LPT cascades, Coull [2] found that endwall losses can be decomposed into two major components: dissipation in the endwall boundary layer and induced losses by secondary flows, which scale with streamwise vorticity. According to Denton and Pullan [3], the secondary flow itself exhibits several sources of loss, such as flow interactions inside the blade passage and downstream mixing losses. Particularly, the interaction of the passage vortex and the blade suction surface, resulting in the counter rotating vortex, was found to have a strong contribution to the overall losses by Cui and Tucker [1] as well as Bear et al. [4]. The endwall flow development is also largely dependent on the inflow

conditions. The effects of periodically incoming wakes were investigated in the T106A and T106Div turbine cascades using measurements and numerical simulations (CFD) by Ciorciari et al. [5,6]. Both approaches have shown an attenuation of the secondary flow. In contrast to the relatively small effects of incoming wakes, Volino et al. [7] found the influence of the inlet boundary layer to be much larger. Schubert and Niehuis [8] came to a similar conclusion when evaluating the turbine cascade exit flow; however, they found that the endwall flow development inside the blade passage is significantly affected by both factors, but in different manners. The vast majority of research dealing with secondary flow investigations has been centered around probe-based measurements: mostly up- and downstream of the blade passage. More recently, some published works have diverged from this classic approach by incorporating more modern experimental methods. For example, Sinkwitz et al. [9] and Lopez et al. [10] utilized hot-film sensor arrays on the near-endwall suction surface, and Chemnitz and Niehuis [11] analyzed the potential of particle image velocimetry (PIV) in comparison to five-hole-probe (FHP) and constant temperature anemometry (CTA) measurements in turbine cascade exit flow.

Despite the vast research activity in recent years, the accurate prediction and reduction of endwall loss is expected to remain a challenge for many years to come [3]. Aimed at providing a further step in the continued understanding of endwall flow and its determining factors, an extensive research program funded by the Deutsche Forschungsgemeinschaft (DFG) was launched in 2018 by four German university institutes, see Engelmann et al. [12]. Within this conglomerate, the Institute of Jet Propulsion of the University of the Bundeswehr Munich covered low-pressure turbine aspects at high-speed flow conditions. This paper is based on the design work and first experimental and CFD results by Schubert et al. [8,13]. They used a particular turbine cascade design to investigate the effects of boundary layer conditions and periodically incoming wakes on the secondary flows and losses. The subsequent goal was to validate, complement, and specify the previous findings by conducting state-of-the-art optical measurements inside the blade passage, which poses a far greater challenge in terms of experimental setup. Thereby, the present work will demonstrate how the classic approach to secondary flow investigations can be extended and enhanced to form a more comprehensive picture. The discussion of PIV results shall be the focus of part one of this two-part publication, while the second part will present unsteady pressure-sensitive paint (i-PSP) measurements.

2. Methods

2.1. Test Case

The presented experiments were conducted using a linear cascade of the T106A low-pressure turbine profile. The key geometric and flow parameters are summarized in Table 1. The T106 cascade has a long research history, and the aerodynamic performance of the original design is well known under various operating conditions, see, e.g., Kampitsch et al. [14], Kirik and Niehuis [15], or Michelassi et al. [16]. However, the cascade used here is a redesign that was specifically developed for endwall flow measurements under periodic inflow and high-speed conditions ($M_{2th} = 0.59$, $Re_{2th} = 2 \times 10^5$). The blade profile geometry remains unchanged, though. The main features of the current cascade are a sufficiently thick endwall boundary layer and the ability to perform variations in the boundary layer conditions on this endwall. The challenge regarding the endwall boundary layer stems from a gap between the wind tunnel and the cascade endwalls upstream of the blade passages. This gap, which is needed for the moving bar wake generator, enables a leakage flow driven by a negative pressure gradient. While the freestream flow is not affected, it can act as a boundary layer suction, leading to weak secondary flow. To counteract this problem, the current cascade features an integrated split flat plate at part-span that serves as a turbine endwall (marked in yellow in Figure 1). Using a modular composition of the aft plate, various measurement techniques can be implemented with manageable effort. The endwall boundary layer can be adjusted by misaligning the front plate with respect to the aft plate. During all measurements presented in this paper, the

endwall boundary layer thickness was δ_{99} = 4.62 mm with a shape factor of H_{12} = 1.86 at 45% Chord C upstream of the blade's leading edge (LE). A detailed description of the particular test case design and an investigation of the effects of endwall boundary layer variations on the secondary flow and loss production can be found in [8,13].

Table 1. T106A linear turbine cascade.

Geometric parameters:	
Chord length C	100 mm
Pitch-to-chord ratio P/C	0.799
Aspect ratio H/C	1.31
Flow conditions:	
Exit Mach number M_{2th}	0.59
Exit Reynolds number Re_{2th}	2×10^5
Design inflow angle β_1	127.7°
Design outflow angle β_2	26.8°
Turbulence intensity Tu_1	6.8%
Periodically unsteady inflow conditions:	
Strouhal number Sr	0.66
Flow coefficient ϕ	3.8

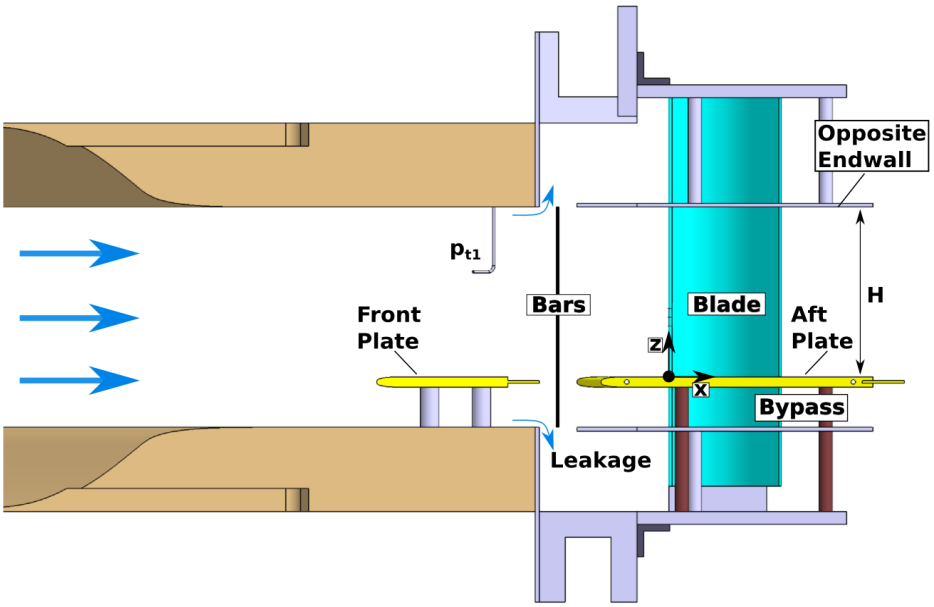

Figure 1. Illustration of the T106A test case featuring a split flat plate endwall (yellow) and moving bars upstream of the low-pressure turbine blades (cyan); adapted from Schubert et al. [8].

2.2. Numerical Setup

Numerical simulations were utilized during the cascade design (pre-test CFD) as well as to support the experimental results (validated post-test CFD) with time-resolved flow data, especially in areas of limited accessibility. The unsteady simulations were performed using the (U)RANS flow solver TRACE by DLR with the $k-\omega$ turbulence model by Wilcox [17] and $\gamma Re_{\theta t}$ transition model by Langtry and Menter [18]. The computational domain covers a single blade pitch with periodic boundary conditions. It is divided into an upstream block group encompassing the front plate, a moving domain containing two bar pitches, and a downstream block group that encompasses the blade passage and aft plate. The leakage flow is simulated by additional outlet panels at the bar gap boundaries. The blade passage is discretized using an OCGH-topology and low-Reynolds wall treatment (non-dimensional wall distance $y+ \leq 1$), resulting in high boundary layer resolution. Sufficient spatial and temporal discretization is ensured by a sensitivity study, which leads

to an overall number of nodes of approximately 8×10^6 and a blade o-grid with 354, 31, and 110 nodes in the i,j,k-directions, respectively. The CFL number is set to 150 in the unsteady simulations, and each moving domain period (two bar pitches) is resolved by 800 time steps. The flow conditions prescribed at the in- and outlet plane match the wind tunnel conditions in the experiment (M_{2th}, $Re_{2th} = f(T_{t1}, p_{t1}, p_3)$, and Tu_1). A detailed description of the computational approach can be found in [13].

The key flow characteristics inside the T106A blade passage are illustrated by means of CFD in Figure 2. Here, axial slices of the entropy generation rate and iso-surfaces of the Q-criterion (colored by streamwise vorticity indicating the sense of rotation) indicate loss production at midspan and the secondary flow region. In the 2D-flow region around midspan, the levels of loss production start off moderately in the predominately aft-loaded T106A. However, near the trailing edge (TE), strong adverse pressure gradients acting on the blade suction surface lead to the formation of a separation bubble. Under periodically unsteady inflow conditions, wake-induced transition periodically forces the suppression of the separation bubble. This unsteady effect is visible in the time-averaged flow in Figure 2 by a lack of alternating vorticity on the rear suction surface. Near the endwall, the formation of secondary flow as described e.g., by Sieverding [19] becomes apparent. When entering the blade passage, strong transverse pressure gradients caused by blade loading force the boundary layer fluid towards the suction surface. During this process, the flow is rolling up, is fed into the passage vortex and the merging horseshoe vortex pressure side leg, lifts off the endwall, and finally impinges on the blade suction surface. In addition to the resulting high losses, the secondary flow can be identified well by overturning close to the endwall and corresponding underturning at the upper edge of vortex interaction. In the case of unsteady inflow, the interaction of the wakes with the endwall boundary layer periodically delays the development of the passage vortex. This leads to the attenuation of the secondary flow further downstream and, hence, a reduction in the secondary losses. A more detailed analysis of the secondary vortex system can be found in [13] and the effect of blade loading is discussed in [6]. Furthermore, the interaction with the suction surface flow, which leads to the corner-vortex and counter-vortex is investigated in Part 2 [20].

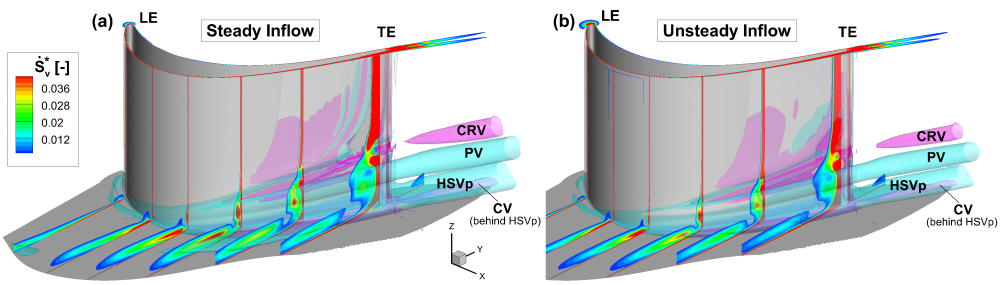

Figure 2. Simulated entropy generation rate ($\dot{S}_v^*$ non-dimensionalized) at several axial slices inside the T106A blade passage under steady (**a**) and periodically unsteady inflow conditions (**b**); adapted from Schubert et al. [13]; (HSVp—pressure side leg of horseshoe vortex; PV—passage vortex; CRV—counter-rotating vortex; CV—corner vortex; LE—leading edge; TE—trailing edge).

2.3. Experimental Setup

The experiments were conducted at the High-Speed Cascade Wind Tunnel (HGK) of the University of the Bundeswehr Munich, see Niehuis and Bitter [21]. The facility allows aerothermodynamic investigations of turbomachinery components at engine-relevant Mach and Reynolds numbers, which can be varied independently with respective uncertainties of 0.17% and 0.28%. For this reason, the main components of the HGK are enclosed by a large plenum chamber with a 4 m diameter and a 12 m length. The absolute pressure in this plenum chamber can be evacuated down to 4 kPa or pressurized up to 1.2 MPa. The wide pressure range together with the large test section dimensions make it possible to perform aerodynamic investigations on relatively large test specimens, even for low operating Reynolds numbers. This mitigates the relative influence of probe-based measurement

techniques on the flow field, especially at the high downstream Mach numbers typically encountered on a turbine cascade [22]. The HGK's test section can be equipped with a wake generator that produces periodically incoming wakes of up to around 500 Hz at the cascade inlet, see Acton and Fottner [23]. The periodically incoming wakes are generated by steel bars with a diameter of 2 mm, i.e., 111% of the T106A trailing edge diameter. The moving bar plane, which runs parallel to the blade passage inlet plane, is located 86% C upstream of the blade leading edge. The ratio of bars to blade count is two-to-one, i.e., $P_b/P = 0.5$, and the bar speed is $V_b = 20\,\mathrm{m/s}$, which leads to a bar passing period of 2 ms (500 Hz). Previous experimental and numerical studies of the T106A turbine cascade have shown that increased bar velocity (higher Strouhal number Sr and lower flow coefficient Φ) results in intensified effects on the secondary flow, see Ciorciari et al. [5]. However, within a reasonable range of unsteady inflow parameters, the observed trends remain unchanged.

The goal of the experiments was to measure an extensive flow field close to the endwall inside and downstream of the blade passage and demonstrate the time-dependent behavior with respect to the periodic bar wake effects. Therefore, two separate measurement setups using particle image velocimetry (PIV) were applied. Measuring a highly resolved passage flow field under high-speed conditions in close vicinity to a parallel wall and under severe vibrations of the wake generator was extremely challenging. In the first setup, the design of the test specimen and the blade-to-blade measurement plane required optical access to the flow passage through several side walls (see Figure 3a,b). Therefore, a single sCMOS camera with 5.5 Mpx resolution was connected to a 35 mm optical lens and a 220 mm long rod endoscope with an 8 mm diameter and 67° opening angle. The optical access into the passage from the opposite endwall is shown in Figure 3c. A light sheet generated by an Innolas Spitlight 1000 Nd:YAG laser with 480 mJ energy per pulse was introduced into the setup from downstream the cascade (see Figure 3d). As a consequence of the cambered blade passage, some areas were shadowed, and data evaluation was impeded. A calibration plate (see Figure 3e) with 2 mm dots arranged with 10 mm constant spacing was specifically tailored to the blade passage to calibrate the 2D2C-PIV images and compensate for the image distortions resulting from the non-ideal optical path through the endoscope. Two planes at $z = 65.5\,\mathrm{mm}$ ($z/H = 0.5$) and $z = 26.2\,\mathrm{mm}$ ($z/H = 0.2$) were investigated, and are named 'midspan' and 'near-wall' later in the text. The second—in this case, stereoscopic (or 2D3C) PIV setup, which delivers three velocity vector components—aims to resolve axial measurement plane 2 (MP 2) located 40% C_x downstream of the blade trailing edge (see Figure 4a). As depicted in Figure 4b, the setup featured two sCMOS cameras, and due to limited optical accessibility, the measurement plane had to be captured via two camera mirrors. The axial light sheet was formed at the bottom of the cascade and guided into the measurement as shown in Figure 4a,c. DEHS oil droplets with a mean diameter of 0.9 µm were used as seeding particles. This type of tracer particle ensures sufficient dynamic response to the flow at low static pressures, see Humble et al. [24] and Bitter et al. [25]. For each measurement, a set of 10,000 PIV images was processed by a 48-by-48 px cross-correlation with 50% overlap and a magnification factor of 1/10, leading to a resolution of 5 mm per velocity vector.

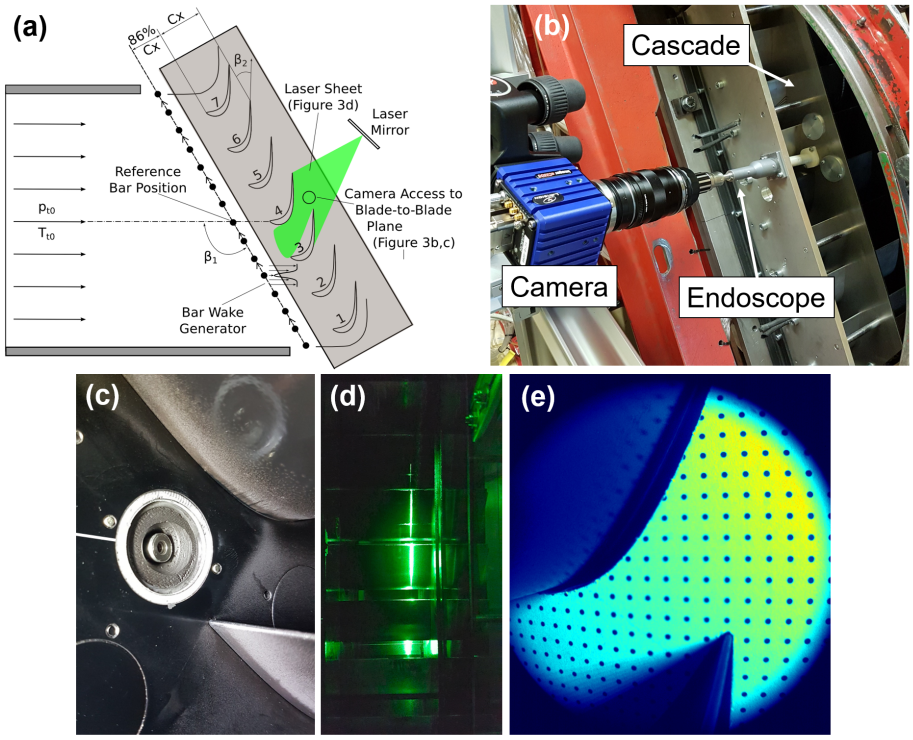

Figure 3. The 2D2C PIV setup for blade-to-blade measurements inside the T106A linear cascade; (**a**) schematic of the cross-sectional side view; (**b**) endoscopic camera setup; (**c**) optical access into the flow channel; (**d**) PIV laser sheet at $z/H = 0.2$; (**e**) camera calibration target in the field of view.

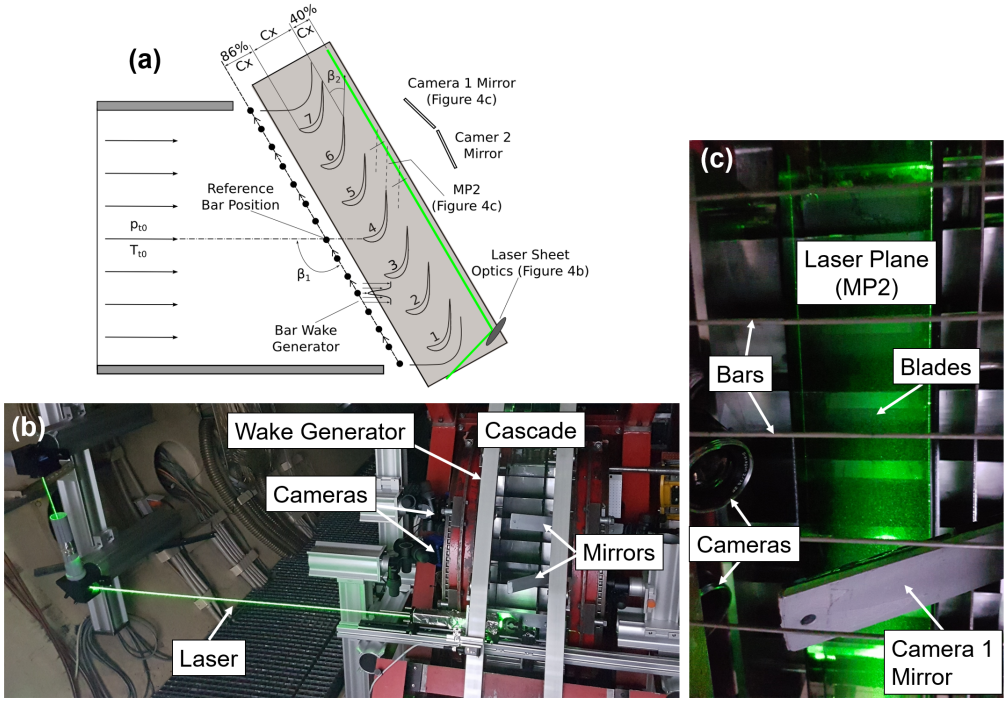

Figure 4. PIV setup for 2D3C measurements in an axial plane (MP 2) located 40% C_x downstream of the blade passage; (**a**) schematic of the cross-sectional side view; (**b**) camera setup and laser guidance to the test section; (**c**) laser sheet in the cascade exit flow.

A phase-averaging method according to Bitter and Niehuis [26] was performed in both PIV setups whereby all velocity fields were related to the bar reference position outlined

in Figure 5. The recording of both the camera trigger timing and the bar position signals at more than 1 MHz ensured precise sorting of all images and enabled a time-dependent discussion of the periodic wake effects in both PIV measurements, which were performed subsequently. The image sets were recorded at 15.1 Hz, while the dominant bar passing frequency was 502 Hz. The data had to be synchronized in post-processing by establishing a correlation between the geometric bar position y_b and the temporal bar period t_{BP}. The first step is to define a reference bar position. In the experimental setup, a bar was aligned with the leading edge of the measurement blade by placing a steel ruler on top and leveling it (see Figure 5a). This reference bar position was then identified by measuring the current pitchwise distance $\Delta y_{b,ref}$ to the next trigger point of an optical sensor, which registers each passing bar (see Figure 5b,c). Finally a timestamp τ was assigned for each measurement point by determining the relative time difference to the next bar trigger (see Figure 5d)

$$\frac{\tau}{t_{BP}} = \frac{t}{t_{BP}} - \frac{\Delta y_{b,ref}}{P_b}. \tag{1}$$

In addition to synchronization, the measured data were binned and subsequently averaged according to their position within the bar passing period τ/t_{BP}. As seen in Figure 5e, this method led to a statistically uniform distribution of measurement points per τ-bin. This sorting method can be adjusted on demand. The more bins that are chosen, the higher the temporal resolution of the bar wake passing through the passage but the lower the number of PIV images per bin for averaging the flow field. For the following discussions, 20 bins were chosen that included about 470 frames each. The synchronization process was also applied to the CFD data by determining the reference bar position and setting the correlating timestamp to zero (see Figure 5f).

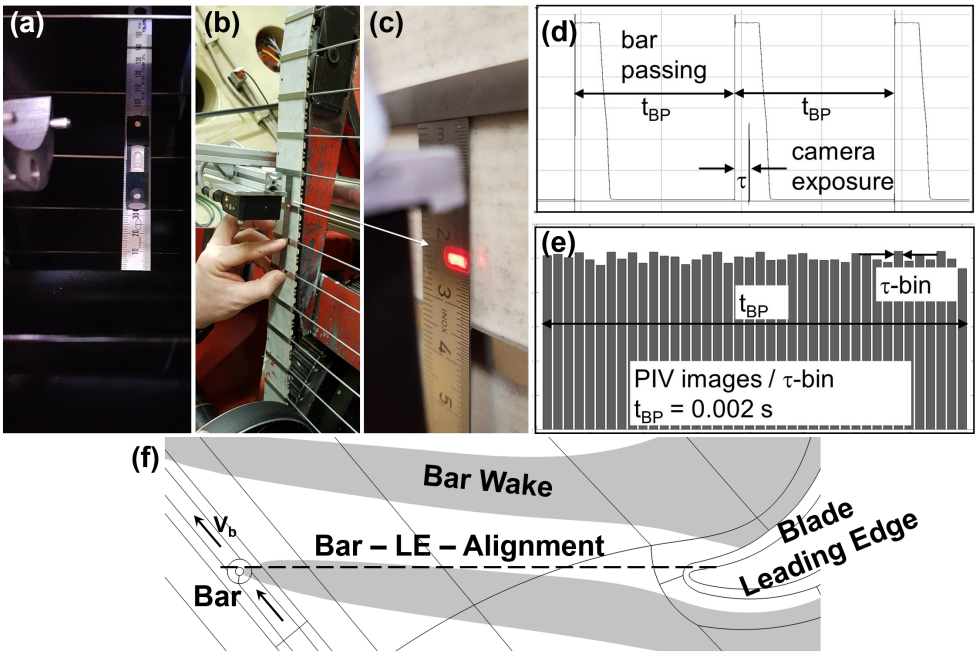

Figure 5. Phase-locking and synchronization method; (**a**–**c**) alignment of the spatial bar position with the temporal trigger signals of the bar counter; (**d**) assignment of a timestamp τ based on the relative position during a bar passing period; (**e**) binning and subsequent averaging in τ-bins of 0.1 ms; (**f**) application of the synchronization process to CFD by setting the reference bar position to $\tau = 0$.

3. Results

3.1. Time-Averaged Flow Fields

The mean Mach number distributions averaged over all 10,000 PIV vector fields are compared to five-hole-probe (FHP) measurements (performed in [8]) and to CFD in Figure 6. The upper row shows the axial exit flow fields under steady conditions (no bar wakes) and the lower row highlights the mean flow with incoming wakes. The results from both experimental techniques exhibit a good match in terms of flow topology and absolute values, which validates the presented PIV setup. Only at z/H = 0.2, where the pitchwise-averaged loss peak is located, are the interacting passage vortex (PV) and the counter-rotating vortex (CRV) slightly less distinct in the PIV measurements. The unsteady inflow conditions created by periodically incoming wakes lead to secondary flow attenuation, which is equally apparent in both data sets. The following discussion of the phase-locked PIV data in Section 3.2, including additional flow properties such as turbulent kinetic energy, will highlight the added benefit and the potential of the presented optical measurements as a supplement to the classic probe-based approach. The validated CFD setup [13] predicts a narrower but more intense blade wake and secondary flow in the downstream flow field. This is a well-documented characteristic of RANS-based flow simulations with eddy-viscosity modeling. However, the important value of overall integral losses (ζ_{FHP}= 4.7%, ζ_{CFD} = 4.6%) as well as the effect of periodically incoming wakes show a good match with the measurements.

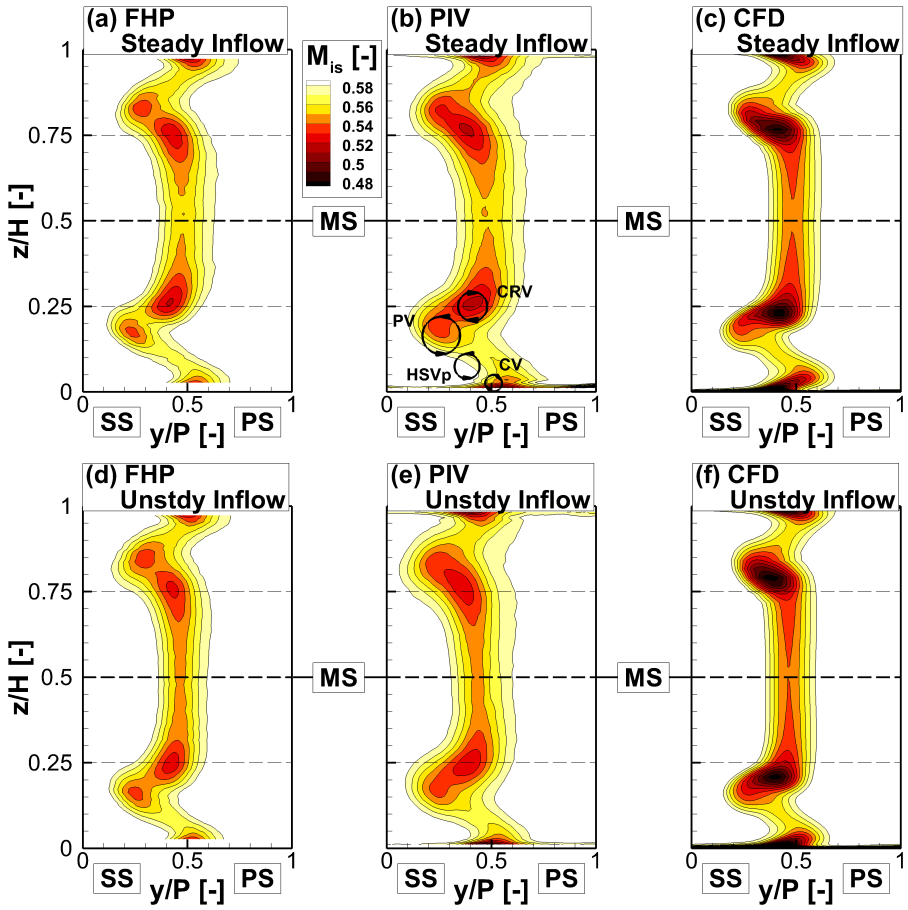

Figure 6. Time-averaged velocity distributions illustrated by isentropic Mach number in the downstream flow field (MP 2) under steady (**a**–**c**) and periodically unsteady inflow conditions (**d**–**f**).

In Figure 7, time-averaged blade-to-blade flow fields measured near the endwall at z/H = 0.2 are shown under steady and periodically unsteady inflow conditions. The velocity values in the left and center plots were ensemble-averaged over the entire image

series and normalized by the theoretic exit velocity of V_{2th} = 195.8 m/s at M_{2th} = 0.59. On the right, the time-averaged effect of the periodically incoming wakes is highlighted by the absolute velocity difference (blue—positive; red—negative). Throughout the passage flow field, the absolute velocity is slightly lower under periodically unsteady inflow conditions, resulting in a negative delta. The effect is strongest in the blade wake, leading to a higher time-averaged velocity deficit. The measured mean inlet velocity loss matches well with previous analytical calculations and CTA measurements by Schubert et al. [8], validating the PIV setup in the blade-to-blade plane. In a rotating turbine with multiple blade rows, the inlet losses close to the endwall will likely be even higher because the incoming wakes are superimposed with upstream secondary flows. In the white areas, especially close to the suction surface of the upper blade, data availability is limited due to the strong background illumination caused by direct laser reflections. Unfortunately, in this region, the secondary vortex system is partially formed and interacts with the blade profile flow, as seen in Figure 2. However, downstream of the trailing edge, a blue area is apparent on the suction side of the blade wake, which leads to the position on the passage vortex core in MP 2 (see *P*3 in Figure 7). This positive velocity delta illustrates a reduction in the velocity deficit due to vortex dissipation and thus implies attenuation of the secondary flow.

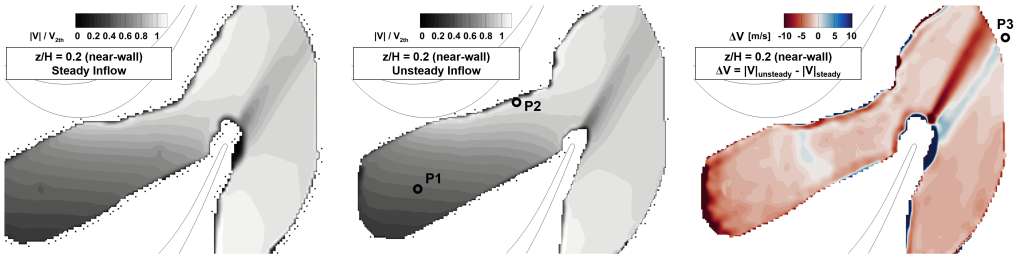

Figure 7. Time-averaged passage flow field at z/H = 0.2 (near-endwall) under steady (**left**) and periodically unsteady (**middle**) inflow conditions; (**right**) $\Delta|V|$ between the two cases of inflow conditions.

An alternative way to quantify the time-averaged secondary flow attenuation by the incoming wakes is by measuring the flow angle perturbation, as illustrated in Figure 8. The reference FHP measurements on the right side of Figure 8 illustrate the spanwise distribution of the pitchwise-averaged secondary outflow angle $\Delta\beta_{sec}$ in the axial plane MP 2 [8]. It is apparent that the vortex motion of the secondary flow, which is mainly driven by the dominant passage vortex, causes overturning in the nearest proximity of the endwall, followed by a region of underturning. Thus, the level of over-/underturning is a gauge of the secondary flow intensity. The 'near-wall' blade-to-blade plane of the PIV measurements was chosen to be located at the peak of the pitchwise-averaged underturning (z/H = 0.2). Since the secondary flow angle is calculated by subtracting the midspan flow field, the two visible passage flow fields in Figure 8 are reduced in size. This is a consequence of the 67° opening angle of the camera endoscope. It is apparent that the positive flow angle difference, i.e., underturning, starts slightly downstream of the midpoint of the passage ($x/C_x \approx 0.6$) as a reaction to the strong transverse pressure gradients, which force the initial overturning in the endwall boundary layer. Under periodically unsteady inflow conditions, the level of underturning is reduced inside the passage and in the downstream flow field. The PIV data indicate the same quantifiable trend as the probe measurements but in a much larger and less accessible measurement field. In addition to the secondary losses associated with the dissipation of the vortices, aerodynamic performance suffers from high over-/underturning since the downstream blade rows experience severe off-design conditions. Hence, endwall flow effects such as over-/underturning must be considered in the design of a turbomachinery stage.

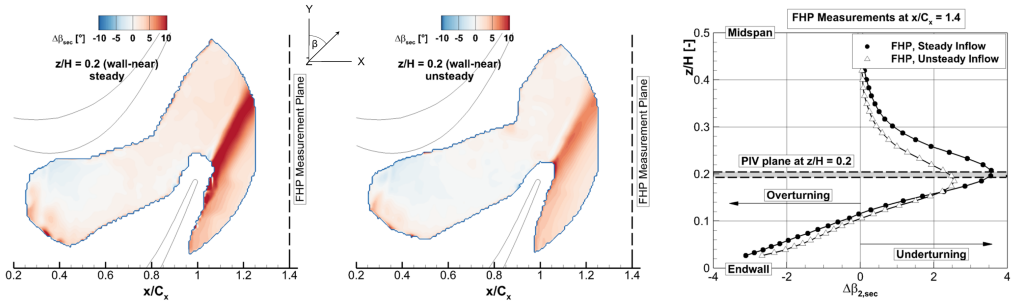

Figure 8. Time-averaged flow angle difference with respect to midspan at $z/H = 0.2$ ($\Delta\beta_{sec} = \beta - \bar{\beta}_{MS}$) under steady (**left**) and periodically unsteady (**middle**) inflow conditions; (**right**) $\Delta\beta_{sec}$ measured with a five-hole-probe at $x/C_x = 1.4$ downstream of the cascade.

3.2. Phase-Locked Flow Fields

Figure 9 shows the temporal behavior of the passage flow field near the endwall ($z/H = 0.2$) at four time steps τ of one bar passing period t_{BP}. The normalized absolute velocity fluctuation is given by $|V|'/V_{2th} = (|\bar{V}|(\tau) - \langle|V|\rangle)/V_{2th}$, where $|\bar{V}|(\tau)$ is the mean absolute velocity of a τ-bin, $\langle|V|\rangle$ is the ensemble average over the entire time series, and V_{2th} is the theoretical turbine exit velocity. The data were averaged for 20 time steps per period, resulting in around 470 PIV images per τ-bin. The flow field exhibits alternating positive and negative velocity fluctuations with an amplitude of about 3.5% in the front part of the passage. The relative velocity deficit of the wake is indicated by blue color. The streamline deformation of the wake passing through the passage is evident. The biggest contributors to the stretching and bowing are the strong acceleration near the pressure surface and the transverse pressure gradients towards the suction surface. Aided by the relatively low flow coefficient of the present periodic inflow, the wakes are almost parallel to the blade profile at around the passage throat. As the freestream mixing of the bar wakes accumulates in the flow direction, the measured wakes become less distinct, and the levels of velocity fluctuations continually decrease. For data synchronization, $\tau/t_{BP} = 0$ was defined by one random bar being located upstream in the design inflow direction of the reference blade leading edge. Based on the inflow velocity triangles of the moving bars, the wake reaches the leading edge of the blade slightly later in time. The corresponding phase lag between the bar position and the wake entry into the passage was calculated to be about $-45°$. Also, indicated in Figure 9 by arrowheads is every eighth velocity vector. This illustrates the relative flow direction and highlights the 'negative-jet-effect' of the bar wakes. This effect, which is indicated by blue color and reverse arrowheads (lower right to upper left), is a typical phenomenon in multistage turbomachinery as a consequence of the rotor–stator interaction. It was comprehensively studied by Hodson et al. [27]. In the present case, the flow vectors clearly show an alternating relative flow angle β'. The negative jet imposes relative fluid transport towards the suction surface. Where the negative jet impinges on the blade suction surface, it is periodically inducing a local positive pressure gradient on the boundary layer, which is prone to flow separation, especially downstream of the passage throat due to high loading and decelerating flow. In addition to the mean velocity deficit, the cylindrical bar wakes produce a turbulence intensity increase of around 20% in their cores [26]. Further downstream, these levels are mixed with the main flow inlet turbulence intensity of about 6.8%. The resulting periodic increase in turbulence triggers an earlier suction surface boundary layer transition (wake-induced transition), which increases the robustness against flow separation. The overall effect of the negative jet on the blade suction surface flow will be discussed in more detail in the second part of this two-part publication using high-speed pressure-sensitive paint measurements.

A comparison of the velocity fluctuations and the passage flow angles between the experiments and the numerical simulations is performed in Figure 10. The data for the time plot were extracted at location $P1$ ($x/C_x = 0.3$), which is marked in Figure 7. Good correlation for both phase and amplitude between experiments and CFD is evident. The

lower peak amplitudes of around 3%-points for the measured data is partially due to the fact that the CFD data are exported at a higher number of 80 time steps per period, while the measured fluctuations are phase averaged in 20 τ-bins.

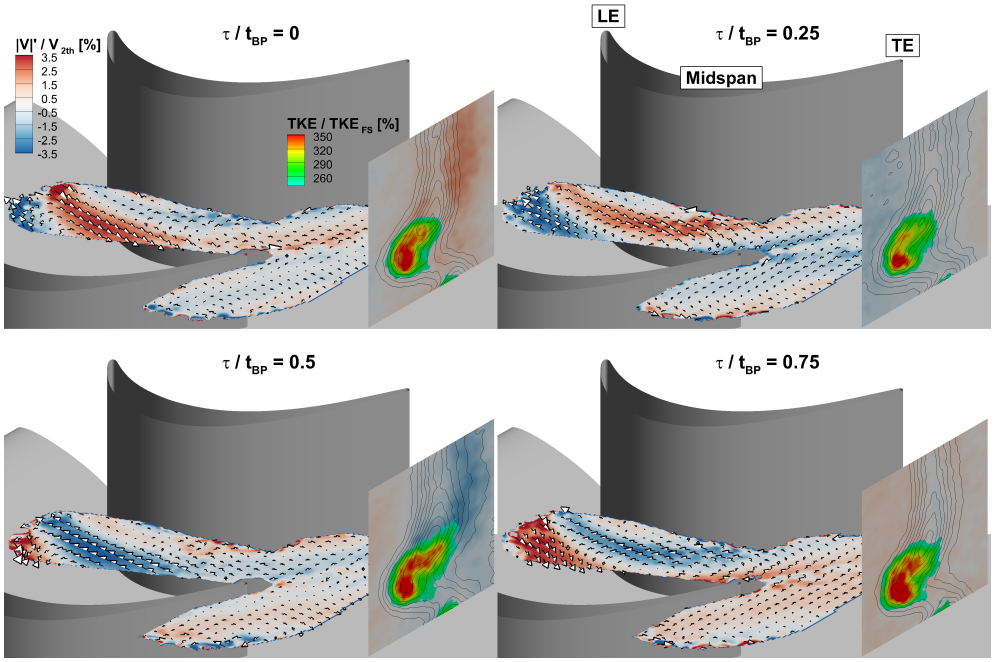

Figure 9. Transport of the bar wake velocity deficit through the T106A turbine passage close to the endwall (z/H = 0.2) at four time steps and its effect on the downstream flow field.

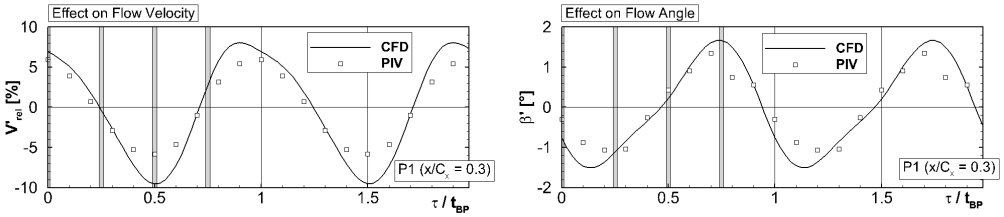

Figure 10. Evolution of the bar wake effect on the near-endwall (z/H = 0.2) passage flow field at position $P1$ (see Figure 10) over time; comparison of velocity deficit and the flow angle between CFD and phase-locked PIV (gray positions in the time plot mark the displays in Figure 9).

Next to the PIV blade-to-blade plane, Figure 9 also includes the PIV measurements in the downstream flow field. The transport of the bar wakes is clearly traceable all throughout the blade passage into the downstream axial plane (MP 2), which illustrates the quality of the two isolated measurements and the applied synchronization method. The additional black velocity contour lines and turbulent kinetic energy enables the relation between the sequence of the moving bar wakes and their effects on the downstream flow field. There are two major indicators by which these effects were evaluated: the pitchwise extension of the secondary flow field and the intensity of the vortex interaction. As the bar wake travels from left to right through the axial plane, it overlaps with the secondary flow field on the suction side of the blade. During this process, the extension of the secondary flow field remains relatively stable. However, the width of the blade wake is significantly increased, especially on the pressure side of the blade (τ/t_{BP} = 0.25 and 0.5). On the other hand, when the bar wake is out of the frame in MP 2, the blade wake is significantly narrower (τ/t_{BP} = 0 and 0.75). In order to better quantify these effects, the flow velocity iso-line value of $|V|/V_{2th}$ = 95% was defined as the boundary of the secondary flow field and the blade wake. Its position was then measured on the suction side and pressure side in each time step. The resulting periodic shift at z/H = 0.2 relative to the time-averaged position

is shown in Figure 11a. The suction-side boundary is an indicator of the secondary flow extension, while the pressure-side boundary reflects the blade wake. Both assumptions are validated by confirming that the periodic sequences are in phase to key reference signals (see below). In all cases, positive values represent widening and negative values represent narrowing. The maximum blade wake extension is around three times higher than the maximum secondary flow extension. However, the most important finding here is not related to amplitudes but rather a phase lag of $-108°$, i.e., $\Delta\tau/t_{BP} = -0.3$ between the secondary flow extension and the blade wake extension. This phase lag is unique to the secondary flow and different from the behavior at midspan. Here, the start of the widening of the downstream blade wake corresponds to the overlap with the bar wake. As the bar wake passes through the axial plane, the suction- and pressure-side blade wake boundaries at midspan are affected simultaneously, i.e., $0°$ phase lag (see Figure 11b). This results in an increase in the wake width of up to 165%. All three midspan sequences are virtually in-phase ($18°$ phase lag) with the pressure-side extension at $z/H = 0.2$, proving it to be representative of the blade wake.

The secondary vortex intensity, as the second evaluation indicator, is measured by turbulent kinetic energy relative to the mean freestream TKE. It is apparent in Figure 9 that the TKE level increases as the bar wake passes through the secondary flow region ($\tau/t_{BP} = 0.25$ and 0.5). However, it continues to increase beyond the passing of the pressure side ($\tau/t_{BP} = 0.75$). Hence, the TKE evolution in the secondary flow region is not synchronized with the overlap of the bar wake in MP 2. In fact, the periodic change of averaged local TKE in Figure 11a exhibits the same phase lag of $-108°$ to the bar wake passing as the secondary flow extension. However, for the secondary flow intensity, it is the low levels of TKE that are associated with the bar wake effects. Therefore, both signals are in sync even though they appear to have a $180°$ lag. This means the lowest intensity correlates to the highest pitchwise extension, or in other words, at that moment, the secondary vortices are less distinct due to a higher degree of mixing.

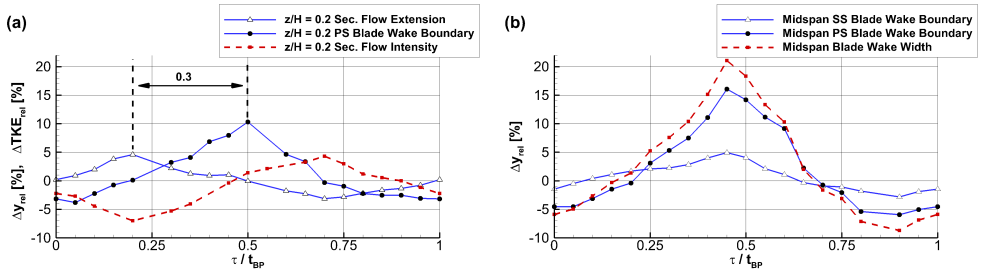

Figure 11. Periodic effect of the bar wakes on the downstream flow field (MP 2); (**a**) secondary flow extension $\Delta y_{rel} = (y - \langle y \rangle)/P$ and intensity $\Delta TKE_{rel} = (TKE - \langle TKE \rangle)/\langle TKE \rangle$ at $z/H = 0.2$; (**b**) blade wake extension Δy_{rel} at midspan.

Overall, these findings indicate that the fully developed secondary flow downstream of the blade passage is highly resistant to a direct perturbation due to overlapping with the bar wakes. Instead, the observed periodic changes in secondary flow extension and intensity is caused further upstream. Starting from the passage vortex core position in MP 2 (see *P*3 in Figure 7), the mean origin of these effects can be calculated based on the identified phase lag of ($\Delta\tau/t_{BP} = -0.3$ i.e., -0.6 ms) and the measured blade-to-blade velocity field. It is located inside the blade passage at $x/C_x = 0.72$ (see *P*2 in Figure 7). Around this location, endwall boundary layer fluid that has been driven towards the suction surface is about to be detached, rolled up, and fed into the passage vortex. The perturbation of this process by wake interaction and the consequent secondary flow attenuation was previously investigated using numerical simulations of the present test case in [13].

4. Conclusions

An experimental campaign was conducted using a T106A linear turbine cascade with an additional part-span endwall under challenging measurement conditions with periodically incoming wakes with a frequency of 500 Hz. In previous investigations, the authors utilized a combination of probe-based measurements and CFD to identify attenuation of the downstream secondary flow caused by wake interaction inside the blade passage. The primary goal of the experiments presented here was to validate, complement, and specify these findings. This was achieved by implementing and synchronizing two isolated phase-locked PIV measurement setups in a blade-to-blade plane close to the endwall and an axial plane downstream of the passage. Classic downstream five-hole-probe flow angle measurements were extended by combining PIV distributions at midspan and close to the endwall to quantify the change in over-/underturning caused by the wakes throughout the passage. Wake stretching and bowing could be traced throughout the blade passage and beyond. In this context, the 'negative-jet-effect' could clearly be illustrated, and supporting CFD showed a good match in phase and amplitude. In the downstream flow field, the bar wakes periodically increased the width of the blade wake by up to 165%. The fully developed secondary flow, on the other hand, was highly resistant to a direct perturbation by overlapping bar wakes. The periodic increase in secondary flow extension and in-phase decrease in turbulent kinetic energy exhibited a phase lag of $-108°$, i.e., $\Delta\tau/t_{BP} = -0.3$ to the bar wake overlap. It was concluded that the secondary flow attenuation is caused further upstream by wake interaction with the endwall boundary layer and, hence, the vortex formation. By combining the identified phase lag and the measured blade-to-blade velocity field, the mean origin of this effect was located inside the blade passage at around $x/C_x = 0.72$. Overall, it has been demonstrated that, particularly for secondary flow investigations under periodic inflow conditions, optical measurements such as phase-locked PIV provide a valuable addition to classic probe-based measurement approaches.

The results presented here are an essential basis for the subsequent investigation of the near-endwall blade suction surface effects in the second part of this two-part publication. A preview of the comprehensive experimental data set comprising periodically unsteady suction surface pressure fields is given in Figure 12. The surface data were measured with unsteady pressure-sensitive paint (i-PSP). The i-PSP measurements were performed using the intensity method, high-power uv-LED excitation, and a high-speed camera sampled at 30 kHz. Single- to double-digit Pascal pressure amplitudes could be resolved precisely and correlate well with CFD. Furthermore, two frequency filtering methods were compared to identify distinct flow features in the frequency spectrum up to several kilohertz.

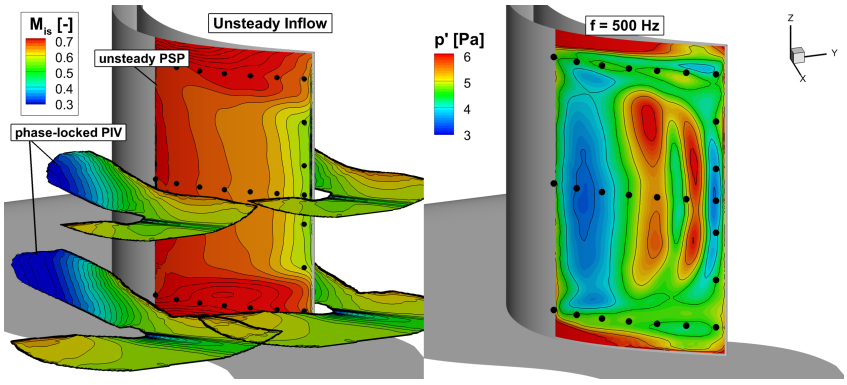

Figure 12. Illustration of the experimental data set available for the T106A test case under unsteady inflow conditions; (**left**) duplicated PIV passage flow fields presented in this paper and time-averaged isentropic surface Mach number on the blade suction surface measured with unsteady pressure-sensitive paint; (**right**) high-resolution surface pressure amplitude measurement (PSP) stimulated by the dominant wake generator frequency around 500 Hz. Black dots show markers for image mapping.

Author Contributions: Conceptualization, T.S. and M.B.; Methodology, T.S. and M.B.; Software, T.S.; Validation, T.S.; Formal analysis, T.S.; Investigation, T.S.; Resources, D.K.; Data curation, T.S.; Writing—original draft, T.S.; Writing—review & editing, T.S. and M.B.; Visualization, T.S.; Supervision, D.K. and M.B.; Project administration, T.S. and M.B.; Funding acquisition, T.S. and M.B. All authors have read and agreed to the published version of the manuscript.

Funding: The numerical design as well as the experimental investigations presented in this paper were performed in the framework of the joint project PAK 948 'Flow near the endwall of turbomachinery blading' funded by Deutsche Forschungsgemeinschaft under funding code Ma 4922/8-1.

Data Availability Statement: The raw data supporting the conclusions of this article will be made available by the authors on request.

Conflicts of Interest: The authors declare no conflicts of interest.

Nomenclature

Latin symbols	
C	chord length
H	channel height, i.e., blade span
H_{12}	boundary layer shape factor
M	Mach number
p	pressure
P	pitch
Re	Reynolds number
$\dot{S}_v^*$	non-dimensional entropy generation rate per unit volume, $\dot{S}_v \times (C \times T_{2,th})/(\rho_{2,th} \times V_{2,th})$
Sr	Strouhal number, $(V_b/P_b) \times (C/V_{x1})$
T	temperature
Tu	turbulence intensity
t	time
V	velocity
V'	velocity fluctuation
$\|V\|$	absolute velocity
$\langle V \rangle$	ensemble averaged velocity
x, y, z	axial, pitchwise, and spanwise coordinates
Greek symbols	
β	flow pitch angle
δ_{99}	boundary layer thickness
ϕ	flow coefficient, V_{x1}/V_b
τ	synchronized timestamp
ζ	total pressure loss coefficient
Abbreviations	
CV	corner vortex
CRV	counter-rotating vortex
DEHS	Di-Ethyl-Hexyl-Sebacat
EW	endwall
FHP	five-hole-probe
FS	freestream
HSVp	horseshoe vortex pressure side leg
i-PSP	unsteady pressure-sensitive paint
Laser	light amplification by stimulated emission of radiation
MP 2	measurement plane 2, 40% C_x downstream TE
MS	midspan
PV	passage vortex
sCMOS	scientific complementary metal–oxide–semiconductor
Subscripts	
1	inflow condition
2	downstream measurement plane

b	bar
BP	bar passing
t	stagnation quantity
sec	secondary

References

1. Cui, J.; Tucker, P.G. Numerical Study of Purge and Secondary Flows in a Low Pressure Turbine. In Proceedings of the ASME Turbo Expo 2016: Turbomachinery Technical Conference and Exposition, Seoul, Republic of Korea, 13–17 June 2016; ASME GT2016-56789.
2. Coull, J.D. Enwall Loss in Turbine Cascades. *J. Turbomach.* **2017**, *139*, 081004. [CrossRef]
3. Denton, J.; Pullan, G. A Numerical Investigation into the Sources of Endwall Loss in Axial Flow Turbines. In Proceedings of the ASME Turbo Expo 2012: Turbine Technical Conference and Exposition, Copenhagen, Denmark, 11–15 June 2012; ASME GT2012-69173.
4. Bear, P.; Wolff, M.; Gross, A.; Marks, C.R.; Sondergaard, R. Experimental Investigation of Total Pressure Loss Development in a Highly Loaded Low-Pressure Turbine Cascade. *J. Turbomach.* **2018**, *140*, 031003. [CrossRef]
5. Ciorciari, R.; Kirik, I.; Niehuis, R. Effects of Unsteady Wakes on Secondary Flows in the Linear T106 Turbine Cascade. *J. Turbomach.* **2014**, *136*, 091010. [CrossRef]
6. Ciorciari, R.; Schubert, T.; Niehuis, R. Numerical Investigation of Secondary Flow and Loss Development in a Low Pressure Tubrine Cascade with Divergent Endwalls. *Int. J. Turbomach. Propuls. Power* **2018**, *3*, 5. [CrossRef]
7. Volino, R. Effects on Endwall Boundary Layer Thickness and Blade Tip Geometry on Flow through High Pressure Turbine Passages. In Proceedings of the ASME Turbo Expo 2014: Turbine Technical Conference and Exposition, Düsseldorf, Germany, 16–20 June 2014; ASME GT2014-27013.
8. Schubert, T.; Chemnitz, S.; Niehuis, R. The Effects of Inlet Boundary Layer Condition and Periodically Incoming Wakes on Secondary Flow in a Low Pressure Turbine Cascade. *J. Turbomach.* **2021**, *143*: 041001. [CrossRef]
9. Sinkwitz, M.; Winhart, B.; Engelmann, D.; di Mare, F. Time-Resolved Measurements of the Unsteady Boundary Layer in an Annular Low-Pressure Turbine Configuration With Perturbed Inlet. *J. Turbomach.* **2021**, *144*, 011001. [CrossRef]
10. Lopes, G.; Simonassi, L.; Lavagnoli, S. Impact of Unsteady Wakes on the Secondary Flows of a High-Speed Low-Pressure Turbine Cascade. *Int. J. Turbomach. Propuls. Power* **2023**, *8*, 36. [CrossRef]
11. Chemnitz, S.; Niehuis, R. A Comparison of Turbulence Levels from Particle Image Velocimetry and Constant Temperature Anemometry Downstream of a Low-Pressure Turbine Cascade at High-Speed Flow Conditions. *J. Turbomach.* **2020**, *142*, 071008. [CrossRef]
12. Engelmann, D.; Sinkwitz, M.; di Mare, F.; Koppe, B.; Mailach, R.; Ventosa-Molina, J.; Fröhlich, J.; Schubert, T.; Niehuis, R. Near-Wall Flow in Turbomachinery Cascades—Results of a German Collaborative Project. *J. Turbomach. Propuls. Power* **2021**, *6*, 9.
13. Schubert, T.; Niehuis, R. Numerical Investigation of Loss Development in a Low-Pressure Turbine Cascade with Unsteady Inflow and Varying Inlet Endwall Boundary Layer. In Proceedings of the ASME Turbo Expo 2021: Turbomachinery Technical Conference and Exposition, Virtual, 7–11 June 2021; ASME GT2021-59696.
14. Kampitsch, M.; Stadtmüller, P.; Fottner, L. Investigations of Wake-Induced Transition on the LPT Cascades T106A-EIZ and T106D-EIZ. In Proceedings of the ERCOFTAC Workshop, La Clusaz, France, 19–23 March 2000.
15. Kirik, I.; Niehuis, R. Comparing the Effect of Unsteady Wakes on Parallel and Divergent Endwalls in a LP Turbine Cascade. In Proceedings of the 11th International Gas Turbine Congress, Tokyo, Japan, 15–20 November 2015; IGTC2015-137.
16. Michelassi, V.; Chen, L.; Pichler, R.; Sandberg, R.D. Compressible Direct Numerical Simulation of Low-Pressure Turbines—Part II: Effect of Inflow Disturbances. *J. Turbomach.* **2015**, *137*, 071005. [CrossRef]
17. Wilcox, D.C. *Turbulence Modeling for CFD*, 4th ed.; DCW Industries: La Canada, CA, USA, 2004.
18. Langtry, R.B.; Menter, F.R. Transition Modeling for General CFD Applications in Aeronautics. In Proceedings of the 43rd AIAA Aerospace Sciences Meeting and Exhibit, Reno, NV, USA, 10–13 January 2005; AIAA Paper 2005-522.
19. Sieverding, C. Recent Progress in the Understanding of Basic Aspects of Secondary Flows in Turbine Blade Passages; *ASME J. Eng. Gas Turbines Power.* **1985**, *107*, 248–257. [CrossRef]
20. Schubert, T.; Kožulović, D.; Bitter, M. Characterization of the Endwall Flow in a Low-Pressure Turbine Cascade Perturbed by Periodically Incoming Wakes. Part 2: Unsteady Blade Surface Measurements Using Pressure-Sensitive Paint. *Aerospace* **2024**, *11*, 404. [CrossRef]
21. Niehuis, R.; Bitter, M. The High-Speed Cascade Wind Tunnel at the Bundeswehr University Munich after a Major Revision and Upgrade. *Int. J. Turbomach. Propuls. Power* **2021**, *6*, 41. [CrossRef]
22. Börner, M.; Bitter, M.; Niehuis, R. On the Challenge of Five-Hole-Probe Measurements at High Subsonic Mach Numbers in the Wake of Transonic Turbine Cascades. *J. Global Power Propuls. Soc.* **2018**, *2*: 453–464. [CrossRef]
23. Acton, P.; Fottner, L. The Generation of Instationary Flow Conditions in the High-Speed Cascade Wind Tunnel of the German Armed Forces University Munich. In Proceedings of the 13th Symposium on Measuring Techniques, Zurich, Switzerland, 5–6 September 1996.

24. Humble, R.; Scarano, F.; Oudheusden, B.; Tuinstra, M. PIV Measurements of a Shock Wave/Turbulent Boundary Layer Interaction. In Proceedings of the 13th International Symposium on Applications of Laser Techniques to Fluid Mechanics, Lisbon, Portugal, 26–29 June 2006.
25. Bitter, M.; Kurz, J.; Kähler, C.; Niehuis, R. Investigations of a low-pressure turbine blade by means of simultaneous optical velocity and pressure measurements. In Proceedings of the 18th International Symposium on Applications of Laser Techniques to Fluid Mechanics, Lisbon, Portugal, 4–7 July 2016.
26. Bitter, M.; Niehuis, R. Effects of Periodic Inflow Turbulence on the Statistics in the Wake of a Linear LPT Cascade at Jet-Engine relevant Test Conditions. In Proceedings of the 13th International Symposium on Particle Image Velocimetry, Munich, Germany, 22–24 July 2019.
27. Hodson, H.P.; Hynes, T.P.; Greitzer, E.M.; Tan, C.S. A Physical Interpretation of Stagnation Pressure and Enthalpy Changes in Unsteady Flow. *J. Turbomach.* **2012**, *134*, 060902. [CrossRef]

4.6 Publication 5

4.6.1 Summary

The second part of the two-part publication on optical secondary flow measurements was motivated by the loss analysis in Publication 3. There, the interaction of the secondary flow with the suction surface was identified as a major source of loss. The following aspects were covered with the objective to relate the dynamics of the passing wakes identified in part 1 (Publication 4) to their effects on the surface flow topology.

1. A measurement setup utilizing Unsteady Pressure-Sensitive Paint (i-PSP) was implemented to capture highly resolved and phase-locked pressure fields on the blade suction surface. Under challenging conditions, a sampling rate of 30 kHz was achieved while ensuring high data quality. The in-situ-calibrated PSP exhibited a coefficient of determination (R2 value) of 98.3 % and RMS pressure deviations of 0.39 % to the reference pressure tap data. To the author's knowledge, this marked the first published application of PSP specifically for secondary flow investigations in a turbine cascade. Instead of being limited to selective points as usual in a probe-based approach, the measurements covered the entire blade span all the way to the endwall and from 64 % axial chord to the trailing edge. In the 2D flow region of the highly loaded rear suction surface, the dominant pressure fluctuations were associated to the reattachment of the separation bubble rather than the bubble itself. Closer to the endwall, the imprints of the horseshoe vortex pressure side leg and the passage vortex were identified by a combination of bent iso-lines indicating lower static pressure and elevated pressure fluctuations. The counter-rotating vortex was located just above the corresponding passage vortex separation line. It correlated with a thin band of low pressure fluctuations and was confirmed by supplemental CFD shear stress data. Under periodically unsteady inflow conditions, the time-averaged secondary flow attenuation and thus less pronounced vortex imprints on the blade surface were illustrated by reduced iso-line curvature and a shift towards the endwall i.e. reduced passage vortex liftoff.

2. In order to isolate the amplitudes of the wake-induced fluctuations, two methods of frequency based data filtering were compared. The first method was based on a data conversion into the Fourier space. In the second method, a spectral proper orthogonal decomposition (SPOD) was applied and averaged over 100 time steps. A common challenge in the analysis of time-resolved data is to correctly associate unknown amplitude peaks in the frequency spectrum to their flow phenomena of origin. By the example of the separation bubble oscillation at 678 Hz, it was demonstrated how SPOD-based frequency-filtering can be utilized to accomplish this task by visualizing the fluctuation patterns associated to the specific frequency range.

3. By combining the phase-locked and synchronized PIV and PSP measurements, the movement and negative-jet-effect of the bar wakes across the suction surface could be traced. The periodic pressure signals revealed a wake induced negative pressure gradient in space i.e. positive gradient in time of 98 Pa/ms. This effect which is also a function of wake orientation and thus flow coefficient, was intensified in the secondary

flow region with respect to midspan with a local maximum of plus 33 % near the passage vortex imprint. More detail on this finding is provided in the supplemental data in Section 4.6.3.

Overall, the findings in Publication 4 & 5 have demonstrated that phase-locked optical measurements such as PIV and i-PSP provide remarkable value to secondary flow investigations under periodic inflow conditions and thus justify the considerable implementation effort.

4.6.2 Postprint

aerospace

MDPI

Article

Characterization of the Endwall Flow in a Low-Pressure Turbine Cascade Perturbed by Periodically Incoming Wakes, Part 2: Unsteady Blade Surface Measurements Using Pressure-Sensitive Paint

Tobias Schubert, Dragan Kožulović and Martin Bitter *

Institute of Jet Propulsion, University of the Bundeswehr Munich, Werner-Heisenberg-Weg 39, 85577 Neubiberg, Germany
* Correspondence: martin.bitter@unibw.de

Abstract: Unsteady pressure-sensitive paint (i-PSP) measurements were performed at a sampling rate of 30 kHz to investigate the near-endwall blade suction surface flow inside a low-pressure turbine cascade operating at engine-relevant high-speed and low-Re conditions. The investigation focuses on the interaction of periodically incoming bar wakes at 500 Hz with the secondary flow and the blade suction surface. The results build on extensive PIV measurements presented in the first part of this two-part publication, which captured the 'negative-jet-effect' of the wakes throughout the blade passage. The surface pressure distributions are combined with CFD to analyze the flow topology, such as the passage vortex separation line. By analyzing data from phase-locked PIV and PSP measurements, a wake-induced moving pressure gradient negative in space and positive in time is found, which is intensified in the secondary flow region by 33% with respect to midspan. Furthermore, two methods of frequency-filtering based on FFT and SPOD are compared and utilized to associate a pressure fluctuation peak around 678 Hz with separation bubble oscillation.

Keywords: pressure-sensitive paint; surface flow measurement; turbine cascade; unsteady flow

Citation: Schubert, T.; Kožulović, D.; Bitter, M. Characterization of the Endwall Flow in a Low-Pressure Turbine Cascade Perturbed by Periodically Incoming Wakes, Part 2: Unsteady Blade Surface Measurements Using Pressure-Sensitive Paint. *Aerospace* **2024**, *11*, 404. https://doi.org/10.3390/aerospace11050404

Academic Editor: Lin Chen

Received: 14 March 2024
Revised: 6 May 2024
Accepted: 7 May 2024
Published: 16 May 2024

1. Introduction

The establishment of high-lift blade designs in modern jet engines and the ongoing trend to reduce weight by lowering the solidity in low-pressure turbine (LPT) vanes has triggered a lot of research on endwall flow in recent years. The main motivation is the significant contribution to overall losses due to high pressure gradients in the blade passage and thus intensified endwall flow. In the case of low-aspect-ratio LPT blades, for which a larger range of the blade span is affected, the endwall losses are approximated to account for one third of the overall losses, see [1]. Based on a numerical parametric design study in LPT cascades, Coull [2] found that endwall losses can be decomposed into two major components: dissipation in the endwall boundary layer and induced losses by secondary flows, which scale with streamwise vorticity. According to Denton and Pullan [3], the secondary flow itself exhibits several sources of loss, such as flow interactions inside the blade passage and downstream mixing losses. Particularly, the interaction of the passage vortex and the blade suction surface, resulting in the counter rotating vortex, was found to have a strong contribution to the overall losses by Cui and Tucker [1] as well as Bear et al. [4]. The endwall flow development is also largely dependent on the inflow conditions. The effects of periodically incoming wakes were investigated in the T106A and T106Div turbine cascades using measurements and numerical simulations (CFD) by Ciorciari et al. [5,6]. Both approaches have shown an attenuation of the secondary flow. In contrast to the relatively small effects of incoming wakes, Volino et al. [7] found the influence of the inlet boundary layer to be much larger. Schubert and Niehuis [8] came to a similar conclusion when evaluating the turbine cascade exit flow; however, they found that

the endwall flow development inside the blade passage is significantly affected by both factors, but in different manners. The vast majority of research dealing with secondary flow investigations has been centered around probe-based measurements: mostly up- and downstream of the blade passage. More recently, some published works have diverged from this classic approach by incorporating more modern experimental methods. For example, Sinkwitz et al. [9] and Lopez et al. [10] utilized hot-film sensor arrays on the near-endwall suction surface, and Chemnitz and Niehuis [11] analyzed the potential of particle image velocimetry (PIV) in comparison to five-hole-probe (FHP) and constant temperature anemometry (CTA) measurements in turbine cascade exit flow.

Despite the vast research activity in recent years, the accurate prediction and reduction of endwall loss is expected to remain a challenge for many years to come [3]. Aimed at providing a further step in the continued understanding of endwall flow and its determining factors, an extensive research program funded by the Deutsche Forschungsgemeinschaft (DFG) was launched in 2018 by four German university institutes, see Engelmann et al. [12]. Within this conglomerate, the Institute of Jet Propulsion of the University of the Bundeswehr Munich covered low-pressure turbine aspects at high-speed flow conditions. This paper is based on the design work and first experimental and CFD results by Schubert et al. [8,13]. They used a particular turbine cascade design to investigate the effects of boundary layer conditions and periodically incoming wakes on the secondary flows and losses. The subsequent goal was to validate, complement, and specify the previous findings by conducting state-of-the-art optical measurements inside the blade passage, which poses a far greater challenge in terms of experimental setup. Thereby, the present work will demonstrate how the classic approach to secondary flow investigations can be extended and enhanced to form a more comprehensive picture. While the discussion of phase-locked PIV results was the focus of the first part [14] of this two-part publication, the second part will present unsteady pressure-sensitive paint (i-PSP) measurements on the blade suction surface.

In view of the high potential of the pressure-sensitive paint technique (PSP) demonstrated in the classical fields of experimental aerodynamics, its published application in turbomachinery research is rather low, compare, e.g., Liu et al. [15] or Lepicovsky and Bencic [16]. The standard works of Liu et al. [17] or Gregory et al. [18] reveal a large number of PSP applications covering nearly all branches of aerodynamics. The quality of the PSP results is impacted by various external factors, such as surface contamination, non-uniform surface temperatures, or limited optical access. This sensitivity often prevents the quantitative usage of the PSP technique in the area of rotating turbomachinery beyond simplified lab tests, as underlined, e.g., by Peng and Liu [19]. Nevertheless, Gao et al. [20] described the big potential of the turbomachinery research linked to (linear) blade cascades for the application and development of the PSP technique. As, e.g., Marks et al. [21], Gao et al. [22], and Dong et al. [23] have shown in steady inflow test cases, the knowledge of (unsteady) surface pressure enables a better understanding of complex aerodynamics like they may appear in a linear cascade, especially if the vortex interaction in the secondary flow regime is in focus. The author's motivation in choosing unsteady PSP to further resolve the surface dynamics of the wakes was raised by the experience of applying this experimental technique to answer turbomachinery-related research questions, compare Bitter et al. [24–26].

2. Methods

2.1. Test Case

The presented experiments were conducted using a linear cascade of the T106A low-pressure turbine profile. The key geometric and flow parameters are summarized in Table 1. The T106 cascade has a long research history, and the aerodynamic performance of the original design is well known under various operating conditions, see, e.g., Kampitsch et al. [27], Kirik and Niehuis [28], or Michelassi et al. [29]. However, the cascade used here is a redesign that was specifically developed for endwall flow measurements under

periodic inflow and high-speed conditions ($M_{2th} = 0.59$, $Re_{2th} = 2 \times 10^5$). The blade profile geometry remains unchanged, though. The main features of the current cascade are a sufficiently thick endwall boundary layer and the ability to perform variations in the boundary layer conditions on this endwall. The challenge regarding the endwall boundary layer stems from a gap between the wind tunnel and the cascade endwalls upstream of the blade passages. This gap, which is needed for the moving bar wake generator, enables a leakage flow driven by a negative pressure gradient. While the freestream flow is not affected, it can act as a boundary layer suction, leading to weak secondary flow. To counteract this problem, the current cascade features an integrated split flat plate at part-span that serves as a turbine endwall (marked in yellow in Figure 1). Using a modular composition of the aft plate, various measurement techniques can be implemented with manageable effort. The endwall boundary layer can be adjusted by misaligning the front plate with respect to the aft plate. During all measurements presented in this paper, the endwall boundary layer thickness was $\delta_{99} = 4.62$ mm with a shape factor of $H_{12} = 1.86$ at 45% Chord C upstream of the blade's leading edge (LE). A detailed description of the particular test case design and an investigation of the effects of endwall boundary layer variations on the secondary flow and loss production can be found in [8,13].

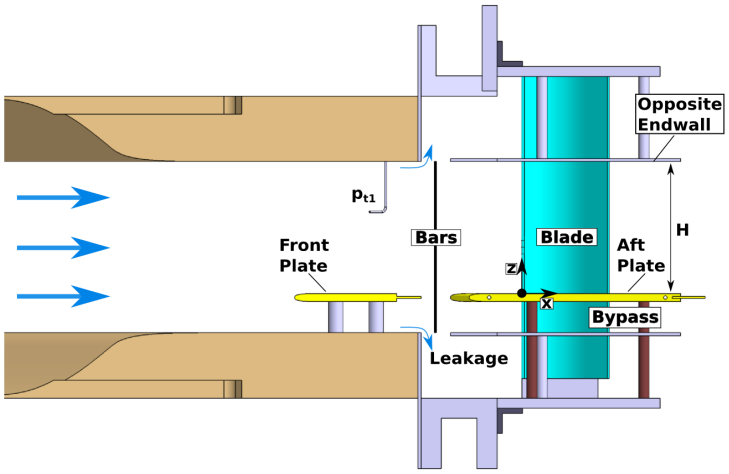

Figure 1. Illustration of the T106A test case featuring a split flat plate endwall (yellow) and moving bars upstream of the low-pressure turbine blades (cyan); adapted from Schubert et al. [8].

Table 1. T106A linear turbine cascade.

Geometric parameters:	
Chord length C	100 mm
Pitch-to-chord ratio P/C	0.799
Aspect ratio H/C	1.31
Flow conditions:	
Exit Mach number M_{2th}	0.59
Exit Reynolds number Re_{2th}	2×10^5
Design inflow angle β_1	127.7°
Design outflow angle β_2	26.8°
Turbulence intensity Tu_1	6.8%
Periodically unsteady inflow conditions:	
Strouhal number Sr	0.66
Flow coefficient ϕ	3.8

2.2. Numerical Setup

Numerical simulations were utilized during the cascade design (pre-test CFD) as well as to support the experimental results (validated post-test CFD) with time-resolved flow data, especially in areas of limited accessibility. The unsteady simulations were performed using the (U)RANS flow solver TRACE by DLR with the $k - \omega$ turbulence model by

Wilcox [30] and $\gamma Re_{\theta t}$ transition model by Langtry and Menter [31]. The computational domain covers a single blade pitch with periodic boundary conditions. It is divided into an upstream block group encompassing the front plate, a moving domain containing two bar pitches, and a downstream block group that encompasses the blade passage and aft plate. The leakage flow is simulated by additional outlet panels at the bar gap boundaries. The blade passage is discretized using an OCGH-topology and low-Reynolds wall treatment (non-dimensional wall distance $y+ \leq 1$), resulting in high boundary layer resolution. Sufficient spatial and temporal discretization is ensured by a sensitivity study, which leads to an overall number of nodes of approximately 8×10^6 and a blade o-grid with 354, 31, and 110 nodes in the i,j,k-directions, respectively. The CFL number is set to 150 in the unsteady simulations, and each moving domain period (two bar pitches) is resolved by 800 time steps. The flow conditions prescribed at the in- and outlet plane match the wind tunnel conditions in the experiment (M_{2th}, $Re_{2th} = f(T_{t1}, p_{t1}, p_3)$, and Tu_1). A detailed description of the computational approach can be found in [13].

The key flow characteristics inside the T106A blade passage are illustrated by means of CFD in Figure 2. Here, axial slices of the entropy generation rate and iso-surfaces of the Q-criterion (colored by streamwise vorticity indicating the sense of rotation) indicate loss production at midspan and the secondary flow region. In the 2D-flow region around midspan, the levels of loss production start off moderately in the predominately aft-loaded T106A. However, near the trailing edge (TE), strong adverse pressure gradients acting on the blade suction surface lead to the formation of a separation bubble. Under periodically unsteady inflow conditions, wake-induced transition periodically forces the suppression of the separation bubble. This unsteady effect is visible in the time-averaged flow in Figure 2 by a lack of alternating vorticity on the rear suction surface. Near the endwall, the formation of secondary flow as described e.g., by Sieverding [32] becomes apparent. When entering the blade passage, strong transverse pressure gradients caused by blade loading force the boundary layer fluid towards the suction surface. During this process, the flow is rolling up, is fed into the passage vortex and the merging horseshoe vortex pressure side leg, lifts off the endwall, and finally impinges on the blade suction surface. In addition to the resulting high losses, the secondary flow can be identified well by overturning close to the endwall and corresponding underturning at the upper edge of vortex interaction. In the case of unsteady inflow, the interaction of the wakes with the endwall boundary layer periodically delays the development of the passage vortex. This leads to the attenuation of the secondary flow further downstream and, hence, a reduction in the secondary losses. A more detailed analysis of the secondary vortex system and the associated loss generation mechanisms can be found in [13].

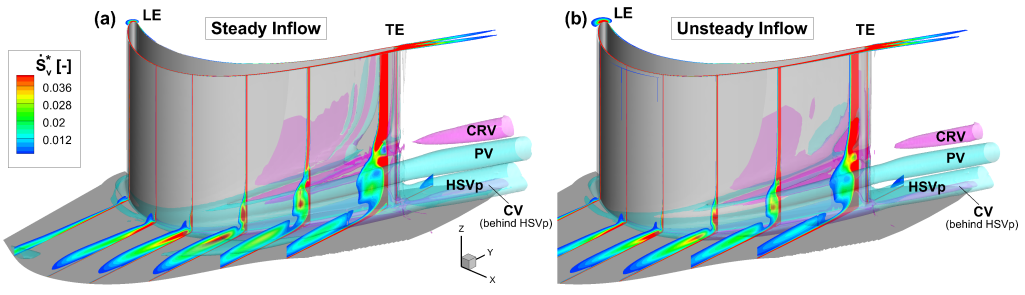

Figure 2. Simulated entropy generation rate ($\dot{S}_v^*$ non-dimensionalized) at several axial slices inside the T106A blade passage under steady (**a**) and periodically unsteady inflow conditions (**b**); adapted from Schubert et al. [13]; (HSVp—pressure side leg of horseshoe vortex; PV—passage vortex; CRV—counter-rotating vortex; CV—corner vortex; LE—leading edge; TE—trailing edge).

2.3. Experimental Setup

The experiments were conducted at the High-Speed Cascade Wind Tunnel (HGK) of the University of the Bundeswehr Munich, see Niehuis and Bitter [33]. The facility allows aerothermodynamic investigations of turbomachinery components at engine-relevant Mach

and Reynolds numbers, which can be varied independently with respective uncertainties of 0.17% and 0.28%. For this reason, the main components of the HGK are enclosed by a large plenum chamber with a 4 m diameter and a 12 m length. The absolute pressure in this plenum chamber can be evacuated down to 4 kPa or pressurized up to 1.2 MPa. The wide pressure range together with the large test section dimensions make it possible to perform aerodynamic investigations on relatively large test specimens, even for low operating Reynolds numbers. This mitigates the relative influence of probe-based measurement techniques on the flow field, especially at the high downstream Mach numbers typically encountered on a turbine cascade [34]. The HGK's test section can be equipped with a wake generator that produces periodically incoming wakes of up to around 500 Hz at the cascade inlet, see Acton and Fottner [35]. The periodically incoming wakes are generated by steel bars with a diameter of 2 mm, i.e., 111% of the T106A trailing edge diameter. The moving bar plane, which runs parallel to the blade passage inlet plane, is located 86% C upstream of the blade leading edge. The ratio of bars to blade count is two-to-one, i.e., $P_b/P = 0.5$, and the bar speed is $V_b = 20\,\mathrm{m/s}$, which leads to a bar passing period of 2 ms (500 Hz). Previous experimental and numerical studies of the T106A turbine cascade have shown that increased bar velocity (higher Strouhal number Sr and lower flow coefficient Φ) results in intensified effects on the secondary flow, see Ciorciari et al. [5]. However, within a reasonable range of unsteady inflow parameters, the observed trends remain unchanged. In addition to the mean velocity deficit, the bar wakes produce a turbulence intensity increase of around 20% in their core. Further detail including the downstream turbulence decay can be found in [36].

The focus of the present investigations is on the interaction between the blade profile flow, the periodically incoming wakes, and the secondary flow. For this purpose, intensity-based pressure-sensitive paint (PSP) was utilized to capture the pressure distribution on the suction surface. The PSP measurement principle is based on the detection of oxygen-dependent intensity of a fluorescence. For the fluorescence to be active, the luminophore, in the present case platinum(II)-tetrakis-fluorphenyl-porphyrin (PtTFPP), must be photo-chemically exited by near ultra-violet illumination. The oxygen dependency of the fluorescent intensity comes from a process known as oxygen quenching. Here, the excited molecules collide with ambient oxygen molecules and release their radiation energy until a relaxed state is reached. Therefore, the degression of fluorescence, and hence the intensity at a certain instance, can be linked to oxygen concentration, i.e., oxygen partial pressure. According to Henry's law, the static pressure of a gas mixture, in this case ambient air, is directly proportional to its oxygen partial pressure. This leads to the following polynomial known as the Stern–Volmer relation

$$\frac{I_{ref}}{I} = A(T) + B(T)\left(\frac{p}{p_{ref}}\right)^{n(T)}. \tag{1}$$

The coefficients $A(T)$, $B(T)$, and $n(T)$ exhibited a temperature dependency of $\approx$2.3%/K [26], but are also greatly affected by the composition of the active PSP layer. For the present experiments, the active PSP layer consisted of the luminophore and a porous, oxygen-permeable polymer-ceramic binder according to the formulation presented in Gregory et al. [18]. The coating was applied using a spray paint gun with a thickness of $\approx$20 µm and a mean roughness of $\approx$7 µm. Hence, a calibration specific to the measurement setup is required. In the present case, this was performed in two ways, both at constant $T_{t0} = 293\,\mathrm{K}$. The first method was a static pressure variation in the shutdown wind tunnel before testing. The second was an in situ calibration during testing using the static pressure taps on the blade surface. For the final results, the latter method was applied using a linear fit. As a illumination source, a wide UV-LED panel with a low-pass cut-off wavelength of 395 nm was mounted onto the wake generator (see Figure 3a,b). As seen in Figure 3c, a homogeneous illumination of the entire visible suction surface was achieved. The visible markers on the blade surface are an important feature for the data post-processing, which

allow a projection of the 2D image data onto a blade-fitted 3D grid. Due to the limited optical accessibility around the wake generator, the high-speed 4 Mpx sCMOS camera access (Phantom V2640) had to be realized using a mirror (see Figure 3a,b). Nevertheless, the full span of the highly curved suction surface was captured from $x/C_x = 0.64$ to the trailing edge. In order to enable an investigation of the periodic wake effects beyond the time average, the measurement setup was optimized for fast PSP response times. Ultimately, a 30 kHz sampling rate of a 896 × 432 px window was achieved for a measurement time of 8 s resulting in 240,000 intensity images. After each measurement, the wind tunnel and wake generator were shut down while keeping a constant chamber pressure p_c and inflow total temperature T_{t0} to record the reference intensity I_{ref} under static conditions for 0.5 s, i.e., 15,000 images. With each signal (I) and reference intensity (I_{ref}) measurement, 15,000 additional unilluminated images were recorded, averaged, and subtracted from the illuminated images in order to reduce background effects. An edge-preserving Gaussian bilateral image filter was applied, resulting in a final uniform data resolution of 1 mm.

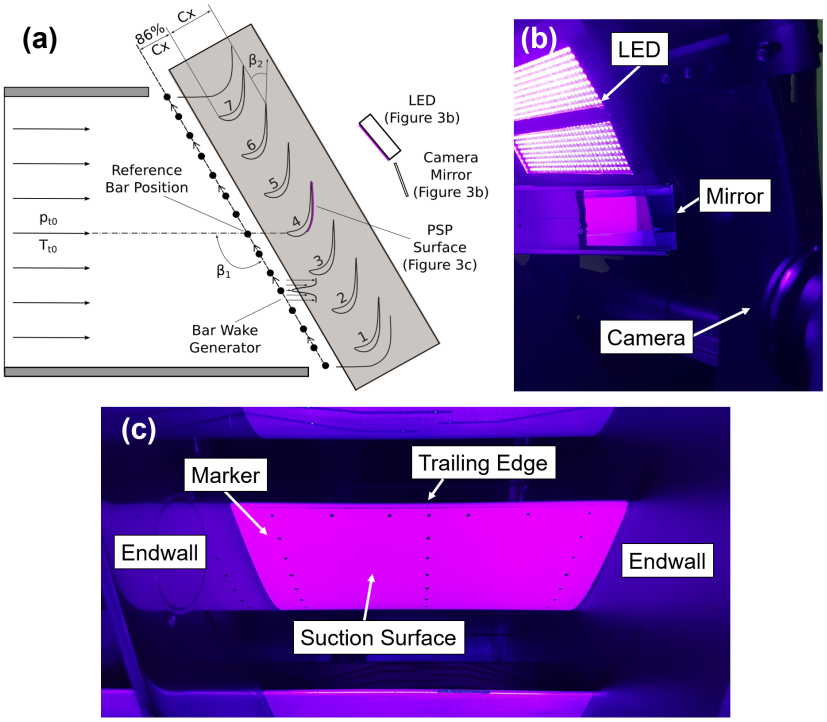

Figure 3. Experimental setup for unsteady pressure-sensitive paint (i-PSP) measurements in the T106A turbine cascade; (**a**) schematic of the cross-sectional side view; (**b**) camera access via a mirror and UV-light illumination; (**c**) camera view on the suction surface of the measurement blade (#4).

2.3.1. Validation

The PSP measurements were validated by a comparison to reference data from static pressure taps. Figure 4 illustrates the relative error after the in situ calibration with respect to each pressure tap $\Delta p_{rel} = (p_{PSP} - p_{PPT})/p_{PPT}$ and the resulting isentropic Mach number distribution at the midspan of the blade suction surface. The PSP data mostly exhibit slightly higher pressure values, i.e., a lower Mach number except for a slightly increased peak Mach number at $x/C_x = 0.67$ and a more distinct pressure plateau at the separation bubble near the trailing edge. However, the linear fit applied in the in situ calibration with a slope of 4.9 lead to an overall good match of the reference points with a R^2 value of 98.3% and RMS pressure deviations of 0.39% with a maximum of ±0.6%.

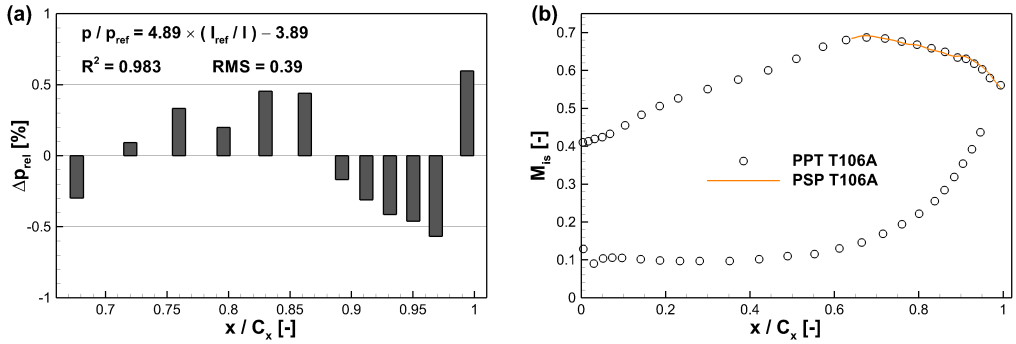

Figure 4. Comparison of the surface pressure measured with PSP, to static pressure taps at the midspan of the T106A turbine cascade under periodically unsteady inflow conditions; (**a**) relative pressure difference; (**b**) isentropic Mach number distribution.

2.3.2. Data Synchronization

In order to enable an investigation of the time-dependent effects of periodically incoming wakes, a phase-locking method according to Bitter and Niehuis [36] was applied to the PSP measurements as well as both PIV setups presented in part 1 [14]. Here, it is critical that the PSP sampling frequency and the dominant bar passing frequency (502 Hz) are decoupled so that the pitchwise bar positions are randomly distributed during the measurements. Synchronization is achieved in post-processing by establishing a correlation between the geometric bar position y_b and the temporal bar period t_{BP}. The first step is to define a reference bar position. In the experimental setup, a bar was aligned with the leading edge of the measurement blade by placing a steel ruler on top and leveling it (see Figure 5a). This reference bar position was then identified by measuring the current pitchwise distance $\Delta y_{b,ref}$ to the next trigger point of an optical sensor, which registers each passing bar (see Figure 5b,c). Finally, a timestamp τ was assigned for each measurement point by determining the relative time difference to the next bar trigger (see Figure 5d).

$$\frac{\tau}{t_{BP}} = \frac{t}{t_{BP}} - \frac{\Delta y_{b,ref}}{P_b}. \tag{2}$$

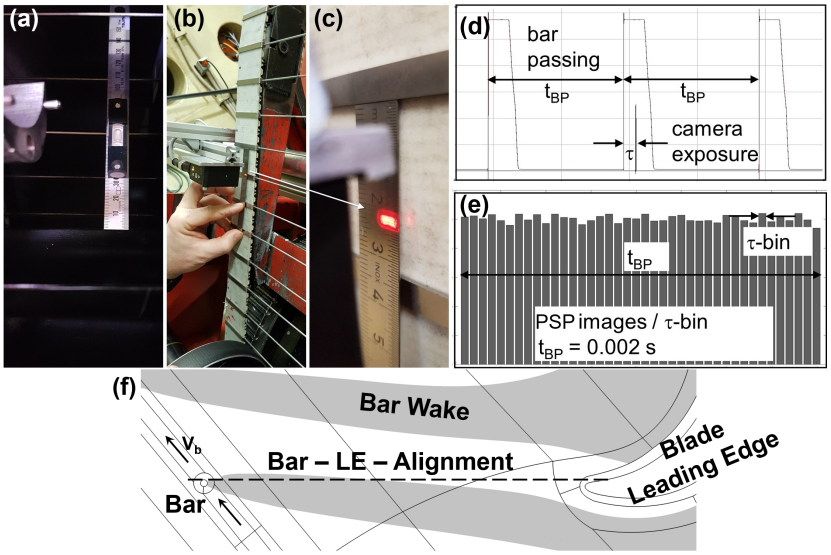

Figure 5. Phase-locking and synchronization method; (**a**–**c**) alignment of the spatial bar position with the temporal trigger signals of the bar counter; (**d**) assignment of a timestamp τ based on the rel. position in a bar passing period; (**e**) phase-averaging by binning in τ-bins of 25 µs; (**f**) application of the synchronization process to CFD by setting the reference bar position to $\tau = 0$.

In addition to data synchronization, binning the measured data according to their position within a bar passing period τ/t_{BP} was applied for phase-averaging. As seen in Figure 5e, this method led to a statistically uniform distribution of measurement points per τ-bin. This sorting method can be adjusted on demand. The more bins chosen, the higher the temporal resolution of the bar wake passing through the passage, but the lower the number of PSP images per bin for averaging the flow field. For the following discussions, 80 bins were chosen, including about 375 frames each. The synchronization process was also applied to the CFD data by determining the reference bar position and setting the correlating timestamp to zero (see Figure 5f).

3. Results

3.1. Time-Averaged Flow Fields

The ensemble, i.e., time-averaged static pressure fields on the rear section of the blade suction surface are illustrated in Figure 6. Only the lower half of the blade is displayed in cases under steady and periodically unsteady inflow conditions. Under steady inflow, the influence of the separation bubble on the rear suction surface is clearly visible. Downstream of the peak-Mach number line the positive pressure gradient (Mach number decrease) is interrupted by a pressure plateau, even a slight decrease, before further increasing to the exit pressure p_2. The outer limits of this region can be identified by the pressure inflection points $\frac{\partial^2 p}{\partial s^2} = 0$ (see 1a in Figure 6a). The downstream inflection points, where turbulent flow reattachment occurs, are accompanied by the high standard deviation of the pressure fluctuations (see 1b Figure 6b). This spanwise high-fluctuation band exhibits a upstream curvature in the transition to the secondary flow region. The position of the downstream inflection points is matched well in the numerical simulations in Figure 6c. However, the separation bubble with negative wall shear stress values due to local backflow is much narrower than in the measured PSP. Near the endwall, the secondary flows completely alter the blade pressure distribution by inducing lower static pressure. More precisely, the impingement of the horseshoe vortex pressure side leg (HSVp) effects the region closest to the endwall (see 2). The bent iso-lines above (see 3a) and the corresponding elevated fluctuations (see 3b) are a result of the surface flow interaction with the passage vortex (PV). The local streamlines on the upper side of the passage vortex point away from the blade surface, resulting in the PV separation line, which is not distinctly identifiable based on sole pressure data. With the support of CFD, it becomes apparent by a thin band of very low wall shear stress values (see 4 in Figure 6c). The resulting formation of the counter-rotating vortex (CRV) can be identified by a diagonal band of elevated shear stress just above the separation line (see 5a). Except for a slightly lower spanwise position, this correlates with a low-p'-band in the PSP data (see 5b). Also, the corner vortex forces local flow separation in the corner region between the endwall and the blade (see 6). Under periodically unsteady inflow conditions, the secondary flow is attenuated and, therefore, its imprint on the blade surface is less pronounced. Also, the passage vortex liftoff of the endwall is reduced (see 3c), leading to a larger 2D flow region around midspan. Here, an earlier wake-induced boundary layer transition results in a time-averaged suppression of the separation bubble. In the surface plots, this is apparent by the continuous pressure increase (see 1c), an upstream shift of a high-pressure fluctuation band (see 1d), and a lack of negative shear stress values due to local backflow (see 1e).

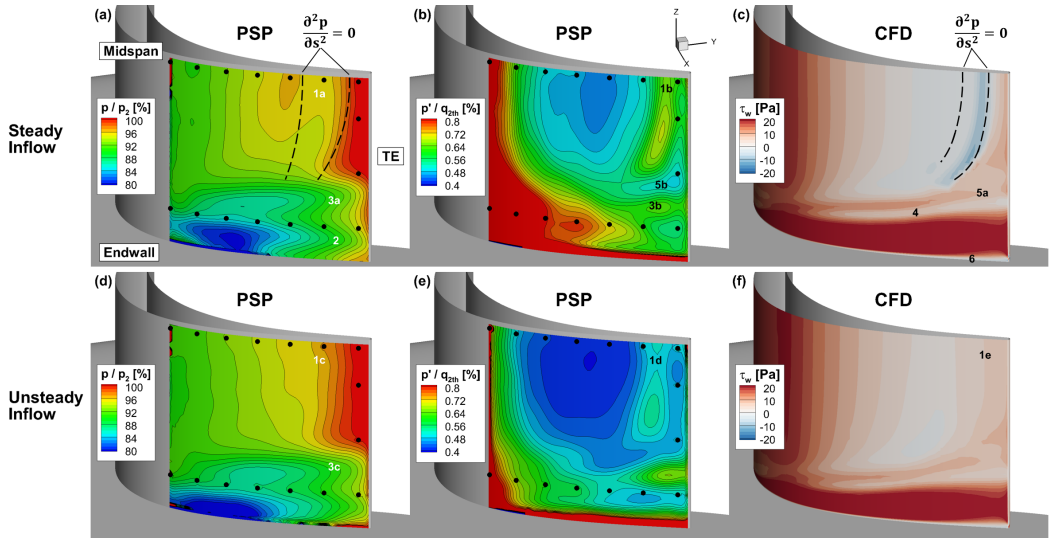

Figure 6. Measured static pressure distribution and supplemental CFD on the T106A suction surface under steady (**a**–**c**) and periodically unsteady (**d**–**f**) inflow conditions; (**a**,**d**) time-averaged pressure (PSP); (**b**,**e**) standard deviation of pressure fluctuations (PSP); (**c**,**f**) wall shear stress (CFD).

The frequency spectrum of the PSP measurement data is illustrated in Figure 7. As can be seen by the decreasing pressure amplitudes over the entire frequency range of 15 kHz, the measurement setup enabled a high-speed detection of small pressure fluctuations down to the single-digit Pascal range. The sporadic pressure peaks at very high frequencies can be attributed to aliasing effects. The dominant pressure signal of the bar wake generator at 502 Hz and its higher harmonics are clearly captured.

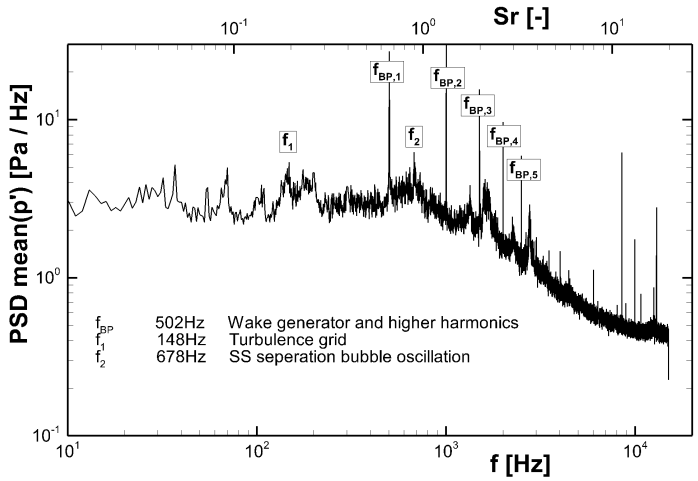

Figure 7. Power spectrum density of the mean pressure amplitudes (PSP) at midspan under periodically unsteady inflow conditions.

In order localize the wake-induced fluctuations amplitudes, two methods of frequency-based data filtering are compared in Figure 8. This was achieved by data conversion into the Fourier space (a) or by applying a spectral proper orthogonal decomposition averaged over 100 time steps (b,c). In the FFT-based data, the 2D flow at 502 Hz features spanwise (vertical) bands of high and low fluctuations. This pattern is similar to the alternating vorticity around midspan in the CFD results (see Figure 2a), and is associated to the wake effect on the highly loaded rear suction surface. The highly resolved distributions of pressure amplitudes and phase (not shown here) at distinct frequencies can also be used as input and validation data for frequency-based CFD methods, like the harmonic balance approach [37]. In the SPOD data at 502 Hz, two regions of positive and negative fluctuations

are present in the 2D flow. Both coincide with one of the consecutive high–low p'-patterns in the FFT data. In the secondary flow region, the fluctuations of the passage vortex are more clearly identifiable by a narrow streamwise band of fluctuation levels close to zero. This finding is in accordance to the phase-locked data discussed in the next chapter, where the periodic movement of the pressure iso-lines is limited to the streamwise direction. Just below this region is the fluctuation imprint of the HSV pressure side leg with negative amplitudes, indicating an opposite sense of fluctuation. Without prior knowledge of a source frequency, as in case of the wake generator, it can be difficult to associate pressure fluctuation peaks. In these cases, SPOD can be a valuable post-processing method to identify the fluctuation source. For example, at f_2 = 678 Hz, the amplitude distribution shows only negative signs and the dominant values are located near the trailing edge in the reattachment region. In the non-frequency-filtered data, this region is confined by the dominant secondary flow. In contrast, at f_2, it extends all the way to the endwall with little disturbance. Thus, this fluctuation peak can be associated to the separation bubble oscillation, which is confirmed by similar frequency ranges of comparable turbine blade profiles [36]. Some of the higher harmonics of the bubble oscillation, which is not distinctly at one frequency but rather a narrow range can be seen between the bar wake harmonics $f_{BP,2-5}$.

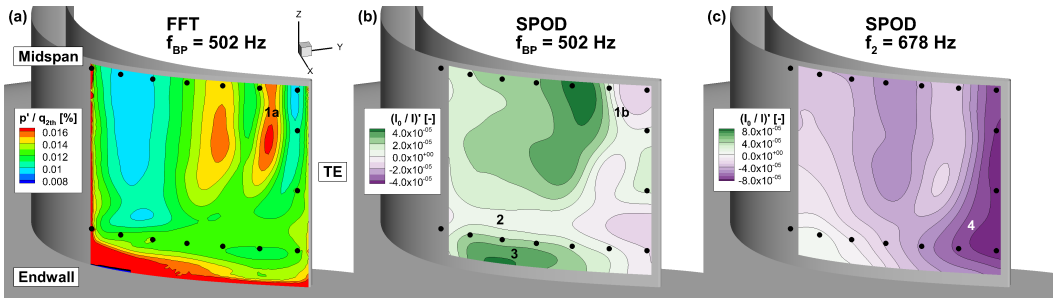

Figure 8. PSP measurements on the T106A suction surface stimulated by the first harmonic wake generator frequency of 502 Hz and the separation bubble osculation at 678 Hz; (**a**) FFT-based filtered pressure amplitudes; (**b**,**c**) first SPOD mode of the measured intensity ratios averaged over 100 time steps.

3.2. Phase-Locked Flow Fields

In order to further analyze the timely sequence leading to the presented time-averaged pressure fields, the phase-locked pressure fluctuations on the blade surface are illustrated at four time steps τ of one bar passing period t_{BP} in Figure 9. The normalized pressure fluctuations are given by $p'/q_{2th} = (\bar{p}(\tau) - \langle p \rangle)/q_{2th}$, where $\bar{p}(\tau)$ is the mean surface pressure of a τ-bin, $\langle p \rangle$ is the ensemble average over the entire time series, and q_{2th} is the theoretical dynamic pressure of the turbine exit flow. The indicated mean bar wake positions were determined by phase-locked PIV measurements in the blade-to-blade plane of the passage presented in part 1 [14]. Since the PIV data did not fully extend to the blade surface due to background reflections, the wake surface position had to be extrapolated (see Figure 10). The inherent uncertainties are mitigated by a validity check based on the measured imprint in the PSP surface data. At $\tau/t_{BP} = 0$, the bar wake impinges on the captured suction surface section and effects the majority of the flow with induced upstream higher pressure followed by downstream lower pressure (red to blue). In the secondary flow region closer to the endwall, the low pressure area extents to the trailing edge and the imprint of the passage vortex is apparent. This indicates an attenuation of the secondary flow even before the wake arrives.

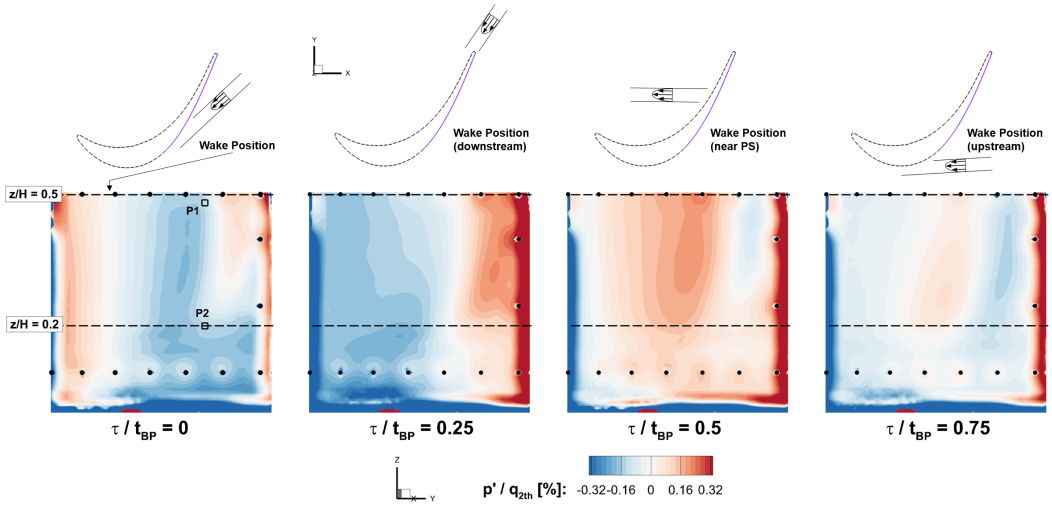

Figure 9. Phase-locked PSP pressure fluctuations measured on the T106A suction surface at four time steps of the bar passing period (the respective wake position is indicate above and the mean flow direction is from left to right).

Although the time-averaged PV liftoff is hereby reduced by the wakes, its phase-locked movement in spanwise direction is close to zero. Once the bar wake has traveled further downstream, only the high-pressure region associated to the wake is present close to the trailing edge at τ/t_{BP} = 0.25. In contrast to the previous time step, this effect extends over the entire blade span, albeit it is less intense near the endwall. Immediately after the wake has completely passed at around τ/t_{BP} = 0.35 , the pressure fluctuations across the captured suction surface section are close to zero. Halstead et al. describe this part of the bar period as a calming region in their time-space illustration at midspan [38]. The present results indicate that this description can be extended to the secondary flow region, where only minimal differences to the time-averaged flow field are present and the passage vortex imprint is not identifiable in p'-distribution (see Figure 11). At τ/t_{BP} = 0.5, the bar wake is located in the blade passage far from the suction surface (see Figure 10). This time step has the closest resemblance to the steady inflow case, which was measured separately as a reference. Most of the suctions surface exhibits elevated levels of pressure except for the 2D flow region close to the trailing edge. Here, a quick streamwise change from positive to negative pressure fluctuations indicates the reattachment of a separation bubble, which has formed in the absence of the bar wakes. The last time step in Figure 9 at τ/t_{BP} = 0.75 shows the upstream wake presence entering the field of view by a low pressure region on the left. However, the effects on the rear section are already establishing with a diminishing gradient in the 2D flow and near-endwall levels closer to the time-average.

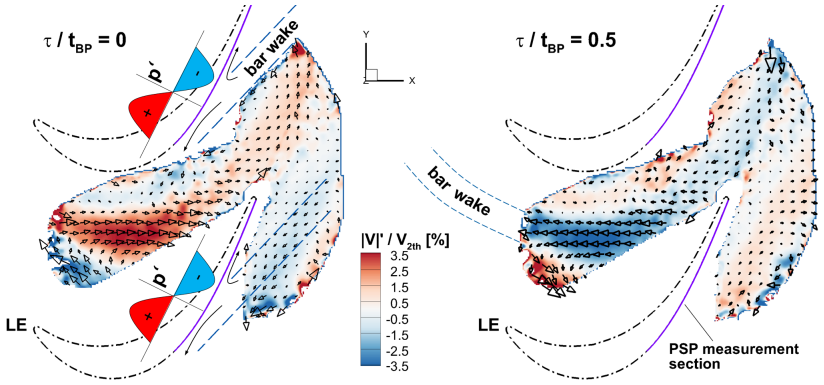

Figure 10. Phase-locked PIV measurements of the bar wake velocity deficit in the T106A turbine passage close to the endwall (z/H = 0.2) at two time steps and its effect on the blade surface pressure; adapted from part 1 [14].

A time-space correlation is used to further illustrate the phase-locked wake movement across the blade surface in Figure 11. The position of the wake, moving downstream in time, can be identified by a diagonal lane of relatively strong positive pressure gradients in time $\frac{\partial p}{\partial t} > 0$ (p' blue to red). The same effect appears as a negative spatial pressure gradient $\frac{\partial p}{\partial s} < 0$ (p' red to blue). The gradients connect a region of high pressure upstream of the wake and low pressure downstream of the wake. This sequence, also clearly visible in Figure 12, can be explained by the 'negative-jet-effect', where the velocity deficit of a bar wake forms a jet with negative flow direction relative to the free stream velocity. As illustrated in the sketch in Figure 10, the opposing pressure regions are a result of the relative streamline directions of the impinging negative jet. For example, downstream of the wake, i.e., before its passing, the negative jet streamline curvature points in the mean surface flow direction leading to an increased flow velocity and lower static surface pressure. The absolute amount of time Δt needed for the wake to move across the suction surface is mainly dependent on the Strouhal number. However, more relevant for the present investigation is the amount of time relative to one bar passing period $\Delta\tau/t_{BP}$, which is determined by the wake orientation inside the blade passage and thus the flow coefficient. Due to the relatively high flow coefficient in the present test case, the bowed wake has a very acute angle with respect to the rear suction surface (see Figure 10 and part 1 [14] for further detail). Therefore, the incline of the diagonal wake-lane in Figure 11 is quite flat. Moreover, the wake shape and orientation has an effect on the surface streamline curvature and, according to Hodson et al. [39], consequently, an effect on the amplitude of the up- and downstream pressure regions. This is the reason for the higher pressure gradients at $z/H = 0.2$ (see 1 in Figure 11c) than at midspan.

The part of the period where a separation bubble has formed in the absence of a wake can be identified by a local decrease in pressure (see 2a in Figure 11a) and a change from a high- to low-pressure fluctuation (p' red to blue), starting at ≈90% C_x at midspan (see 2b). This is not to be confused with the negative spatial pressure gradient induced by the wakes. In addition to the pressure gradient effect, the wake also induces a local turbulence increase, which strengthens the boundary layer robustness. This important factor cannot directly be captured by the sole surface pressure measurements and requires supplemental experimental or CFD data. In the present case, it leads to an earlier turbulent transition at midspan and a resulting periodic suppression of the separation bubble inside the wake-lanes. A difference between the two spanwise slices is apparent in the p' peak around $\tau/t_{BP} = 0.15$. The high amplitude at midspan is a result of the low reference pressure in the bubble reattachment region and, therefore, fades towards the endwall.

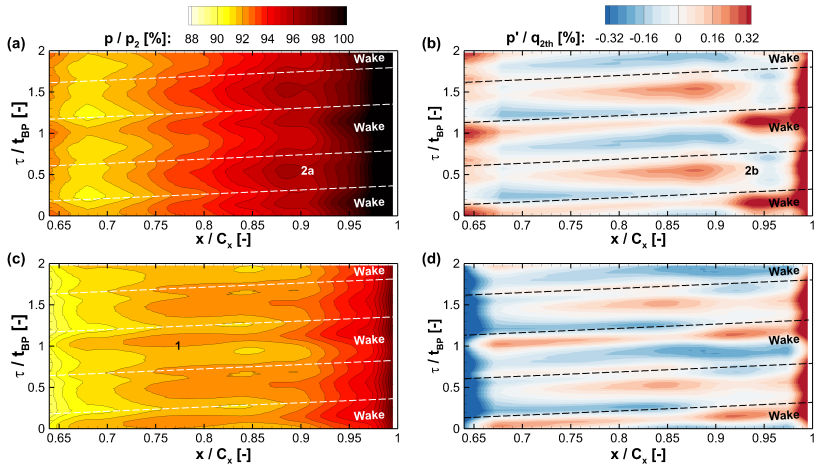

Figure 11. Time-space correlation of the measured static pressure distributions at midspan of the suction surface (**a**,**b**) and close to the endwall at $z/H = 0.2$ (**c**,**d**).

A comparison of the measured phase-locked pressure fluctuations with CFD results was performed in two locations, as illustrated in Figure 12. Position $P1$ is located in the 2D flow region around midspan, where the separation bubble appears ($x/C_x = 0.91$). $P2$ is located at the same streamwise position, but at $z/H = 0.2$, where the endwall effects become a factor (see Figure 9). The wake-induced upstream high-pressure and downstream low-pressure regions are apparent in both locations, with $p'/q_{2th} \approx \pm 0.16\%$ at $P1$ and $p'/q_{2th} \approx \pm 0.22\%$ at $P2$. The intensified wake effect near the endwall found in Figure 11 can be quantified here by a 33% increase of the 98 Pa/ms pressure gradient at midspan. Despite the different flow regimes at the two positions, the pressure fluctuations are in phase. This also holds true for the CFD data, however, there is a phase shift to the PSP signals of around 36°, i.e., $\Delta\tau/t_{BP} \approx 0.1$. While the pressure amplitudes and the basic periodic sequence can be reproduced in the numerical simulations, the predictions are not as accurate as in the case of the velocity field in the front part of the blade passage ($x/C_x = 0.3$). Here, a phase shift between 0° and 36° was presented in part 1 [14]. The main difference at $P1$ is an exaggeration of the low-pressure region before the wake passing, and thus a severe increase in the pressure gradient of 188%. This is caused by a well-known attenuation of the wake mixing process in RANS-based simulations, leading to more pronounced wakes further downstream. Adjusting the wake mixing to measured values would require a large increase in the modeled turbulent length scale, which, in return, would lead to unrealistic loss production levels. At $P2$ ($z/H = 0.2$), the wake-induced pressure gradient is well reproduced with a delta to the measurements of -7%, but during the wake absence, the pressure levels are elevated in the CFD. Overall, resolving the unsteady pressure fluctuations with single- to double-digit Pascal amplitudes is challenging for conventional simulation methods. Therefore, highly resolved surface pressure data measured with unsteady PSP, as presented here, has a high potential for CFD validation and provides a reference for improving numerical methods.

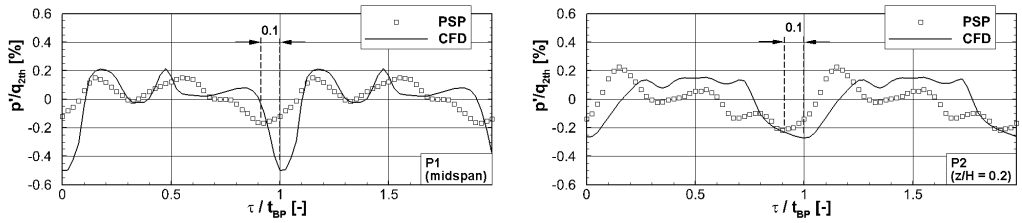

Figure 12. Comparison of CFD predictions of pressure fluctuations to phase-locked PSP measurements at position $P1$ (**left**) & $P2$ (**right**) marked in Figure 9.

4. Conclusions

An experimental campaign was conducted using the T106A linear turbine cascade with an additional part-span endwall under challenging measurement conditions with periodically incoming wakes with a frequency of 500 Hz. In previous investigations, the authors utilized a combination of probe-based measurements and CFD to identify an attenuation of the downstream secondary flow caused by wake interaction inside the blade passage. The primary goal of the experiments presented here was to validate, complement, and specify these findings.

The present work was split into two parts. The first part [14] dealt with resolving the unsteady passage flow field in a blade-to-blade plane with phase-locked PIV measurements. By tracing the wake throughout the passage, the 'negative-jet-effect' was clearly illustrated and the wake transport was related to the periodic secondary flow effects in an axial plane downstream of the passage. The goal of the second part was to resolve the static pressure field on the blade suction surface including the effects of the passing wakes. For this purpose, unsteady pressure-sensitive paint (i-PSP) was utilized at a 30 kHz sampling rate. The measurement area extended all the way to the endwall, enabling the identification of the secondary vortex imprints by low static pressure. In the 2D flow region around

midspan, the dominant pressure fluctuations were associated to the high blade loading at the rear suction surface. Here, the reattachment region with high p' is more apparent than the separation bubble itself. By combining phase-locked PIV and PSP data, the movement of the bar wakes across the suction surface was traced, which caused an upstream high-pressure and a downstream low-pressure region with around $\pm 0.2\%$ of the dynamic exit pressure (p'/q_{2th}). The resulting negative pressure gradient in space and positive gradient in time of 98 Pa/ms was increased in the secondary flow region by 33%. Furthermore, two methods of frequency-filtering based on FFT and SPOD were compared. By the example of separation bubble oscillation at 768 Hz, it was demonstrated how the latter can be utilized to associate a specific frequency range to its source flow phenomenon.

The PSP surface pressure data provided insight into the wake-perturbed secondary flow interaction and the resulting profile flow topology, but for some aspects, supplemental data are necessary. One example is the use of wall shear stress analysis to localize the passage vortex separation line and the resulting counter-rotating vortex. In the present case, RANS-based CFD proved to be a vital addition with sufficient accuracy despite a phase shift of around 36° and an exaggeration of the wake-induced pressure gradient at midspan. However, matching the unsteady single- to double-digit Pascal pressure fluctuations was more challenging than in the case of the passage flow field presented in part 1. Overall, it has been demonstrated that, particularly for secondary flow investigations under periodic inflow conditions, phase-locked optical measurements such as PIV and unsteady PSP provide a valuable addition to classic probe-based measurement approaches.

Author Contributions: Conceptualization, T.S.; Methodology, T.S. and M.B.; Software, T.S.; Validation, T.S.; Formal analysis, T.S.; Investigation, T.S.; Resources, D.K.; Data curation, T.S.; Writing—original draft, T.S.; Writing—review & editing, T.S. and M.B.; Visualization, T.S.; Supervision, D.K. and M.B.; Project administration, T.S. and M.B.; Funding acquisition, T.S. and M.B. All authors have read and agreed to the published version of the manuscript.

Funding: The numerical design as well as the experimental investigations presented in this paper were performed in the framework of the joint project PAK 948 "Flow near the endwall of turbomachinery blading" funded by Deutsche Forschungsgemeinschaft under the funding code Ma 4922/8-1.

Data Availability Statement: The raw data supporting the conclusions of this article will be made available by the authors on request.

Conflicts of Interest: The authors declare no conflicts of interest.

Nomenclature

Latin Symbols

C	chord length
H	channel height, i.e., blade span
M	Mach number
p	pressure
p'	pressure fluctuations
$\langle p \rangle$	ensemble-averaged pressure
P	pitch
q	dynamic pressure
R^2	coefficient of determination
Re	Reynolds number
s	blade surface coordinate
$\dot{S}_v^*$	non-dimensional entropy generation rate per unit volume, $\dot{S}_v \times (C \times T_{2,th})/(\rho_{2,th} \times V_{2,th})$
Sr	Strouhal number, $(V_b/P_b) \times (C/V_{x1})$
T	temperature
t	time
V	velocity
x, y, z	axial, pitchwise, and spanwise coordinate

Greek Symbols	
ϕ	flow coefficient, V_{x1}/V_b
τ	synchronized timestamp
Abbreviations	
CV	corner vortex
CRV	counter rotating vortex
EW	endwall
HSVp	horseshoe vortex pressure side leg
i-PSP	unsteady pressure-sensitive paint
LE	leading edge
MS	midspan
PIV	particle image velocimetry
PSP	pressure-sensitive paint
PV	passage vortex
TE	trailing edge
sCMOS	scientific complementary metal oxide semiconductor
Subscripts	
1	inflow condition
2	exit flow condition
b	bar
BP	bar passing
t	stagnation quantity
th	theoretical value after isentropic change of state

References

1. Cui, J.; Tucker, P.G. Numerical Study of Purge and Secondary Flows in a Low Pressure Turbine. In Proceedings of the ASME Turbo Expo 2016: Turbomachinery Technical Conference and Exposition, Seoul, Republic of Korea, 13–17 June 2016; ASME GT2016-56789.
2. Coull, J.D. Enwall Loss in Turbine Cascades. *J. Turbomach.* **2017**, *139*, 081004. [CrossRef]
3. Denton, J.; Pullan, G. A Numerical Investigation into the Sources of Endwall Loss in Axial Flow Turbines. In Proceedings of the ASME Turbo Expo 2012: Turbine Technical Conference and Exposition, Copenhagen, Denmark, 11–15 June 2012; ASME GT2012-69173.
4. Bear, P.; Wolff, M.; Gross, A.; Marks, C.R.; Sondergaard, R. Experimental Investigation of Total Pressure Loss Development in a Highly Loaded Low-Pressure Turbine Cascade. *J. Turbomach.* **2018**, *140*, 031003. [CrossRef]
5. Ciorciari, R.; Kirik, I.; Niehuis, R. Effects of Unsteady Wakes on Secondary Flows in the Linear T106 Turbine Cascade. *J. Turbomach.* **2014**, *136*, 091010. [CrossRef]
6. Ciorciari, R.; Schubert, T.; Niehuis, R. Numerical Investigation of Secondary Flow and Loss Development in a Low Pressure Tubrine Cascade with Divergent Endwalls. *Int. J. Turbomach. Propuls. Power* **2018**, *3*, 5. [CrossRef]
7. Volino, R. Effects on Endwall Boundary Layer Thickness and Blade Tip Geometry on Flow through High Pressure Turbine Passages. In Proceedings of the ASME Turbo Expo 2014: Turbine Technical Conference and Exposition, Düsseldorf, Germany, 16–20 June 2014; ASME GT2014-27013.
8. Schubert, T.; Chemnitz, S.; Niehuis, R. The Effects of Inlet Boundary Layer Condition and Periodically Incoming Wakes on Secondary Flow in a Low Pressure Turbine Cascade. *J. Turbomach.* **2021**, *143*, 041001. [CrossRef]
9. Sinkwitz, M.; Winhart, B.; Engelmann, D.; di Mare, F. Time-Resolved Measurements of the Unsteady Boundary Layer in an Annular Low-Pressure Turbine Configuration With Perturbed Inlet. *J. Turbomach.* **2021**, *144*, 011001. [CrossRef]
10. Lopes, G.; Simonassi, L.; Lavagnoli, S. Impact of Unsteady Wakes on the Secondary Flows of a High-Speed Low-Pressure Turbine Cascade. *Int. J. Turbomach. Propuls. Power* **2023**, *8*, 36. [CrossRef]
11. Chemnitz, S.; Niehuis, R. A Comparison of Turbulence Levels from Particle Image Velocimetry and Constant Temperature Anemometry Downstream of a Low-Pressure Turbine Cascade at High-Speed Flow Conditions. *J. Turbomach.* **2020**, *142*, 071008. [CrossRef]
12. Engelmann, D.; Sinkwitz, M.; di Mare, F.; Koppe, B.; Mailach, R.; Ventosa-Molina, J.; Fröhlich.; Schubert, T.; Niehuis, R. Near-Wall Flow in Turbomachinery Cascades—Results of a German Collaborative Project. *J. Turbomach. Propuls. Power* **2021**, *6*, 9. [CrossRef]
13. Schubert, T.; Niehuis, R. Numerical Investigation of Loss Development in a Low-Pressure Turbine Cascade with Unsteady Inflow and Varying Inlet Endwall Boundary Layer. In Proceedings of the ASME Turbo Expo 2021: Turbomachinery Technical Conference and Exposition, Virtual, 7–11 June 2021; ASME GT2021-59696.
14. Schubert, T.; Kožulović, D.; Bitter, M. Characterization of the Endwall Flow in a Low-Pressure Turbine Cascade Perturbed by Periodically Incoming Wakes, Part 1: Flow Field Investigations with Phase-Locked Particle Image Velocimetry. *Aerospace* 2024, *11*, 403. [CrossRef]

15. Liu, T.; Torgerson, S.; Sullivan, J.; Johnston, R.; Fleeter, S. Rotor Blade Pressure Measurement in a High Speed Axial Compressor Using Pressure and Temperature Sensitive Paints. In Proceedings of the 35th Aerospace Sciences Meeting and Exhibit, Reno, NV, USA, 6–9 January 1997.
16. Lepicovsky, J.; Bencic, T. Use of Pressure-Sensitive Paint for Diagnostics in Turbomachinery Flows with Shocks. *Exp. Fluids* **2002**, *33*, 531–538. [CrossRef]
17. Liu, T.; Sullivan, J.; Asai, K.; Klein, C.; Egami, Y. *Pressure and Temperature Sensitive Paints*, 2nd ed.; Experimental Fluid Mechanics; Springer: Berlin, Germany, 2021.
18. Gregory, J.; Sakaue, H.; Liu, T.; Sullivan, J. Fast Pressure-Pensitive Paint for Flow and Acoustic Diagnostics. *Ann. Rev. Fluid Mech.* **2014**, *46*, 303–330. [CrossRef]
19. Peng, D.; Liu, Y. Fast Pressure-Sensitive Paint for Understanding Complex Flows: From Regular to Harsh Environments. *Exp. Fluids* **2020**, *61*, 1–22.
20. Gao, L.; Gao, J.; Wang, H.; Liu, B.; Zhou, Q. Application of PSP Technique to Pressure Measurement on Cascade Surface. *J. Eng. Thermophys.* **2011**, *32*, 411–414.
21. Marks, C.; Fletcher, N.; Sondergaard, R. Vortex Unsteadiness in the Endwall Region of a High-Lift Low-Pressure Turbine Passage. *J. Turbomach.* **2022**, *145*, 011012. [CrossRef]
22. Gao, L.; Yang, G.; Gao, T.; Li, R.; Hu, X. Experimental Investigation of a Linear Cascade with Large Solidity Using Pressure Sensitive Paint and Dual-Camera System. *J. Therm. Sci.* **2021**, *30*, 682–695. [CrossRef]
23. Dong, Z.; Gu, F.; Chen, R.; Yang, J.; Zhou, W.; Liu, Y.; Peng, D. Three-Dimensional Pressure Field Measurement on Turbine Guide Vanes Using a Dynamic Distortion Correction Endoscopic Pressure-Sensitive Paint Technique. *Exp. Fluids* **2023**, *64*, 97. [CrossRef]
24. Bitter, M.; Wartzek, F.; Übelacker, S.; Schiffer, H.P.; Kähler, C. Investigation of a Distorted Transonic Compressor Flow using Two-Component Pressure-Sensitive Paint. In Proceedings of the 10th Pacific Symposium on Flow Visualization and Image Processing (PSFVIP 10), Naples, Italy, 15–18 June 2015.
25. Bitter, M.; Kurz, J.; Kähler, C.; Niehuis, R. Investigations of a Low-Pressure Turbine Blade by Means of Simultaneous Optical Velocity and Pressure Measurements. In Proceedings of the 18th International Symposium on Applications of Laser Techniques to Fluid Mechanics, Lisbon, Portugal, 4–7 July 2016.
26. Bitter, M.; Stotz, S.; Niehuis, R. On High-Resolution Pressure Amplitude and Phase Measurements Comparing Fast-Response Pressure Transducers and Unsteady Pressure-Sensitive Paint. *J. Turbomach.* **2021**, *143*, 031012. [CrossRef]
27. Kampitsch, M.; Stadtmüller, P.; Fottner, L. Investigations of Wake-Induced Transition on the LPT Cascades T106A-EIZ and T106D-EIZ. In Proceedings of the ERCOFTAC Workshop, La Clusaz, France, 19–23 March 2000.
28. Kirik, I.; Niehuis, R. Comparing the Effect of Unsteady Wakes on Parallel and Divergent Endwalls in a LP Turbine Cascade. In Proceedings of the 11th International Gas Turbine Congress, Tokyo, Japan, 15–20 November 2015; IGTC2015-137.
29. Michelassi, V.; Chen, L.; Pichler, R.; Sandberg, R.D. Compressible Direct Numerical Simulation of Low-Pressure Turbines—Part II: Effect of Inflow Disturbances. *J. Turbomach.* **2015**, *137*, 071005. [CrossRef]
30. Wilcox, D.C. *Turbulence Modeling for CFD*, 4th ed.; DCW Industries: La Canada, CA, USA, 2004.
31. Langtry, R.B.; Menter, F.R. Transition Modeling for General CFD Applications in Aeronautics. In Proceedings of the 43rd AIAA Aerospace Sciences Meeting and Exhibit, Reno, NV, USA, 10–13 January 2005; AIAA Paper 2005-522.
32. Sieverding, C. Recent Progress in the Understanding of Basic Aspects of Secondary Flows in Turbine Blade Passages. *ASME J. Eng. Gas Turbines Power.* **1985**, *107*, 248–257. [CrossRef]
33. Niehuis, R.; Bitter, M. The High-Speed Cascade Wind Tunnel at the Bundeswehr University Munich after a Major Revision and Upgrade. *Int. J. Turbomach. Propuls. Power* **2021**, *6*, 41. [CrossRef]
34. Börner, M.; Bitter, M.; Niehuis, R. On the Challenge of Five-Hole-Probe Measurements at High Subsonic Mach Numbers in the Wake of Transonic Turbine Cascades. *J. Global Power Propuls. Soc.* **2018**, *2*, 453–464. [CrossRef]
35. Acton, P.; Fottner, L. The Generation of Instationary Flow Conditions in the High-Speed Cascade Wind Tunnel of the German Armed Forces University Munich. In Proceedings of the 13th Symposium on Measuring Techniques, Zurich, Switzerland, 5–6 September 1996.
36. Bitter, M.; Niehuis, R. Effects of Periodic Inflow Turbulence on the Statistics in the Wake of a Linear LPT Cascade at Jet-Engine relevant Test Conditions. In Proceedings of the 13th International Symposium on Particle Image Velocimetry, Munich, Germany, 22–24 July 2019.
37. Frey, C.; Ashcroft, G.; Kersken, H.P.; Voigt, C. A Harmonic Balance Technique for Multistage Turbomachinery Applications. In Proceedings of the ASME Turbo Expo 2014: Turbine Technical Conference and Exposition, Düsseldorf, Germany, 16–20 June 2014; ASME GT2014-25230.
38. Halstead, D.E.; Wisler, D.C.; Okiishi, T.H.; Walker, G.J.; Hodson, H.P.; Shin, H. Boundary Layer Development in Axial Compressors and Turbines: Part 3 of 4–LP Turbines. *J. Turbomach.* **1997**, *119*, 225–237. [CrossRef]
39. Hodson, H.P.; Hynes, T.P.; Greitzer, E.M.; Tan, C.S. A Physical Interpretation of Stagnation Pressure and Enthalpy Changes in Unsteady Flow. *J. Turbomach.* **2012**, *134*, 060902. [CrossRef]

4.6.3 Supplemental Data

Wake Induced Pressure Gradients (PSP)

In Publication 5, PSP measurements of the periodic pressure signals were presented in two positions on the suction surface (see P1 & P2 in Figure 9 & 12 of Publication 5). Here, the negative-jet-effect of the wakes induced a negative pressure gradient in space i.e. positive gradient in time. With respect to position P1 near midspan the pressure gradient increased by 33 % in position P2 in the secondary flow region. To underline the observed trend, supplemental data points are evaluated at different spanwise positions illustrated in Figure 4.3a. The extracted periodic pressure signals at those positions are illustrated in Figure 4.3b. Here, the indicated pressure gradients connect the respective upstream high-pressure region (after wake passing) and the downstream low-pressure region (before wake passing). With further distance from midspan, the amplitude of the high-pressure region increases. The maximum amplitude is located in-between the counter-rotating vortex and passage vortex at a spanwise position of $z/H = 0.24$). This leads to a continuous increase of the wake induced pressure gradients as illustrated in Figure 4.3c. Closer to the endwall, the amplitude of the high-pressure region after the wake passing decreases. However, the beginning of the pressure rise is delayed which leads to high gradients despite a moderate difference in amplitude between the low- and high-pressure regions. The presented results clearly indicate an altered interaction of the secondary flow with the suction surface by an amplified negative-jet-effect of the wakes.

Wall Shear Stress (CFD)

To continue the effort of aligning the experimental and CFD data sets, the Publication 4 & 5 included comparisons of synchronized numerical predictions with the respective phase-locked flow parameters of the two optical measurements. The periodic velocity disturbance by the wakes (PIV) was matched well in amplitude and phase. However, the prediction of unsteady single- to double-digit-Pascal pressure fluctuations (PSP) on the suction surface posed a bigger challenge, especially at midspan. However, in the field of interest closer to the endwall, sufficient accuracy was achieved with a phase shift of 36° and a underprediction in the local wake induced pressure gradient in time of around 7 %. Ultimately the supplemental CFD data proved to be immensely beneficial for the validation and interpretation of the complex periodic flow fields captured in the experiments. Especially wall shear stress τ_w distributions on the blade suction surface provided widespread information about the flow topology and local boundary layer conditions. The blade wall shear stress illustration presented in Publication 5 is extended by the endwall distributions and visualized vortex cores in Figure 4.4. The latter allow a crosscheck of the shear-stress-based localization of the passage vortex separation line, counter-rotating vortex, and corner vortex (see 1–3 in Figure 4.4a). All of them are a result of vortex-blade-interaction and are hard to identify solely based on pressure data. In the 2D flow region, the wall shear stress in the laminar boundary layer continuously decreases in streamwise direction as the local Reynolds number increases. Near the trailing edge, the strong positive pressure gradient forces flow separation. Also, the time-averaged

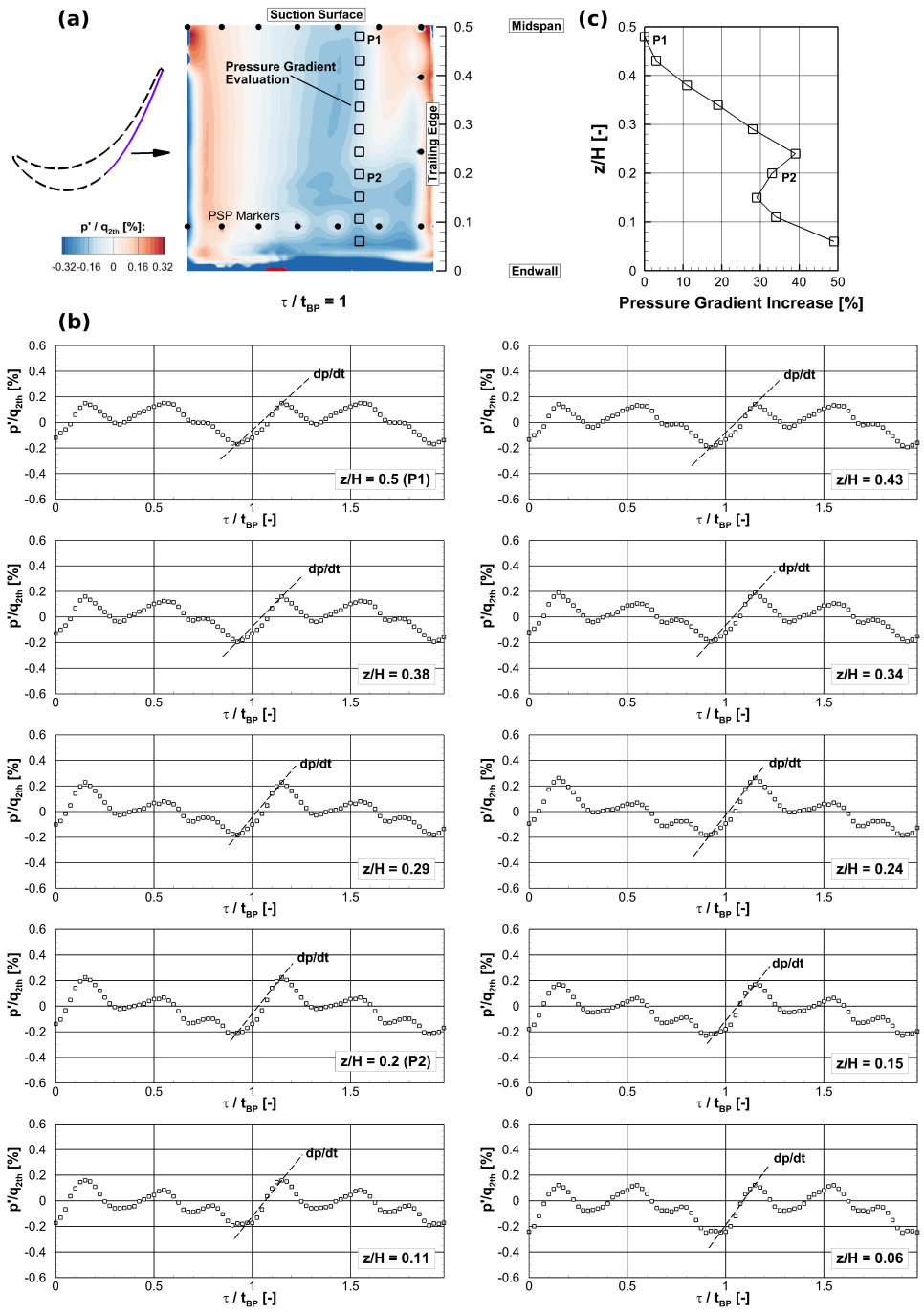

Fig. 4.3: PSP measurements of the wake induced pressure gradients on the T106A blade suction surface; (a) Selected spanwise positions for pressure gradient evaluation; (b) Indication of the wake induced gradients in the periodic pressure signals; (c) Relative increase of the pressure gradients with respect to midspan.

suppression of the separation bubble found in the CFD via a lack of alternating vorticity in Publication 3 and experimentally in Publication 5 is confirmed here (see 4).

Shifting the focus to the endwall shear stress distribution reveals an area of severe flow separation with local backflow extending from 81 % to 111 % of the axial passage length (see 5). The vortex cores illustrate the significance of the horseshoe vortex pressure side leg (HSVp) in this process. It appears that the migration of the HSVp across the passage towards the suction surface triggers the flow separation. Consequently the HSVp and developing passage vortex (PV) are fed by endwall boundary layer entrainment. The resulting increase in HSVp size impacts the liftoff of the passage vortex and thus the spanwise secondary flow extension. While many secondary flow studies focus their attention on the passage vortex, the horseshoe vortex as demonstrated here, plays a significant role and must not be neglected in a comprehensive analysis. The effect of periodically unsteady inflow illustrated in Figure 4.4c is apparent by the significantly smaller separation area on the endwall. The CTA-measurements in Figure 4.2 of Publication 2 revealed a more turbulent boundary layer upstream of the passage caused by the bar wake interaction. This delays the upstream separation line and thus leads to a weaker horseshoe vortex (see 6 in Figure 4.4d). Inside the passage, the weaker flow separation due to the increased boundary layer robustness leads to a reduced supply to the devolving HSVp and PV. This has a direct effect on their growth and liftoff, but also the consequent generation of the counter-rotating vortex. Ultimately the size and intensity of the fully developed secondary flow downstream of the passage is reduced as illustrated in Figure 4.4d. The endwall separation area can be linked to the PIV analysis in Publication 4, where the mean origin of the wake effects on the downstream passage vortex

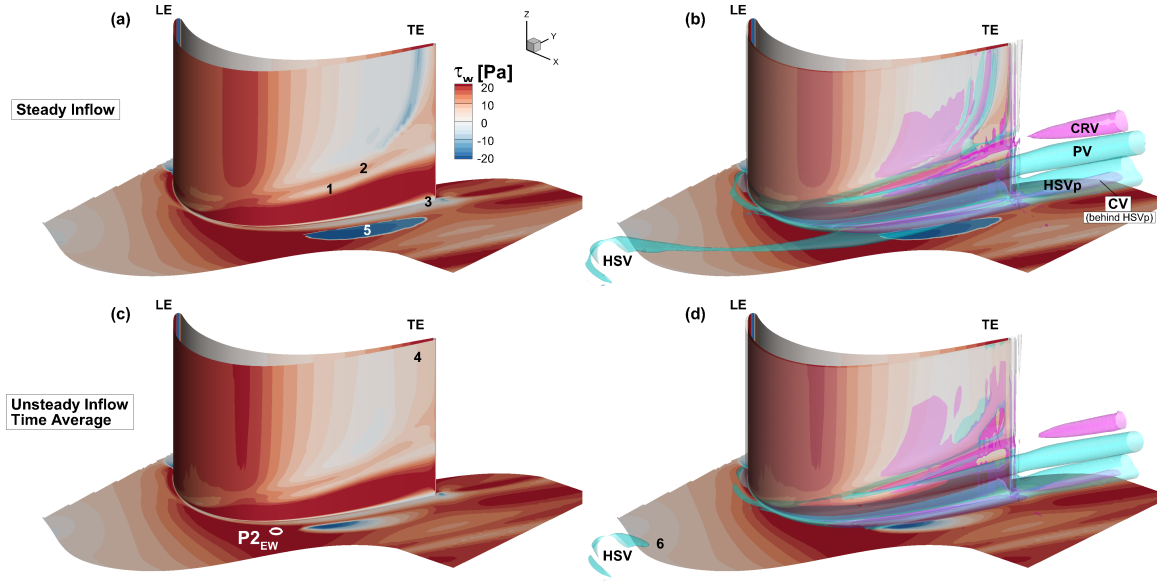

Fig. 4.4: Numerical simulation of the time-averaged wall shear stress in the T106A turbine cascade; (a) & (b) Steady inflow conditions; (c) & (d) Periodically unsteady inflow conditions. Point $P2_{EW}$ in (c) indicates the mean origin of the wake effects on the passage vortex core identified in the PIV measurements of Publication 4.

core was identified. Its projection on the endwall is located just upstream of the separation area which further stresses its importance and highlights the consistency of the findings (see $P2_{EW}$ in Figure 4.4c).

4.7 Publication 6

4.7.1 Summary

The experimental work culminating in Publication 6 was motivated by previous CFD based findings. More precisely, the wall shear stress analysis, later presented in Publication 5, started an investigation on potential measurement techniques to supplement the PSP data. After diligent consideration, the choice fell on Temperature-Sensitive Paint due to its promising characteristics in fast responsiveness, potential to provide absolute shear stress values, and its methodological similarities to PSP. However, the implementation of this measurement technique is quite complex in terms of TSP layering and composition sensitivity, surface heating power and homogeneity, and optical accessibility. Therefore, it was decided to conduct a preliminary study in a simplified test case. The resulting publication in collaboration with DLR – Institute of Aerodynamics and Flow Technology covered the following main aspects.

1. The main goal was to characterize the performance of a modified ultra-fast Ru(phen)-based Temperature-Sensitive Paint whose composition was tuned specifically to resolve low-temperature and high-frequency surface fluctuations in subsonic applications. The test case consisted of an aluminum flat plate with a low-thermal-conductivity insert with embedded temperature sensors. The front of the measurement surface area featured a vertical cylinder which generated the test signal in the form of vortex shedding with frequencies up to 4,300 Hz. To increase commonality, the tests were conducted under the same flow conditions as in the T106A turbine cascade in terms of static pressure, inflow turbulence intensity, and Mach number range. In order to generate a sufficient signal-to-noise ratio, a relatively high heating power of up to $2.7\,\mathrm{kW/m^2}$ was necessary to induce a sufficient temperature gradient between the measurement surface and the flow. This was achieved with a heating layer underneath the active coating comprised of carbon nanotubes (CNT). Ultimately, the implemented setup with a high sampling rate of 40,000 Hz enabled the resolution of temperature fluctuation down to $10^{-5}\,\mathrm{K}$ as well as pattern reconstruction of dominant coherent flow structures and their higher harmonics through SPOD analysis.
2. Utilizing a Fourier law approach, the normalized convective heat transfer coefficient (HTC) was calculated based on the measured surface temperature fields and the embedded internal temperature sensors. While thermal radiation can be neglected in the present temperature ranges, an impact on the heat transfer values due to conductive losses was found and estimated as a function of electric heating power. An accurate determination of the convective HTC would require a more comprehensive 3D heat transfer model and is the basis for a subsequent determination of wall shear stress values from the measured TSP data. However, both of these steps were beyond the scope of the initial test campaign which successfully demonstrated the application of an ultra-fast TSP setup for high-frequency resolution of small temperature fluctuation under turbine cascade relevant flow conditions.

4.7.2 Postprint

sensors

MDPI

Article

An Ultra-Fast TSP on a CNT Heating Layer for Unsteady Temperature and Heat Flux Measurements in Subsonic Flows

Martin Bitter [1,*], Michael Hilfer [2], Tobias Schubert [1], Christian Klein [2] and Reinhard Niehuis [1]

[1] Institute of Jet Propulsion, Bundeswehr University Munich, Werner-Heisenberg-Weg 39, 85577 Neubiberg, Germany; tobias.schubert@unibw.de (T.S.); reinhard.niehuis@unibw.de (R.N.)
[2] Institute of Aerodynamics and Flow Technology, German Aerospace Center, Bunsenstraße 10, 37073 Göttingen, Germany; michael.hilfer@dlr.de (M.H.); christian.klein@dlr.de (C.K.)
* Correspondence: martin.bitter@unibw.de

Abstract: In this paper, the authors demonstrate the application of a modified Ru(phen)-based temperature-sensitive paint which was originally developed for the evaluation of unsteady aerothermodynamic phenomena in high Mach number but short duration experiments. In the present work, the modified TSP with a temperature sensitivity of up to −5.6%/K was applied in a low Mach number long-duration test case in a low-pressure environment. For the demonstration of the paint's performance, a flat plate with a mounted cylinder was set up in the High-Speed Cascade Wind Tunnel (HGK). The test case was designed to generate vortex shedding frequencies up to 4300 Hz which were sampled using a high-speed camera at 40 kHz frame rate to resolve unsteady surface temperature fields for potential heat-transfer estimations. The experiments were carried out at reduced ambient pressure of p_∞ = 13.8 kPa for three inflow Mach numbers being $Ma_\infty = [0.3; 0.5; 0.7]$. In order to enable the resolution of very low temperature fluctuations down to the noise floor of 10^{-5} K with high spatial and temporal resolution, the flat plate model was equipped with a sprayable carbon nanotube (CNT) heating layer. This constellation, together with the thermal sensors incorporated in the model, allowed for the calculation of a quasi-heat-transfer coefficient from the surface temperature fields. Besides the results of the experiments, the paper highlights the properties of the modified TSP as well as the methodology.

Keywords: ultra-fast temperature-sensitive paint; time-resolved heat transfer; subsonic cylinder flow; vortex shedding modes

Citation: Bitter, M.; Hilfer, M.; Schubert, T.; Klein, C.; Niehuis, R. An Ultra-Fast TSP on a CNT Heating Layer for Unsteady Temperature and Heat Flux Measurements in Subsonic Flows. *Sensors* **2022**, *22*, 657. https://doi.org/10.3390/s22020657

Academic Editors: Yasuhiro Egami, Hiroki Nagai and Yu Matsuda

Received: 1 December 2021
Accepted: 14 January 2022
Published: 15 January 2022

1. Introduction

The non-intrusive detection of surface temperature and pressure fields was boosted in the last decades through the introduction and further development of coatings containing sensitive luminophores. A wide variety of temperature- and pressure-sensitive paints is currently available, covering nearly all fields of experimental fluid mechanics ranging from microscopic to macroscopic and from low-speed to high Mach number flows as recently summarized in Liu et al. [1]. Nearly 40 years ago, the development started with paints which were able to measure steady or quasi-steady distributions of surface quantities. Through the last years, the rising demands on unsteady data for validating modern time-resolved computational methods such as Large-Eddy Simulation has motivated the development of new paints capable of providing this data. Matsumura et al. are one of the pioneers in measuring quantitative unsteady temperature fields [2]. A review of recent achievements in the field of unsteady PSP & TSP is given in [3].

Unfortunately, the majority of available luminophores used for these paints has a certain sensitivity to both, pressure and temperature, which somehow affects the accuracy of the final result [1]. To reduce pressure dependency in a TSP, the luminophores are usually encapsulated into binder materials such as poly-amide (PA), poly-urethan (PU) or nylon

(Ny), resulting in higher layer thicknesses which reduce the response time of the active layer due to increased temperature penetration time through the binder. In contrast, these compositions allow for stronger emission intensities and better signal-to-noise ratio (SNR).

The original version of the ultra-fast-response TSP used in the present work, was initially designed for its application in short-duration facilities generating high enthalpy flows such as the High Enthalpy Shock Tunnel Göttingen (HEG) [4–7]. Typically, such facilities allow for short-duration flow experiments in the order of milliseconds, but expose strong temperature gradients. These applications call for TSPs which can react ultra fast but do not necessarily need to be very sensitive because the strong temperature gradients provide high SNR.

The original TSP had a temperature sensitivity of about −3%/K, being a slightly more sensitive kind of paint compared to other luminophores such as Europium or Ruthenium complexes. Ozawa and Lawrence [8] employed Ru(phen) as luminophor embedded in an ethanol-soluble PA-based polymer to measure the short-duration heat flux on a generic re-entry capsule during supersonic flow in a shock tube. They resolved flow structures in the low microsecond range as the sampling rates were as high as 180 kHz during their tests. Such high recording rates determine low integration times which, in turn, require enormous amounts of optical excitation power. As examined for organic silicon polymers by Sharma et al. [9], a strong increase in excitation energy typically is closely linked to the raise of introduced thermal energy which both cause a remarkable photo-degradation of the luminophores even during the short duration experiment.

Apart from high-enthalpy flow facilities, TSPs are widely used in large industrial wind tunnels, e.g., for transition detection of boundary layers on airfoils or wings. A heated model surface is widely used to increase the SNR in such a TSP application. Klein et al. [10,11], developed a sprayable heating layer based on carbon nanotubes (CNT) which can be applied in a homogeneous and even layer onto a model surface. A voltage is applied to the CNT layer, whose high electrical resistance leads to a well controllable and homogeneously heated surface.

The main intention of this paper is to introduce a modified version of the original TSP, which is well suited for long-lasting experiments in subsonic flows. The goal is to combine an increased paint sensitivity with a CNT heating layer to reach high SNR. This paper will demonstrate, (a) the ability of that TSP to resolve high-frequency but low-temperature fluctuations under subsonic flow conditions and, (b) that these (unsteady) surface temperature fields are suited for quantitative heat transfer estimations. The following sections introduce paint specific characteristics as well as the experimental demonstration test case, which is a cylinder mounted on a flat plate and being exposed to cross flow.

2. Modified Fast-Response Temperature Sensitive Paint

As stated above, for the desired test cases in this paper, both, the sensitivity and the SNR of the TSP had to be improved to enable the resolution of low-temperature fluctuations. In [12], Schramm and Hilfer reported on the experimental investigation of response time of similar Ru(phen) and polyamide-based type TSP with temperature sensitivities above −5%/K and overall TSP-Layer response time τ around 3 µs. The utilized Ru(phen) was the Dichlorotris (1,10-phenanthroline) Ruthenium(II) hydrate 98%, with a lifetime of 1 µs.

Typical absorption and emission spectra of the luminophor are shown in Figure 1. Ru(phen) can be excited over a range of wavelengths with a maximum around 450–460 nm. Emission maximum of Ru(phen) is found around 600 nm. Based on the investigations in [12] an implementation of this TSP-system was considered for subsonic and transonic facilities with highly unsteady flows. Until recently, most of the TSP-investigations in sub- and transonic wind tunnels concentrated on steady flows using luminophores with relatively long response time of around 100 µs in case of Europium-based luminophores, compare listed values in the appendix of Liu et al. [1]. Additionally, the luminophores are usually embedded in relatively thick active layers above 30 µm which allows for higher emission intensities but reduces the response time of the active layer due to high temperature

penetration time through the active layer. Recently, Miozzi et al. [13] showed the ability of Europium based paint to resolve unsteady flow phenomena in a water channel with frequencies up to 200 Hz. Natural wall temperature variance between different boundary flow regimes is usually quite low and can be calculated according to [14] using the recovery factor r for turbulent and laminar flow as follows:

$$T_{aw} = T_{\infty} \cdot \left[1 + \frac{r(\gamma - 1)}{2} \cdot Ma_{\infty}^2\right] \quad (1)$$

where $r_{tur} \propto Pr^{1/3}$ is the turbulent and $r_{lam} \propto Pr^{1/2}$ the laminar recovery factor. In order to increase the temperature variance, a temperature difference between the model and the flow has to be applied so the convective heat transfer coefficient α can be employed instead of recovery factor calculation with $\alpha_{tur} > \alpha_{lam}$ [15]. This can be accomplished by heating or cooling the model or the medium. In this work, a heating of the model surface is accomplished using spray-able carbon nanotubes (CNT) heating layer as developed by Klein et al. [10,11]. The thickness of the CNT layer being ≈40 µm was adjusted according to a desired electrical resistance. Applying a voltage, which typically ranges up to 120 V, heats up the surface. The conducting CNT layer must be insulated from the top surface against accidental contact by experimenters and against short circuit from metal parts inside the model. Therefore, the CNT-Layer was embedded in between two uniformly distributed PU-based insulation layers of about 20 µm thickness each.

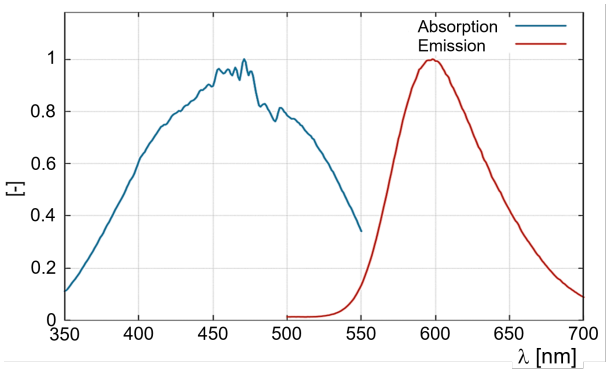

Figure 1. Emission and excitation spectra of Ru(phen) embedded in the nylon matrix which was dissolved in ethanol to be spayed on a sample by spray gun.

In order to resolve fast flow changes using TSP three main characteristics have to be evaluated and optimized. For one, the thickness of the active layer has to be reduced to a minimum. In the present setup, the thickness of the active layer, which was applied by a conventional Sata HVLP spray gun with 1 mm nozzle diameter, is measured to be around 1 µm ± 0.2 µm using a Perthometer (Mahr Perthometer S2 with MarSurf GD 25). The surface roughness of the active layer was measured to be $R_a \approx 0.1$ µm. With thinner layers the emission intensities are significantly reduced assuming constant excitation intensity. For the emission to be still detectable, better cameras or more powerful excitation sources are required. The second consideration is the temperature sensitivity of the active layer, where higher temperature sensitivity allows for a resolution of lower temperature changes. Also, flow characteristics which are faster than the complete temperature diffusion time of the TSP layer can be resolved, since even a partial diffusion is still detectable in this case. In a series of tests, Schmid et al. [16] found the optimal paint composition for highest temperature sensitivity to be at −5.4%/K. The emission spectra changing with calibration temperature are depicted on the left in Figure 2 for the most promising composition.

Last but not least, an important consideration is the pressure dependency of the luminophor. Ru(phen)-based luminophores are usually pressure sensitive. For a luminophor to be pressure sensitive it has to have the ability to transfer energy from the exited molecule to the oxygen molecule without generating an emission photon in the visible range. In

the present case the luminophores are embedded in a nylon matrix with very low oxygen permeability. The polymer was modified by the vendor to be soluble in ethanol. On the right in Figure 2 the pressure dependency of the modified paint is presented. Freshly applied to a paint sample and immediately calibrated in a static calibration chamber, a 3 micron active layer shows a maximal pressure dependency of up to ≈8%/100 kPa. A second set of samples was allowed to dry for several hours under dark ambient conditions. After drying and restrained illumination, the pressure dependency of the sample with 1 micron active layer dropped to about 0.5%/100 kPa. The next chapter presents the paint characteristics which were examined during the in-situ calibration directly on the model in the test section.

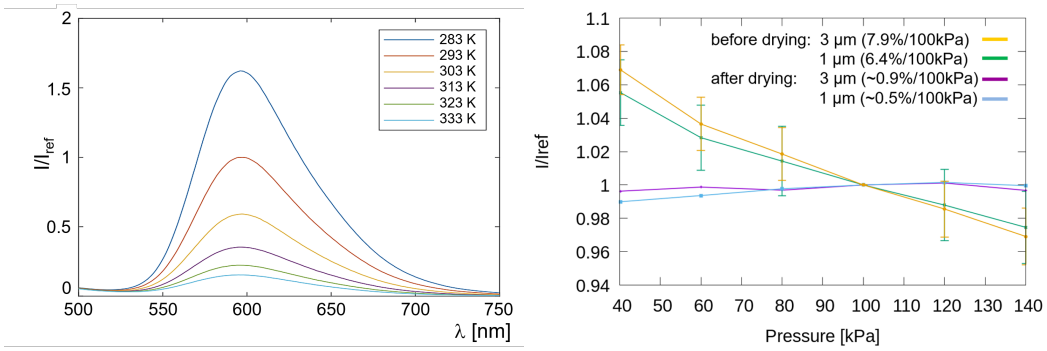

Figure 2. (**Left**) Emission spectra for TSP calibrated at p_{ref} = 100 kPa for various temperatures. (**Right**) pressure dependency of TSP for different layer thicknesses, before and after drying and illuminating, from [17].

3. Test Environment and Methodology

3.1. Experimental Setup

For the demonstration of the paint's ability to resolve high-frequency low-temperature fluctuations in subsonic flows, a flat plate wind tunnel model made from aluminum was used, as illustrated in Figure 3. The measurements were carried out on the surface of a poly-urethane (PU) part, inserted in the upper surface of the model. The PU-insert has a machined pocket of 100 µm depth which holds the various coating layers as sketched in the detail of the figure. Two thin copper film conductors were integrated into the pocket to evenly supply the electrical heating power to the carbon nanotube layer, see [11].

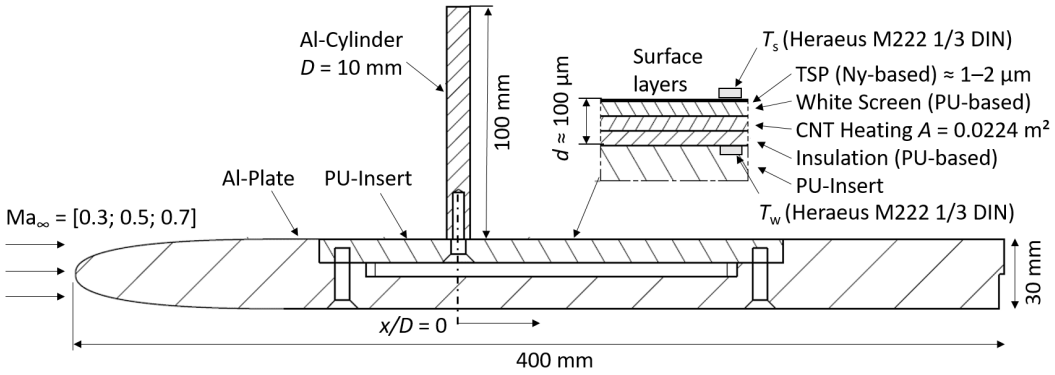

Figure 3. Flat-plate test specimen for the high-speed TSP measurements in the wind tunnel. Layer dimensions not to scale.

Two static RTDs of type Heraeus M222 1/3 DIN with 0.1 K accuracy were used to determine reference temperatures during the TSP measurements. One sensor (T_s) was fixed on top of the measurement surface using arctic silver glue. The installation was located outside the interesting wake flow field because it formed a tiny bump of about 1 mm height which may also slightly affect the accuracy of the measured recovery temperature. The

second sensor (T_w) was integrated in the PU-insert, just underneath the insulation layer. From practical reasons, both sensors were located at a distance of $x/D = 7$ downstream of the cylinder. An aluminum cylinder of D = 10 mm is mounted approx. 135 mm downstream of the leading edge. It has a height of 100 mm which widely impeded strong 3d-interaction with the tip. The cylinder was electrically insulated against the first surface layer to prevent a short circuit with the high currents from the heating layer. However, this thin electrical insulation does not provide a high thermal insulation, which can lead to thermal currents from or into the cylinder as discussed further in the next section. The cylinder is supposed to generate high-frequency temperature fluctuations, which will be captured in the ensuing TSP measurements.

The experiments in this work were conducted in the High-Speed Cascade Wind Tunnel (HGK) of the Institute of Jet Propulsion at the Bundeswehr University Munich [18]. The HGK test facility is a continuously operating, open loop wind tunnel. The main components of the wind tunnel are located inside a cylindrical pressure chamber, which enables an independent Mach and Reynolds number variation through the variation of the ambient pressure down to approx. 3.5 kPa at minimum.

The flat plate, as it was set up in the wind tunnel test section including the required test equipment, is shown in Figure 4. Five high-power LED emitters (type Luminus CBT-120) with 20 W optical output each were equipped with band pass filters with λ_{LED} = 450 ± 40 nm and focused on the region of interest for a homogeneous TSP excitation even at low integration time. The high-speed camera (type Phantom V2640) for image data acquisition was equipped with a 570 nm long-pass filter. It was set up at a working distance of about 300 mm from the flat plate and was tuned to capture the TSP fluorescence at a frame rate of 40 kHz over a sequence length of 1 s.

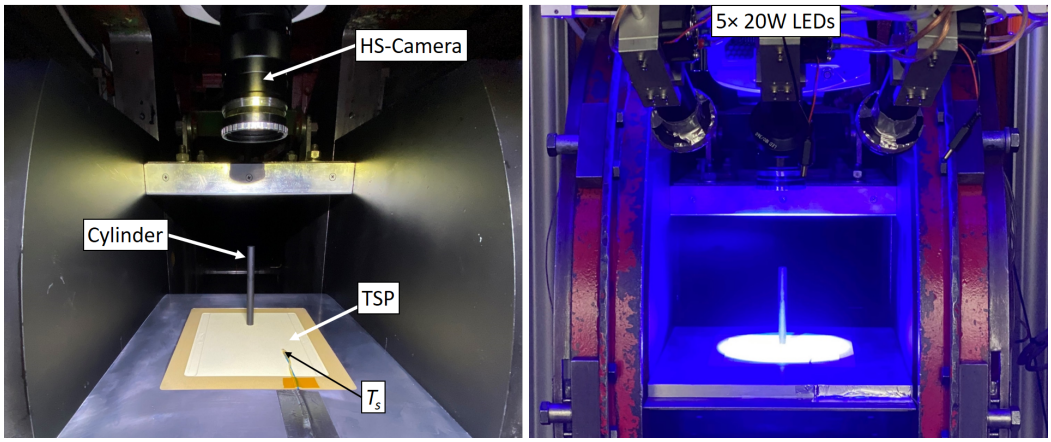

Figure 4. Experimental setup and test equipment for the high-speed TSP measurements in the wind tunnel facility.

3.2. Methodology

3.2.1. Operating Conditions

As one of the main intentions of the test series was to demonstrate the ability of the TSP to precisely resolve low-amplitude surface temperature fluctuations in order to enable time-resolved heat transfer measurements in sub sonic flows, the tests were conducted for three different inflow Mach numbers $Ma_\infty = [0.3; 0.5; 0.7]$ at a constant ambient pressure of 13.8 kPa. The changing inflow conditions relate to different Reynolds numbers based on the diameter of the cylinder. All aerodynamic operating conditions are listed in Table 1. The Prandtl number was assumed constant at Pr = 0.74.

3.2.2. TSP Calibration

The intensity response which was finally applied for the calculation of the temperature field was in-situ calibrated directly on the flat plate model. In order to re-check for a po-

tential pressure-dependency of the paint as outlined above, the calibration was performed at atmospheric pressure p_∞ = 95.3 kPa and at operating pressure p_∞ = 13.8 kPa while the wind tunnel was at rest.

Table 1. Aerodynamic operating conditions for the high-speed TSP measurements. Adiabatic wall temperatures assume turbulent boundary layer states at the position of the reference sensor and a recovery factor of $r = 0.91$ for all operating points.

Ma_∞	Re_D	p_∞ [kPa]	q_∞ [kPa]	p_t [kPa]	u_∞ [m/s]	T_t [K]	T_{aw} [K]	f_{shed} [Hz]
0.3	95k	13.8	0.89	14.7	102.1	293.15	292.7	1850
0.5	165k	13.8	2.57	16.4	167.4	293.15	291.9	2760
0.7	245k	13.8	5.35	19.1	229.5	293.15	290.8	4320

Figure 5 shows the in-situ calibration curves, where the surface temperature was tuned by heating the model and the intensity data was picked in the vicinity of the surface temperature sensor T_s which served as reference. The reference condition was at ambient pressure p_{ref} = 13.8 kPa and surface temperature $T_{ref} = 22\,^\circ$C. The Ru(phen)-based TSP applied to the model exhibits its highest sensitivity of about -5.6%/K at atmospheric conditions. However, even under low-pressure conditions it is remarkably high at about -4.7%/K. Contrary to the results presented in the section above, the applied paint composition still exhibits a slightly higher pressure dependency of 2.8%/100 kPa after drying and before testing. It is expected that the drying time was slightly less compared to the paint samples due to the tight test schedule. Due to the fact that the experiments were carried out under low pressure conditions and under the assumption that the pressure fluctuations in the cylinder wake are 15% of the dynamic pressure according to [19], this would lead to maximum pressure amplitudes of about 750 Pa, compare Table 1. At the available sensor saturation of about 2300 cts , the pressure fluctuations would lead to intensity fluctuations below 0.5 cts (i.e., 0.48 cts) which cannot be adequately resolved by the camera. Accordingly, the pressure dependency is expected to have no relevance on the accuracy of the TSP temperature fields from these demonstration tests.

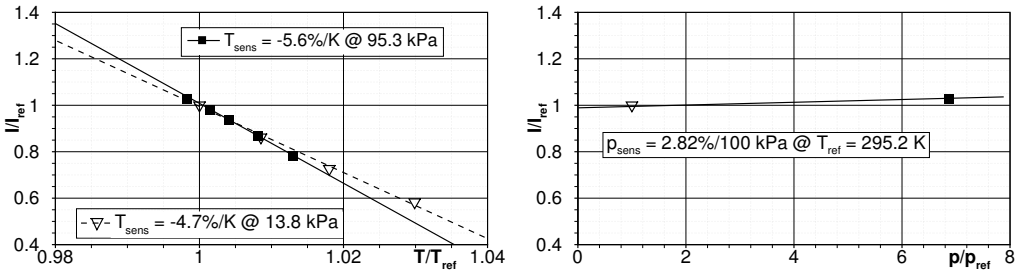

Figure 5. In-situ calibration curves for Ru(phen)-based Temperature Sensitive Paint under different ambient pressures showing the temperature sensitivity (**left**) and the pressure dependency (**right**).

3.2.3. Image Acquisition and Data Reduction

The TSP suffers degradation from intense excitation resulting in reduced luminosity, which was the main motivation to keep the acquisition sequence short (i.e., in the range of seconds) and thereby enable testing at multiple operating points. The 40 kHz camera frame rate (i.e., 40,000 wind-on images over 1 s sequence length; 1000 images at reference) determined an effective sensor area of 333 × 1530 px^2. The integration time t_i was varied between 24 µs for $Ma_\infty = 0.3$ and 15 µs for $Ma_\infty = 0.7$. The LEDs were allowed to warm up for 0.1 s prior of the image acquisition and operated continuously during the sequence. All relevant image system conditions are listed in Table 2.

Table 2. Operating conditions of the imaging system for the high-speed TSP measurements.

FOV $[px]$	Frame Rate [Hz]	t_{seq} [s]	λ_{LED} [nm]	λ_{em} [nm]	t_i [µs]
333×1530	40,000	1	450 ± 40	570 LP	[15; 20; 24]

Each operating point was started with a wind-on image set at $q''_{el} = 0$ followed by up to 4 image sets of various heating settings. Directly after the last heating point was measured, the TSP reference images were acquired under wind-off conditions. During each set point, all relevant parameter—including the start/stop trigger of the imaging system and the LED trigger were logged in the wind tunnel data system. This sensor data was up-sampled and made available at every single intensity image through post-processing. The minimum and maximum heating settings are listed in Table 3.

Table 3. Min./max. thermal conditions for the individual inflow conditions.

Ma_∞	U [V]	I [A]	q''_{el} [W/m^2]	T_s [K]	T_w [K]
0.3	[0; 85]	[0; 0.41]	[0; 1556]	[294.8; 307.5]	[295.4; 317.1]
0.5	[0; 110]	[0; 0.53]	[0; 2603]	[293.3; 308.2]	[293.7; 321]
0.7	[0; 110]	[0; 0.54]	[0; 2652]	[290.6; 302.1]	[291.1; 313]

The original spatial resolution of the intensity images was reduced by a factor of 16 (i.e., 4 pixel in x- & y-direction were binned together) in order to handle the whole data stack in memory for image processing. An effect of the binning on fundamental findings in the results is not expected because all dominant structures in the flow were still resolved as shown later in the Mode 1 energy spectra.

The absolute surface temperature T_{TSP} was retrieved from a second order polynomial in-situ fit which was applied to the intensity ratio I_{ref}/I at each set point. The offset between the raw TSP temperatures and the T_s readings was calculated in the vicinity of T_s which was still visible in the field of view (FOV). This offset was simply subtracted from the entire raw TSP temperature map.

Every test case was mainly analyzed in the frequency domain in order to emphasize the paint's ability to measure high-frequency but low-amplitude temperature fluctuations. To recover the local amplitudes, a standard windowed FFT as implemented in Matlab was used. The full signal (40,000 samples) was chopped into consecutive segments of 4000 samples. The segments had an overlap of 50% (i.e., 2000 samples). Hence, 19 segments were Fourier-transformed and finally averaged. The frequency resolution was 10 Hz. Additionally, the usage of the spectral proper orthogonal decomposition (SPOD), as presented by Towne [20], enables the separation of dominant characteristic modes in the flow field and calculates their spatial and temporal development. This method was applied to reconstruct the dominant vortex shedding modes expected to occur at a reduced frequency (or Strouhal number) of $Sr \approx 0.2$. The spatial and temporal resolution of these dominant shedding frequencies and even their higher harmonics called for the high-kilohertz frame rates.

3.2.4. Heat Transfer Coefficient

It is known, that precise heat transfer coefficient (HTC) measurements using heated surfaces are challenging with respect to the precise distinction of the conductive, convective and radiative portions of the heat flux, compare e.g., [21–23]. The work of Estorf [24] emphasizes the calculation of the complex multi-lateral heat fluxes through a finite model in order to estimate high-accuracy heat fluxes from image-based temperature fields. The individual portions sum up to the total electric power introduced into the system as follows:

$$q''_{el} = q''_{conv} + q''_{cond} + q''_{rad}. \tag{2}$$

The quantitative heat transfer coefficient α is expressed by:

$$\alpha = \frac{q''_{conv}}{T_{TSP} - T_{aw}} \tag{3}$$

by means of the convective exchange between the surface and the flow q''_{conv}, the measured surface temperature T_{TSP} and the adiabatic wall temperature T_{aw}. Anyhow, since the methodology behind a fully comprehensive estimation of all portions is rather complex and would be out of the scope of the work presented here, the simple and widely used Fourier law will be applied. The authors are aware that there are multiple approaches which can be used in order to improve the accuracy of the measured HTC. Unfortunately, plenty of them are computationally highly demanding, such as proposed e.g., by [21]. The Fourier law as used in Temperature-Sensitive Paint applications e.g., by [2,22,25,26] for estimating q''_{conv} formulates as follows:

$$q''_{conv} = k/d \cdot (T_w - T_{TSP}) \tag{4}$$

where k is the thermal conductivity, d the thickness of the corresponding heated layer and T_w the internal wall temperature. In order to keep the conductive losses into the model small and, in turn, assure validity of a 1 d heat transfer model at a first glance, low thermal conductivity of the model's base material is essential. The chosen PU (Obomodulan Sahara) for the insert exhibits a high mechanical strength to withstand the aerodynamic forces and it has a reasonable low thermal conductivity of k = 0.233 W/mK compared to aluminum whose value is about thousand times larger. Hence, it is expected, that the electrical heating power nearly completely turns into convective heat flux. The conductive and radiative fluxes q''_{cond} and q''_{rad} were neglected.

The adiabatic wall temperature is usually retrieved from a local surface pressure or Mach number distribution correlated with the boundary layer condition by using the according recovery factor in Equation (1). As the flat plate model suffered from missing surface pressure taps and as the investigated flow field is widely three-dimensional and highly dynamic, this approach was not productive here. Hence, the steady T_{aw} distribution was estimated from the averaged temperature fields for various heating settings at each aerodynamic operating point as follows:

1. An electric voltage setting was applied to the CNT layer which results in a heated surface. The model was allowed to stabilize its conditions which were monitored by the internal and external sensors T_w and T_s.
2. The heat flux q''_{el} was calculated from the current and voltage given by the power supply according to $q''_{el} = U \cdot I / A_{CNT}$.
3. The surface temperature was measured with TSP and averaged at each q''_{el} set point.

Finally, a linear fit function T_{TSP}-vs.-q''_{el} was applied to every pixel in the field of view. The intersect value of each fit at $q''_{el} = 0$ delivered the local adiabatic wall temperature. Figure 6 presents the determination coefficient R^2 as a measure of the goodness of the linear fit for $Ma_\infty = 0.5$ and $Ma_\infty = 0.7$. (Note: for the $Ma_\infty = 0.3$ test case the authors performed two other heating settings apart from the adiabatic case $q''_{el} = 0$. Hence, the determination coefficient for a linear approximation is $R^2 = 1$ per definition.)

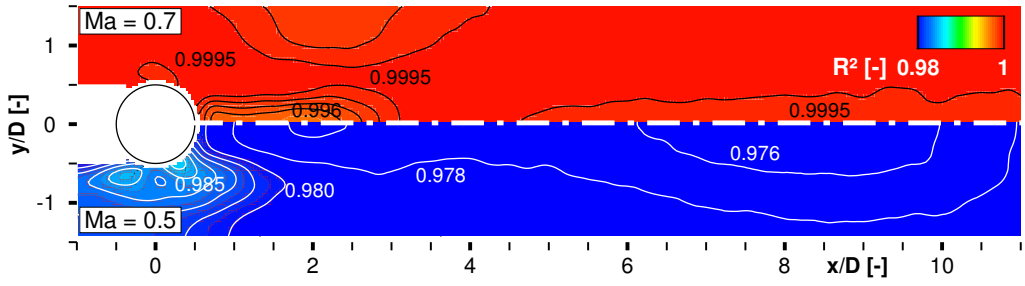

Figure 6. Determination coefficient R^2 of linear fit T_{TSP}-vs.-q''_{el} for estimation of the adiabatic wall temperature T_{aw} compared for $Ma_\infty = 0.7$ and $Ma_\infty = 0.5$.

The plot shows a very good correlation $R^2 \rightarrow 1$ between the heating power and the measured surface temperature, slightly better for $Ma_\infty = 0.7$. As a consequence of the cylinder being made from aluminum and the weak thermal insulation, a slightly different fit quality and hence a larger uncertainty in the estimated adiabatic wall temperature is present in the near vicinity of the cylinder. The white area upstream of the cylinder were masked out due to shadowing.

4. Results

At first, a result of the SPOD analysis shows the T' amplitude spectrum of the mode with the highest energy content in Figure 7 for all three test Mach numbers. All spectra reveal a dominant peak in the region of $Sr \approx 0.17$ and a second weaker one around $Sr \approx 0.34$. The Strouhal numbers were calculated based one the shedding frequency f_{shed}, the cylinder diameter D and the free-stream velocity u_∞ from Table 1. Most likely, the representative velocity might not be the inflow velocity in this case but slightly less. Based on the fact, that TSP measures a wall-bounded footprint of flow structures which widely move inside the boundary layer of the turbulent cylinder wake, the Sr values may be slightly less than the expected values of 0.2, compare [19,27]. The sudden expansion of the open test section downstream of the pitot probe at the test section inlet may be another reason. Anyhow, for this Ru(phen)-based TSP it can be stated that the noise floor for detecting temperature amplitudes is in the order of 10^{-5} K when using averaging spectral approaches. (Note: For $Ma_\infty = 0.3$, the peak at $Sr = 0.34$ highly likely collapses with the noise floor and cannot be clearly resolved.)

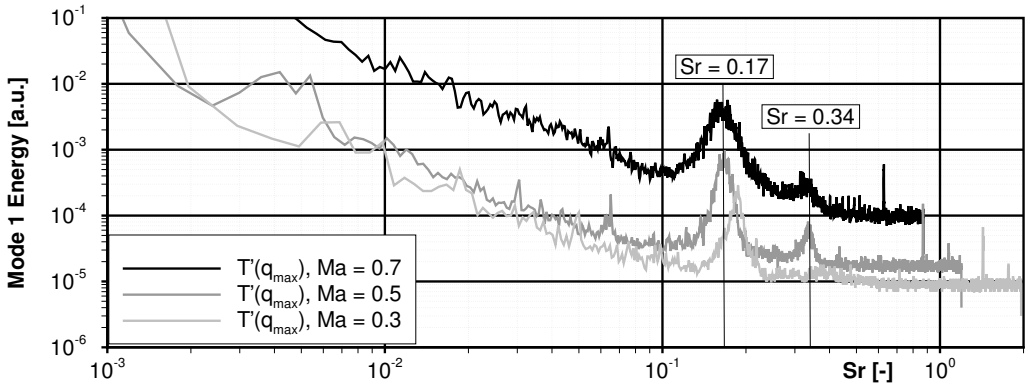

Figure 7. Mode 1 energy spectra for all inflow Mach numbers calculated by means of a spectral proper orthogonal decomposition.

As a second result of the SPOD analysis, the spatial development of the dominant vortex shedding and its higher harmonic was calculated for $Ma_\infty = 0.7$ as exemplary depicted in Figure 8. The pattern in the upper plot shows a highly resolved alternating von-Kármán vortex street in the wake, whereas the dominant structures start to establish from $x/D \approx 2$. Their inclined appearance is the consequence of the local convection velocity which is lower inside and higher outside of the cylinder wake. The lower plot displays the reconstructed footprint from the first harmonic of the coherent structures as they develop at $Sr = 0.34$. Halving of the structures' spatial dimension that coincides with a doubled frequency is clearly observable comparing both plots. Reconstructed time series data showing the temporal development of the characteristic modes can be provided as supplementary material with this paper.

The local temperature fluctuation amplitudes in the FOV at $Sr = 0.17$ for the highest and lowest test Mach number close the spectral analysis of the coherent structures as well as the discussion of the paint's potential to resolve low-amplitude temperature fluctuations. Figure 9 shows the fluctuation amplitudes and the corresponding phase angles as a result of the windowed FFT comparing $Ma_\infty = 0.3$ and $Ma_\infty = 0.7$. Both, higher fluctuation amplitudes and a downward shifted position of the local maximum is expected and evident

for $Ma_\infty = 0.7$. The widening of the wake which is coupled with an outward transportation of the dominant structures was clearly resolved. The evaluation potential of the available data set is fairly inexhaustible. Unfortunately, a deeper fluid-mechanical interpretation would be out of scope of the present paper but will be focused in a projected paper following this work.

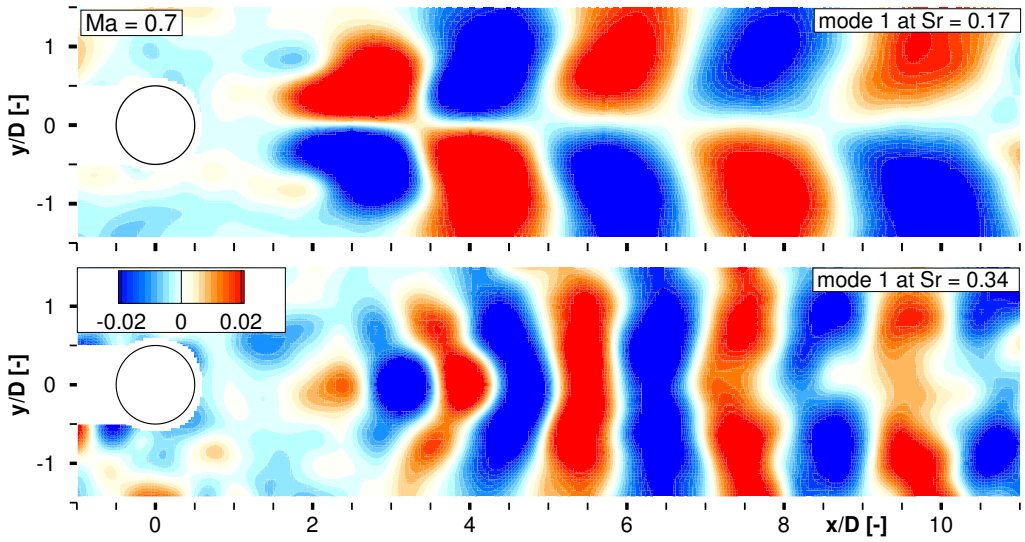

Figure 8. Reconstruction of characteristic flow patterns at $Sr = 0.17$ (**top**) and $Sr = 0.34$ (**bottom**) for $Ma_\infty = 0.7$.

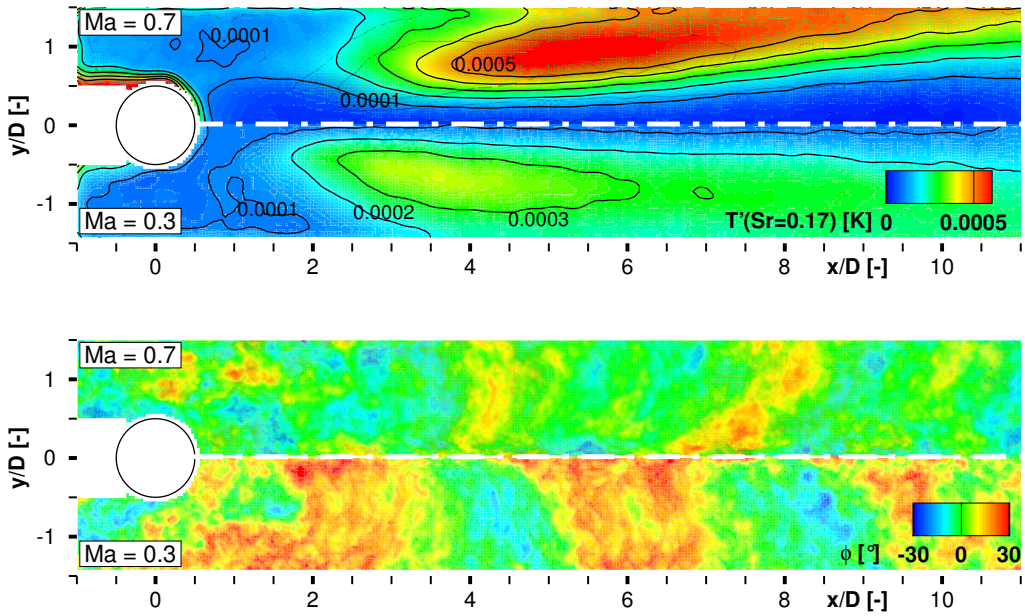

Figure 9. Local temperature fluctuation amplitudes (**top**) and phase angle ϕ (**bottom**) at $Sr = 0.17$ compared for $Ma_\infty = 0.3$ and $Ma_\infty = 0.7$.

Finally, the measured surface heat transfer will be discussed, whose estimation from the TSP fields was the second major goal of this campaign. The discussion is started with the adiabatic wall temperature fields, which were calculated from the local fit method outlined above. Figure 10 shows the result of the T_{TSP}-vs.-q''_{el} fitting for $Ma_\infty = 0.5$ and $Ma_\infty = 0.7$. The field plots for T_{aw} show a strong foot print of the 3-d wake flow. Note the individual color levels of both plot halfs.

The temperatures in the outer parts of the FOV at $x/D \approx 4$ are in good agreement with the theoretically calculated adiabatic wall temperature at the surface sensor for which the corresponding inflow Mach number and a recovery factor of $r = 0.91$ (turbulent boundary layer) was relevant. The wake flow regime exhibits a lower adiabatic wall temperature compared to the undisturbed flow field due to the strong turbulent mixing between the outer flow at a static temperature of $T_\infty = [279; 266]$ K, respectively for $Ma_\infty = [0.5; 0.7]$, and the thermal boundary layer. The temperature field develops widely symmetric whereas the core of the cylinder wake extends up to $x/D \approx 2.5$. Figure 11 shows the comparison of the local thermal fluxes in the cylinder wake between $Ma_\infty = 0.3$ and $Ma_\infty = 0.5$ at the maximum heating set point $q''_{el,max}$. The displayed quantity $(T_w - T_{TSP})/(T_{TSP} - T_{aw})$ can be interpreted as normalized or quasi-HTC without acknowledging the material's thermal conductivity and the accurate wall thickness. Note that the upper half of the plot has a different color level compared to the lower part. The overall contour level is higher for $Ma_\infty = 0.5$, as expected. As the aspired layer thickness d is very thin but could only be estimated since PU being the non-conductive carrying material, small deviations in the thickness estimation would have an enormous effect on the quantitative HTC value. Knowing d and k precisely would end up in a scaling of the shown thermal flux distributions, but, unfortunately is a major topic for accurate heat transfer measurements as outlined above.

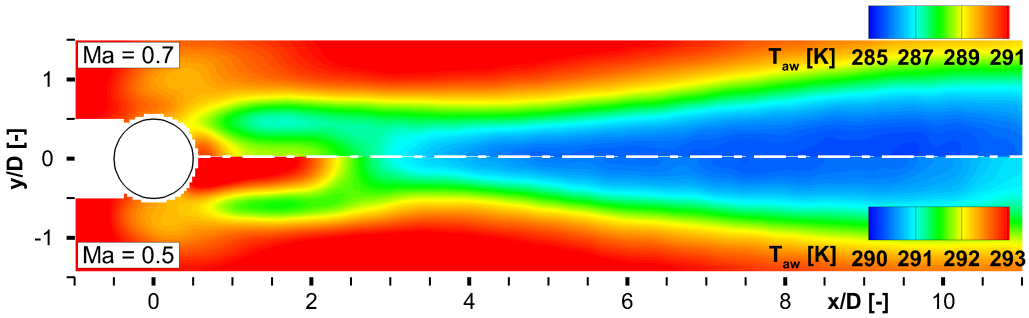

Figure 10. Adiabatic wall temperature distribution in the wake of the cylinder compared for $Ma_\infty = 0.7$ and $Ma_\infty = 0.5$.

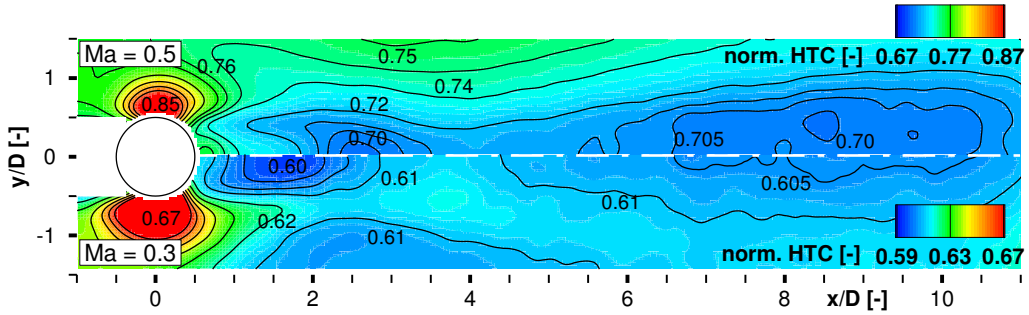

Figure 11. Quasi heat transfer coefficient norm. HTC $= (T_w - T_{TSP})/(T_{TSP} - T_{aw})$ compared for $Ma_\infty = 0.5$ and $Ma_\infty = 0.3$ at maximum el. heat flux $q''_{el,max}$.

The thermal fluxes are highest in the region of the strongest flow acceleration at the outboard sides of the cylinder for both Mach numbers. Vice versa, it is lowest in the central wake region. Further downstream from $x/D > 4$, the thermal flux values remain widely constant.

Figure 12 collects the integral normalized HTC values for all operating points. For this plot, the HTC map as displayed in the previous figure was calculated for each operating point and averaged over the entire FOV. The integral values were plotted versus the electrical heat flux q''_{el}. The expected trend of rising HTC with increasing Mach number is clearly evident. In case the assumption of the simple Fourier law holds, the HTC should be constant per definition throughout each Mach number for every electrical heat flux as

indicated by the dotted line for $Ma_\infty = 0.5$ or the dashed line for $Ma_\infty = 0.7$, respectively. As the HTC values decrease slightly for raised heating powers, it is concluded, that the internal conductive loss flux q''_{cond} cannot be neglected. The heat loss was estimated in a first glance from the percentage drop of the HTC values as indicated by the numbers in the figure. Calculating the slopes for the losses at both Mach numbers, conductive losses of about 9.5% per 1 kW/m^2 heating power were estimated.

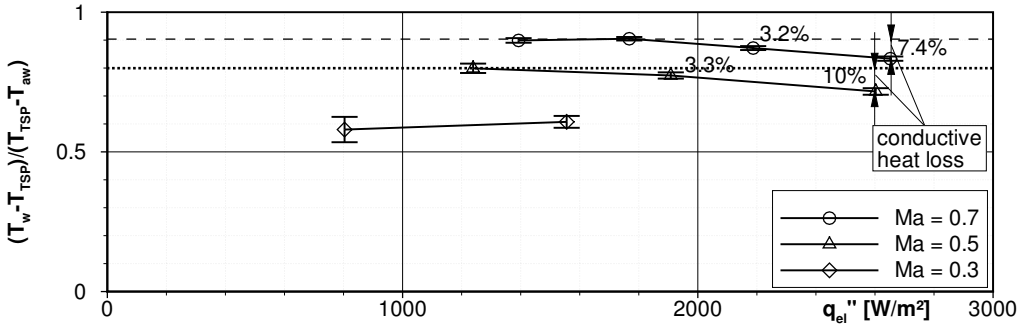

Figure 12. Integral quasi-HTC for all tested operating points including conductive loss approximation.

As stated above, this paper is entirely focused on the measurement of high-frequency but low-temperature fluctuation and the usage of such fields to recover heat transfer coefficients. The motivation of this paper does not raise a claim in a low-uncertainty heat flux estimation, at all. The former two were demonstrated with convincing results as discussed so far. In case the latter is of interest, there were some approaches mentioned above but many more can be found in literature. In principle, the application of the proposed method, so far, enables the calculation of unsteady HTC-fields as well. Anyhow, the fundamental discussion of such results and their comparison to the steady HTC fields would not deliver any deeper substantial insights. Therefore, it will be avoided at this point. In any way it should be noted that the test specimen, which will be used for such measurements and which was equipped with steady RTDs during the experiments presented here, should be equipped with reference thermocouples being able to follow the high-frequency temperature fluctuations - at least on the model surface. This would allow for the precise determination of high-frequency surface temperatures or HTC, similar as presented for unsteady PSP by Bitter et al. [28].

5. Summary and Outlook

This paper presents the characteristics and performance of a modified version of an ultra-fast Ru(phen)-based temperature-sensitive paint whose composition was tuned to resolve low-temperature but high-frequency flow events in subsonic flows. The modified paint revealed a higher temperature sensitivity of up to −5.6%/K and a fairly low pressure dependency of 2.8%/100 kPa.

An experimental test series was carried out at subsonic inflow conditions and reduced ambient pressure of 13.8 kPa in the High-Speed Cascade Wind Tunnel of the Bundeswehr University in Munich. For the demonstration of the paint's potential, a cylinder of D = 10 mm was mounted on a flat plate model and exposed to inflow Mach numbers ranging from $Ma_\infty = 0.3$–0.7. The test case was designed to generate vortex shedding frequencies up to 4300 Hz which had to be recognized by the modified TSP. The wall-bounded temperature footprint around the cylinder and in the wake was measured with a high-speed TSP system capturing intensity images at 40,000 Hz frame rate.

The generation of a sufficiently high SNR, which enables the detection of the low-temperature fluctuations during the TSP measurement, was realized applying a sprayable carbon nanotube heating layer underneath the active coating. The CNT layer which acts like an electrical resistance and consequently heats up if a voltage is applied. Doing so, a heating power up to 2600 W/m^2 was applied to the CNT layer to increase the temperature difference between the flow and the model surface by up to 10 K.

The results clearly reveal that the utilized combination from the modified ultra-fast TSP with the CNT-layer was generating sufficient SNR which enables the detection of temperature fluctuations down to a noise floor of 10^{-5} K. The frame rate of 40 kHz was sufficiently high to resolve and reconstruct the pattern of dominant coherent structures over all investigated subsonic flow Mach numbers.

Special attention was devoted to the derivation of the (unsteady) heat transfer coefficient from the measured TSP fields. The authors were aware of the challenge and potential methods to calculate high precision heat fluxes. However, a first-order Fourier approach was applied at a first glance to generate a quasi-HTC from the measured temperature fields and a temperature sensor incorporated into the model. Especially, the integral quasi-HTC values revealed that there were conductive losses of around 9.5% per 1 kW/m^2 heat flux which cannot be neglected as presumed in the 1d Fourier approach. The consideration of these conductive losses by applying a sophisticated but more demanding approach may improve the HTC results significantly in future test campaigns.

This paper impressively presents the benefits of the Ru(phen)-based TSP which has high sensitivity and enables the detection of low temperature fluctuations in subsonic flows in combination with a CNT heating layer. It was also shown, that this is an attractive method to measure unsteady HTCs. At all, the discussion of a quantitative HTC with enhanced measurement accuracy was accepted to be far off the scope of this paper. Same holds for a deeper fluid-mechanical interpretation of the cylinder flow and its characteristics. This is projected to happen in an upcoming paper.

Author Contributions: Conceptualization, M.B.; methodology, M.B., M.H. and T.S.; software, M.B.; validation, all; formal analysis, M.B. and M.H.; investigation, M.B., M.H. and T.S.; CNT application, C.K.; resources, T.S., C.K. and R.N.; data curation, M.B.; writing—original draft preparation, M.B., M.H. and T.S.; writing—review and editing, all; visualization, M.B.; supervision, R.N.; project administration, R.N.; funding acquisition, R.N. All authors have read and agreed to the published version of the manuscript.

Funding: This research was partly funded by Deutsche Forschungsgemeinschaft DFG under grant number PAK 948 pt 3 and partly within DLR Project SuperCOOL.

Institutional Review Board Statement: Not applicable.

Informed Consent Statement: Not applicable.

Data Availability Statement: Selected data can be provided upon request.

Acknowledgments: We acknowledge financial support by Universität der Bundeswehr München.

Conflicts of Interest: The authors declare no conflict of interest.

Abbreviations

The following abbreviations are used in this manuscript:

CNT	Carbon nanotubes
FFT	Fast Fourier transformation
FOV	Field of view
HGK	High-Speed Cascade Wind Tunnel of the Bundeswehr University Munich
HTC	Heat transfer coefficient, quasi-HTC = $\frac{T_w - T_{TSP}}{T_{TSP} - T_{aw}}$
LED	Light-emitting diode
Ny	Nylon
PA, PU	Poly-amide, poly-urethane
P-/TSP	Pressure-/Temperature-Sensitive Paint
Ru(phen)	Dichlorotris (1,10-phenanthroline) Ruthenium(II) hydrate 98%
RTD	Resistant temperature detector
SNR	Signal-to-noise ratio
SPOD	Spectral proper orthogonal decomposition (after [20])

Symbols

α	Heat transfer coefficient $= k/d \cdot \frac{T_w - T_{TSP}}{T_{TSP} - T_{aw}}$ [W/(m^{2}K)]
A_{CNT}	Heated CNT surface area [m^2]
d	Layer thickness [µm]
D	Cylinder diameter [mm]
f	Frequency [Hz]
γ	Heat capacity ratio [-]
k	Thermal conductivity [W/(mK)]
λ	Wavelength [nm]
Ma_∞	Inflow Mach number [-]
p_∞	Ambient pressure [kPa]
p_t	Total pressure [kPa]
Pr	Prandtl number [-]
q_∞	Dynamic pressure [kPa]
q''_{el}	Electrically generated heat flux $= U \cdot I / A_{CNT}$ [W/m^2]
q''_{cond}	Conductive heat flux [W/m^2]
q''_{conv}	Convective heat flux [W/m^2]
q''_{rad}	Radiative heat flux [W/m^2]
r	Recovery factor[-]
R^2	Determination coefficient of a (linear) fit [-]
Re_D	Reynolds number based on cylinder diameter D = 10 mm [-]
Sr	Non-dimensional frequency; Strouhal number $= f \cdot D/u$
t_i	Camera integration time [µs]
T'	Temperature fluctuation [K]
T_{aw}	Adiabatic wall temperature [K]
T_t	Total temperature [K]
T_{TSP}	Surface temperature field measured with TSP [K]
T_s	Temperature at surface sensor [K]
T_w	Temperature at wall sensor [K]
u	Inflow velocity [m/s]
x; x/D	Axial; normalized axial coordinate
y; y/D	Span-wise; normalized span-wise coordinate

References

1. Liu, T.; Sullivan, J.P.; Asai, K.; Klein, C.; Egami, Y. *Pressure and Temperature Sensitive Paints*, 2nd ed.; Springer: Cham, Switzerland, 2021.
2. Matsumura, S.; Berry, S.A.; Schneider, S.P. Flow Visualization Measurement Techniques for High-Speed Transition Research in the Boeing/AFOSR Mach-6 Quiet Tunnel. In Proceedings of the 39th AIAA/ASME Joint Propulsion Conference and Exhibit, Huntsville, AL, USA, 20–23 July 2003; AIAA Paper 2003-4583.
3. Gregory, J.W.; Sakaue, H.; Liu, T.; Sullivan, J.P. Fast Pressure-Sensitive Paint for Flow and Acoustic Diagnostics. *Annu. Rev. Fluid Mech.* **2014**, *46*, 303–330. [CrossRef]
4. Laurence, S.J.; Ozawa, H.; Lieber, D.; Martinez Schramm, J.; Hannemann, K. Investigation of unsteady/quasi-steady scramjet behavior using high-speed visualization techniques. In Proceedings of the 18th AIAA International Space Planes and Hypersonic Systems and Technologies Conference, Tours, France, 24–28 September 2012.
5. Martinez Schramm, J.; Hannemann, K.; Ozawa, H.; Beck, W.; Klein, C. Development of Temperature Sensitive Paints in the High Enthalpy Shock Tunnel Göttingen, HEG. In Proceedings of the 8th European Symposium on Aerothermodynamics for Space Vehicles, Lisbon, Portugal, 2–6 March 2015.
6. Ozawa, H. Experimental study of unsteady aerothermodynamic phenomena on shock-tube wall using fast-response temperature-sensitive-paints. *Phys. Fluids* **2016**, *28*, 046103. [CrossRef]
7. Martinez Schramm, J.; Schmidt, L. Internal application of ultra-fast temperature sensitive paint to hydrogen combustion flow. In *New Results in Numerical and Experimental Fluid Mechanics XIII*; Dillmann, A., Heller, G., Krämer, E., Wagner, C., Tropea, C., Jakirlić, S., Eds.; Springer: Cham, Switzerland, 2021; pp. 121–131.
8. Ozawa, H.; Laurence, S. Experimental investigation of the shock-induced flow over a wall-mounted cylinder. *J. Fluid Mech.* **2018**, *849*, 1009–1042. [CrossRef]
9. Sharma, A.; Katiyar, M.; Deepak; Shukla, S.K.; Seki, S. Effect of ambient, excitation intensity and wavelength, and chemical structure on photodegradation in polysilanes. *J. Appl. Phys.* **2007**, *102*, 104902. [CrossRef]
10. Klein, C.; Henne, U.; Sachs, W.; Beifuß, U.; Ondrus, V.; Bruse, M.; Lesjak, R.; Löhr, M. Application of Carbon Nanotubes (CNT) and Temperature-Sensitive Paint (TSP) for the Detection of Boundary Layer Transition. In Proceedings of the 52nd AIAA Aerospace Sciences Meeting (AIAA SciTech 2014), National Harbor, MD, USA, 13–17 January 2014.

11. Klein, C.; Henne, U.; Yorita, D.; Beifuß, U.; Ondrus, V.; Hensch, A.-K.; Longo, R.; Hauser, M.; Guntermann, P.; Quest, J. Application of Carbon Nanotubes and Temperature-Sensitive Paint for the Detection of Boundary Layer Transition under Cryogenic Conditions. In Proceedings of the 55th AIAA Aerospace Sciences Meeting (AIAA SciTech 2017), Grapevine, TX, USA, 9–13 January 2017.
12. Martinez Schramm, J.; Hilfer, M. Time response calibration of ultra-fast temperature sensitive paints for the application in high temperature hypersonic flows. In *New Results in Numerical and Experimental Fluid Mechanics XII*; Dillmann, A., Heller, G., Krämer, E., Wagner, C., Tropea, C., Jakirlić, S., Eds.; Springer: Cham, Switzerland, 2020; pp. 143–152.
13. Miozzi, M.; Di Felice, F.; Klein, C.; Costantini, M. Taylor hypothesis applied to direct measurement of skin friction using data from Temperature Sensitive Paint. *Exp. Therm. Fluid Sci.* **2020**, *110*, 109913. [CrossRef]
14. Schlichting, H.; Gersten, K. *Grenzschicht-Theorie*; 10. Auflage; Springer: Berlin/Heidelberg, Germany, 2006; pp. 232–234.
15. Tropea, C.; Yarin, L.A.; Foss, J.F. *Handbook of Experimental Fluid Mechanics*; Springer: Berlin/Heidelberg, Germany, 2007; Chapter 7.4, pp. 543–547.
16. Schmidt, L. Application of Temperature Sensitive Paint to Determine the Heat Flux in a Hypersonic Hydrogen Combustion FLow. Bachelor's Thesis, DLR, Göttingen, Germany, 2021.
17. Dimond, B.D. (DLR, Göttingen, Germany); Hilfer, M. (DLR, Göttingen, Germany). Evaluation of Pressure Sensitivity of UHS-TSP. Internal communication, 2021.
18. Niehuis, R.; Bitter, M. The High-Speed Cascade Wind Tunnel at the Bundeswehr University Munich after a Major Revision and Upgrade. *Int. J. Turbomach. Propuls. Power* **2021**, *6*, 41. [CrossRef]
19. Zhang, C.; Moreau, S.; Sanjosé, M. Turbulent flow and noise sources on a circular cylinder in the critical regime. *AIP Adv.* **2019**, *9*, 085009. [CrossRef]
20. Towne, A.; Schmidt, O.T.; Colonius, T. Spectral proper orthogonal decomposition and its relationship to dynamic mode decomposition and resolvent analysis. *J. Fluid Mech.* **2018**, *847*, 821–867. [CrossRef]
21. Gomes, R.A.; Niehuis, R. Film Cooling Effectiveness Measurements on Highly Loaded Blades with Flow Separation. In Proceedings of the 8th European Conference on Turbomachinery (ETC), Graz, Austria, 23–27 March 2009.
22. Liu, T.; Cai, Z.; Lai, J.; Rubal, J.; Sullivan, J.P. Analytical method for determining heat flux from temperature-sensitive-paint measurements in hypersonic tunnels. *J. Thermophys. Heat Transf.* **2010**, *24*, 85–94. [CrossRef]
23. Aberle, S.; Bitter, M.; Hoefler, F.; Benignos, J.C.; Niehuis, R. Implementation of an In-Situ Infrared Calibration Method for Precise Heat Transfer Measurements on a Linear Cascade. *J. Turbomach.* **2019**, *141*, 021004. [CrossRef]
24. Estorf, M. Image based heating rate calculation from thermographic data considering lateral heat conduction. *Int. J. Heat Mass Transf.* **2006**, *49*, 2545–2556. [CrossRef]
25. Liu, T.; Campbell, B.; Sullivan, J. Heat Transfer Measurement on a Waverider at Mach 10 Using Fluorescent Paint. *J. Thermophys. Heat Transf.* **1995**, *9*, 605–611. [CrossRef]
26. Chen, L.; Kawase, C.; Nonamura, T.; Asai, K. Dynamic surface heat transfer and re-attachment flow measurement using luminescent molecular sensors. *Int. J. Heat Mass Transf.* **2020**, *155*, 119684. [CrossRef]
27. Lehmkuhl, O.; Rodríguez, I.; Borrell, R.; Oliva, A. Low-frequency unsteadiness in the vortex formation region of a circular cylinder. *Phys. Fluids* **2013**, *25*, 085109. [CrossRef]
28. Bitter, M.; Stotz, S.; Niehuis, R. On High-Resolution Pressure Amplitude and Phase Measurements Comparing Fast-Response Pressure Transducers and Unsteady Pressure-Sensitive Paint. *J. Turbomach.* **2021**, *143*, 031012. [CrossRef]

5 Conclusions and Outlook

A comprehensive investigation of the secondary flow in a low-pressure turbine cascade has been conducted under periodic inflow conditions generated by bar wakes. The three main research objectives stated in Chapter 1 were successfully achieved.

The first objective was to come up with a multi-methodology approach to generate a comprehensive data set. The benefit of this methodology should be evident compared to the classic secondary flow investigation approach with probe-based measurements up- and downstream of the blade passage. This was achieved by combining several innovative methods in all stages of the research project starting with an improved cascade design based on pretest CFD analysis. The main design feature was a moveable flat-plate endwall inserted at part-span of the blades. Contrary to the baseline T106 cascade, this feature enabled an independent variation of the inlet boundary layer. This resulted in more distinct secondary flow and consistent effects of the incoming wakes. Furthermore, provisions for robust implementation of advanced measurement setups provided a solid foundation for the subsequent research activities.
Initially, the flow was characterized utilizing pressure and CTA probe measurements up- and downstream of the blade passage. Subsequently, this classic investigation approach centered around probe-based measurements was extended and enhanced by the implementation of advanced optical measurement techniques inside the passage. PIV measurements were enabled by a camera endoscope guided through the cascade sidewalls to resolve the unsteady passage flow field in a blade-to-blade plane close to the endwall. The data was phase-locked and synchronized to a second PIV setup in the downstream axial plane. On the blade suction surface, unsteady Pressure-Sensitive Paint (i-PSP) was utilized to capture highly resolved pressure fields at a sampling rate of 30 kHz. To the author's knowledge, this marked the first published application of i-PSP specifically for secondary flow investigations in a turbine cascade. Also, the potential of ultra-fast Temperature-Sensitive Paint (TSP) was evaluated to provide experimental surface temperature and wall shear stress data. Even though the final application on the turbine cascade endwall could not be concluded in the present work, its potential was demonstrated using a flat-plate test case. Furthermore, a continuous combination of different experimental results and supplemental CFD clearly highlighted the added value in their synergy to form a more complete data set and therefore a more comprehensive view on the secondary flow phenomena.
Although the up- and downstream secondary flow measurements based on the classic probe-based approach provided valuable findings, the applied multi-methodology approach was crucial for the achievement of the subsequent research objectives. Especially the flow analysis inside the blade passage revealed that a sole exit flow evaluation, as commonly conducted, does not provide a complete picture. For example, the effects of periodic inflow were compared to the effects of endwall boundary layer variation as part of research objective two. Here, the findings inside the passage were quite different from the exit flow field and revealed

the underlying mechanisms. Furthermore, the synchronization of periodic flow data from different optical measurements and CFD was the basis for achieving research objective three. Thereby, the periodic flow disturbances by the incoming wakes could be related to secondary flow phenomena on the suction surface and in the exit flow field. Another example is the localization of the mean origin of the wake induced secondary flow attenuation. This was achieved by combining two perpendicular PIV planes and CFD wall shear stress data. In conclusion, the presented comprehensive multi-methodology investigation produced valuable findings beyond what is possible with a classic probe-based approach. Therefore, its benefit and further potential has been successfully demonstrated.

To achieve the second objective, the effects of periodic inflow conditions produced by incoming bar wakes on the secondary flow were quantified and analyzed extensively. In the time-averaged flow field downstream of the passage, the wakes caused an attenuation of the secondary flow. This led to a reduction in maximum values of over-/underturning as well as peak and integral secondary losses. Also, a spanwise shift of the passage vortex towards the endwall was observed. The latter correlated with a reduced size of the horseshoe vortex pressure side leg. The amplitude of these effects was not constant, but consistently increased with higher inlet endwall boundary layer thickness. Furthermore, a strong similarity was found between the wake effects and the effects of a reduction in endwall boundary layer thickness on the secondary flow. However, further analysis inside the blade passage revealed different underlying mechanisms and different effects on the secondary loss generation. Decreasing the inlet endwall boundary layer height resulted in a nearly constant reduction of the secondary- and overall loss generation. This effect started around the midpoint of the blade passage. On the contrary, the effect of periodic inflow can be summarized as a spatial redistribution between the loss components. Wake interaction with the blade boundary layer and migration of the dissipating wakes caused a premature loss increase. This was followed by an attenuation of the profile- and secondary loss generation in the aft section of the blade passage. The different mechanisms contributing to the observed secondary flow attenuation are listed below. To put the observed effects into perspective, also an increased frontal blade loading was analyzed in the T106Div with divergent endwalls. Here, the strong pressure gradients acting on the endwall flow triggered a significant secondary loss increase starting at the entrance of the passage instead of the aforementioned delayed loss increase. The change in integral overall losses downstream of the blade passage due to the altered blade loading was around one order of magnitude higher than the relatively small periodic wake effect in this regard.

The final objective was achieved by combining the phase-locked and synchronized PIV and PSP measurements. Thereby, the movement of the bar wakes was successfully traced throughout the blade passage and their 'negative-jet-effect' was analyzed across the suction surface. Here, the periodic surface pressure signals revealed a wake induced negative pressure gradient in space i.e. positive gradient in time. The effect was intensified in the secondary flow region with respect to midspan with a local maximum of plus 33 % near the passage vortex imprint. This altered the secondary flow interaction with the suction surface flow most notably by a spanwise shift of the passage vortex separation line towards the endwall. Furthermore, the dynamics of the periodic wake convection were related to two in-phase effects on the downstream secondary flow. The first was a periodic decrease of up to 12 % in passage vortex turbulent kinetic energy (TKE). The second periodic effect was an

increase in pitchwise extension which was around three times smaller than the blade wake extension. It was concluded, that the secondary flow is more resistant to direct periodic wake perturbation. The two observed effects (wider vortex with lower TKE) indicate a more diffuse secondary flow and are not represented by the common measure of penetration depth. Also, both effects exhibited a phase lag of -108° to the bar wake overlap in the measurement plane. It was concluded that the secondary flow attenuation is caused further upstream by wake interaction with the endwall boundary layer and thus the vortex formation. By re-tracing the blade-to-blade velocity field based on the phase lag, the mean origin was located just upstream of a large separation area on the endwall. This separation was triggered by the migration of horseshoe vortex pressure side leg and was significantly reduced in case periodically incoming wakes.

Overall, the following mechanism were identified as contributors to the observed secondary flow attenuation.

- The effect of periodically incoming wakes can be foremost attributed to their interaction with the endwall boundary layer. This leads to a lower boundary layer shape factor at almost constant thickness and thus increased separation robustness. As a result, the roll up of the horseshoe vortex is delayed and the development of the passage vortex by separation and entrainment of the endwall crossflow is weakened. Instead, a reduction of the endwall boundary layer thickness affects the amount of available fluid material for separation and entrainment. Lastly, an increase in blade loading increases the transverse pressure gradients acting on the endwall boundary layer. This results in stronger passage crossflow, boundary layer separation, and vortex augmentation.

- Outside of the endwall boundary layer, the passing wakes interfere with the secondary vortices and promote their dissipation. This leads to less pronounced i.e more diffuse downstream secondary flow.

- Wake-induced transition on the suction surface reduces or even suppresses the separation bubble and thus weakens the trailing vortex.

- The pitchwise movement of the incoming wakes induces a negative flow incidence which leads to a slightly lower blade loading and thus lower transverse pressure gradients.

Outlook

The identification of the different mechanisms affecting the secondary flow development provides a starting point for secondary flow considerations in a turbine design process. To sum up in a generalized statement there are two broad approaches to limiting secondary flows and the associated losses:

- The root cause of the secondary flow development can be altered by reducing the transverse pressure gradients acting on the endwall boundary layer. This can be achieved by actions such as lower/delayed flow turning i.e. blade loading near the endwall, local endwall contouring, or the use of high aspect ratio splitter blades or endwall fences.

- The effect of the root cause can be limited by reducing the supply of endwall boundary layer material for the vortex development via separation and entrainment. This can be achieved by reducing the boundary layer thickness or increasing its robustness against flow separation. The latter is one of the main mechanisms of periodically incoming wakes which induce high levels of turbulence by interacting with the inlet boundary layer.

The presented results have shown that periodically unsteady inflow conditions should be taken into account during secondary flow evaluation and the design of control methods. A method which targets a similar mechanism as incoming wakes do, will most likely not be as effective as a steady inflow evaluation might predict. One example is the use of endwall turbulators to increase the boundary layer robustness in order to limit secondary flow development and augmentation. This principal applies to multiple aspects of secondary flow development as the presented results have shown an impact on the endwall boundary layer robustness, vortex mixing, and altered interaction with the blade suction surface. The effectiveness and benefit of any method applied individually or superimposed is unique to the particular turbine flow application depending on for example inflow conditions and blade aspect ratio. Therefore, they ultimately have to be evaluated on component level by trading against potential detrimental effects on other flow aspects such as increased friction losses or weight penalties. Nevertheless, the effects of periodically unsteady inflow on the effectiveness of secondary flow control methods present an interesting option for subsequent research.

The presented test case and multi-methodology investigation approach also provides a solid foundation for subsequent parameter variations such as the operating conditions in terms of Mach and Reynolds number, inlet endwall boundary layer conditions, or the flow coefficient of the incoming wakes. This is a natural follow-up activity to the presented investigation of the mechanisms of wake disturbed secondary flow development. The general effect of these influencing factors on the time-averaged downstream secondary flow has been presented partly by Ciorciari [18] and in the present work in case of endwall boundary layer variation. However, detailed questions remain as for example on the influence of the orientation of the wakes which is a function of the flow coefficient. More precisely, the influence on the negative-jet-effect are of interest and thus on the periodic pressure gradients induced on the suction surface near the endwall. While the presented test case already enables wide-range operating point variations and independent endwall boundary layer variation, the experimental investigation of low flow coefficients requires a redesign of the linear wake generator. A large extension of the wake generator's operating range to high relative bar speeds is very challenging in a high-speed cascade wind tunnel and might require a fundamental shift to an annulus cascade segment with a rotating wake generator. Alternatively, parameter variations beyond the experimental limitations can be covered by numerical simulations. The validity of this approach has been confirmed by the present work which included a persistent comparison of the CFD predictions with the experimental results.

Further progress can also be achieved in the development, adaptation and implementation of advanced measurement techniques specifically for secondary flow investigations in turbine cascades. Particularly the high potential of Temperature-Sensitive Paint (TSP) has been demonstrated in the present work by the successful experimental flat-plate test case. The

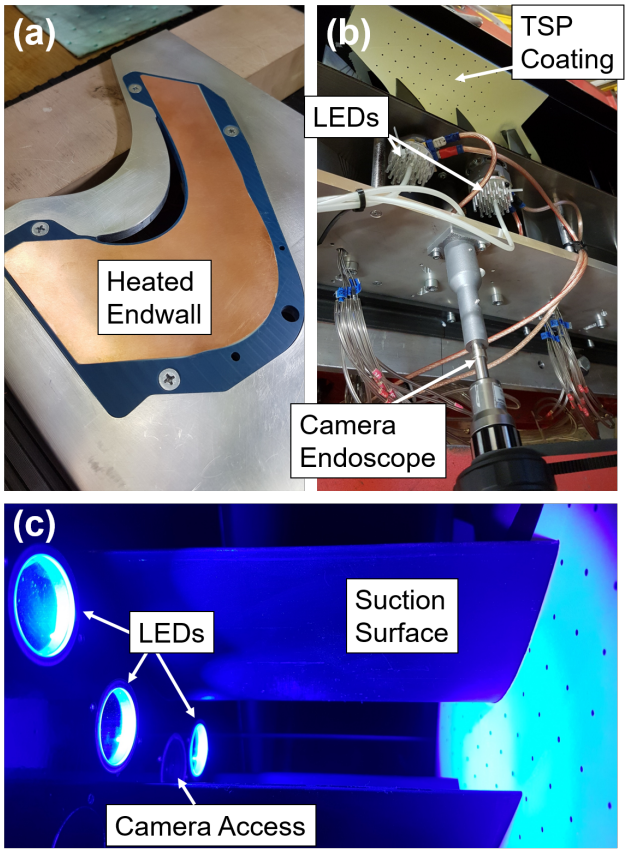

Fig. 5.1: Initial test setup for ultra-fast TSP measurements on the endwall of the T106A turbine cascade

implemented setup reached a high sampling rate of 40,000 Hz with a resolution of the temperature fluctuations down to 10^{-5} K. This enabled the determination of local convective heat transfer coefficients as well as pattern reconstruction of dominant coherent flow structures and their higher harmonics through SPOD analysis. An application in a turbine cascade can provide blade and endwall surface temperature distributions and information on their sensitivity to flow parameter variations. Due to high temperatures in modern low-pressure turbines, the identification of surface hot spots and thus potential cooling implementation is of particular interest. The second major aspect of the potential of TSP is the measurement of highly resolved wall shear stress distributions. The presented CFD predictions on the cascade blade and endwall were essential in the analysis of the endwall flow and its crucial role in the secondary vortex development. Here, widespread experimental data would be of tremendous value for the validation of the challenging CFD predictions of the endwall boundary layer conditions and flow separation. Following the successful preliminary TSP tests on a flat plate, high efforts were made to transfer the gained knowledge to an application on the T106A turbine cascade endwall. The most challenging aspect of the new setup was the transition from a rectangular to a passage-shaped measurement area as shown in Figure 5.1a. Carbon nanotubes were successfully used as an electric resistance heating layer

in the flat-plate tests. However, the distance between the anode and cathode at the edges of the passage-shaped area is not constant. This would result in a non-homogenous temperature distribution. Instead, a total of nine resistance heating pads were distributed over the lower side of a passage-shaped copper sheet embedded in a low thermal conductivity insert (blue component in Figure 5.1a). The optical access was again implemented via a camera endoscope building on the experience from the presented blade-to-blade PIV measurement setup (Figure 5.1b). Custom LED-mounts were also placed in the opposite endwall next to the endoscope. The resulting illumination i.e. excitation of the measurement area with blue (450 nm) light can be seen in Figure 5.1c. The access panels in the endwall were designed to be interchangeable to enable different camera field of views and illumination patterns. Even though all components of the experimental setup were tested individually beforehand, unfortunately, the first wind tunnel tests under engine-relevant conditions did not produce sufficient signal-to-noise ratios to yield viable results. An insufficient sensitivity (intensity change per temperature change) of the active TSP layer was identified as the root cause. Thus, the temperature fluctuations caused by the wakes were too low to generate sufficient intensity fluctuation amplitudes. This issue can be countered by increasing the temperature gradient between the hot endwall surface and the flow. However, the implemented heating pads were not able to generate the necessary heating power beyond their design conditions. An additional minor improvement of the measurement setup can be achieved by utilizing a custom passage-shaped array of LEDs instead of individual high-power LEDs. Thus, the appearance of shadows can be minimized. Nevertheless, the tested setup provides a valuable starting point for further development of TSP applications in turbine cascades as its potential has been demonstrated through the flat-plate test case and the wall shear stress CFD analysis.

Bibliography

[1] ACARE: *Goals – Achieving Climate Neutral Air Mobility.* https://www.acare4europe.org/acare-goals/, visited on April 22 2025.

[2] Bear, P., Wolff, M., Gross, A., Marks, C.R., and Sondergaard, R.: *Experimental Investigation of Total Pressure Loss Development in a Highly Loaded Low-Pressure Turbine Cascade.* J. Turbomach. 140(3), 2018. https://doi.org/10.1115/1.4038413.

[3] Becker, K., Heitkamp, K., and Kügeler, E.: *Recent Progress in a Hybrid-Grid CFD Solver for Turbomachinery Flows.* Proceedings of the Fifth European Conference on Computational Fluid Dynamics ECCOMAS CFD, Lisabon, Portugal, June 14–17, 2010.

[4] Becz, S., Majewski, M.S., and Langston, L.S.: *An Experimental Investigation of Contoured Leading Edges for Secondary Flow Loss Reduction.* Proceedings of the ASME Turbo Expo 2004: Power for Land, Sea, and Air, GT2004-53964, Vienna, Austria, June 14–17, 2004. https://doi.org/10.1115/GT2004-53964.

[5] Benner, M.W., Sjolander, S.A., and Moustapha, S.H.: *An Empirical Prediction Method for Secondary Losses in Turbines—Part II: A New Secondary Loss Correlation.* J. Turbomach. 128(2), 2006. https://doi.org/10.1115/1.2162594.

[6] Benton, S.I., Bernardini, C., Bons, J.P., and Sondergaard, R.: *Parametric Optimization of Unsteady End Wall Blowing on a Highly Loaded Low-Pressure Turbine.* J. Turbomach. 136(7), 2014. https://doi.org/10.1115/1.4026127.

[7] Benton, S.I., Bons, J.P., and Sondergaard, R.: *Secondary Flow Loss Reduction Through Blowing for a High-Lift Front-Loaded Low-Pressure Turbine Cascade.* J. Turbomach. 135(2), 2012. https://doi.org/10.1115/1.4007531.

[8] Bitter, M., Kurz, J., Kähler, C., and Niehuis, R.: *Investigations of a Low-Pressure Turbine Blade by Means of Simultaneous Optical Velocity and Pressure Measurements.* 18th International Symposium on Applications of Laser Techniques to Fluid Mechanics, Lisbon, Portugal, July 4–7, 2016.

[9] Bloxham, M. and Bons, J.P.: *Leading-Edge Endwall Suction and Midspan Blowing to Reduce Turbomachinery Losses.* J. Propul. Power 26(6), 2010. https://doi.org/10.2514/1.46105.

[10] Bode, C.: *Verbesserte Wiedergabe der Turbulenz in Turbinenströmungen und deren Einfluss auf das dreidimensionale Grenzschichtverhalten.* Doctoral Thesis, Technical University of Braunschweig, Brunswick, Germany, 2018, ISBN 978-3-947623-02-0.

[11] Bohn, D.: *Untersuchung zweier verschiedener axialer Überschallverdichterstufen unter besonderer Berücksichtigung der Wechselwirkungen zwischen Lauf- und Leitrad.* Doctoral Thesis, RWTH Aachen, Aachen, Germany, 1977.

[12] Bons, J.P., Benton, S., Bernardini, C., and Bloxham, M.: *Active Flow Control for Low-Pressure Turbines.* AIAA J. 56(7), 2018. https://doi.org/10.2514/1.J056697.

[13] Chemnitz, S.: *Turbulenzproduktion stromab einer hochbelasteten Niederdruckturbinenkaskade unter Einfluss der Profilbelastung und des Seitenwandgrenzschichtzustandes.* Doctoral Thesis, University of the Bundeswehr Munich, Neubiberg, Germany, 2022, ISBN 978-3-8439-5066-4.

[14] Chemnitz, S. and Niehuis, R.: *A Comparison of Turbulence Levels from Particle Image Velocimetry and Constant Temperature Anemometry Downstream of a Low-Pressure Turbine Cascade at High-Speed Flow Conditions.* J. Turbomach. 142(7), 2020. https://doi.org/10.1115/1.4046272.

[15] Chen, Y., Yang, L., and Zhong, J.: *Numerical Study on Endwall Fence With Varying Geometrical Parameters in a Highly-Loaded Compressor Cascade.* Aerosp. Sci. Technol. 94, 2019. https://doi.org/10.1016/j.ast.2019.105390.

[16] Chibli, H.A., Abdelfattah, S.A., Schobeiri, M.T., and Kang, C.: *An Experimental and Numerical Study of the Effects of Flow Incidence Angles on the Performance of a Stator Blade Cascade of a High Pressure Steam Turbine.* Proceedings of the ASME Turbo Expo 2009: Power for Land, Sea, and Air, GT2009-59131, Orlando, Florida, USA, June 8–12, 2009. https://doi.org/10.1115/GT2009-59131.

[17] Chung, J.T. and Simon, T.W.: *Effectiveness of the Gas Turbine Endwall Fences in Secondary Flow Control at Elevated Freestream Turbulence Levels.* Proceedings of the ASME 1993 International Gas Turbine and Aeroengine Congress and Exposition, 93-GT-051, Cincinnati, Ohio, USA, May 24–27, 1993. https://doi.org/10.1115/93-GT-051.

[18] Ciorciari, R.: *Analysis of Unsteady Secodary Flows in Linear Low-Pressure Turbine Cascades.* Doctoral Thesis, Bundeswehr University Munich, Neubiberg, Germany, 2017, ISBN 978-3-8439-3564-7.

[19] Ciorciari, R., Kirik, I., and Niehuis, R.: *Effects of Unsteady Wakes on Secondary Flows in the Linear T106 Turbine Cascade.* J. Turbomach. 136(9), 2014. https://doi.org/10.1115/1.4027374.

[20] Clark, C.J., Pullan, G., Curtis, E., and Goenaga, F.: *Secondary Flow Control in Low Aspect Ratio Vanes Using Splitters.* J. Turbomach. 139(9), 2017. https://doi.org/10.1115/1.4036190.

[21] Clinckemaillie, J., Fattorini, L., Fontani, T., Nuyts, C., Wain, G., and Arts, T.: *Aerodynamic Performance of a Very-High-Lift Low-Pressure Turbine Airfoil (T106C) at Low Reynolds and High Mach Number Including the Effect of Incoming Periodic Wakes.* Proceedings of the 11th European Conference on Turbomachinery Fluid Dynamics and Thermodynamics, ETC2015-251, Madrid, Spain, March 23–27, 2015. https://www.euroturbo.eu/publications/proceedings-papers/etc2015-251/.

[22] Coton, T.: *Unsteady Wake-Boundary Layer Interaction on Advanced High Lift Low Pressure Turbine Airfoils.* Doctoral Thesis, Von Karman Institute / Université de Liège, Liège, Belgium, 2003.

[23] Coull, J.D.: *Endwall Loss in Turbine Cascades.* J. Turbomach. 139(8), 2017. https://doi.org/10.1115/1.4035663.

[24] Coull, J.D. and Hodson, H.P.: *Predicting the Profile Loss of High-Lift Low Pressure Turbines.* J. Turbomach. 134(2), 2011. https://doi.org/10.1115/1.4002961.

[25] Cui, J. and Tucker, P.G.: *Numerical Study of Purge and Secondary Flows in a Low Pressure Turbine.* Proceedings of the ASME Turbo Expo 2016: Turbomachinery Technical Conference and Exposition, GT2016-56789, Seoul, South Korea, June 13–17, 2016. https://doi.org/10.1115/GT2016-56789.

[26] Curtis, E.M., Hodson, H.P., Banieghbal, M.R., Denton, J.D., Howell, R.J., and Harvey, N.W.: *Development of Blade Profiles for Low-Pressure Turbine Applications.* J. Turbomach. 119(3), 1997. https://doi.org/10.1115/1.2841154.

[27] de la Blanco, E.R., Hodson, H.P., Vasquez, R., and Torre, D.: *Influence of the State of the Inlet Endwall Boundary Layer on the Interaction Between Pressure Surface Separation and Endwall Flows.* J. Power and Energy 217(4), 2003. https://doi.org/10.1243/095765003322315496.

[28] Denton, J.D.: *Loss Mechanisms in Turbomachines.* J. Turbomach. 115(4), 1993. https://doi.org/10.1115/1.2929299.

[29] Denton, J.D. and Pullan, G.: *A Numerical Investigation Into the Sources of Endwall Loss in Axial Flow Turbines.* Proceedings of the ASME Turbo Expo 2012: Turbine Technical Conference and Exposition, GT2012-69173, Copenhagen, Denmark, June 11–15, 2012. https://doi.org/10.1115/GT2012-69173.

[30] Donovan, M.H., Wolff, M., Marks, C.R., Sondergaard, R., and Veley, E.: *Periodic Forcing of an Endwall Vortex in a Highly Loaded Low Pressure Turbine.* Proceedings of the AIAA Scitech 2019 Forum, AIAA 2019-0621, San Diego, California, USA, January 7–11, 2019. https://doi.org/10.2514/6.2019-0621.

[31] Duden, A.: *Strömungsbeeinflussung zur Reduzierung der Sekundärströmungen in Turbinengittern.* Doctoral Thesis, Bundeswehr University Munich, Neubiberg, Germany, 1999, ISBN 978-3-8265-4965-6.

[32] Engelmann, D., Sinkwitz, M., di Mare, F., Koppe, B., Mailach, R., Ventosa-Molina, J., Fröhlich, J., Schubert, T., and Niehuis, R.: *Near-Wall Flow in Turbomachinery Cascades – Results of a German Collaborative Project.* J. Turbomach. Propuls. Power 6(2), 9, 2021. https://doi.org/10.3390/ijtpp6020009.

[33] Franke, M., Röber, T., Kügeler, E., and Ashcroft, G.: *Turbulence Treatment in Steady and Unsteady Turbomachinery Flows.* Proceedings of the Fifth European Conference on Computational Fluid Dynamics ECCOMAS CFD, Lisabon, Portugal, June 14–17, 2010.

[34] Förster, F., Sims-Williams, D., Ingram, G., and Dominy, R.: *Time Resolved Measurements in the Durham Cascade.* Proceedings of the ASME 2011 Turbo Expo: Turbine Technical Conference and Exposition, GT2011-45838, Vancouver, British Columbia, Canada, June 6–10, 2011. https://doi.org/10.1115/GT2011-45838.

[35] German Aerospace Center (DLR), Institute of Propulsion Technology: *TRACE Theory.* https://www.trace-portal.de/userguide/trace/page_theory.html, visited on April 22 2025.

[36] Goldstein, R.J., Jin, P., Papa, M., and Gori, F.: *Flow Visualisation and Heat/Mass Transfer in a Linear Turbine Cascade With Tip Clearance.* Australian J. Mech. Eng. 4(1), 2007. https://doi.org/10.1080/14484846.2007.11464515.

[37] Goldstein, R.J. and Spores, R.A.: *Turbulent Transport on the Endwall in the Region Between Adjacent Turbine Blades.* J. Heat Transfer 110(4a), 1988. https://doi.org/10.1115/1.3250586.

[38] Goldstein, R.J., Wang, H.P., and Jabbari, M.Y.: *The Influence of Secondary Flows Near the Endwall and Boundary Layer Disturbance on Convective Transport From a Turbine Blade.* Proceedings of the ASME 1994 International Gas Turbine and Aeroengine Congress and Exposition, 94-GT-165, The Hague, The Netherlands, June 13–16, 1994. https://doi.org/10.1115/94-GT-165.

[39] Gomes, R.A., Kurz, J., and Niehuis, R.: *Development and Implementation of a Technique for Fast Five-Hole Probe Measurements Downstream of a Linear Cascade.* J. Turbomach. Propuls. Power 3(1), 6, 2018. https://doi.org/10.3390/ijtpp3010006.

[40] Gregory, J.W., Sakaue, H., Liu, T., and Sullivan, J.P.: *Fast Pressure-Sensitive Paint for Flow and Acoustic Diagnostics.* Ann. Rev. Fluid Mech. 46(1), 2014. https://doi.org/10.1146/annurev-fluid-010313-141304.

[41] Halstead, D.E., Wisler, D.C., Okiishi, T.H., Walker, G.J., Hodson, H.P., and Shin, H.W.: *Boundary Layer Development in Axial Compressors and Turbines: Part 3 of 4 – LP Turbines.* J. Turbomach. 119(2), 1997. https://doi.org/10.1115/1.2841105.

[42] Hartland, J. and Gregory-Smith, D.: *A Design Method for the Profiling of End Walls in Turbines.* Proceedings of the ASME Turbo Expo 2002: Power for Land, Sea, and Air, GT2002-30433, Amsterdam, The Netherlands, June 3–6, 2002. https://doi.org/10.1115/GT2002-30433.

[43] Hawthrone, W.R.: *Secondary Circulation in Fluid Flow.* Proc. R. Soc. Lond. A 206(1086), 1951. https://doi.org/10.1098/rspa.1951.0076.

[44] Hawthrone, W.R.: *Rotational Flow Through Cascades Part I. The Components of Vorticity.* Q. J. Mech. Appl. Math. 8(3), 1955. https://doi.org/10.1093/qjmam/8.3.266.

[45] Hjärne, J., Chernoray, V., Larsson, J., and Löfdahl, L.: *An Experimental Investigation of Secondary Flows and Loss Development Downstream of a Highly Loaded Low Pressure Turbine Outlet Guide Vane Cascade.* Proceedings of the ASME Turbo Expo

2006: Power for Land, Sea, and Air, GT2006-90561, Barcelona, Spain, May 8–11, 2006. https://doi.org/10.1115/GT2006-90561.

[46] Hodson, H.P. and Dominy, R.G.: *Three-Dimensional Flow in a Low-Pressure Turbine Cascade at its Design Condition.* J. Turbomach. 109(2), 1987. https://doi.org/10.1115/1.3262083.

[47] Hodson, H.P. and Howell, R.J.: *High Lift Low Pressure Turbines.* Proceedings of Minnowbrook III: Workshop on Boundary Layer Transition and Unsteady Aspects of Turbomachinery Flows, Blue Mountain Lake, New York, USA, August 20–23, 2000. https://ntrs.nasa.gov/citations/20020067662.

[48] Hodson, H.P., Hynes, T.P., Greitzer, E.M., and Tan, C.S.: *A Physical Interpretation of Stagnation Pressure and Enthalpy Changes in Unsteady Flow.* J. Turbomach. 134(6), 2012. https://doi.org/10.1115/1.4007208.

[49] Hoheisel, H.: *Test Cases for Computation of Internal Flows in Aero Engine Components: Test Case E/CA6, Subsonic Turbine Cascade T106.* AGARD Propulsion and Energetics Panel Working Group 18 Report, AGARD-AR-275, 1990.

[50] Howell, R.J., Ramesh, O.N., Hodson, H.P., Harvey, N.W., and Schulte, V.: *High Lift and Aft-Loaded Profiles for Low-Pressure Turbines.* J. Turbomach. 123(2), 2001. https://doi.org/10.1115/1.1350409.

[51] Humble, R., Scarano, F., Oudheusden, B., and Tuinstra, M.: *PIV Measurements of a Shock Wave/Turbulent Boundary Layer Interaction.* Proceedings of the 13th International Symposium on Applications of Laser Techniques to Fluid Mechanics, Lisbon, Portugal, June 26–29, 2006.

[52] IATA: *Net Zero Carbon 2050 Resolution.* https://www.iata.org/en/programs/sustainability/flynetzero/, visited on April 22 2025.

[53] IATA: *Global Outlook for Air Transport – Deep Change.* 2024. https://www.iata.org/en/iata-repository/publications/economic-reports/global-outlook-for-air-transport-june-2024-report.

[54] ICAO: *Consolidated Statement of Continuing ICAO Policies and Practices Related to Environmental Protection - Carbon Offsetting and Reduction Scheme for International Aviation.* 2022. https://www.icao.int/environmental-protection/CORSIA/Documents/Resolution_A41-22_CORSIA.pdf.

[55] ICAO: *Effects of Novel Coronavirus (COVID-19) on Civil Aviation: Economic Impact Analysis.* 2023. https://www.icao.int/sustainability/Documents/COVID-19/ICAO_Coronavirus_Econ_Impact.pdf.

[56] Infantino, D., Satta, F., Simoni, D., Ubaldi, M., Zunino, P., and Bertini, F.: *Phase-Locked Investigation of Secondary Flows Perturbed by Passing Wakes in a High-Lift LPT Turbine Cascade.* Proceedings of the ASME Turbo Expo 2015: Turbine Technical Conference and Exposition, GT2015-42480, Montreal, Quebec, Canada, June 15–19, 2015. https://doi.org/10.1115/GT2015-42480.

[57] Ingram, G., Gregory-Smith, D., Rose, M., Harvey, N.W., and Brennan, G.: *The Effect of End-Wall Profiling on Secondary Flow and Loss Development in a Turbine Cascade.* Proceedings of the ASME Turbo Expo 2002: Power for Land, Sea, and Air, GT2002-30339, Amsterdam, The Netherlands, June 3–6, 2002. https://doi.org/10.1115/GT2002-30339.

[58] Ireland, P.T. and Jones, T.V.: *Liquid Crystal Measurements of Heat Transfer and Surface Shear Stress.* Meas. Sci. Technol. 11(7), 2000. https://doi.org/10.1088/0957-0233/11/7/313.

[59] Kawai., T., Shinoki, S., and Adachi, T.: *Visualization of Secondary Flow in a Turbine Cascade With and Without Boundary Layer Fences.* Proceedings of the 2nd International Symposium on Fluid Control, Measurement, Mechanics, and Flow Visualization, Sheffield, UK, September 5–9, 1988.

[60] Kawai., T., Shinoki, S., and Adachi, T.: *Secondary Flow Control and Loss Reduction in a Turbine Cascade Using Endwall Fences.* JSME International Journal, Series II, 32(3), 1989. https://doi.org/10.1299/jsmeb1988.32.3_375.

[61] King, L.V.: *On the Convection of Heat from Small Cylinders in a Stream of Fluid: Determination of the Convection Constants of Small Platinum Wires with Applications to Hot Wire Anemometry.* Phil. Trans. Roy. Soc. 90(622), 1914. https://doi.org/10.1098/rspa.1914.0089.

[62] Kirik, I. and Niehuis, R.: *Comparing the Effect of Unsteady Wakes on Parallel and Divergent Endwalls in a LP Turbine Cascade (T106A-EIZ and T106D-EIZ).* Proceedings of the 11th International Gas Turbine Congress., IGTC2015-137, Tokyo, Japan, November 15–20, 2015.

[63] Kirik, I. and Niehuis, R.: *Experimental Investigations on Effects of Unsteady Wakes on the Secondary Flows in the Linear T106 Turbine Cascade.* Proceedings of the ASME Turbo Expo 2015: Turbine Technical Conference and Exposition. GT2015-43170, Montreal, Quebec, Canada, June 15–19, 2015. https://doi.org/10.1115/GT2015-43170.

[64] Kirik, I. and Niehuis, R.: *Influence of Unsteady Wakes on the Secondary Flows in the Linear T106 Turbine Cascade.* Proceedings of the ASME Turbo Expo 2016: Turbomachinery Technical Conference and Exposition, GT2016-56350, Seoul, South Korea, June 13–17, 2016. https://doi.org/10.1115/GT2016-56350.

[65] Koschichow, D., Fröhlich, J., Ciorciari, R., and Niehuis, R.: *Analysis of the Influence of Periodic Passing Wakes on the Secondary Flow near the Endwall of a Linear LPT Cascade Using DNS and U-RANS.* Proceedings of the 11th European Conference on Turbomachinery Fluid Dynamics and Thermodynamics, ETC2015-151, Madrid, Spain, March 23–27, 2015. https://www.euroturbo.eu/publications/proceedings-papers/etc2015-151/.

[66] Koschichow, D., Fröhlich, J., Kirik, I., and Niehuis, R.: *DNS of the Flow Near the Endwall in a Linear Low Pressure Turbine Cascade with Periodically Passing*

Wakes. Proceedings of the ASME Turbo Expo 2014: Turbine Technical Conference and Exposition, GT2014-25071, Düsseldorf, Germany, June 16–20, 2014. https://doi.org/10.1115/GT2014-25071.

[67] Lakshminarayana, B. and Horlock, J.H.: *Secondary Flows and Losses in Cascades and Axial-Flow Turbomachines*. Int. J. Mech. Science 5(3), 1963. https://doi.org/10.1016/0020-7403(63)90055-9.

[68] Lampart, P.: *Investigation of Endwall Flows and Losses in Axial Turbines. Part I. Formation of Endwall Flows and Losses*. J. Theo. and Appl. Mech. 47(2), 2009. https://www.ptmts.org.pl/jtam/index.php/jtam/article/view/v47n2p321/308.

[69] Lange, C.F., Durst, F., and Breuer, M.: *Correction of Hot-Wire Measurements in the Near-Wall Region*. Experiments in Fluids, 26(5), 1999. https://doi.org/10.1007/s003480050312.

[70] Langston, L.S.: *Secondary Flows in Axial Turbines – A Review*. Ann. NY Acad. Sci. 934(1), 2001. https://doi.org/10.1111/j.1749-6632.2001.tb05839.x.

[71] Lengani, D., Simoni, D., Ubaldi, M., Zunino, P., Bertini, F., and Michelassi, V.: *Accurate Estimation of Profile Losses and Analysis of Loss Generation Mechanisms in a Turbine Cascade*. J. Turbomach. 139(12), 2017. https://doi.org/10.1115/1.4037858.

[72] Lichtfuß, H.J.: *Anwendung neuer Entwurfskonzepte auf Profile für axiale Turbomaschinen, Teil II: Optimale Geschwindigkeitsverteilungen für die Auslegung von Verdichter- und Turbinengittern*. ZTL-Abschlussbericht Bericht 78/054 B, MTU-München, 1979.

[73] Lopes, G., Simonassi, L., and Lavagnoli, S.: *Impact of Unsteady Wakes on the Secondary Flows of a High-Speed Low-Pressure Turbine Cascade*. Int. J. Turbomach. Propuls. Power 8(4), 36, 2023. https://doi.org/10.3390/ijtpp8040036.

[74] Mahendran, M. and Sitaram, N.: *Computational Study of Mach Number Effects on Secondary Flows in a Linear Turbine Cascade*. Proceedings of the 8th International Symposium on Experimental and Computational Aerothermodynamics of Internal Flows, ISAIF8-0084, Lyon, France, July 2–6, 2007.

[75] Mailach, R. and Vogeler, K.: *Recent German Research on Periodical Unsteady Flow in Turbomachinery*. Flow Turbulence Combust 83(4), 2009. https://doi.org/10.1007/s10494-009-9203-5.

[76] Michálek, J., Monaldi, M., and Arts, T.: *Aerodynamic Performance of a Very High Lift Low Pressure Turbine Airfoil (T106C) at Low Reynolds and High Mach Number With Effect of Free Stream Turbulence Intensity*. J. Turbomach. 134(6), 2012. https://doi.org/10.1115/1.4006291.

[77] Moon, Y.J. and Koh, S.R.: *Counter-Rotating Streamwise Vortex Formation in the Turbine Cascade With Endwall Fence*. Computers and Fluids 30(4), 2001. https://doi.org/10.1016/S0045-7930(00)00026-8.

[78] Moore, H. and Gregory-Smith, D.G.: *Transition Effects on Secondary Flows in a Turbine Cascade.* Proceedings of the ASME 1996 International Gas Turbine and Aeroengine Congress and Exhibition, 96-GT-100, Birmingham, UK, June 10–13, 1996. https://doi.org/10.1115/96-GT-100.

[79] Murty, G.V.R. and Venkatrayulu, N.: *Effect of Incidence on Secondary Flows in a Linear Turbine Cascade.* Proceedings of the ASME 1994 International Gas Turbine and Aeroengine Congress and Exposition, 94-GT-381, The Hague, The Netherlands, June 13–16, 1994. https://doi.org/10.1115/94-GT-381.

[80] Niehuis, R. and Bitter, M.: *The High-Speed Cascade Wind Tunnel at the Bundeswehr University Munich after a Major Revision and Upgrade.* Int. J. Turbomach. Propuls. Power 6(4), 41, 2021. https://doi.org/10.3390/ijtpp6040041.

[81] Perdichizzi, A.: *Mach Number Effects on Secondary Flow Development Downstream of a Turbine Cascade.* J. Turbomach. 112(4), 1990. https://doi.org/10.1115/1.2927705.

[82] Pullan, G.: *Secondary Flows and Loss Caused by Blade Row Interaction in a Turbine Stage.* J. Turbomach. 128(3), 2006. https://doi.org/10.1115/1.2182001.

[83] Pullan, G., Denton, J.D., and Curtis, E.: *Improving the Performance of a Turbine With Low Aspect Ratio Stators by Aft-Loading.* J. Turbomach. 128(3), 2006. https://doi.org/10.1115/1.2182000.

[84] Pullan, G., Denton, J.D., and Dunkley, M.: *An Experimental and Computational Study of the Formation of a Streamwise Shed Vortex in a Turbine Stage.* J. Turbomach. 125(2), 2003. https://doi.org/10.1115/1.1545766.

[85] Raffel, M., Willert, C.E., Scarano, F., Kähler, C.J., Wereley, S.T., and Kompenhans, J.: *Particle Image Velocimetry: A Practical Guide – 3rd Edition.* Springer International Publishing, Cham, Switzerland, 2018. https://doi.org/10.1007/978-3-319-68852-7.

[86] Rezasoltani, M. and Schobeiri, M.T.: *Effect of Endwall Contouring on the Performance of a Three-Stage HP Turbine.* Proceedings of GPPS Forum 18 Global Power and Propulsion Society, GPPS-2018-0145, Montreal, Quebec, Canada, May 7–9, 2018. https://doi.org/10.5281/zenodo.1345056.

[87] Romero, S. and Gross, A.: *Numerical Investigation of Active Flow Control of Low-Pressure Turbine Endwall Flow.* J. Propul. Power 35(5), 2019. https://doi.org/10.2514/1.B37281.

[88] Sauer, H., Müller, R., and Vogeler, K.: *Reduction of Secondary Flow Losses in Turbine Cascades by Leading Edge Modifications at the Endwall.* J. Turbomach. 123(2), 2001. https://doi.org/10.1115/1.1354142.

[89] Sauer, H., Schmidt, R., and Vogeler, K.: *Influence of Chord Length and Inlet Boundary Layer on the Secondary Losses of Turbine Blades.* J. Turbomach. 134(1), 2012. https://doi.org/10.1115/1.4003244.

[90] Schobeiri, M.T.: *Turbomachinery Flow Physics and Dynamic Performance – 2nd Edition.* Springer Berlin, Heidelberg, Germany, 2012. https://doi.org/10.1007/978-3-642-24675-3.

[91] Schobeiri, M.T. and Lu, K.: *Endwall Contouring Using Continuous Diffusion: A New Method and its Application to a Three-Stage High Pressure Turbine.* J. Turbomach. 136(1), 2014. https://doi.org/10.1115/1.4023970.

[92] Sciacchitano, A. and Wieneke, B.: *PIV Uncertainty Propagation.* Meas. Sci. Technol. 27, 2016. https://doi.org/10.1088/0957-0233/27/8/084006.

[93] Sharma, O.P. and Butler, T.L.: *Predictions of Endwall Losses and Secondary Flows in Axial Flow Turbine Cascades.* J. Turbomach. 109(2), 1987. https://doi.org/10.1115/1.3262089.

[94] Sieverding, C.H.: *Recent Progress in the Understanding of Basic Aspects of Secondary Flows in Turbine Blade Passages.* J. Eng. Gas Turbines and Power 107(2), 1985. https://doi.org/10.1115/1.3239704.

[95] Sinkwitz, M., Winhart, B., Engelmann, D., di Mare, F., and Mailach, R.: *Experimental and Numerical Investigation of Secondary Flow Structures in an Annular Low Pressure Turbine Cascade Under Periodic Wake Impact – Part 1: Experimental Results.* J. Turbomach. 141(2), 2019. https://doi.org/10.1115/1.4042284.

[96] Sinkwitz, M., Winhart, B., Engelmann, D., and Mare, F. di: *Time-Resolved Measurements of the Unsteady Boundary Layer in an Annular Low-Pressure Turbine Configuration With Perturbed Inlet.* J. Turbomach. 144(1), 2022. https://doi.org/10.1115/1.4051711.

[97] Stadtmüller, P. and Fottner, L.: *A Test Case for the Numerical Investigation of Wake Passing Effects on a Highly Loaded LP Turbine Cascade Blade.* Proceedings of the ASME Turbo Expo 2001: Power for Land, Sea, and Air. Volume 1: Aircraft Engine; Marine; Turbomachinery; Microturbines and Small Turbomachinery, 2001-GT-0311, New Orleans, Louisiana, USA, June 4–7, 2001. https://doi.org/10.1115/2001-GT-0311.

[98] Sugioka, Y., Hiura, K., Chen, L., Matsui, A., Morita, K., Nonomura, T., and Asai, K.: *Unsteady Pressure-Sensitive-Paint (PSP) Measurement in Low-Speed Flow: Characteristic Mode Decomposition and Noise Floor Analysis.* Exp. Fluids 60(108), 2019. https://doi.org/10.1007/s00348-019-2755-9.

[99] Vera, M., Zhang, X.F., Hodson, H.P., and Harvey, N.W.: *Separation and Transition Control on an Aft-Loaded Ultra-High-Lift LP Turbine Blade at Low Reynolds Numbers: High-Speed Validation.* J. Turbomach. 129(2), 2007. https://doi.org/10.1115/1.2437220.

[100] Volino, R.J.: *Effects on Endwall Boundary Layer Thickness and Blade Tip Geometry on Flow Through High Pressure Turbine Passages.* Proceedings of the ASME Turbo Expo 2014: Turbine Technical Conference and Exposition, GT2014-27013, Düsseldorf, Germany, June 16–20, 2014. https://doi.org/10.1115/GT2014-27013.

[101] Volino, R.J., Galvin, C.D., and Brownell, C.J.: *Effects of Unsteady Wakes on Flow Through High Pressure Turbine Passages With and Without Tip Gaps.* Proceedings of the ASME Turbo Expo 2014: Turbine Technical Conference and Exposition, GT2014-27006, Düsseldorf, Germany, June 16–20, 2014. https://doi.org/10.1115/GT2014-27006.

[102] Wang, H.P., Olson, S.J., Goldstein, R.J., and Eckert, E.R.G.: *Flow Visualization in a Linear Turbine Cascade of High Performance Turbine Blades.* J. Turbomach. 119(1), 1997. https://doi.org/10.1115/1.2841006.

[103] Weiss, A.P. and Fottner, L.: *The Influence of Load Distribution on Secondary Flow in Straight Turbine Cascades.* J. Turbomach. 117(1), 1995. https://doi.org/10.1115/1.2835631.

[104] Wieneke, B.: *PIV Uncertainty Quantification from Correlation Statistics.* Meas. Sci. Technol. 26, 2015. https://doi.org/10.1088/0957-0233/26/7/074002.

[105] Xue, Y., Wu, Y., Li, Z., Zhang, Z., and Shi, X.: *Flow Mechanism of a Highly Loaded Low Pressure Turbine Cascade with Integrated-Optimized End Wall Contouring and Root Lean.* Physics of Fluids 36(1), 2024. https://doi.org/10.1063/5.0186775.

[106] Yamamoto, A. and Nouse, H.: *Effects of Incidence on Three-Dimensional Flows in a Linear Turbine Cascade.* J. Turbomach. 110(4), 1988. https://doi.org/10.1115/1.3262222.

[107] Yuan, H., Wu, Y., Zhou, S., Wang, M., Lu, X., and Zhang, Y.: *Nonuniform Height Endwall Fence Optimization of a Low-Pressure Turbine Cascade.* Int. J. Mech. Sci. 250, 2023. https://doi.org/10.1016/j.ijmecsci.2023.108301.

[108] Zess, G.A. and Thole, K.A.: *Computational Design and Experimental Evaluation of Using A Leading Edge Fillet on a Gas Turbine Vane.* Proceedings of the ASME Turbo Expo 2001: Power for Land, Sea, and Air, 2001-GT-0404, New Orleans, Louisiana, USA, June 4–7, 2001. https://doi.org/10.1115/2001-GT-0404.

[109] Zheng, X.S. and Rutherford, D.: *Fuel Burn of New Commercial Jet Aircraft: 1960 to 2019.* ICCT White Paper, 2020. https://theicct.org/sites/default/files/publications/Aircraft-fuel-burn-trends-sept2020.pdf.